Crystal engineering of novel organic-inorganic compounds of N- and O-donor dipyridyl ligands

by

Lesego J. Moitsheki

B.Sc. (Hons), University of North West, South Africa.
M.Sc., Potchefstroom University, South Africa.

Thesis presented to the
UNIVERSITY OF CAPE TOWN
for the degree of
DOCTOR OF PHILOSOPHY

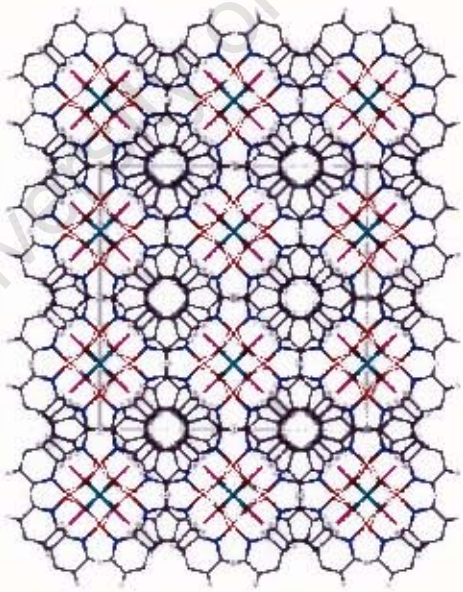

Department of Chemistry, University of Cape Town
Rondebosch, 7701, South Africa

August 2006

Acknowledgements

I would like to thank:

- My supervisors, Prof. Susan A. Bourne and Prof Luigi R. Nassimbeni for their invaluable guidance, dedication as well as excellent ideas and inspiration throughout my doctoral studies.

- Prof Mino R. Caira for his expertise and willingness to help.

- Dr H. Su for single x-ray diffraction data collection.

- Supramolecular chemistry research group (UCT) for their friendship and support. Most of all for a warm welcome to the laboratory and making my daily working atmosphere pleasant. Thank you for valuable discussions.

- My family, girlfriend and various friends for their support and encouragement.

- Thanks granny Debora for taking responsibility of raising me up since childhood.

- UCT/CSIR, UCT Council B and KW Johnston scholarships for financial support.

Publications and conferences

Parts of thesis have been published:

1. 'Catena-Poly[[methanoltrinitratothallium(III)]-μ-*4,4'*-bipyridine-*N,N'*-dioxide thallium(III)', Lesego J. Moitsheki, Susan A. Bourne and Luigi R. Nassimbeni, *Acta Cryst.* (2006). **E62**, m677 – m679.
2. 'A coordination polymer of thallium(III) nitrate with *4,4'*-bipyridine-*N,N'*-dioxide', Lesego J. Moitsheki, Susan A. Bourne and Luigi R. Nassimbeni, *Acta Cryst.* (2006). **E62**, m542 – m544.
3. 'Anion dependent structural diversity in cobalt(II) complexes of *4,4'*-bipyridine-*N,N'*-dioxide', Susan A. Bourne and Lesego J. Moitsheki, *CrystEngComm*, 2005, **7**, 674 – 681.
4. 'Catena-Poly[[bis(thiocyanato-*κN*)cobalt(II)]-di-*μ*-2-aminobenzonitrile-$\kappa^2 N,N'$]', Lesego J. Moitsheki, Susan A. Bourne and Luigi R. Nassimbeni, *Acta Cryst.* (2005). **E61**, m2580 – m2581.

Parts of this thesis have been presented at the following conferences:

1. Poster entitled: Crystal engineering in lanthanide coordination polymers of 4,4´-Dipyridyl-N,N´-dioxide (bpdo), 37th South African Chemical Institute Conference (37th SACI), Pretoria, South Africa, 5-9 July 2004.
2. Oral presentation entitled: Crystal Engineering of Metal-Organic Frameworks (MOF's) using 4,4'-bipyridine-*N,N'* dioxide, SACI Young Scientist Mini Symposium, Stellenbosch, South Africa, 2 June 2005.
3. Poster entitled: Crystal Engineering of Metal-Organic Frameworks using 4,4'-bipyridine-*N,N'* dioxide, 20th International Union of Crystallography (IUCr) Congress, Florence, Italy, 23-31 August 2005
4. Poster entitled: Crystal Engineering of Metal-Organic Frameworks using 4,4'-bipyridine-*N,N'* dioxide, 37th ICCC conference, Cape Town, South Africa, 13-18 August 2006.

Abstract

Title	:	**Crystal engineering of novel organic-inorganic compounds of N and O-donor dipyridyl ligands**
Author	:	**Lesego J. Moitsheki**
Date	:	**August 2006**

Crystal engineering based upon organic-inorganic compounds has made rapid progress in recent years. These compounds are known to combine the inherent advantages of both organic and inorganic substances. In this thesis, a range of metal compounds were investigated. These include compounds of actinides, lanthanides, transition and main group metals using dipyridyl ligands (4,4'-bipyridine-*N,N'*-dioxide (bpdo), 1,2-bis(4-pyridyl)ethane (BPE) and 1,2-di(4-pyridyl)ethylene (DPE)). Compounds prepared were characterised by x-ray diffractometry. Thermal analysis (thermogravimetry (TG), differential scanning calorimetry (DSC) and hot stage microscopy (HSM)) was used to determine the thermal behaviour of these compounds. Microanalysis was used to confirm elemental composition.

Changing the metal geometry while using the same spacer ligand showed a significant effect on the type of organic-inorganic compounds obtained. The effect of the metal salt anion was also examined. Crystal structures show that the materials we obtained were either polymeric or discrete molecules which form a 2D or 3D network by means of supramolecular interactions.
An interesting study was demonstrated by $Co(NO_3)_2$ metal salt. Six different $Co(NO_3)_2$ compounds were prepared at various temperatures (278 K, ambient (295 K – 298 K), 295 K, 298 K and 313 K), while varying solvents ratios.

Isothermal TG has been used to measure kinetic parameters for guest release and decomposition of selected compounds.

Abbreviations and symbols

α	Angle between b and c unit cell vectors or extent of reaction
β	Angle between a and c unit cell vectors
γ	Angle between a and b unit cell vectors
A	Arrhenius pre-exponential factor
bp	Boiling point
CSD	Cambridge Structural Database
DSC	Differential scanning calorimetry
E_a	Activation energy
EtOH	Ethanol
F	Structure factor
F (000)	Number of electrons in the unit cell
HSM	Hot stage microscopy
k	Rate constant
MeOH	Methanol
mp	Melting point
M_r	Molecular mass
1D	One dimensional
2D	Two dimensional
3D	Three dimensional
R	Gas constant = 8.314 $J.K^{-1}.mol^{-1}$
SBU	Secondary building units
T_{on}	Onset temperature
TG	Thermogravimetry
U	Isotropic or anisotropic displacement parameter
V	Unit cell volume
Z	Number of formula units in the unit cell

Table of contents

Chapter 1

Introduction

Aspects of Supramolecular Chemistry

"It is an almost impossible task to write a useful definition of supramolecular chemistry. The field is ever changing as it advances, and researchers will have their own understanding and sets of terminology." – J.W Steed, *Encyclopaedia of Supramolecular Chemistry*, 2004, **2**, 1401.

Jean-Marie Lehn[1] (1978) introduced the concept and expression "supramolecular chemistry" and defined it as being '*concerned with the entities of higher molecular complexity than molecules themselves – chemistry of molecular assemblies held together and organised by means of intermolecular, binding interactions.*' In 1987 the Nobel prize in chemistry was awarded to D.J. Cram, J-M. Lehn and C.J. Pederson for their respective work in the field of supramolecular chemistry. A year later (1988), J-M. Lehn defined supramolecular chemistry informally in his Nobel lecture as "chemistry beyond molecules".[2] The discovery of the chlorine clathrate hydrate [$Cl_2 \cdot 6H_2O$] by Davy[3] in 1811 is considered to have initiated the discipline of supramolecular chemistry. X-rays and their use in structure elucidation were then discovered in 1895 and 1912 respectively which enhanced the growth in this field.

A number of informative books about this field have been written including ten volumes entitled 'Comprehensive Supramolecular Chemistry' published in 1996[4] and the two volume 'Encyclopaedia of Supramolecular Chemistry' published in 2004.[5] Much recent work is now focused on 'Crystal Engineering' defined as the area of supramolecular chemistry devoted to the controlled design of crystalline materials with specific properties. The formation of a crystal is a process of self-assembly of molecules from solution or vapour. It relies on molecular recognition and it is regarded as one of the core concepts of supramolecular chemistry. Crystallography is the ultimate tool in the field of supramolecular chemistry for the understanding of crystal structures, crystal growth and molecular interations.

Due to the rapid and extensive growth of this field, it is impossible to present a comprehensive review of the subject. This introduction will mainly highlight the specific parts of the field which are directly relevant to this study and describe their basic concepts and principles.

Crystal Engineering

"Molecular crystal engineering is the bottom-up construction of functional materials, starting from molecular or ionic building blocks assembled by means of noncovalent interactions." – D. Braga and F. Grepioni, *Encyclopaedia of Supramolecular Chemistry*, 2004, **1**, 357.

Developments in inorganic crystal engineering are composed of two major themes: coordination polymer construction and the use of hydrogen-bonding between suitable building blocks. A substantial number of rationally designed poly-dimensional coordination networks have been constructed by using the concepts of crystal engineering. A major theme in crystal engineering is the preparation of predictable open framework materials with reasonably open space and stability even after the removal of guest. A huge amount of work thus far has used bridging ligands which offer two or more donor units (such 4,4'-bipyridine and its analogues) bound to different metals. [6-12]

The networks designed include diamondoid,[6,7,13-16] bilayer,[17-19] brick wall,[20] helices,[21] honeycomb,[22] ladder,[7,17,20,23] rectangular grids,[24,25,26], square grids[27-33] and triangular grids.[34] The idea is to construct compounds which carry advantages of both organic and inorganic substances.[35] When the intermolecular interaction that holds the building blocks of an infinite repeating system is a coordination bond, the product is termed a coordination polymer. As long as the axially coordinated ligand is bidentate, it is expected that the product should be polymeric. Other types of infinite supramolecular compounds are due to hydrogen bonding, π-interactions and other molecular interactions which are collectively named as "supramolecular synthons".

Supramolecular synthons

G.R. Desiraju developed and defined the concept of *supramolecular synthons* as the "structural units within supermolecules which can be formed and/or assembled by known or conceivable synthetic operations involving intermolecular interations".[36] The term *synthon* was initially introduced by Corey in 1967, in the context of organic chemical reactions.

Surprisingly, the subject of hydrogen bonding is still under debate and a definition has been controversial over the years. Desiraju[37] has written a book in which he made a substantial contribution to the study of hydrogen bonding and other intermolecular interactions. A hydrogen bond, X–H···A (X, donor; A, acceptor), is an interaction wherein a hydrogen atom is attracted to two atoms, X and A, rather than just one and so acts like a bridge between them.[38] The strength of attraction always increases with the increase in electronegativity of X and A. Hydrogen bonds are electrostatic interactions but the proportion of the electrostatic nature can differ. The concept of the hydrogen bond as an electrostatic interaction dates back to Pauling's work who assumed that the H atom would be deshielded only if X and A are very electronegative (Br, Cl, F, N, O) and this in turn will result in sufficiently high electrostatic attraction between H and A to call this interaction a bond. Hydrogen bonds are directional interactions which prefer linear geometries.[39]

Examples of conventional strong hydrogen bond interactions include O–H···O and N–H···O, while weak hydrogen bond interactions are C–H···O, C–H···N, P–H···O, M–H···O (M = metal), I···I, O···I, N···Cl, C···H, C···C and C–H···π. The distance between the donor and acceptor atoms range from 2.2 Å – 4.0 Å with a typical hydrogen bonded O···O interaction distance of 2.5 Å – 2.8 Å. The conservative distance for C···O interaction is 3.25 Å in a C–H···O geometry, while H···N is 2.41 Å in C–H···N.[38,40]

Intermolecular interactions which are specific to organic-inorganic hybrid compounds were studied by Braga and co-workers.[41,42]

Gillion *et al.*[43] did some work based on the use of the M–X···H–N hydrogen bond synthons to prepare crystalline salts through charge-assisted hydrogen bonding interactions between hydrogenated bipyridine ligands (4,4'-H_2bipy) and different metal halide anions, MX_4 (M = Pt, Pb, Pd, Zn, Co, Hg, Mn and Cd; X = Cl and Br). Crystalline materials which are held together by charge-assisted hydrogen bonding interactions and coulombic forces between organometallic building blocks such as the dicarboxylic acids $Fe(C_5H_4COOH_2)$ and $[Co(C_5H_4COOH_2]^{2+}$ were subsequently reported.[44]

The other kind of interaction is the M···M interaction. The common types are Ag···Ag and Au···Au interactions that are generally known to influence molecular conformation and crystal packing.[8,45-48]

π···π interactions

Janiak[49a] carried out a geometrical analysis on π···π stacking in metal complexes with aromatic nitrogen-containing ligands based on a Cambridge Structural Database (CSD) search. The study revealed that a face-face π···π alignment where most of the ring planes area overlaps was a rare phenomenon. The usual π···π interaction is an offset or slipped stacking. π···π interaction is commonly used for stacks of aromatic rings with approximately parallel molecular planes separated by interplanar distances of about 3.3 – 3.8 Å. For centroid to centroid distances up to 3.8 Å the displacement angle lied around 20°. An increased reference of π···π in recent years can be noted, but still few details are given. A study on the nature of π···π interaction using an electrostatic model to explain the strong geometrical requirements for interactions between aromatic molecules was performed on porphyrins.[49b]

Molecular organic-inorganic hybrids

In recent years a notable amount of research has been done in the area of molecular organic-inorganic hybrids. Compounds of different dimensionality have been synthesised and characterised. The ligands containing two 4-

pyridyl donors have been extensively used to construct compounds of different topological architectures. The principle is to utilise a building block approach to synthesise several novel networks with a high degree of porosity that can be used for various functions such as gas storage, catalysis, solvent adsorption and separation, water purification, etc. In this case, researchers are faced with the challenge of choosing the right spacer ligand with a specific desired pore size and function. Metals are classified as connectors and ligands as linkers. Examples of different linkers used for organic-inorganic hybrids are shown Figure 1.1.[50]

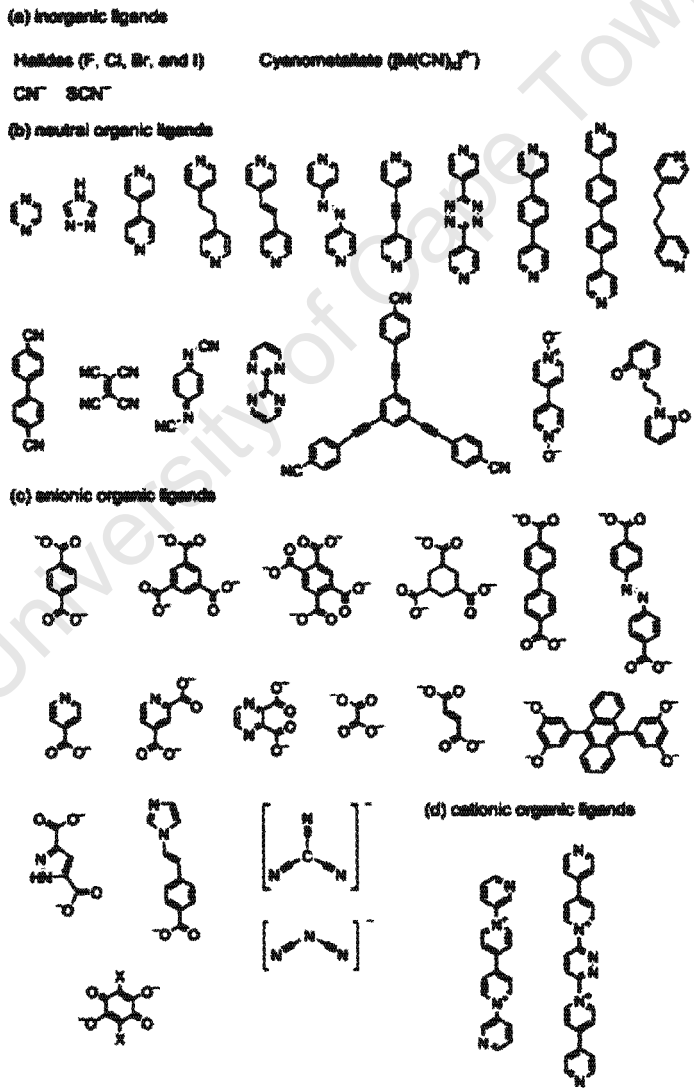

Figure1.1: Examples of linkers used as building blocks.[50]

Literature and CSD[51] (Version 5.27, November 2005) search revealed that less research has been carried out on actinides and lanthanides using bpy, BPE and/or DPE. A number of compounds obtained showed crystal structures connected through hydrogen bonding between the inorganic chains, lattice water and bpy, to form infinite supramolecular chains. In most reported compounds, bpy is protonated $[H_2bpy]^{2+}$. [73-79]

To the best of our knowledge based on the CSD,[51] lanthanides and actinides research using the bpdo ligand has not been extensively explored. Unlike with pyz and bpy, bpdo is less likely to form coordination polymers with transition metals. In cases where they do, the polymer prepared is a one dimensional with adjacent chains connected by intermolecular interactions giving rise to a two layered architecture.[80-83]

Ma *et al.*[84] have constructed Cu(II) compounds with variable dimensionality from mononuclear and trinuclear coordination and have one and two dimensions. These compounds further demonstrate the difficulty of achieving open framework coordination polymers using bpdo. The mononuclear compound consists of Cu(II) coordinated by six bpdo ligands $[Cu(bpdo)_6]^{2+}$ and balanced by two uncoordinated perchlorate anions, while the trinuclear compound is a Cu^{2+} ion located at the centre of inversion and coordinated by two bpdo ligands (Figure 1.3(a) and (b)). The other crystal structure is an ionic pair consisting of a hydrated $[Cu(H_2O)_6]^{2+}$ cation, two Cl^- and bpdo molecules, and two crystal lattice water molecules. Ma[34] also carried out some work on Co(II), Ni(II), Cu(II) and Zn(II), but employing different preparation methods. The crystal structures achieved were isostructural. An attempt with Fe(II) and Cd(II) gave discrete ions of $[M(H_2O)_5(bpdo)]^{2+}$ and SO_4^{2-} anions with four water molecules of solvation.[85] Their recent work on Mn(II) and Co(II) produced a three dimensional hydrogen bonded diamondoid network with metal centres bridged by double bpdo ligands.[86]

Due to vast work done on metal-organic hybrids using these linkers, the literature discussed here will be mostly related to the work carried out in this thesis. The background will cover a broad scope of various metals.

The assembly of molecules in a coordination compound is through covalent and/or intermolecular forces. Coordination numbers ranges from 2 – 7 (transition metals) and 7 – 10 (lanthanides and actinides), depending on the metal and its oxidation state giving rise to different geometries (T- or Y-shaped, tetrahedral, square planar, square pyramidal, trigonal pyramidal, octahedral, trigonal-prismatic, pentagonal-bipyramidal and the corresponding irregular forms.[50]

Most frequently used linkers are the neutral organic ligands such as pyrazine (pyz) and bipyridine (bpy). A CSD[51] search revealed that ~1500 and ~350 crystal structures including pyz and bpy respectively have been reported. Charmant *et al.*[52] have recently reported one dimensional coordination polymers of $Bi(SC_6F_5)$ using dipyridyl ligands which consist of five and six coordination sites $[Bi(SC_6F_5)_3(thf/dmf)(L)_n]$; (L = bpy, BPE and *n* ranges from 1 – 3) occupied by the thiolate and pyridyl ligands. The five coordination geometry is uncommon in bismuth complexes.
Lead containing coordination polymers $[PbX_2(bpy/pyz)]_n$ (X = Cl, Br, I) resulted in 2D polymers with adjacent polymer chains bridged by halides.[53-56]

Most researchers often use transition metals as versatile connectors in the preparation of coordination polymers. Hou and co-workers have recently reported three Mn(II) coordination polymers using bpy that show nonlinear optical activity (NLO, measured by Z-scan technique).[57]

Silver complexes are known to produce very interesting crystal structures with unusual intermolecular interaction. A Ag(I) polymer which consists of cationic complex chains, anionic complex chains and solvent water molecules have been reported. The polymer has two different silver coordination geometries: trigonal (cationic chain) and square planar (anionic chain). The crystal structure shows a typical Ag···Ag separation between neighbouring chains of

3.398 Å.[48] Similar kind of M···M interaction with Ag···Ag = 3.175 Å was also reported.[47]

In addition, more recent coordination polymers of bpy,[28,30,33,58-63] pyrazine,[64-67] 1,2-bis(4-pyridyl)ethane (BPE) and 1,2-di(4-pyridyl)ethylene (DPE),[68-72] have been reported.

Previously, microporous silicas and aluminosilicates such as zeolites have been utilised for separation, storage and heterogenous catalysis, but recent research has shown that more versatile metal-organic frameworks with desired cavity size can be prepared using inorganic coordination polymers. Biradha and Fujita[9] have demonstrated this concept by choosing a longer bifunctional ligand, to obtain bigger square grid networks. The use of an electron rich ligand containing an anthracene moiety formed opened square grids (Figure 1.2) only in the presence of nitrobenzene or cyanobenzene, while in the presence of benzene it formed interpenetrated grids.

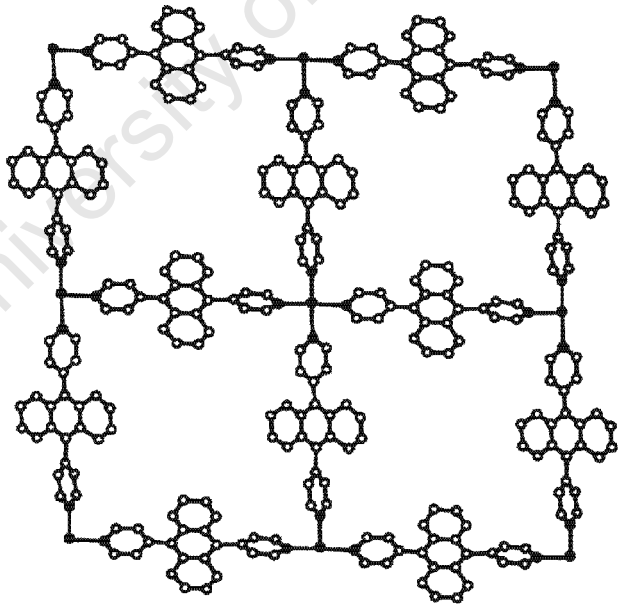

Figure 1.2: The 2D square grid network of $\{[Ni\{9,10\text{-bis}(4\text{-pyridyl})\text{anthracene}\}_2(H_2O)]\cdot 2NO_3\}_n$. Picture adopted from Kitangawa *et al.* [50]

Literature and CSD[51] (Version 5.27, November 2005) search revealed that less research has been carried out on actinides and lanthanides using bpy, BPE and/or DPE. A number of compounds obtained showed crystal structures connected through hydrogen bonding between the inorganic chains, lattice water and bpy, to form infinite supramolecular chains. In most reported compounds, bpy is protonated $[H_2bpy]^{2+}$. [73-79]

To the best of our knowledge based on the CSD,[51] lanthanides and actinides research using the bpdo ligand has not been extensively explored. Unlike with pyz and bpy, bpdo is less likely to form coordination polymers with transition metals. In cases where they do, the polymer prepared is a one dimensional with adjacent chains connected by intermolecular interactions giving rise to a two layered architecture.[80-83]

Ma *et al.*[84] have constructed Cu(II) compounds with variable dimensionality from mononuclear and trinuclear coordination and have one and two dimensions. These compounds further demonstrate the difficulty of achieving open framework coordination polymers using bpdo. The mononuclear compound consists of Cu(II) coordinated by six bpdo ligands $[Cu(bpdo)_6]^{2+}$ and balanced by two uncoordinated perchlorate anions, while the trinuclear compound is a Cu^{2+} ion located at the centre of inversion and coordinated by two bpdo ligands (Figure 1.3(a) and (b)). The other crystal structure is an ionic pair consisting of a hydrated $[Cu(H_2O)_6]^{2+}$ cation, two Cl^- and bpdo molecules, and two crystal lattice water molecules. Ma[34] also carried out some work on Co(II), Ni(II), Cu(II) and Zn(II), but employing different preparation methods. The crystal structures achieved were isostructural. An attempt with Fe(II) and Cd(II) gave discrete ions of $[M(H_2O)_5(bpdo)]^{2+}$ and SO_4^{2-} anions with four water molecules of solvation.[85] Their recent work on Mn(II) and Co(II) produced a three dimensional hydrogen bonded diamondoid network with metal centres bridged by double bpdo ligands.[86]

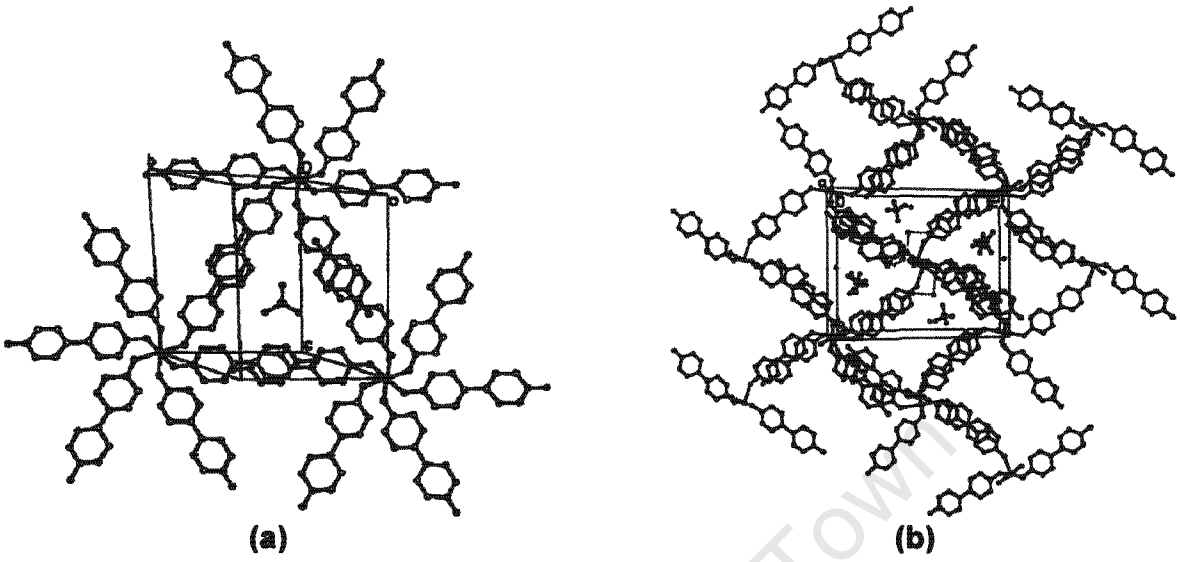

Figure 1.3: Cu(II) complexes using bpdo. **(a)** mononuclear and **(b)** trinuclear compounds.[84]

Enviromentally unstable crystals which immediately lose solvent when removed from mother liquor were obtained from mixture of methanolic solutions of bpdo and $Zn(SiF_6)$: $[Zn(MeOH)_2(bpdo)_3](SiF_6)\cdot 3MeOH$, while $Zn(NO_3)_2$ produced a crystal structure that is composed of discrete $[Zn(bpdo)_6]^{2+}$ cations and uncoordinated nitrate anions.[87] Crystallisation of Co(II) gave a compound which is isostructural to that with $Zn(NO_3)_2$.
$M(NO_3)_2$ (M = Co, Ni) crystal structures of the formula $[M(NO_3)_2(H_2O]\cdot(bpdo)_4$ were also reported.[6]

Long and co-workers[7] constructed Tb(III) polymers with either zigzag or ladder shapes using bpdo. The zigzag chains are linked by hydrogen bonding forming a 3D diamondoid shape, while the latter formed channels which accommodated CH_2Cl_2, C_2Cl_4 and CH_3OH solvent molecules. They further demonstrated that coordination polymers of various structural topologies can be prepared with other lanthanide group metals.[11,88-91]

A novel one dimensional chain of Eu(III) complex $[Eu_2(BTA)(bpdo)]_n$ (BTA = benzoyltrifluoroacetone)[92] containing dimers bridged by terminal oxygen

atoms of bpdo ligands was elucidated. The dimer showed an Eu···Eu interation with distances of 4.26 Å.

To our knowledge and the CSD,[51] no actinide metal-organic compounds using bpdo have been reported.

Other interesting coordination polymers of different ligands have been previously reported. Amongst others, coordination polymers of $M(NCS)_2$ with 2-, 3- and 4-aminobenzonitrile (ABN) isomers, investigated by Vujovic *et al.*[93,94], possesses different kinds of hydrogen bonding networks. In addition to hydrogen bonded networks, the ABN isomers also form one-, two- and three-dimensional polymeric networks as a result of different coordination preferences, such as coordination to the metal centre using either amine or cyanide N atoms, or in a bridging fashion (using both N donors).

Crystal engineering has developed rapidly and there are other challenges beyond crystal structure elucidation. The question which arises is what useful properties can be exploited with the resulting compound? Champness[95] has written a review paper which is entitled "Coordination frameworks – where next?" The significant challenge is to synthesise coordination frameworks with specific properties and functionality.

Gas Storage and sorption of organic vapors

The new development is metal-organic frameworks (MOFs) as a new form of robust porous materials constructed using secondary building units (SBUs). SBUs are molecular units used as a basis for the design of highly porous zeolite-like compounds with certain specific functions. Figure 1.4 shows a selection of porous functions demonstrated by porous coordination polymers.[50]

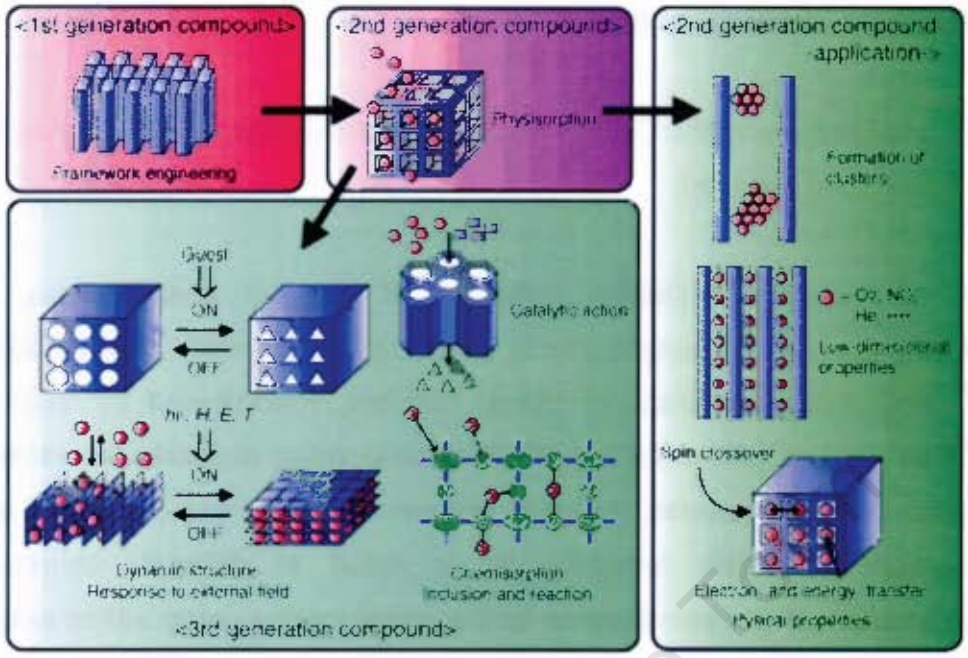

Figure 1.4: A selection of porous functions demonstrated by porous coordination polymers.[50]

By using the concept of SBUs, Rowsell and Yaghi[96] have constructed a series of metal frameworks of different sizes, but the same cubic topology, which exhibit the desired functional properties (Figure 1.5).

atoms of bpdo ligands was elucidated. The dimer showed an Eu···Eu interation with distances of 4.26 Å.

To our knowledge and the CSD,[51] no actinide metal-organic compounds using bpdo have been reported.

Other interesting coordination polymers of different ligands have been previously reported. Amongst others, coordination polymers of $M(NCS)_2$ with 2-, 3- and 4-aminobenzonitrile (ABN) isomers, investigated by Vujovic *et al.*[93,94], possesses different kinds of hydrogen bonding networks. In addition to hydrogen bonded networks, the ABN isomers also form one-, two- and three-dimensional polymeric networks as a result of different coordination preferences, such as coordination to the metal centre using either amine or cyanide N atoms, or in a bridging fashion (using both N donors).

Crystal engineering has developed rapidly and there are other challenges beyond crystal structure elucidation. The question which arises is what useful properties can be exploited with the resulting compound? Champness[95] has written a review paper which is entitled "Coordination frameworks – where next?" The significant challenge is to synthesise coordination frameworks with specific properties and functionality.

Gas Storage and sorption of organic vapors

The new development is metal-organic frameworks (MOFs) as a new form of robust porous materials constructed using secondary building units (SBUs). SBUs are molecular units used as a basis for the design of highly porous zeolite-like compounds with certain specific functions. Figure 1.4 shows a selection of porous functions demonstrated by porous coordination polymers.[50]

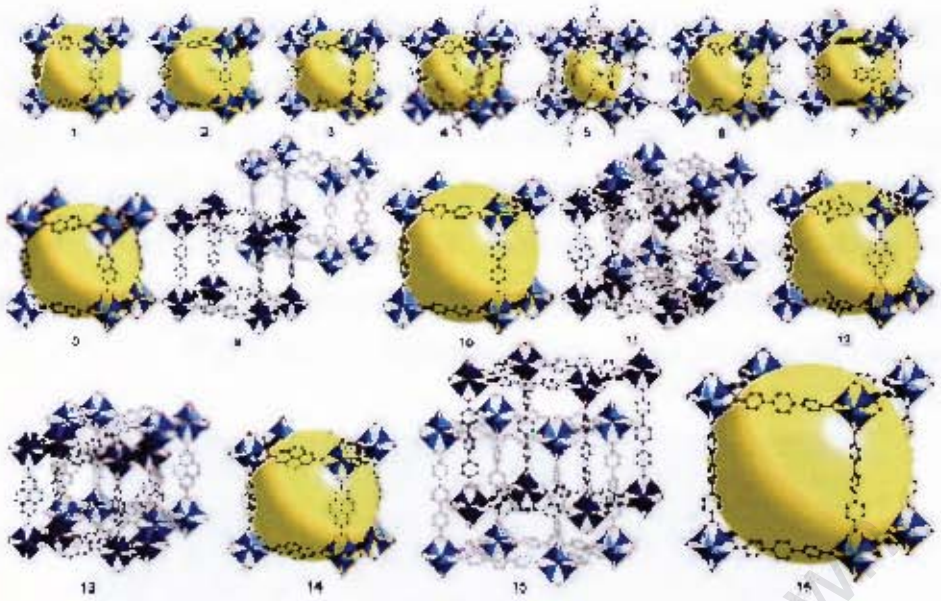

Figure 1.5: A series of 16 metal-organic frameworks of the formula $Zn_4O(L)_3$, L = rigid linear dicarboxylate created by Rowsell and Yaghi.[96]

Some remarkable research on gas absorption by porous metal-organic crystals has been done by Yaghi and co-workers.[96-101] These compounds showed some strong potential as adsorbents for argon (Ar) or nitrogen (N_2) storage and sorption of organic vapors of CH_2Cl_2, $CHCl_3$, C_6H_6, CCl_4, C_6H_{12}. More work on sorption of Ar, CO_2, N_2 gases and organic vapors was further explored by Chui,[102] Li,[103] Barthelet,[104] Noro.[105] Maji[106] and co-workers.

Kondo *et al.*[107] reported a bilayer framework structure capable of reversible adsorption of CH_4, N_2 and O_2 at ambient temperature. Recently, three dimensional metal complexes from copper dicarboxylates and triethylenediamine which have an ideal porosity capable of high CH_4 adsorption were synthesised.[108]

Fossil fuels are a primary source of energy, but the production process possesses several problems such as increasing level of pollution and low conversion efficiency. Hydrogen-based fuel cells have emerged as the possible alternative technology for mobile applications; hence hydrogen storage and separation research is critical. Atwood *et al.*[109] prepared

main difficulty in controlling these reactions is grinding time and pressure exerted by the operator giving rise to changes in temperature. Solid-solid reactions are considered as a "green route" to crystal engineering. Braga and Grepioni have done some significant work in preparing coordination compounds of different ligands using the co-grinding methodology. Recently, they used $[Fe(\eta^5\text{-}C_4H_5\text{-}1\text{-}C_5H_4N)_2]$ to prepare a series of mixed-metal compounds with various transition metal salts.[116-120]

The study of solid-solid reactions dates back to 1970, the year in which Rastogi did some work on classification of solid state reactions.[121] In the solid state, the reactant molecules cannot move freely as compared to other phases, hence solid reactions are diffusion-controlled reactions. Toda,[122] Rothernberg[123] and their co-workers demonstrated that solid state reactions can proceed to completion more efficiently than in solution.

Trask *et al.*[124] employed the "solvent drop grinding" methodology to control polymorphic product of cocrystallisation of caffeine and glutaric acid.

Kinetic study

Kinetics theory of the solid state has been comprehensively discussed by Brown.[125] For a homogenous reaction, the rate of reaction is conveniently measured by the decrease in concentration of reactants or the increase in concentration of products at constant temperature. The rate can be expressed as:

$$R = k_T f \text{ (concentration of reactants and products)}$$

where k_T is the rate coefficient which is a function of temperature. k_T is related to the temperature by the Arrhenius equation:

$$k_T = Ae^{-E_a/RT} \qquad (\text{or } Ln\ k_T = -E_a/RT + Ln\ A)$$

E_a is defined as the activation energy which reactant molecules must have in order to react, while A is the pre-exponential factor or frequency factor refers to the number of collisions, but which has no ready interpretation when applied to the solid state.

For a heterogeneous reaction of the general form

$$A\ (s) + nB\ (g) \rightarrow AB_n\ (s)$$

the change in concentration of the reactants or products cannot be used to follow the reaction, but instead the reaction is monitored by the extent of the reaction, α, defined as:

$$a = (m_i - m_t)/(m_i - m_f)$$

m_i is the initial mass of the reactants, m_f is the final mass of the products and m_t is the mass of sample at any time t.

α can be measured as a function of time at constant temperature for kinetic studies. In that case, the generalised experimental α-time curve under isothermal conditions has the features illustrated in Figure 1.7, which consists surface adsorption or desorption (A), the formation of nuclei called the induction period (B), acceleration period (C), maximum rate of reaction (D), deceleration period (E) and completion of the reaction (F).

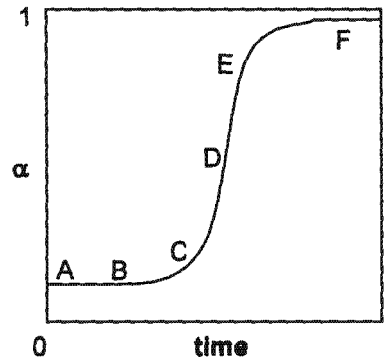

Figure 1.7: The generalised isothermal α-time curve for a solid state reaction.

The kinetic analysis of isothermal reactions involves attempting to relate the experimentally measured α and t values with values predicted for a limited set of models based on processes of nucleation and growth, diffusion or geometrical progress of the reactant/product interface. The expressions derived from these ideal geometrical models can all be written in their integral forms $f(\alpha) = kt$, as summarised in Table 1.1.[125]

Table 1.1: Broad classification of solid-state rate expressions.

		Kinetic model	$f(\alpha) = kt$
Sigmoid α-time curves		**B1** Prout-Tompkins	$\ln[\alpha/(1-\alpha)]$
		A2 Avrami-Erofeev	$[-\ln(1-\alpha)]^{1/2}$
		A3 Avrami-Erofeev	$[-\ln(1-\alpha)]^{1/3}$
		A4 Avrami-Erofeev	$[-\ln(1-\alpha)]^{1/4}$
Acceleratory α-time curves		**P1** power law	$\alpha^{1/n}$
		E1 exponential law	$\ln\alpha$
Deceleratory α-time curves	based on geometrical models	**R2** contracting area	$1-(1-\alpha)^{1/2}$
		R3 contracting volume	$1-(1-\alpha)^{1/3}$
	based on diffusion mechanisms	**D1** one-dimensional	α^2
		D2 two-dimensional	$(1-\alpha)\ln(1-\alpha)+\alpha$
		D3 three-dimensional	$[1-(1-\alpha)^{1/3}]^2$
		D4 Ginstling-Brounshtein	$(1-2\alpha/3)-(1-\alpha)^{2/3}$
	based on "order of reaction"	**F1** first order	$-\ln(1-\alpha)$
		F2 second order	$1/(1-\alpha)$
		F3 third order	$[1/(1-\alpha)]^2$

About this study

This study targeted the preparation of hybrid organic-inorganic compounds of dipyridyl ligands (bpdo, BPE and DPE) using various metals. Most of this work covers compounds prepared using bpdo. BPE and DPE were only used in preparing gold complexes (Chapter 6). The aim was to prepare 1-, 2- and/or 3D networks which combine advantages of organic (structural diversity, luminescence) and inorganic (high electron mobility, mechanical and thermal stability) substances. These compounds were to be considered for use in for various functions such as gas storage, catalysis, solvent adsorption and separation, and water purification.

A range of metal complexes were studied. These include compounds of actinides (U(VI)), lanthanides (Tb(III), Gd(III)), transition (Co(II), Cu(II), Zn(II), Au(III)) and main group (Tl(III), Pb(II)) metals with various metal anions to form either discrete or coordination polymers. The crystal structures of these compounds have been elucidated using single x-ray diffractometry and further characterisation was performed by IR, PXRD, thermal and elemental analyses. These compounds were prepared using different crystallisation methods (described in Chapter 2) which also gave rise to different structural topologies.

The structure of compounds which were crystallised from variable solvent mixtures, or obtained at different crystallisation temperatures, were elucidated. We also studied their kinetics of desolvation and decomposition.

All of the compounds studied possesses $\pi\cdots\pi$ interactions due to aromatic rings of the dipyridyl ligands and hydrogen bond networks. In some cases, isostructural compounds were prepared.

This work also demonstrates that by changing metal geometries, while using the same spacer ligand, has an effect on the type of metal-organic compounds obtained.

References

1. J-M. Lehn, *Pure Appl. Chem.*, 1978, **50**, 871.
2. J-M. Lehn, *Angew. Chem., Int. Ed. Engl.* (Nobel lecture), 1988, **27**, 89.
3. H. Davy, *Philos. Trans. R. Soc. London.*, 1811, **1**, 101.
4. J.L. Atwood, J.E.D. Davies, D.D. MacNicol and F. Vögtle, *Comprehensive Supramolecular Chemistry*, Vol. 1-10, eds., Pergamon, Oxford, 1996.
5. J.L. Atwood and J.W. Steed, *Encyclopaedia of Supramolecular Chemistry*, Vol. 1-2, eds. Marcel Dekker, Inc., New York, 2004.
6. A.J. Blake, M.T. Brett, N.R. Champness, A.N. Khlobystov, D-L. Long, C. Wilson and M. Schröder, *Chem. Commun.*, 2001, 2258.
7. D-L. Long, A.J. Blake, N.R. Champness, C. Wilson and M. Schröder, *Chem. Eur.*, 2002, **8**, 2026.
8. A. J. Blake, N. R. Champness, P. Hubberstey, W-S. Li, M. A. Withersby, M. Schröder, *Coord. Chem. Rev.*, 1999, **183**, 117.
9. K. Biradha and M. Fujita, *J. Chem. Soc., Dalton Trans.*, 2000, 3805.
10. S-L. Ma, W-X. Zhu, G-H. Huang, D-Q. Yuan, X. Yan, *J. of Mol. Struc.*, 2003, **646**, 89.
11. D-L. Long, A.J. Blake, N.R. Champness, C. Wilson and M. Schröder, *J. Am. Chem. Soc.*, 2001, **123**, 3401.
12. C.S. Lai and E.R.T. Tiekink, *CrystEngComm.*, 2004, **6**, 593.
13. M. Hayashi, Y. Miyanoto and T. Oguni, *J. Chem. Soc., Chem. Commun.*, 1992, 1752.
14. L.R. MacGillvray, S. Subramanian and M.J. Zaworokto, *J. Chem. Soc., Chem. Commun.*, 1994, 1325.
15. L. Carlucci, G. Ciani, D. M. Prosperio, and A, Sironi, *J. Chem. Soc., Chem. Commun.*, 1992, 2755.
16. O.M. Yaghi and H. Li, *J. am. Chem. Soc.*, 1995, **117**, 10401.
17. T.L. Hennigar, D.C MacQaurrie, P. Losier, R.D. Rogers and M.J. Zaworokto, *Angew. Chem., Int. Ed. Engl.*, 1997, **36**, 972.
18. M. Kondo, T Yoshimoto, K. Seki, H. Matsuzaka and S. Kitagawa, *Angew. Chem., Int. Ed. Engl.*, 1997, **36**, 1725.

19. K.N. Power, T.L. Hennigar, and M.J. Zaworokto, *New J. Chem.*, 1998, 177.

20. M. Fujita, Y.J. Kwon, O Sasaki, K. Yamaguchi, and K. Ogura, *J. Am. Chem. Soc.*, 1995, **117**, 7287.

21. K. Biradha, C. Seward, M.J. Zaworokto, *Angew. Chem., Int. Ed.,* 1999, **38**, 492.

22. G.B. Gardner, D. Venkataraman, J.S. Moore, and S. Lee, *Nature (London)*, 1995, **374**, 792.

23. P. Losier and M.J. Zaworokto, *Angew. Chem., Int. Ed. Engl.,* 1996, **35**, 2779.

24. L.R. MacGillvray, R.H. Groeneman and J.L. Atwood, *J. Am. Chem. Soc.*, 1998, **120**, 2676.

25. M-L. Tong, X-M. Chen, X-L. Yu and T.C.W. Mak, *J. Chem. Soc., Dalton. Trans.*, 1998, 5.

26. S.A. Bourne, J. Lu, B. Moulton and M.J. Zaworokto, *Chem. Commun.*, 2001, 861.

27. R.W. Gable, B.F. Hoskins and R. Robson, *J. Chem. Soc., Chem. Commun.*, 1990, 1677.

28. M. Fujita, Y.J. Kwon, S. Washizu and K. Ogura, *J. Am. Chem. Soc.*, 1994, **116**, 1151.

29. S. Subramanian and M.J. Zaworokto, *Angew. Chem., Int. Ed. Engl.*, 1995, **34**, 2127.

30. J. Lu, T. Paliwala, S.C. Lim, C. Yu, T. Niu and A.J. Jacobson, *Inorg. Chem.*, 1997, **36**, 923.

31. M-L. Tong, B-H. Ye, J-W. Cai, X-M. Chen and S.W. Ng, *Inorg. Chem.*, 1998, **37**, 2645.

32. K. Biradha, K.V. Domasasevitch, C. Seward, C. Hogg, B. Moulton and M.J. Zaworokto, *Chem. Commun.,* 1999, 1327.

33. K. Biradha, K.V. Domasasevitch, C. Hogg, B. Moulton, K.N. Power and M.J. Zaworokto, *Cryst. Eng.,* 1999, **2**, 37.

34. B-Q. Ma, S Gao, H-L. Sun and G-X. Xu, *J. Soc., Dalton Trans.,* 2001, 130.

35. D. Mitzi, *J. Chem. Soc., Dalton Trans.*, 2001, 1.

36. G.R. Desiraju, *Angew. Chem., Int. Ed. Engl.*, 1995, **34**, 2311.

37. G.R. Desiraju, Crystal engineering: The Design of Organic Solids, Elsevier, Amsterdam, 1989.
38. G.R. Desiraju, *Acc. Chem. Res.*, 2002, **35**, 565.
39. T. Steiner, *Cryst. Rev.*, 1996, **Vol 6**, 1.
40. J.W. Steed and J.L. Atwood, *Supramolecular Chemistry*, John Wiley and Sons, LTD., Chichester, 2000.
41. D. Braga and F. Grepioni, *Acc. Chem. Res.*, 1994, **27**, 51.
42. D. Braga, F. Grepioni and G.R. Desiraju, *Chem Rev.*, 1998, **98**, 1375.
43. A.L. Gillion, G.R. Lewis, A.G. Orpen, S. Rotter, J. Starbuck, X-M. Wang, Y. Rodriguez-Martin and C. Ruiz-Pérez, *J. Chem. Soc., Dalton Trans.*, 2000, 3897.
44. D. Braga, G. Cojazzi, A Abati, L. Maini, M. Polito, L. Scaccianoce and F Grepioni, *J. Chem. Soc., Dalton Trans.*, 2000, 3385.
45. S.S. Pathaneni, G.R. Desiraju, *J. Chem. Soc., Dalton Trans.*, 1993, 319.
46. O. M. Yaghi and Hailian Li, *J. Am. Chem. Soc.*, 1996, 118, 295.
47. D-Q. Zhang, W-H. Zhang, Q-F. Xu, J-P. Lang and S. W. Ng, *Acta crystallogr.*, 2000, **E60**, m1256.
48. L. Ye and Y. Wu, *Acta crystallogr.*, 2005, **E61**, m1894.
49. (a) C. Janiak, *J. Chem. Soc., Dalton Trans.*, 2000, 3885. (b) C.A. Hunter, J.K.M. Sanders, *Am. Chem. Soc.*, 1990, 112, 5525.
50. S. Kitangawa, R. Kituara and S-I. Noro, *Angew. Chem. Int.*, 2004, **43**, 2334.
51. F.H. Allen, *Acta Crystallogr.*, 2002, **B58**, 380.
52. J.P.H. Charmant, A.H.M.M. Jahan, N.C. Norman, A.G. Orpen and T.J. Podesta, *CrystEngComm.*, 2004, **6**, 29.
53. Y. Cui, J. Ren, G. Chen, W. Yu, Y. Qian, *Acta crystallogr.*, 2000, **C56**, e552.
54. K.J. Nordell, K.N. Schultz, K.A. Higgins, M.D. Smith, *Polyhedron*, 2004, **23**, 2161.
55. Y-J. Shi, X-T. Chen, C-X. Cai, Y-Z. Zhang, Z. Xue, X-Z. You, S-M. Peng, G.H. Lee, *Inorg. Chem. Commun.*, 2002, **5**, 621.
56. Y-J. Shi, X-T. Chen, C-X. Cai, Y. Zhang, Z. Xue, X-Z. You, S-M. Peng and G-H. Lee, *Inorg. Chem. Commun.*, 2002, **5**, 621.

57. H. Hou, Y. Wei, Y. Fan, C. Du, C. Du, Y. Zhu, Y. Song, Y. Niu, X. Xin, *Inorg. Chim. Acta.*, 2001, **319**, 212.

58. C. Xei, B. Zhang, X. Liu, X. Wang, H. Kou, G. Shen and D. Shen, *Inorg. Chem. Commun.*, 2004, **7**, 1037.

59. M.C. Aragoni, M. Arca, N. R. Champness, M. De Pasquale, F.A. Devillanova, F. Isaia, V. Lippolis, N.S. Oxtoby and C. Wilson, *CrystEngComm*, 2005, **7**, 363.

60. C-D. Wu, C-Z. Lu, S-F. Lu, H-H. Zhuang and J-S. Huang, *Inorg. Chem. Commun.*, 2001, **5**, 171.

61. C.S. Lai and E.R.T. Tiekink, *CrystEngComm,* 2004, **6**, 593.

62. J.T. Sampanthar and J.J. Vittal, *Cryst. Eng.*, 1999, **2**, 251.

63. O.M. Yaghi and H. Li, *J. Am. Chem. Soc.*, 1996, **118**, 295.

64. S. A. Bourne and M. Kilkenny and L.R. Nassimbeni, *J. Chem. Soc., Dalton Trans.*, 2001, 1176.

65. C. Hu and U. Englert, *CrystEngComm*, 2001, **23**, 1.

66. S. Kitagawa, M. Munakata and T. Tanimura, *Inorg. Chem.*, 1992, 31, 1714.

67. L. Carlucci, G. Ciani, D. Prosperio, and A. Sironi, *J. Am. Chem. Soc.*, 1995, **117**, 4562.

68. Y-B. Dong, M.D. Smith and H-C zur Loye, *J. of Solid State Chem.*, 2000, **155**, 143.

69. J.Y. Lu and A. Babb, *Inorg. Chim. Acta.*, 2001, **318**, 186.

70. Y-Y. Niu, H-W. Hou, Q-F. Zhang, X-Q.Xin, H-K. Fun, S. Chantrapomma and I.A. Razak, *Acta crystallogr.*, 2001, **C57**, 526.

71. D. Ghoshal, T.P. Maji, G. Mostafa, T-H. Lu and N.R. Chaudhuri, *Cryst. Growth and Des.*, 2003, **3**, 9.

72. Y.K. Lee and Soon W. Lee, *Bull. Korean Chem. Soc.,* 2003, **24**, 906.

73. K. Al-Rasoul and T.J.R. Weakley, *Inorg. Chim. Acta.*, 1982, **60**, 191.

74. T.J.R. Weakley, *Inorg. Chim. Acta.*, 1982, **63**, 161.

75. T.J.R. Weakley, *Inorg. Chim. Acta.*, 1984, **95**, 317.

76. N.W. Alcock and D.J. Flanders, *Acta crystallogr.*, 1987, **43**, 1267.

77. A.J. Norquist, M.B. Doran, P.M. Thomas and D. O'Hare, *Dalton Trans.*, 2003, 1168.

78. X. Li, Y-Q. Zou, and H-B. Song, *Acta crystallogr.*, **C60**, m110.

79. Z-T. Yu, Z-L. Liao, Y-S. Jiang, G-H. Li, G-D. Li, and J-S. Chen, *Chem. Commun.*, 2004, 1814.

80. Y. Xu, D. Yuan, Y. Xu, W. Bi, Y. Zhou and M. Hong, *Acta crystallogr.*, 2004, **E60**, m713.

81. A. Nedelcu, Z. Žak, a.M. Madalan, J. Pinkas, M. Andruh, *Polyhedron*, 2003, **22**, 789.

82. M.J. Plater, M.R. St. J. Foreman, A.M.Z. Slawin, *Inorg. Chim. Acta.*, 2000, **303**, 132.

83. A.K. Ghosh, D. Ghoshal, E. Zangrando, J. Ribas and R. Chaudhuri, *Inorg. Chem.*, 2005, **44**, 1786.

84. B.Q. Ma, H-L. Sun, S. Gao and G-X. Xu, *Inorg. Chem.* 2001, **40**, 6247.

85. B.Q. Ma, H-L. Sun, S. Gao and G-X. Xu, *CrystEngComm*, 2001, **35**, 1.

86. B.Q. Ma, H-L. Sun, S. Gao, *Inorg. Chem.* 2005, **44**, 837.

87. D-L. Long, A.J. Blake, N.R. Champness, and M. Schröder, *Chem. Commun.*, 2000, 2273.

88. D-L. Long, A.J. Blake, N.R. Champness, and M. Schröder, *Chem. Commun.*, 2000, 1369.

89. D-L. Long, A.J. Blake, N.R. Champness, C. Wilson and M. Schröder, *Angew. Chem. Int.*, 2001, **40**, 2444.

90. D-L. Long, R.J. Hill, A.J. Blake, N.R. Champness, P. Hubberstey, D.M. Prosperio, C. Wilson and M. Schröder, *Angew. Chem. Int.*, 2004, **43**, 1851.

91. R.J. Hill, D-L. Long, M.S. Turvey, A.J. Blake, N.R. Champness, P. Hubberstey, C. Wilson and M. Schröder, *Chem. Commun*, 2004, 1792.

92. S-L. Ma, C-M. Qi, Q-L. Guo, M-X. Zhao, *J. Mol. Chem.*, 2005, **738**, 99.

93. D. Vujovic, H.G. Raubenheimer and L.R. Nassimbeni, *Dalton Trans.*, 2003, 631.

94. D. Vujovic, H.G. Raubenheimer and L.R. Nassimbeni, *Eur. J. Chem.*, 2004, 2943.

95. N.R. Champness, *Dalton Trans.*, 2006, 877.

96. L.C. Rowsell and O.M. Yaghi, *Micro. and Meso. Mater.*, 2004, **73**, 3.

97. B. Chen, M. Eddaoudi, T.M. Reineke, J.W. Kampf, M. O'Keeffe and O.M. Yaghi, *J. Am. Chem. Soc.*, 2000, **122**, 11559.

98. M. Eddaoudi, H. Li and O.M. Yaghi, *J. Am. Chem. Soc.*, 2000, **122**, 1391.

99. H.K. Chae, M. Eddaoudi, J. Kim, S.I. Hauck, J.F. Hartwig, M. O'Keeffe and O.M. Yaghi, *J. Am. Chem. Soc.*, 2000, **122**, 11559.

100. T.M. Reineke, M. Eddaoudi, M. Fehr, D. Kelly and O.M. Yaghi, *J. Am. Chem. Soc.*, 1999, **121**, 1651.

101. M. Eddaoudi, D.B. Moler, H. Li, B. Chen, T.M. Reineke, M. O'Keeffe and O.M. Yaghi, *Acc. Chem. Res.*, 2001, **34**, 319.

102. S.S-Y. Chui, S.M-F. Lo, J.P.H. Charmant, A.G. Orpen and I.D. Williams, *Science*, 1999, **283**, 1148.

103. H. Li, M. Eddaoudi, M.O'Keeffe, and O.M. Yaghi, *Nature*, 1999, **402**, 276.

104. K. Barthelet, J. Marrot, D. Riou and G. Férey, *Angew Chem. Int. Ed.*, 2002, **41**, 281.

105. S-I. Noro, R. Kituara, M. Kondo, S. Kitagawa, T. Ishii, H. Matsuzaka and M. Yamashita, *J. Am. Chem. Soc.*, 2002, **124**, 2568.

106. T.K. Maji, G. Mostafa, H-C. Chang and S. Kitagawa, *Chem. Commun.*, 2005, 2436.

107. M. Kondo, T. Yoshitomi, K. Seki, H. Matsuzaka and S. Kitagawa, *Angew Chem. Int. Ed.*, 1997, **36**, 1725.

108. K. Seji, *Chem. Commun.*, 2001, 1496.

109. J.L. Atwood, L.J. Barbour and A. Jerga, *Angew Chem. Int. Ed.*, 2004, **43**, 2948.

110. P.M. Forster, J. Eckert, J-S. Chang, S-E. Park, G. Férey and A.K. Cheetham, *J. Am. Chem. Soc.*, 2003, **125**, 1309.

111. N.L. Rosi, M. Eddaoudi, J. Kim, M. O'Keeffe and O.M. Yaghi, *Angew Chem. Int. Ed.*, 2002, **41**, 284.

112. T.M. Reineke, M. Eddaoudi, D. Moler, M. O'Keeffe and O.M. Yaghi, *J. Am. Chem. Soc.*, 2000, **122**, 4843.

113. M. Eddaoudi, J. Kim, J.B. Wachter, H.K. Chae, M. O'Keeffe and O.M. Yaghi, *J. Am. Chem. Soc.*, 2001, **123**, 4368.

114. C.J. Kepert and M.J. Rosseinsky, *Chem. Commun.*, 1999, 375.

115. C.J. Kepert, *Chem. Commun.*, 2006, 695.

116. D. Braga and F. Grepioni, *Coord. Chem. Rev.*, 1999, **183**, 19.

117. D. Braga and F. Grepioni, *J. Chem. Soc., Dalton Trans.*, 1999, 1.

118. D. Braga and F. Grepioni, *Chem. Soc. Rev.*, 2000, **29**, 229.

119. D. Braga and F. Grepioni, *Chem. Commun.*, 2005, 3635.

120. D. Braga, S.L. Giaffreda, F. Grepioni, A. Pettersen, L. Maini, M. Maini, M. Curzi and M. Polito, *Dalton Trans.*, 2006, 1249.

121. R.P. Rastogi, *J. Scient. Ind. Res.*, 1970, **29**, 177.

122. F. Toda, H. Takumi and M. Akehi, *J. Am. Chem. Soc., Chem.. Commun.*, 1990, 1271.

123. G. Rothenberg, A.P. Downie, C.L. Raston and J.L. Scott, *J. Am. Chem. Soc.*, 2001, **123**, 8701.

124. A.V. Trask, W.D.S. Motherwell and W. Jones, *Chem. Commun.*, 2004, 890.

125. M.E. Brown, 'Introduction to Thermal Analysis – Techniques and Applications', Chapter 13, Chapman and Hall, London, 1988.

126. A. Kálmán, L. Párkányi and G. Argay, *Acta. Crystallogr.*, 1993, **B49**, 1039.

Chapter 2

Experimental

General Synthetic Procedure

The organic-inorganic compounds studied were synthesised by diffusion solvent mixtures and slow solvent evaporation methods at 278 K, ambient and 313 K. All syntheses involved the addition of a solution of the organic dipyridyl ligands (4,4'-bipyridine-*N,N'*-dioxide (bpdo), 1,2-bis(4-pyridyl)ethane (BPE) and 1,2-di(4-pyridyl)ethylene (DPE); schematic diagrams shown in Figure 2.1) to the metal salt using various metal:ligand molar ratios to be discussed later in this chapter. All chemicals were purchased from commercial sources and used without further purification and their physical properties are summarised in Table 2.1.

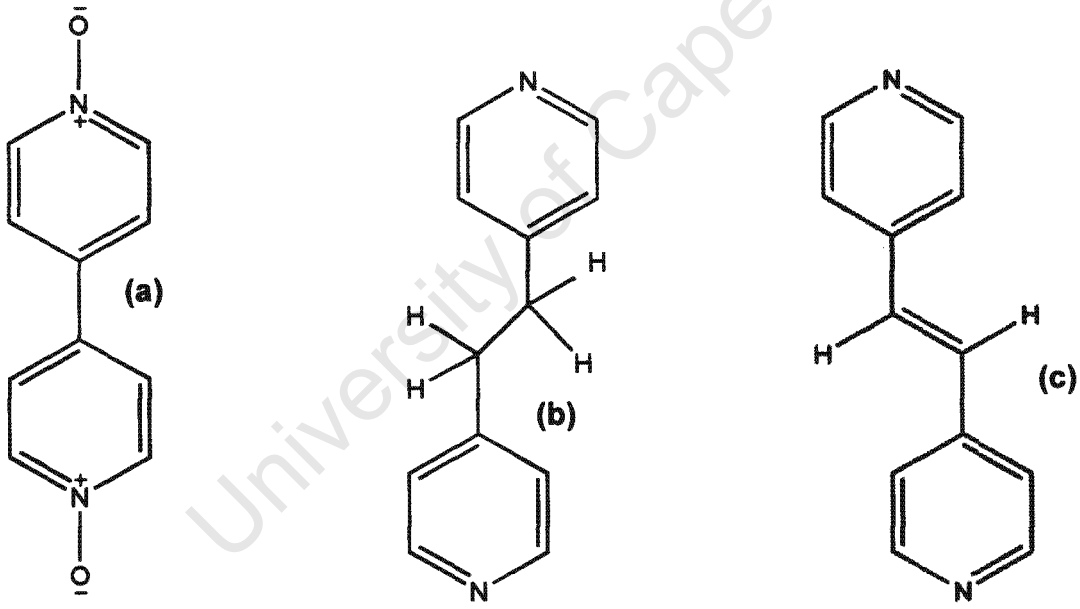

Figure 2.1: Schematic diagrams of dipyridyl ligands. **(a)** 4,4'-bipyridine-*N,N'*-dioxide (bpdo), **(b)** 1,2-Bis(4-pyridyl) ethane (BPE) and **(c)** 1,2-Di(4-pyridyl) ethylene (DPE).

Table 2.1: Physical properties of chemicals used in synthesis.

Compound	Molecular formula	M_r (g.mol^{-1})	bp (°C)*	mp (°C)*	Density** (g.cm^{-3})
Metal salts					
Cobalt bromide	$CoBr_2$	218.75	–	678	4.909
Cobalt chloride	$CoCl_2.6H_2O$	237 93	1048.9	87	1.924
Cobalt iodide	CoI_2	312.74		>515	5.45
Cobalt nitrate	$Co(NO_3)_2.6H_2O$	291 03	–	55-56	2.49
Cobalt sulphate	$Co(SO_4)_2.7H_2O$	281.10	735	96.8	2.03
Copper chloride	$CuCl_2.2H_2O$	170.48	992.8	100	2.54
Gadolinium nitrate	$Gd(NO_3)_3.6H_2O$	451.34		91	2.406
Gold chloride	$H(AuCl_4)$	339.49	–	–	1.025
Lead chloride	$PbCl_2$	278.12	950	501	5.85
Lead bromide	$PbBr_2$	367.01	916	373	6.660
Lead iodide	PbI_2	461.01	954	402	–
Terbium nitrate	$Tb(NO_3)_3.5H_2O$	435.02	–	89.3	–
Thallium nitrate	$Tl(NO_3)_3.3H_2O$	444.43		102-105	–
Uranyl nitrate	$UO_2(NO_3)_2.6H_2O$	502.13	–	–	–
Zinc bromide	$ZnBr_2$	225.19	650	394	4.201
Zinc thiocynate	$Zn(NCS)_2$	181.558	–	–	–
Ligands					
1,2-Bis(4-pyridyl) ethane	$C_{12}H_{12}N_2$	184.24	–	107-110	–
4,4'-bipyridine-*N,N'*-dioxide	$C_{10}H_8N_2O_2$	188.19		220	
1,2-Di(4-pyridyl) ethylene	$C_{12}H_{10}N_2$	182.23		150-153	
Solvents					
Carbon tetrachloride	CCl_4	153.82	76	-23	1.59
Chlorobenzene	C_6H_5Cl	112.56	132	-45	1.107
Chloroform	$CHCl_3$	119.38	60.5-61.5	-63	1.48
Dichloromethane	CH_2Cl_2	84.93	39.8-40	-97	1.32
Dimethylsulfoxide	$(CH_3)_2SO$	78.13	189	16-19	1.10
Ethanol	C_2H_5O	46.07	78	-114	0.79
Methanol	CH_4O	32.04	64.5	-98	0.79

* mp and bp measured at 760mmHg, ** densities measured at 25°C. [1]

Syntheses of metal-organic complexes

(a) Cobalt complexes

(i) $[Co(H_2O)_6]Br_2$. 2(bpdo) . $2H_2O$ (CoB), $[Co(H_2O)_6]Cl_2$. 2(bpdo) . $2H_2O$ (CoC), $[CoI_2(H_2O)_4]$. 2(bpdo) (CoI), $[Co(H_2O)_3(bpdo)(NO_3)]$ NO_3 . bpdo . H_2O (CoN(A)), $[Co(H_2O)_2(bpdo)(NO_3)_2]$ (CoN(B)), $[Co_2(H_2O)_8(bpdo)_2]$ $(NO_3)_4$. $4H_2O$ (CoN(C)), $[Co(H_2O)_5(bpdo)](NO_3)_2$. H_2O (CoN(D)), $[Co(H_2O)_4(NO_3)_2]$. 2(bpdo) (CoN(E)), $[Co(bpdo)_6](NO_3)_2$ (CoN(F)), $[Co(H_2O)_5(bpdo)]SO_4$. $2H_2O$ (CoS).

The compounds were prepared by slow evaporation of a solution containing bpdo and a cobalt metal salt. In a typical preparation, 54.69 mg (0.25 mmol) **$CoBr_2$** was dissolved in 1 mL methanol or ethanol. 3 mL alcoholic solution of bpdo (35.28 mg, 0.19 mmol) was added carefully to the metal solution. The solvent was allowed to evaporate slowly at ambient temperatures and crystals were obtained within a few days. Similar preparations were done using 59.45 mg (0.25 mmol) **$CoCl_2.6H_2O$**, 35.28 mg (0.10 mmol) **CoI_2**, 72.76 mg (0.25 mmol) **$Co(NO_3)_2.6H_2O$** and 70.24 mg (0.25 mmol) **$Co(SO_4)_2.7H_2O$**.

(ii) Using the same chemical quantities as in (i) above, temperature-and-solvent dependent experiments for **$Co(NO_3)_2.6H_2O$** were studied. This was done by growing crystals at (a) different temperatures (278 K, ambient (approximately 295 K – 298 K) and 313 K) using methanol only and (b) different solvent mixtures of methanol and water using the aforementioned temperatures.

(iii) $[CoBr_2(bpdo)(H_2O)_2]_n \cdot H_2O$ (CoB-2) and $[CoCl_2(bpdo)(H_2O)_2]_n \cdot H_2O$ (CoC-2)

Chemical quantities for preparing these two complexes are similar to those in (i) above. Dry **CoB** and **CoC** were allowed to stand on the side bench and

within a week these crystals had transformed to **(CoB-2)** and **(CoC-2)** coordination polymers at ambient temperatures.

(b) Lanthanide complexes

(i) $[Gd(NO_3)_3(bpdo)CH_3OH]_n$ (Gd1), $[Tb(NO_3)_3(bpdo)CH_3OH]_n$ (Tb1), and $[Tl(NO_3)_3(bpdo)CH_3OH]_n$ (Tl1)

These compounds were prepared by layering a methanol solution of bpdo on top of a layer of chlorinated solvents. In a typical preparation, 22.57 mg (0.05 mmol) $Gd(NO_3)_3.6H_2O$ was placed at the bottom of a polytop vial covered with 10 mL of CH_2Cl_2, $CHCl_3$, C_6H_5Cl or CCl_4 solvents. The metal salt does not fully dissolve. A 10 mL methanolic solution of bpdo (14.11 mg, 0.10 mmol) was carefully layered on top. The layers mixed over several days at ambient temperatures and colourless crystals grew at the interface. Similarly, compounds of Tb and Tl were prepared using 21.75 mg (0.05 mmol) $Tb(NO_3)_3.5H_2O$ and and 22.22 mg (0.05 mmol) $Tl(NO_3)_3.3H_2O$.

(ii) $[Gd(NO_3)_3(bpdo)_{1.5}]_n$ CH_2Cl_2 (Gd2), $[Gd(NO_3)_3(bpdo)_{1.5}]_n$ $CHCl_3$ (Gd3) and $[Tl(NO_3)_3(bpdo)_{1.5}]_n$ CH_2Cl_2 (Tl2)

The same chemical quantities and method as in (i) above were used to prepare these complexes. They were prepared by layering an ethanol solution of bpdo on top of a layer of either CH_2Cl_2 or $CHCl_3$ in which metal salt had been placed (but not fully dissolved). The layers mixed over several days at ambient temperatures and colourless crystals grew at the interface and bottom of the vial.

(c) Actinide complex

$[UO_2(NO_3)_2(bpdo)]_n . 2.5H_2O$ (U)

502.13 mg (1.00 mmol) $UO_2(NO_3)_3.6H_2O$ was dissolved in 30 mL of methanol. 20 mL methanolic solution of bpdo (188.18 mg, 1.00 mmol) was added to the

metal salt solution. The mixture was heated to boiling point (337.5 K) with vigorous stirring. The temperature was reduced to 318.0 K and stirred for about 5 hours. The mixture was then filtered through a 0.45 micron filter and placed into a refrigerator for crystallisation. Yellow crystals were obtained within four weeks.

(d) Copper and Lead complexes

$[Cu_2Cl_4(bpdo)_3(H_2O)_2]\cdot(CH_3)_2SO$ (CuC), $PbBr_2(bpdo)_n$ (PbB), $PbCl_2(bpdo)_n$ (PbC) and $PbI_2(bpdo)_n$ (PbI)

17.05 mg (0.10 mmol) **$CuCl_2.2H_2O$** was placed at the bottom of polytop vials covered with 5 mL of CH_2Cl_2 or $CHCl_3$. The metal salt does not fully dissolve. A 5 mL solution of $(CH_3)_2SO$ and bpdo (28.22 mg, 0.15 mmol) was carefully layered on top. Reddish-brown crystals grew in two weeks at the surface of the vial at ambient temperatures. Similar preparations were done using 36.70 mg (0.10 mmol) **$PbBr_2$**, 20.86 mg (0.10 mmol) **$PbCl_2$** and 46.10 mg (0.10 mmol) **PbI_2**.

(e) Gold complexes

$H[AuCl_4]$. (bpdo) (Au1), $H_2[AuCl_4]$. Cl . (BPE) (Au2) and $H_2[AuCl_4]$. Cl . (DPE) (Au3)

35.00 mg (0.18 mmol) bpdo was dissolved in 5 mL methanol and layered cautiously on top of a 3 mL **$H[AuCl_4]$** solution which was commercially prepared in 1 M hydrochloric acid. The solvent was allowed to evaporate slowly at ambient temperatures and yellow crystals formed in one week. Similar preparations were done using 36.85 mg (0.20 mmol) 1,2-Bis(4-pyridyl) ethane and 36.45 mg (0.20 mmol) 1,2-Di(4-pyridyl) ethylene.

(f) Zinc complexes

(i) $Zn_2Br_4(bpdo)_2$ (ZnB1)

The compound was prepared by layering an ethanolic solution of bpdo (28.23 mg, 0.15 mmol) on top of 5mL CH_2Cl_2 or $CHCl_3$ in which 22.52 mg (0.10 mmol) of **$ZnBr_2$** had been placed (but not fully dissolved). The layers mixed over several days at ambient temperature and colourless crystals grew at the interface.

(ii) $[Zn_3Br_6(bpdo)_4(H_2O)_2] \cdot (bpdo)$ (ZnB2) and $[Zn_2Br_4(bpdo)(H_2O)_6] \cdot 2(bpdo) \cdot (H_2O)$ (ZnB3)

22.52 mg (0.10 mmol) **$ZnBr_2$** was dissolved in 1.5 mL methanol. 28.23 mg (0.15 mmol) bpdo was dissolved in 3 mL methanol and added to the metal salt solution. The solvent was allowed to evaporate slowly at ambient temperatures and colourless crystals were achieved in few days. Similar preparations using same chemical quantities as above were done by replacing methanol with ethanol to acquire **ZnB3**.

(iii) $Zn(NCS)_2(bpdo)(H_2O)_2 \cdot H_2O$ (ZnB4)

Ethanolic solutions of $Zn(NCS)_2$ (0.1 mmol, 2 mL) and bpdo (0.40 mmol, 4 mL) were mixed. The mixture was filtered through a 0.5 microns filter and the solvent was allowed to evaporate slowly at ambient temperature. Colourless crystals were afforded in two weeks.

Characterisation

Thermal analysis

Hot Stage Microscopy (HSM)

HSM is a technique used to visualise and study the thermal degradation of compounds during the heating process. HSM was used in this study to observe the thermal decomposition of the organic-inorganic complexes. It may be used to correlate thermal events measured using the TG and DSC with the physical changes occurring in a crystal upon heating, such as guest desorption, melting point, polymorphic transitions, sample recrystallisation, etc. In order to detect guest release phase, the crystal is submerged in an inert medium such as silicone oil and observing the evolution of bubbles upon guest desorption. Another indication of guest loss is that a clear crystal could turn opaque due to partial desolvation. In this thesis, the HSM was mainly used for preliminary identification of the prepared complexes in order to determine the formation of the host-guest inclusion compound. The temperature at which any phenomenon is observed by the HSM may be correlated with the DSC onset temperature. The HSM temperatures at which events were observed were often slightly different from those observed in the TG and DSC experiments. This effect may be due to the different geometries of various instruments as well as differences in particle size of the sample analysed.

The crystals submerged in silicone oil were subjected to the heating process under a Nikon SMZ-10 microscope fitted with a Linkam THMS 600 hot stage connected to a Linkam TP92 temperature controlling unit. All samples were heated at 10 °C min^{-1}. The temperature was controlled by a Linkam CO600 temperature controller. A Nikon SMZ-10 microscope with a Sony Digital Hyper HAD colour video camera was mounted on top to record thermal events. The thermal events were monitored and images captured using program analySIS.[2]

Thermogravimetry (TG)

TG analyses for all compounds were performed on a Mettler Toledo TGA/SDTA851e under N_2 gas purging at flow rate of 30 mL/min. The Mettler TG instrument was calibrated using indium (mp = 156.6 °C) and aluminium (mp = 660.3 °C) in an automated process in which temperature calibration, tau lag calibration and sensor calibration are performed simultaneously.
The crystals were thoroughly dried on a filter paper to remove the surface solvent. Sample weights were typically between 2 and 20 mg. The weighed samples were placed in an open platinum pan. The programmed TG analyses were carried out over a temperature range 30 °C and 500 °C, at the predetermined linear heating rate of 10 °C min^{-1} (20 °C min^{-1} for Co(II) complexes). This technique was primarily used to determine the stoichiometry of the compounds from the percentage weight loss. The samples were continuously purged by a stream of dry nitrogen gas at a flow rate of 30 mL min^{-1}.

TG measures the weight loss of a sample as a function of temperature or time. It is used to establish the stoichiometry of the inclusion compounds as well as for measuring kinetics of desorption by isothermal TG analysis, which measures the mass loss of a sample with time at a fixed temperature. The isothermal TG was employed for kinetic studies, and will be described in the kinetics section.

Differential Scanning Calorimetry (DSC)

DSC measurements were performed using a Perkin Elmer PC series 7 System. The instrument was calibrated using standard materials, i.e. Indium (ΔH = 28.5 J/g, m.p. = 156.6°C) and Zinc (ΔH = 102.1 J/g, m.p. = 419.5°C).
The DSC analyses measure the difference in heat flow between the sample and a reference, in a controlled atmosphere, as a function of temperature, while the sample and reference are subjected to a controlled temperature program. These differences in enthalpy are associated with thermal events

such as guest release, phase transformation, polymorphic changes, recrystallisation and melting. DSC experiments can therefore be used to establish the onset temperatures and enthalpy changes (area under peak = $K\Delta H$) associated with these thermal events. Guest release from the host is usually shown by an endotherm (absorption of heat) while decomposition is by an exotherm (heat released) and this can be detected using the DSC. Endothermic and exothermic reactions are shown by upward and downward peaks, respectively.

The filter-dried and slightly finger-crushed samples ranging in mass between 2 and 10 mg were placed in the crimped, vented aluminium pans with lids and were heated at 10 °Cmin^{-1}, with dry nitrogen as a purging gas at flow rate of 30 mL/min. The DSC yields accurate onset temperatures for guest release and melting points, but enthalpy values for guest release are more problematic. This problem is mainly influenced by failure to control the particle size distribution of the inclusion compounds. Sieving is not employed because guest loss may occur during the sieving process.

Kinetic studies

Kinetics of guest release (desolvation) and decomposition of structure frameworks of both inclusion and metal-organic compounds were performed isothermally using TG techniques. The isothermal TG experiments were done using the programmed Mettler Toledo TGA/SDTA851e (described in TG section above) with dry nitrogen gas purging at the flow rate of 30 mL min^{-1}. The samples were removed from their mother liquor and dried on a filter paper. A series of isothermal TG experiments were carried out at appropriate temperatures selected with reference to the TG mass loss steps. The samples were heated rapidly at the chosen isothermal temperature until the experiment was completed i.e. guest desorption or decomposition was complete. The experiments were repeated at various temperatures which will be described in the appropriate chapters. Data generated by these experiments were converted to the extent of a reaction (α) versus time curves. The curves

obtained were fitted to various kinetic equations to determine the appropriate models.[3] The extent of a reaction, α, is described by $\alpha = (m_i - m_t) / (m_i - m_f)$, where m_i is the initial mass of a compound and m_f is is the final mass, m_t is the mass at any time, t, during the mass loss process. Various kinetic models, of the form $f(\alpha) = kt$, were fitted to the α-time data using the KINETIC program.[4] The kinetic model for which the function, $f(\alpha)$, was linear over the largest range of α was considered as the best fit model.

Microanalysis

Microanalysis was used to further confirm the stoichiometry of the compounds, particularly those whose instability rendered thermogravimetry unreliable. A Fisons EA1108 CHNS-O Elemental Analyser equipment was used to analyse synthesised compounds for carbon (C), nitrogen (N), hydrogen (H) and sulphur (S) content. The analysis was repeated twice for each sample to monitor the reproducibility of the results.

The unstable compounds were kept under mother liquor until analysis, then dried using filter paper. The C, N, H and S contents were calculated and compared with the results obtained from microanalysis.

X-Ray Powder Diffraction (PXRD)

Single crystals were crushed and packed in Markröhrchen non-diffracting glass capillaries supplied by Hilgenberg (Germany) prior to being mounted. These samples were then mounted on a Huber D-83253 Imaging Plate appliance fitted with a Guiner Camera 670, a Huber MC 9300 power supply unit and a Philips PW1120/00 X-ray generator. The generator settings were kept constant at 20 mA and 40 kV while the sample was being bombarded with CuKα radiation (λ = 1.5418 Å). The display and manipulation of the PXRD data thus generated were performed on a desktop computer, which was linked to the instrument. The samples were exposed to radiation for 60 minutes and multiscans of 10 times were used. The 2θ range was truncated from 5 to 40°.

This technique was used to determine the purity of the sample. This was done by careful comparison of the experimental PXRD patterns with the PXRD traces calculated from the refined crystallographic data of the respective complexes.

Fourier Transform Infrared Spectroscopy (FTIR)

FTIR analysis was performed to confirm the protonation of dipyridyl ligands. FTIR spectra were run for dried ligands, ligand kneaded with a small amount of HCl and crystalline material, all as KBr disks. The spectra were recorded on a Perkin Elmer Spectrum One FTIR spectrophotometer over the range 4000 – 500 cm^{-1}.

Preparation for data collection

The crystals of synthesised compounds were grown by solvent diffusion mixtures and solvent slow evaporation.

Crystal structure analysis

Crystals of good quality (shiny and clear) and suitable size were selected for preliminary X-ray photography and data collections. Single crystals were selected on their ability to extinguish plane polarised light uniformly. The crystal was immersed in Paratone N oil[5] and mounted on the glass fibre for data collection at low temperatures using the Nonius Kappa-CCD diffractometer. The preliminary unit cell parameters and space group symmetry were determined using the X-ray diffractometer for all synthesised compounds.

Data collection was done on a Nonius Kappa-CCD diffractometer using graphite-monochromated MoK_α radiation (λ=0.7107Å) produced at 50 kV and 30 mA using Nonius FR590 generator. Data collections performed at low temperatures were carried out by cooling the crystals using a constant stream of nitrogen gas produced by a Cryostream cooler (Oxford Cryosystems) at a flow rate of 20 cm^3min^{-1}. The intensity data were collected at either room or low temperatures depending on the stability of the crystal.

The strategies for data collections were evaluated using the COLLECT[6] software. Intensity data, for all structures, were collected by the standard φ and ω scan techniques and were scaled and reduced to using DENZO-SMN[7] software. Accurate unit cell parameters were refined on all data.

All the structures were solved by direct methods using SHELXS-97.[8] Equivalent reflections were merged and those with $I < 2\sigma(I)$ were suppressed. The space group symmetry was determined by examining systematic absences in the experimental data. This process was facilitated by the

program XPREP.[9] Differentiating between centro- and non-centrosymmetric space groups with the same systematic absences was done by examining the mean $|E^2-1|$ values, where E is the normalized structure factor. If the $|E^2-1|$ value is close to 0.968, the structure is centrosymmetric, whereas if it is close to 0.736 the structure is acentric. The intensity statistics give an initial indication of whether the space group is centrosymmetric or not, but is later confirmed by the successful solution and refinement of the structure.

The structure refinement was done by using the program SHELXL-97,[8] which uses full-matrix least-squares minimisation of the function $(\sum w(F_o^2-kF_c^2)^2)$. The agreement between the observed (F_o) and the calculated (F_c) structure factors is expressed by the residual index, R, which is an indirect measure of the accuracy of the structure and should be low if the model is satisfactory. The residual index R_1 gives the agreement between measured and calculated structure factor amplitudes for the refinement against F (see equation 1), whereas the residual index wR_2 expresses the agreement between intensities for the refinement against F^2 (see equation 2).

$$R_1 = \frac{\sum \| F_o | - | F_c \|}{\sum |F_o|} \qquad (1)$$

$$wR = \sqrt{\frac{\sum w\left(F_o^2 - F_c^2\right)^2}{\sum w\left(F_o^2\right)}} \qquad (2)$$

w is a default weighting scheme (represented by the SHELX command WGHT) and was refined for each structure:

$$w = \frac{1}{\sigma^2 F_o^2 + (aP)^2 + bP} \qquad (3)$$

where $P = \frac{\max(0, F_o^2) + 2F_c^2}{3}$ (4)

Both *a* and *b* were refined for each structure.

The Goodness of Fit (S) was also determined for each structure and is based on F^2 (equation 5)

$$S = \left(\frac{\sum w(F_o^2 - F_c^2)^2}{n - p} \right)^{\frac{1}{2}} \quad (5)$$

where *n* is the number of reflections and *p* is the total number of parameters refined.

Unless otherwise stated, all non-H atoms were refined anisotropically. Hydrogens bonded to carbon atoms were placed in geometrically calculated positions with C–H = 0.95 Å and refined with atomic displacement parameters 1.2 times those of their parent carbons (1.5 times for methyl groups). For most elucidated crystal structures with water molecules, the hydrogen atoms bonded to oxygen atoms were generally not included in the final model.

Additional computer packages

SHELXS-97[8] and SHELXL-97[8] programs were used for structure solution and refinement respectively. A number of other computer programs listed below are included in the graphic interface software X-SEED[10] and were used for further analysis of the structures.

- **ConQuest**[11] program was used to search the **Cambridge Structural Database** (**CSD**)[11] for comparable structures to those presented in this thesis.

- **XPREP**[9] was used to determine the space group and prepare the SHELX input files.

- **X-SEED**[10] was used as a graphical interface for LAYER, SHELXS-97, SHELXL-97, POV-RAY, LAZY PULVERIX and SECTION.

- The **LAYER**[12] program was used to investigate and identify the systematic absences from the intensity data collected from the x-ray diffractometer and the space group symmetry could be determined. It displays the intensity data as simulated precession photographs of all levels of the reciprocal lattice.

- The **SECTION**[13] program was used to view the geometry of the voids formed by packing the crystal structure and in which the guest molecules reside. The guest molecules were removed from the crystal structure and the host molecules were viewed with atoms given their van der Waals radii. The host compound could then be sliced through the unit cell down any selected axis at various intervals. The program assists in investigating the 3 dimensional shapes of the channels or cavities.

- X-ray diffraction patterns were calculated with the aid of the **LAZY PULVERIX**[14] program. The unit cell parameters, space group symmetry, atomic coordinates and thermal parameters were used as input for the program.

- The molecular structures and crystal packing diagrams were drawn using **POV-RAY**[15].

- **SADABS Version 2.03**[16] was used to exploit data redundancy to correct three-dimensional integrated data for errors due X-ray absorption.

- The analysis of the crystal conformation, host-guest interactions and other structural parameters was done using **PLATON**.[17]

References

1. www.sigma-aldrich.com/; The Merck Index, An Encyclopaedia of chemical, drugs and biologicals, 11th Edition, Merck and Co., Inc., 1989; http://www.cas.org/SCIFINDER/.
2. Soft Imaging System GmbH: Digital Solutions for Imaging and Microscopy, Version 3.1 for Windows, © 1987-2000.
3. M.E. Brown, 'Introduction to Thermal Analysis – Techniques and Applications', Chapter 13, Chapman and Hall, London, 1988.
4. L.J. Barbour, KINETIC program, PhD Thesis, University of Cape Town, 1994.
5. Paratone N oil (Exxon Chemical Co., TX, USA).
6. Nonius, COLLECT, Nonius BV, Delft, The Netherlands, 1998.
7. Z. Otwinowski, W. Minor, Methods in Enzymology, part A: Macromolecular Crystallography, Part A edited by C.W. Carter Jr. and R.M. Sweet, Academic Press, New York, 1997, Vol 276, pg. 307-326.
8. G.M. Sheldrick, SHELXS97 and SHELXL97, University of Göttingen, Germany.
9. XPREP, Data Preparation & Reciprocal Space Group Exploration, Version 5.1/NT, © 1997, Bruker Analytical X-ray Systems.
10. L.J. Barbour, *J. Supramol. Chem.* 2001, **1**, 189
11. F.H. Allen, *Acta Crystallogr.*, 2002, **B58**, 380.
12. L.J. Barbour, LAYER, A computer program for the graphic intensity data as simulated precession photographs, *J Appl. Cryst.*, 1999, **32**, 351.
13. L.J. Barbour, SECTION, A computer program for the graphic display of cross sections through a unit cell, *J Appl. Cryst.*, 1999, **32**, 353.
14. K. Yvon, W. Jeitschko, E. Parthe, *J. Appl. Cryst.*, 1977, **10**, 73,.
15. Persistence of Vision, POV-RAY. for Windows, Version 3.1e. watcom.win32, 1999. URL: http://www.povray.org/
16. G.M. Sheldrick, SADABS, Bruker AXS Inc., Madison, Winconsin, USA.
17. A.L. Spek, PLATON, A multipurpose crystallographic tool, Version 20604, © 1980-2004 (A.L. Spek, *J. Appl. Crystallogr.*, 2003, 36, 7).

Chapter 3

(A) Anion dependent structural diversity in Co^{II} complexes of bpdo and transformation of Co^{II} discrete molecules to one dimensional polymers. (B) temperature-and-solvent-dependent study.

This chapter is separated into two parts; **(A) Anion dependent structural diversity in cobalt (II) complexes of bpdo and transformation of Co^{II} to one dimensional polymers, (B) temperature-and-solvent dependent experiments**. **Part (A)** describes the cobalt (II) complexes with bpdo which were prepared and characterised by XRD, thermal analysis and microanalysis. Their topology and dimensionality depends on the counterion used i.e. Br^-, Cl^-, I^-, NO_3^- and $(SO_4)^{2-}$. For Br^- and Cl^- the structures are layered inorganic/organic salts; I^- forms a 3D supramolecular network while both NO_3^- and $(SO_4)^{2-}$ induce the formation of interdigitated layer structures (with different coordination spheres) with a hydrophilic region between the Co(II) ions. The nitrate structure undergoes a reversible order-disorder phase transition at *ca.* 162 K. In all prepared complexes, $\pi...\pi$ interactions are present between the bpdo molecules, possibly providing a directing force for the formation of these structures.

The next section illustrates an interesting characteristic of Br^- and Cl^- complexes, refined and elucidated in this study, which tend to transform into 1D polymer after the crystals were left to stand. Hydrogen bonding through a guest water molecule joins the adjacent chains forming a 2D polymer sheet.

Part (B) describes different crystal structures of the $Co(NO_3)_2$ and bpdo grown at different temperatures i.e. 278 K, ambient (295 K – 298 K), 295 K, 298 K and 313 K.

For each of the crystal structures described in this chapter the crystallographic data, experimental and refinement parameters are given in Table 3.1. The final atomic coordinates, bond lengths and angles, torsion angles, thermal angles, thermal parameters and tables of observed and calculated structure factors for each of the crystal structures are given in the appendices.

Complex preparation

Part (A): Crystals of suitable quality were obtained by slow evaporation at ambient temperature over a period of a week (using the method described in Chapter 2). These complexes were crystallised using either methanol or ethanol as a solvent.

Compounds of **CoB** and **CoC** prepared in **Part (A)** were allowed to stand on an open bench. Within a week, new 1D coordination polymers (**CoB-2** and **CoC-2**) were formed.

The abbreviations for the discrete cobalt complexes in this chapter are as follows:

$[Co(H_2O)_6]Br_2$. 2(bpdo) . $2H_2O$:	**CoB**
$[Co(H_2O)_6]Cl_2$. 2(bpdo) . $2H_2O$:	**CoC**
$[CoI_2(H_2O)_4]$. 2(bpdo):	**CoI**
$[Co(H_2O)_3(bpdo)(NO_3)]$ NO_3 . bpdo . H_2O:	**CoN(A)**
$[Co(H_2O)_2(bpdo)(NO_3)_2]$:	**CoN(B)**
$[Co_2(H_2O)_8(bpdo)_2]$ $(NO_3)_4$. $4H_2O$:	**CoN(C)**
$[Co(H_2O)_5(bpdo)](NO_3)_2$. H_2O:	**CoN(D)**
$[Co(H_2O)_4(NO_3)_2]$. 2(bpdo):	**CoN(E)**
$[Co(bpdo)_6](NO_3)_2$:	**CoN(F)**
$[Co(H_2O)_5(bpdo)]SO_4$. $2H_2O$:	**CoS**
$CoBr_2(bpdo)(H_2O)_2 \cdot H_2O$:	**CoB-2**
$CoCl_2(bpdo)(H_2O)_2 \cdot H_2O$:	**CoC-2**

Part (B): Compounds were prepared similar to as described in **Part (A)**, but at different crystallisation temperatures and solvent ratios.

Microanalysis

Elemental analysis results are given in Table 3.1 and they corresponded well with the calculated elemental mass percentages, except the minor discrepancies observed in **CoN(A)** and **CoN(E)** and **CoC-2** which could be due to the procedure followed in the preparation of the sample for analysis. The experimental values agree with the stoichiometries found in refined structures.

Table 3.1: Elemental analysis results for Co(II) complexes.

Complex	Found %				Calculated %			
	C	H	N	S	C	H	N	S
CoB	32.38	3.96	7.57	–	32.67	3.84	7.62	–
CoC	36.63	4.20	8.19	–	36.94	4.96	8.62	–
CoI	31.10	3.12	7.05	–	31.56	3.18	7.36	–
CoN(A)	37.01	3.08	13.09	–	38.05	3.83	13.31	–
CoN(E)	37.09	3.49	13.17	–	38.05	3.83	13.31	–
CoN(F)	54.11	3.70	13.73	–	54.93	3.69	13.95	–
CoS	25.46	5.04	5.84	6.85	25.59	4.73	5.97	6.83
CoB-2	26.62	2.29	6.15	–	26.05	3.06	6.08	–
CoC-2	30.12	3.67	6.51	–	32.28	3.79	7.53	–

PART (A): Anion dependent structural diversity in cobalt (II) complexes of bpdo

Structure solution and analysis

CoB and CoC

Table 3.2: Crystal data and refinement parameters of **CoB** and **CoC.**

Molecular Formula	$[Co(H_2O)_6]Br_2 . 2(C_{10}H_8N_2O_2) . 2H_2O$	$[Co(H_2O)_6]Cl_2 . 2(C_{10}H_8N_2O_2) . 2H_2O$
Formula weight ($g.mol^{-1}$)	739.25	650.33
Temperature (K)	113	113
Wavelength (Å)	0.71073	0.71073
Crystal System	Monoclinic	Triclinic
Space Group	$P2_1/c$	$P\bar{1}$
a (Å)	10.3728 (2)	6.7328 (2)
b (Å)	6.6329 (1)	10.2841 (3)
c (Å)	20.0945 (4)	10.6577 (3)
α (°)	90	85.200 (1)
β (°)	93.366 (1)	70.023 (1)
γ (°)	90	91.103 (1)
Volume ($Å^3$)	1378.58 (4)	690.21 (3)
Z	2	1
Calculated Density ($g.cm^{-3}$)	1.781	1.565
μ (mm^{-1})	3.588	0.882
F (000)	746	337
Crystal Size (mm)	0.20 x 0.20 x 0.28	0.05 x 0.07 x 0.12
θ Range Scanned (°)	2.0 – 27.9	2.0 – 25.7
Index Range	$-13 < h < 13$, $-8 < k < 8$, $-26 < l < 26$	$-8 < h < 7$, $-12 < k < 12$, $-12 < l < 12$
No. Reflections Collected	22395	13961
No. Unique Reflections	3295	2614
Data completeness (%)	100.0	99.8
Refinement Method	Full-matrix L.S. on F^2	Full-matrix L.S. on F^2
Data / Restraints / Parameters	3295/ 0 / 177	2614 / 0 / 179
Goodness-of-fit on F^2	1.171	1.102
Final R Indices $[I>2\sigma(I)]$	0.0439, 0.1117	0.1055, 0.2736
R Indices (all data)	0.0505, 0.1140	0.1552, 0.3124
Largest Diff. Peak and Hole($e.Å^{-3}$)	0.924, -3.105	1.936, -0.783

The **CoB** compound crystallises in the monoclinic crystal system, in space group $P2_1/c$, while **CoC** crystallised in the $P\bar{1}$ space group which is the triclinic crystal system. Although these compounds are not isostructural, their packing is almost identical, so they will be described together.

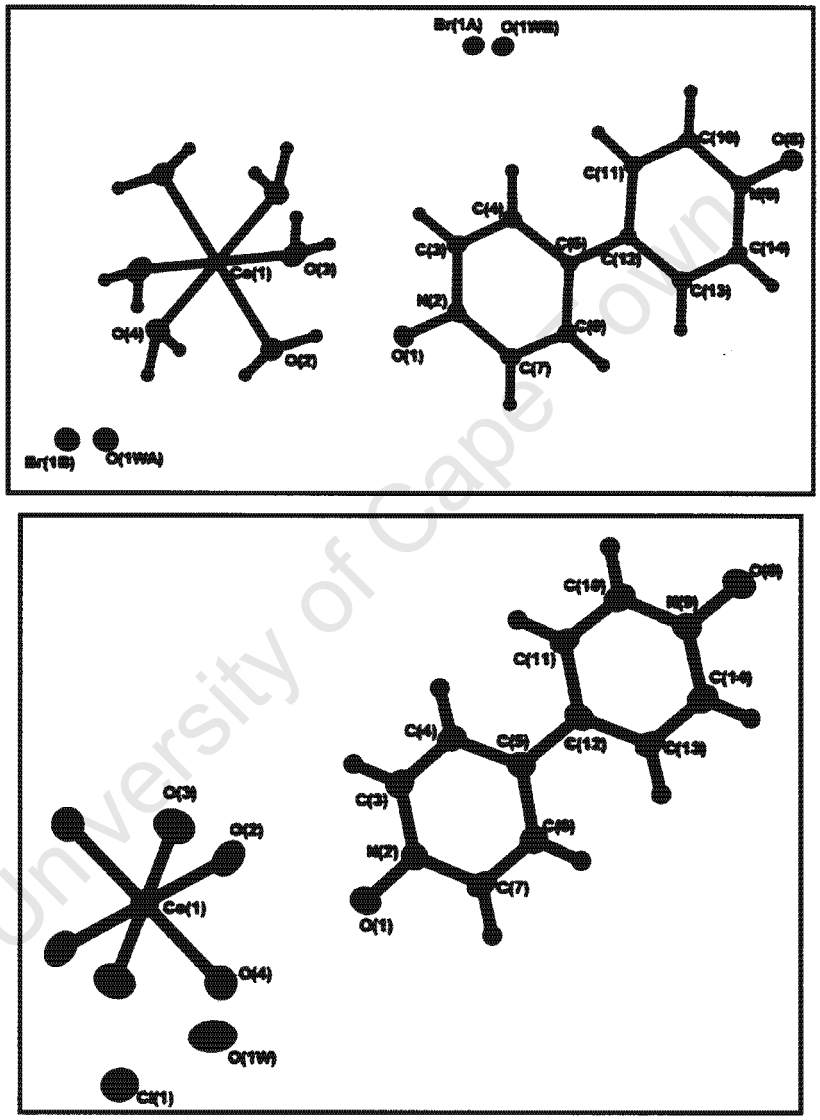

Figure 3.1: Perspective diagrams of **CoB** and **CoC** complexes, showing thermal ellipsoid diagram drawn at 50% probability and atomic labelling.

The $[Co(H_2O)_6]^{2+}$ ion in **CoB** has almost perfect octahedral symmetry (Figure 3.1), with Co–O distances 2.075 to 2.148 Å (literature value 2.085 Å)[1] and O–Co–O angles 87.35 to 92.65°. In **CoC**, Co–O distances range from

The **CoB** compound crystallises in the monoclinic crystal system, in space group $P2_1/c$, while **CoC** crystallised in the $P\bar{1}$ space group which is the triclinic crystal system. Although these compounds are not isostructural, their packing is almost identical, so they will be described together.

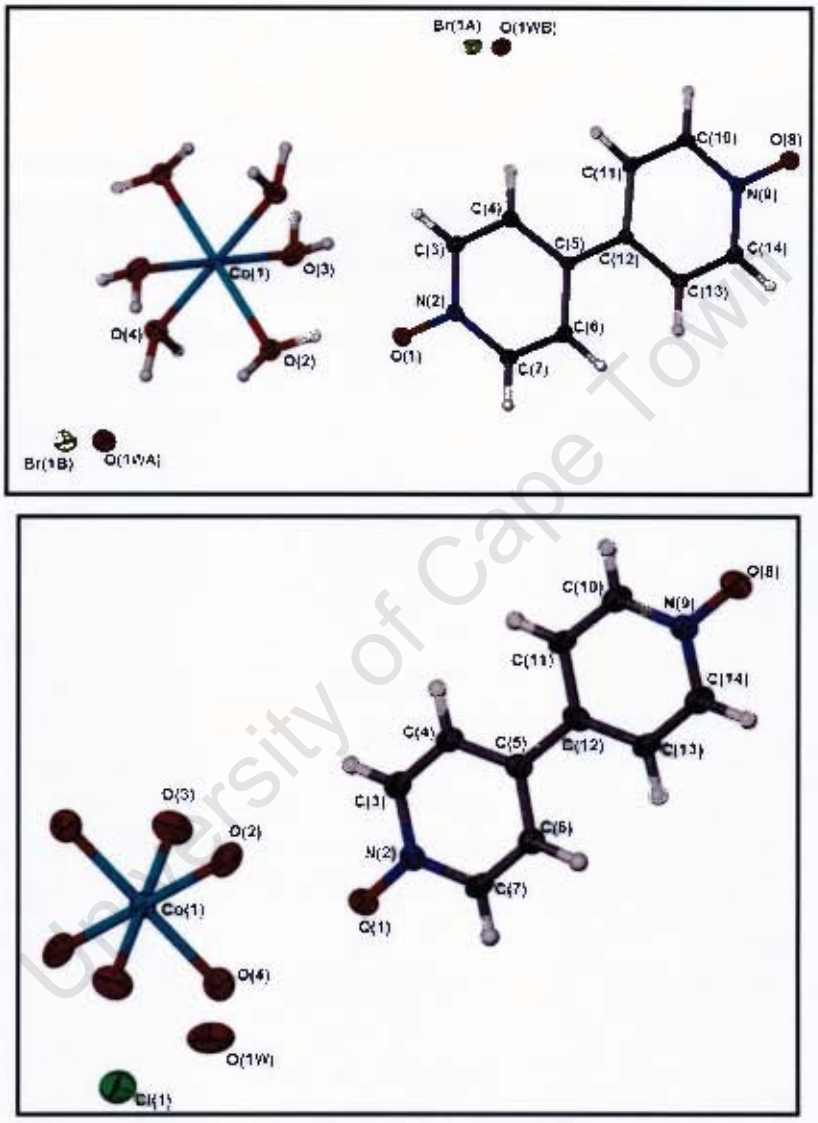

Figure 3.1: Perspective diagrams of **CoB** and **CoC** complexes, showing thermal ellipsoid diagram drawn at 50% probability and atomic labelling.

The $[Co(H_2O)_6]^{2+}$ ion in **CoB** has almost perfect octahedral symmetry (Figure 3.1), with Co–O distances 2.075 to 2.148 Å (literature value 2.085 Å)[1] and O–Co–O angles 87.35 to 92.65°. In **CoC**, Co–O distances range from

PART (A): Anion dependent structural diversity in cobalt (II) complexes of bpdo

Structure solution and analysis

CoB and CoC

Table 3.2: Crystal data and refinement parameters of **CoB** and **CoC**.

Molecular Formula	$[Co(H_2O)_6]Br_2 \cdot 2(C_{10}H_8N_2O_2) \cdot 2H_2O$	$[Co(H_2O)_6]Cl_2 \cdot 2(C_{10}H_8N_2O_2) \cdot 2H_2O$
Formula weight ($g.mol^{-1}$)	739.25	650.33
Temperature (K)	113	113
Wavelength (Å)	0.71073	0.71073
Crystal System	Monoclinic	Triclinic
Space Group	$P2_1/c$	$P\bar{1}$
a (Å)	10.3728 (2)	6.7328 (2)
b (Å)	6.6329 (1)	10.2841 (3)
c (Å)	20.0945 (4)	10.6577 (3)
α (°)	90	85.200 (1)
β (°)	93.366 (1)	70.023 (1)
γ (°)	90	91.103 (1)
Volume ($Å^3$)	1378.58 (4)	690.21 (3)
Z	2	1
Calculated Density ($g\ cm^{-3}$)	1.781	1.565
μ (mm^{-1})	3.588	0.882
F (000)	746	337
Crystal Size (mm)	0.20 x 0.20 x 0.28	0.05 x 0.07 x 0.12
θ Range Scanned (°)	2.0 – 27.9	2.0 – 25.7
Index Range	-13 < h < 13, -8 < k < 8, -26 < l < 26	-8 < h < 7, -12 < k < 12, -12 < l < 12
No. Reflections Collected	22395	13961
No. Unique Reflections	3295	2614
Data completeness (%)	100.0	99.8
Refinement Method	Full-matrix L.S. on F^2	Full-matrix L.S. on F^2
Data / Restraints / Parameters	3295 / 0 / 177	2614 / 0 / 179
Goodness-of-fit on F^2	1.171	1.102
Final R Indices $[I>2\sigma(I)]$	0.0439, 0.1117	0.1055, 0.2736
R Indices (all data)	0.0505, 0.1140	0.1552, 0.3124
Largest Diff. Peak and Hole($e.Å^{-3}$)	0.924, -3.105	1.936, -0.783

Microanalysis

Elemental analysis results are given in Table 3.1 and they corresponded well with the calculated elemental mass percentages, except the minor discrepancies observed in **CoN(A)** and **CoN(E)** and **CoC-2** which could be due to the procedure followed in the preparation of the sample for analysis. The experimental values agree with the stoichiometries found in refined structures.

Table 3.1: Elemental analysis results for Co(II) complexes.

Complex	Found %				Calculated %			
	C	H	N	S	C	H	N	S
CoB	32.38	3.96	7.57	–	32.67	3.84	7.62	–
CoC	36.63	4.20	8.19		36.94	4.96	8.62	–
CoI	31.10	3.12	7.05	–	31.56	3.18	7.36	–
CoN(A)	37.01	3.08	13.09		38.05	3.83	13.31	–
CoN(E)	37.09	3.49	13.17	–	38.05	3.83	13.31	–
CoN(F)	54.11	3.70	13.73	–	54.93	3.69	13.95	–
CoS	25.46	5.04	5.84	6.85	25.59	4.73	5.97	6.83
CoB-2	26.62	2.29	6.15		26.05	3.06	6.08	–
CoC-2	30.12	3.67	6.51	–	32.28	3.79	7.53	–

Complex preparation

Part (A): Crystals of suitable quality were obtained by slow evaporation at ambient temperature over a period of a week (using the method described in Chapter 2). These complexes were crystallised using either methanol or ethanol as a solvent.

Compounds of **CoB** and **CoC** prepared in **Part (A)** were allowed to stand on an open bench. Within a week, new 1D coordination polymers (**CoB-2** and **CoC-2**) were formed.

The abbreviations for the discrete cobalt complexes in this chapter are as follows:

$[Co(H_2O)_6]Br_2 \cdot 2(bpdo) \cdot 2H_2O$:	**CoB**
$[Co(H_2O)_6]Cl_2 \cdot 2(bpdo) \cdot 2H_2O$:	**CoC**
$[CoI_2(H_2O)_4] \cdot 2(bpdo)$:	**CoI**
$[Co(H_2O)_3(bpdo)(NO_3)]\ NO_3 \cdot bpdo \cdot H_2O$:	**CoN(A)**
$[Co(H_2O)_2(bpdo)(NO_3)_2]$:	**CoN(B)**
$[Co_2(H_2O)_8(bpdo)_2]\ (NO_3)_4 \cdot 4H_2O$:	**CoN(C)**
$[Co(H_2O)_5(bpdo)](NO_3)_2 \cdot H_2O$:	**CoN(D)**
$[Co(H_2O)_4(NO_3)_2] \cdot 2(bpdo)$:	**CoN(E)**
$[Co(bpdo)_6](NO_3)_2$:	**CoN(F)**
$[Co(H_2O)_5(bpdo)]SO_4 \cdot 2H_2O$:	**CoS**
$CoBr_2(bpdo)(H_2O)_2 \cdot H_2O$:	**CoB-2**
$CoCl_2(bpdo)(H_2O)_2 \cdot H_2O$:	**CoC-2**

Part (B): Compounds were prepared similar to as described in **Part (A)**, but at different crystallisation temperatures and solvent ratios.

2.081–2.134 and O–Co–O angles 88.99 to 91.01°. Full bond lengths and angles are given in Appendix.

The structure consists of the two $[Co(H_2O)_6]^{2+}$ cations bridged by two bpdo molecules, which are held in place by hydrogen bonds between the (bpdo)-N-O···H O Co (hydrogen bonds are summarised in Table 3.3). The cobalt ion lies on an inversion centre. Four of the coordinated water ligands are occupied in these H-bonds to bpdo. The remaining two each engage in a H-bond to a guest water molecule, which in turn, H-bonds to the bromide ion as shown in Figure 3.2 and summarised in Table 3.3.

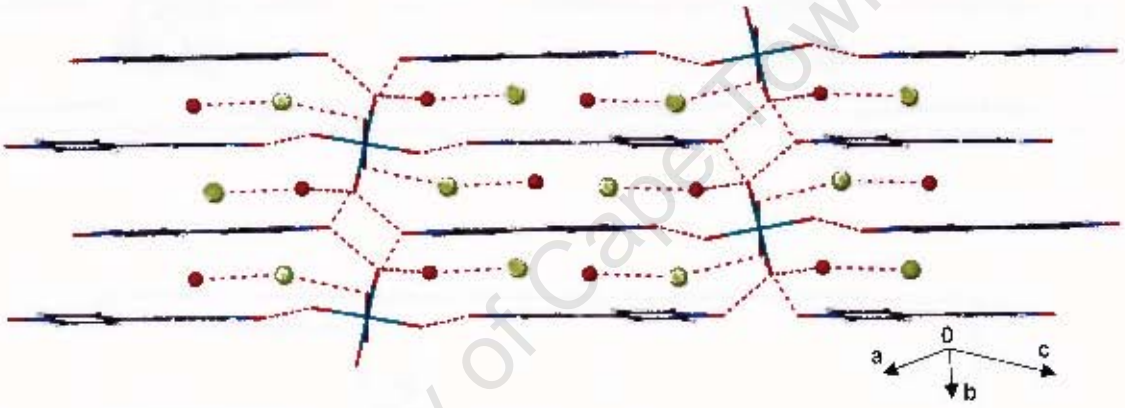

Figure 3.2: Hydrogen bonding interactions in **CoB**.

Each ring in the bpdo molecule is planar, with the two aromatic ring planes twisted by 5.1° (torsion angle) to one another in **CoB** and by 2.0° (torsion angle) in **CoC**. The bromide ion and the guest water molecule are disordered over two sites (site occupancy factors: Br1A and O1WA are 0.925; Br1B and O1WB are 0.075), as indicated in Figure 3.1. Figure 3.3 (a) and (b) shows the packing of these compounds viewed down [100]; it is evident that the structure has the form of layered organic-inorganic hybrid structure with clearly defined zones of parallel stacked aromatic moieties. Adjacent bpdo molecules stack to give offset π···π interactions (details are shown in Table 3.4). Although **CoC** is not isostructural with **CoB** the H-bonding and packing motifs are almost identical with the cobalt ion again lying on an inversion centre. The only difference between **CoB** and **CoC** is the twist angle in the bpdo molecule which is 2.0° in this case. This is illustrated in Figure 3.3(b).

The largest residual peak (1.936 e.Å^{-3}) in **CoC** is located 1.323 Å from Co(1) metal. This peak is probably due to absorption effects which have not been adequately corrected for.

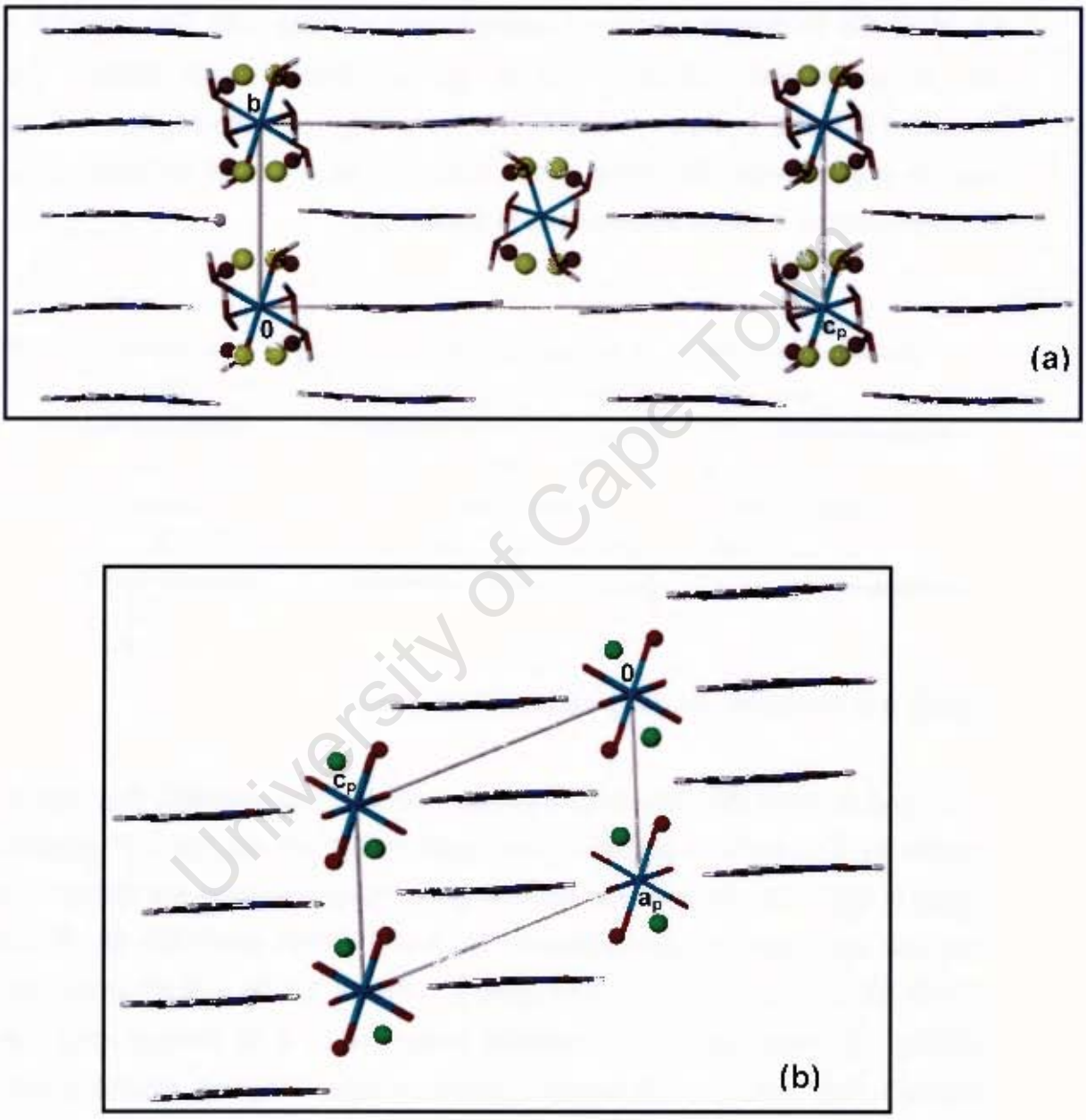

Figure 3.3: **(a)** Packing in **CoB**, showing layered inorganic/organic structure viewed along [100]. **(b)** Packing in **CoC** along [010], illustrating the similarities to (a).

Table 3.3: Hydrogen bonding details in **CoB and CoC** crystal structure.

	D–H (Å)	D···A (Å)	D–H···A (°)	Symmetry operator
CoB				
O2–H21···O1	1.01 (4)	2.701 (5)	160 (6)	x,y,z
O2–H22···Br1A	0.98 (4)	3.293 (3)	165 (5)	x+1,y,z
O2–H22···O1WB	0.98 (4)	2.36 (4)	173 (7)	x+1,y,z
O3–H31···O4	0.98 (4)	2.916 (5)	114 (5)	2-x,2-y,-z
O3–H32···O1WB	0.99 (4)	3.007 (3)	133 (6)	1-x,2-y,-z
O3–H32···Br1A	0.99 (4)	3.241 (3)	159 (5)	1-x,2-y,-z
O4–H41···O1WA	1.04 (4)	2.689 (5)	163 (7)	x,y,z
O4–H41···Br1B	1.04 (4)	3.156 (7)	148 (6)	x,y,z
O4–H42···O1	0.96 (4)	2.755 (4)	169 (6)	x,1+y,z
O1WA···Br1A		3.328 (4)		2-x,2-y,-z
O1WB···Br1B		3.21 (4)		1-x,y,z
O1WB···O1WA		2.91 (4)		1-x,y,z
C7–H7···O8	0.95	3.273 (5)	172	1+x,y,z
C10–H10···O1	0.95	3.312 (5)	171	1-x,2-y,-z
CoC				
O2···O1		2.618 (8)		x,y,z
O2···Cl1		3.065 (6)		-x,1-y,2-z
O3···O1W		2.713 (9)		1-x,1-y,2-z
O3···O8		2.753 (8)		x,1+y,1+z
O4···O8		2.710 (8)		1-x,-y,1-z
O4···Cl1		3.170 (6)		x,y,z
O1W···Cl1		3.200 (8)		1-x,2-y,2-z
C7–H7···O8	0.95	3.28 (1)	173	x,1+y,z
C10–H10···O1	0.95	3.23 (1)	172	x,y-1,z

Table 3.4: π interactions in the **CoB** and **CoC** crystal structures.

	Distance	Symmetry operator
CoB		
*Cg(N9–C14)···Cg(N9–C14)	3.793 (2)	1-x,½+y, ½-z
O8···Cg(N2–C7)	3.244 (4)	1-x, -½+y, ½-z
O8···Cg(N2-C7)	3.407 (4)	1-x, ½+y, ½-z
CoC		
Cg(N2–C7)···Cg(N2–C7)	3.831 (5)	1-x,-y,1-z
Cg(N2–C7)···Cg(N2–C7)	3.819 (6)	2-x,-y,1-z
O1···Cg(N9–C14)	3.372 (6)	1-x,-y,1-z
O1···Cg(N9–C14)	3.434 (5)	2-x,-y,1-z

*Cg = ring centroid

Thermal Analysis

The TG and DSC traces of **CoB** and **CoC** are shown in Figure 3.4(a) and (b) and the results are summarised in the Table 3.5. The TG traces consist of three step mass losses. The first two mass losses are joint (region A and B in Figure 3.4), but could only be differentiated by a hump observed immediately after the first mass loss. This behaviour is shown in Figure 3.4. In both compounds, the first and second mass losses were collectively attributed to the loss of both coordinated and lattice waters (Table 3.5). The third mass loss shows the decomposition of the compound.

The DSC traces in Figure 3.4 show endothermic peaks labelled A and B, which corresponds to the loss of coordinated and guest water; onset temperatures (T_{or}) for these peaks are given in Table 3.5. The third thermal event (exothermic peaks) in each case indicates the loss of some bpdo ligand which then leads to exotherm D (decomposition). The onset temperatures are detailed in Table 3.5.

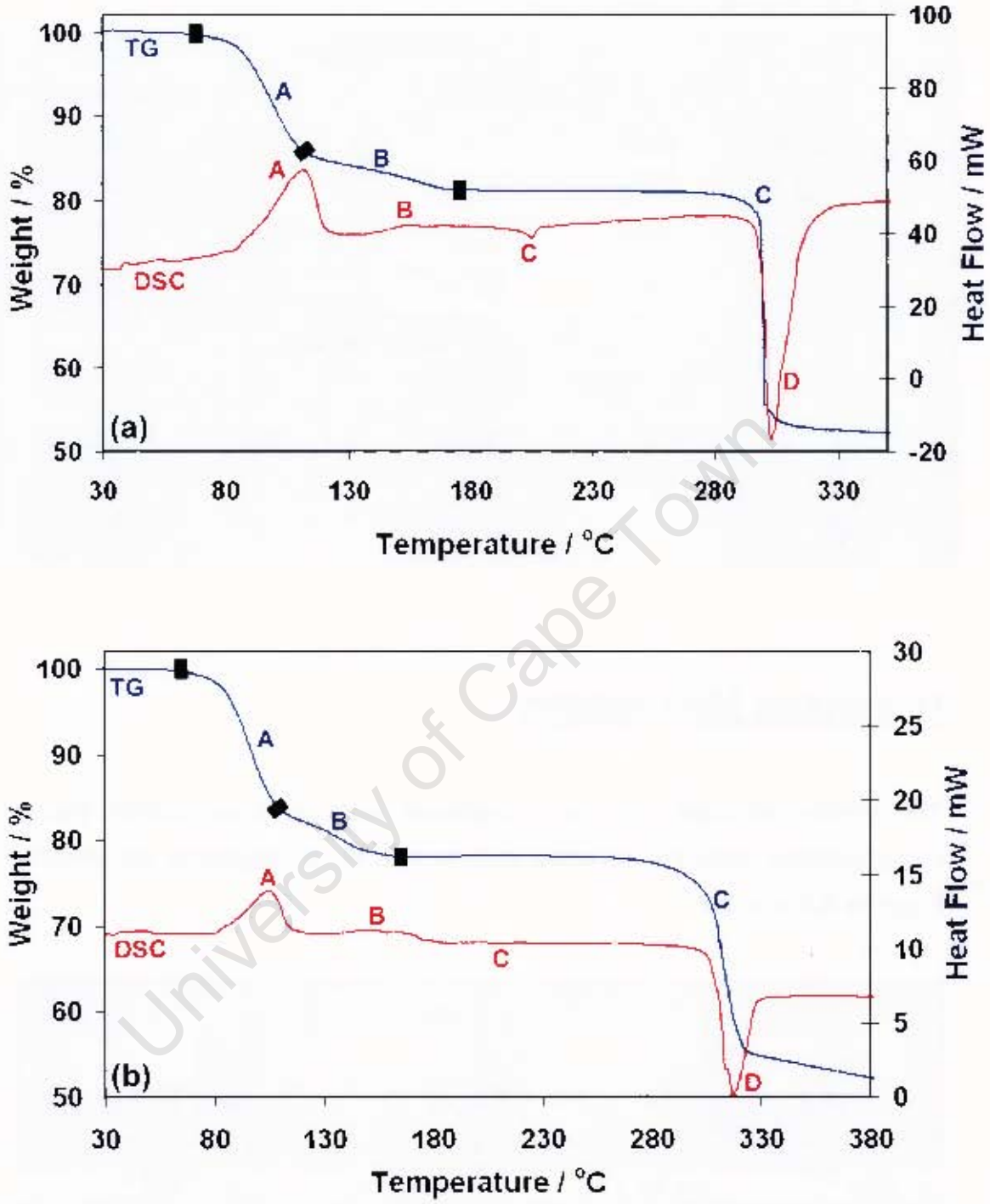

Figure 3.4: TG and DSC traces of **(a) CoB** and **(b) CoC**.

Table 3.5: Thermal analysis results.

	TG Results			
	Calc. % mass loss		Exp. % mass loss	
Complexes	**CoB**	**CoC**	**CoB**	**CoC**
Mass loss A	14.62	16.62	14.57	16.34
Mass loss B	4.87	5.54	4.22	5.73
Total H_2O loss	19.49	22.16	18.79	22.07
complexes	DSC Results			
	T_{on} (°C) Peak A	T_{on} (°C) Peak B	T_{on} (°C) Peak C	T_{on} (°C) Peak D
CoB	89.59	143.8	200.1	299.9
CoC	86.41	133.2	204.0	317.2

Hot Stage Microscopy

The crystals of **CoB** and **CoC** complexes were observed during thermal decomposition using the hot stage microscope and photographs are shown in **Figures 3.5** and **3.6**.

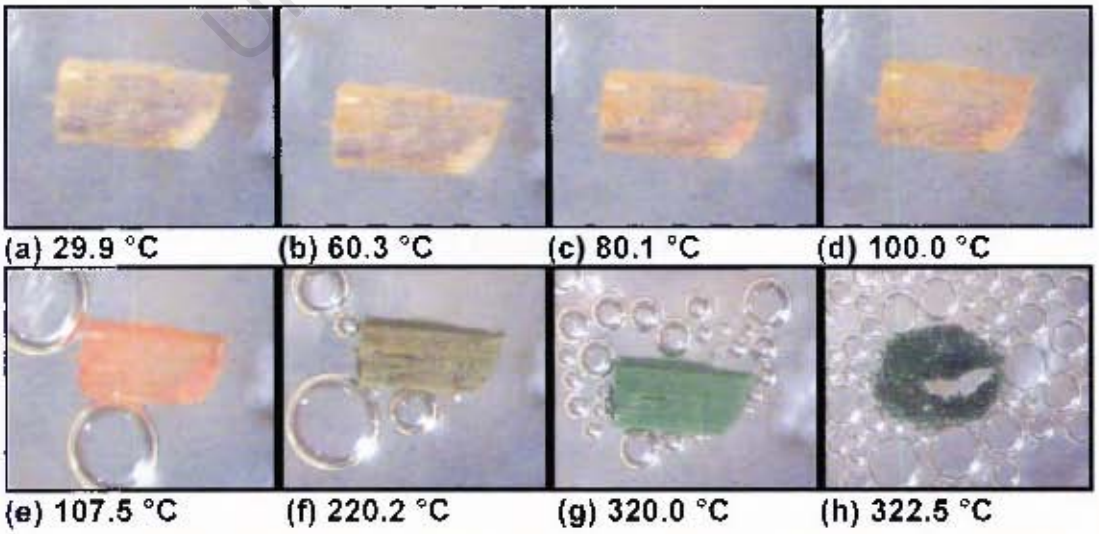

Figure 3.5: Thermal decomposition of **CoB**.

The crystal is stable to ca. 100.0°C. Photograph (d) shows that the crystal is losing its quality and the guest water molecules are released at 107.5 °C (photograph (e)) resulting in the bubbles observed in the silicon oil. The loss of water is also depicted by the change in colour of the crystal.

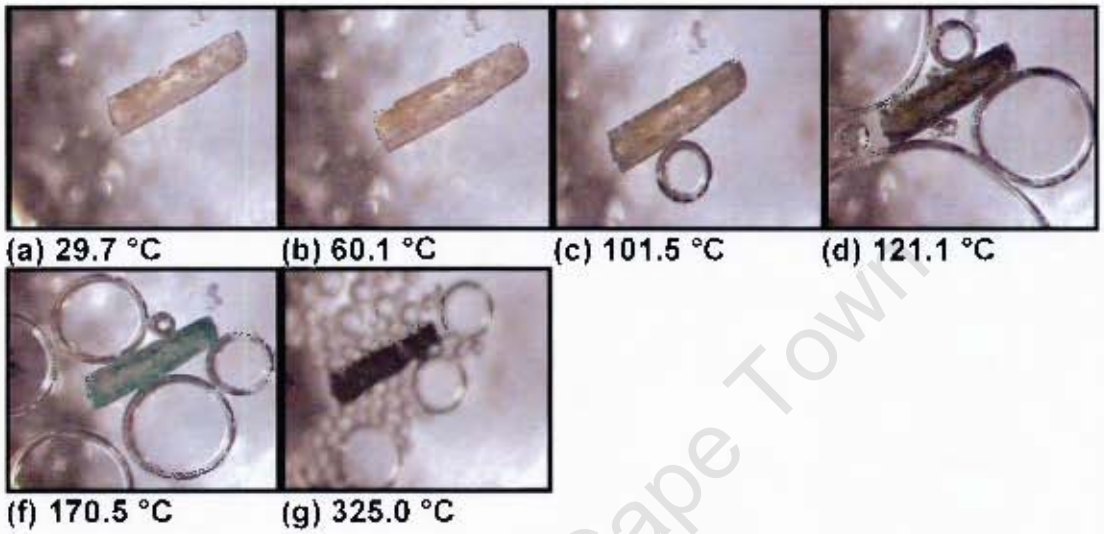

Figure 3.6: Crystals of **CoC** during thermal decomposition. The bubbles of desorbed guest water molecules are observed starting at 101.5 °C (Photograph (c)). At (c), the crystal changed colour to green. The crystal decomposed at 325.0 °C (Photograph (f)).

CoI

Table 3.6: Crystal data and refinement parameters of **CoI.**

Molecular Formula	**$[CoI_2(H_2O)_4]$. $2(C_{10}H_8N_2O_2)$**
Formula weight ($g.mol^{-1}$)	761.16
Temperature (K)	113
Wavelength (Å)	0.71073
Crystal System	Tetragonal
Space Group	$I4_1/acd$
a (Å)	19.151 (3)
b (Å)	19.151 (3)
c (Å)	13.917 (3)
α (°)	90
β (°)	90
γ (°)	90
Volume ($Å^3$)	5102.9 (1)
Z	8
Calculated Density ($g.cm^{-3}$)	2.229
μ (mm^{-1})	3.144
F (000)	2952
Crystal Size (mm)	0.08 x 0.11 x 0.13
θ Range Scanned (°)	2.8 – 27.9
Index Range	-21 < h < 25, -25 < k < 25, -17 < l < 18
No. Reflections Collected	24777
No. Unique Reflections	1533
Data completeness (%)	96.9
Refinement Method	Full-matrix L.S. on F^2
Data / Restraints / Parameters	1533/ 0 / 87
Goodness-of-fit on F^2	1.025
Final *R* Indices $[I>2\sigma(I)]$	0.0186, 0.0399
R Indices (all data)	0.0338, 0.0441
Largest Diff. Peak and Hole ($e.Å^{-3}$)	0.467, -0.511

This compound crystallises in the tetragonal crystal system, in the space group $I4_1/acd$. The water hydrogen atoms were located in a difference electron density map and refined isotropically with independent temperature factors. The remaining hydrogen atoms were positioned geometrically with C–H = 0.95 Å and assigned isotropic temperature factors of $1.2U_{eq}(C)$ of their parent atoms. The cobalt lies on Wyckoff site *c* with point symmetry *-1*, while the Co-I bond is located along a 2-fold rotation axis, thus giving rise to the nearly perfect octahedral geometry in the *trans*-$[CoI_2(H_2O)_4]$ moeity.

Co–I bond lengths are 2.903 Å and Co–O lengths are 2.053 Å. Average literature values are 2.640 Å and 2.085 Å, respectively.[1] Thus the Co–I bond lengths in **CoI** are significantly longer than this average. A search of the CSD[2] for Co–I bonds showed a skewed distribution with a maximum at 2.938 Å (Figure 3.7). There are six other structures reported with Co–I bond lengths between 2.80 and 3.00 Å. While these authors made no comment on the elongation of the Co–I bond, we note that all six have two iodides in the *trans*-conformation (refcodes: IPUBUQ, SAGGIQ, YEZLEU, BOKQOH, EICICO, IPICYC10) as does **CoI**. Furthermore we note that, of 28 structures with bond lengths between 2.57 and 2.60 Å, only six have *trans*-iodides.

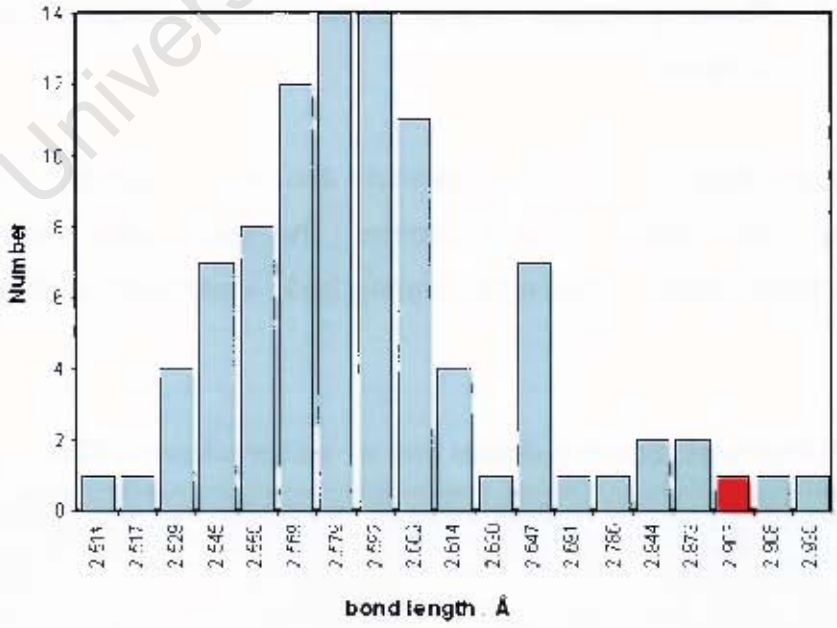

Figure 3.7: A histogram showing distribution of Co–I bond lengths of various crystal structures found in the CSD. A red bar represents **CoI**.

Bond angles between adjacent ligands lie between 87.81 and 92.19°. The ellipsoid diagram and compound atomic labelling is shown in Figure 3.8. The asymmetric unit contains one pyridyl-oxide ring of the bpdo molecule. Operation of the 2-fold rotation axis generates the remainder of the bpdo, and of the $[CoI_2(H_2O)_4]$ ion.

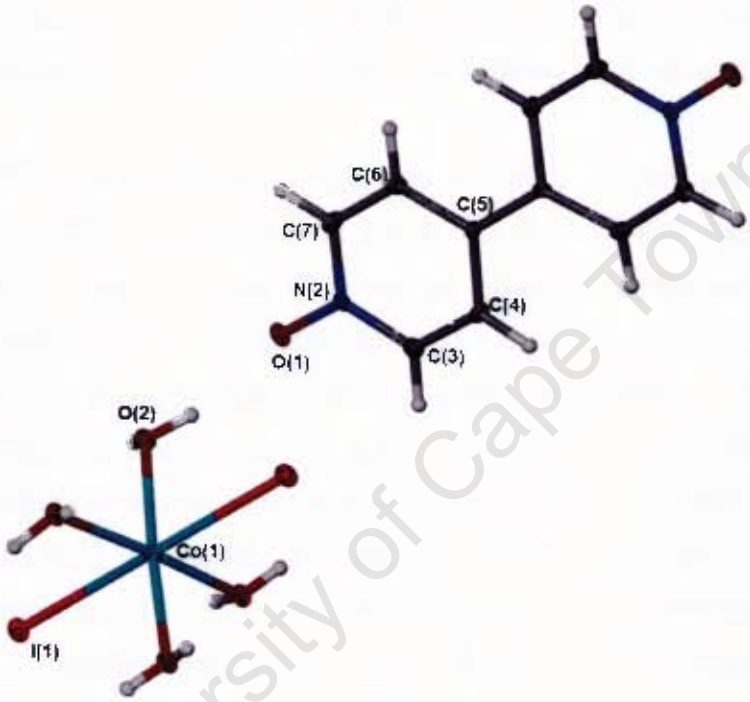

Figure 3.8: Thermal ellipsoid diagram drawn at 50% probability and atomic labelling.

The aromatic rings of the bpdo molecule are planar and their planes are twisted by 3.82° relative to one another. The coordinated water acts as hydrogen bond donor to two neighbouring bpdo molecules (details in Table 3.7).

Table 3.7: Hydrogen bonding details and π···π interactions in **CoI**.

	D–H (Å)	D···A (Å)	D–H···A (°)	Symmetry operator
O2–H2A···O1	0.79 (3)	2.682 (2)	161 (3)	5/4-y, ¼ +x, -z-¼
O2–H2B···O1	0.80 (3)	2.714 (3)	151 (3)	x, y, z
*Cg(N2–C7) ···Cg(N2–C7)		3.672 (3)		x, 2-y, -½-z

*Cg = ring centroid

In turn, each bpdo oxygen accepts two hydrogen bonds from neighbouring $[CoI_2(H_2O)_4]$ molecules (Figure 3.9). Propagation along the 4-fold screw axis and glide plane gives rise to a three dimensional supramolecular network shown in Figure 3.10. The hydrogen network is 3D, but there are two interpenetrating networks – i.e. there are two independent but entangled networks. The π-stacking interaction (Table 3.7) occur between bpdo molecules of different networks. C–H···I interactions (4.13 Å) further stabilises the structure.

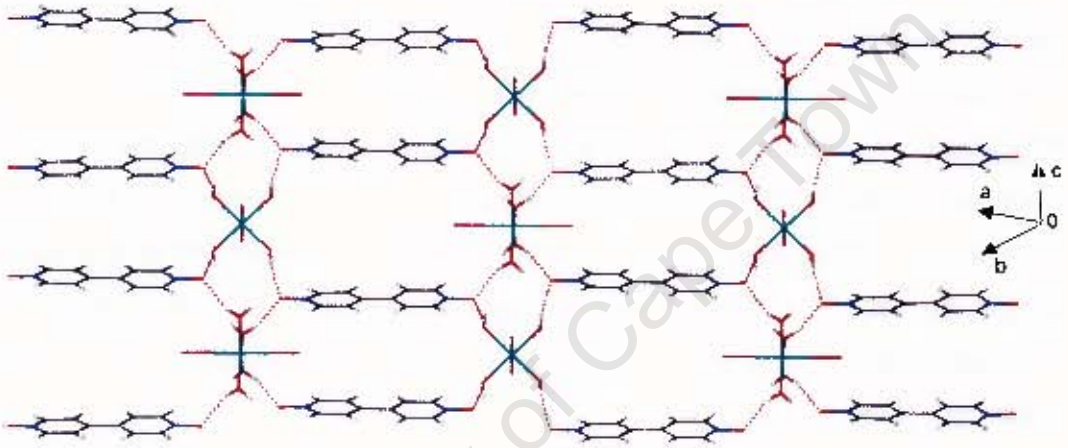

Figure 3.9: Hydrogen bonding in 2-dimensions in **CoI.**

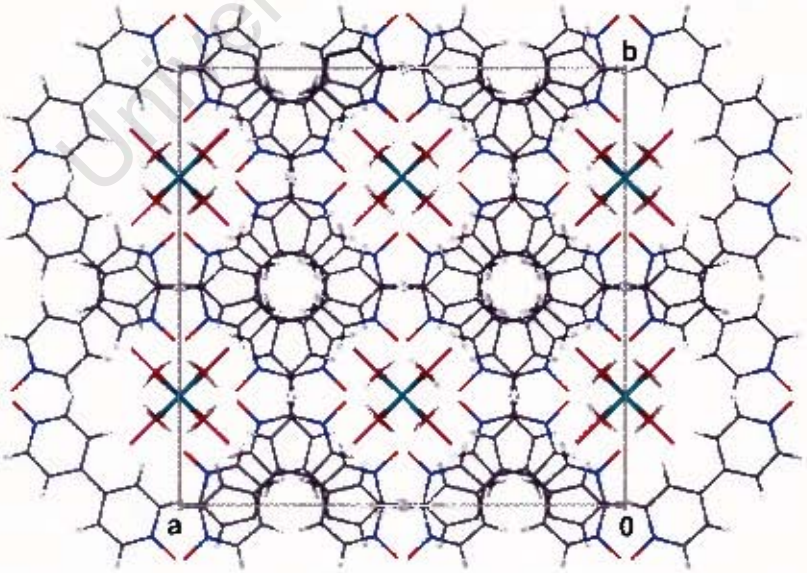

Figure 3.10: Propagation along 4_1 axis generates a 3-dimensional supramolecular network, stabilised by hydrogen bonding and π…π interactions and C–H···I interactions.

Thermal Analysis

The TG and DSC traces of **CoI** are shown in Figure 3.11. The TG traces consists of three step mass loss. The first two mass losses are fused (Figure 3.11) as was observed previously for **CoB** and **CoC** complexes. The first mass losses (area A and B in Figure 3.11) were attributed to the loss of four coordinated waters (Table 3.8). Mass loss A accounts for three coordinated waters, while mass loss B is attributed to one coordinated water molecule. The third mass loss shows the decomposition of the compound. The results are summarised in the Table 3.8.

The DSC is characterised by three peaks (labelled A, B and C). All the water molecules in this compound are coordinated to the central metal as discussed. The first mass loss (endotherm A) corresponded to the loss of three water molecules and the remaining one water molecule is depicted by endotherm B. The third thermal event (exotherm C) demonstrates the decomposition of the compound. The onset temperatures (T_{on}) for these peaks are given in Table 3.8.

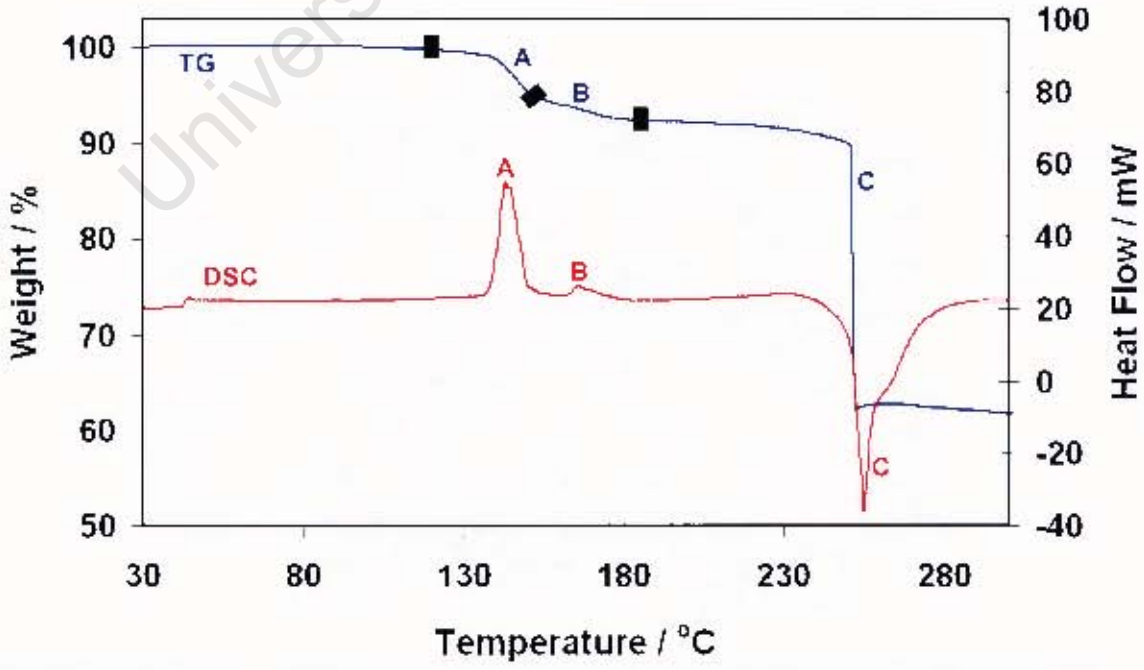

Figure 3.11: TG and DSC traces of **CoI**.

Table 3.8: Thermal analysis results of **Col**.

	TG Results		
	Calc. % mass loss	Exp. % mass loss	
Mass loss A	7.10	6.23	
Mass loss B	2.37	3.10	
Total H_2O loss	9.47	9.33	
complex	DSC Results		
	T_{on} (°C) Peak A	T_{on} (°C) Peak B	T_{on} (°C) Peak C
Col	138.8	162.5	251.5

Hot Stage Microscopy

The crystal of **Col** complex was observed during thermal decomposition and photographs are shown in **Figures 3.11**.

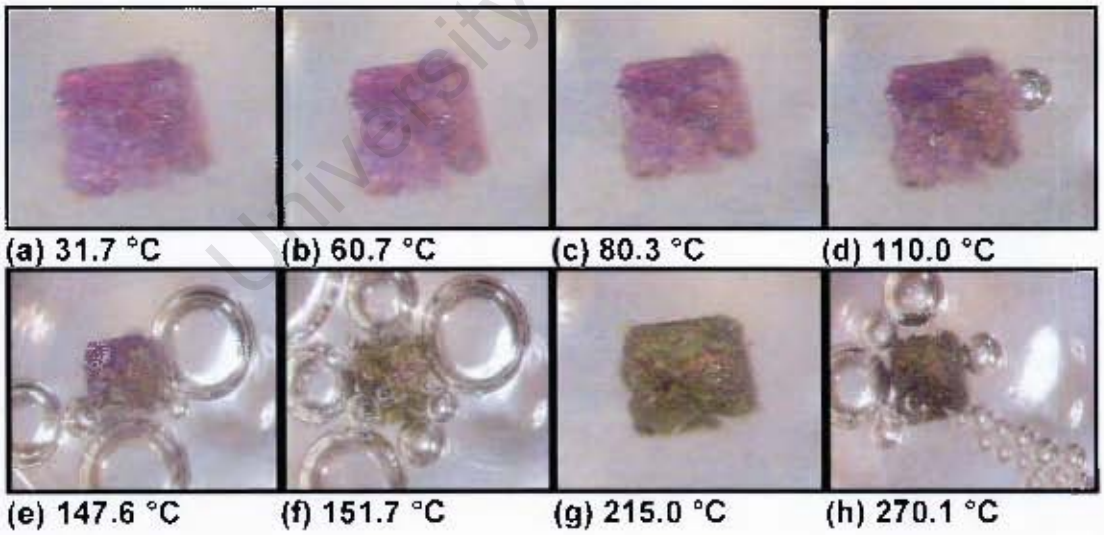

Figure 3.12: Thermal decomposition of **Col.** The bubbles were observed in the silicon oil at 110.0 °C (Photograph (d) indicating loss of water molecules and this resulted in the crystal losing its purple colour to green (Photograph (f)–(g)). The decomposition stage was observed from 270.1°C (Photograph (h)).

(I) CoN(A)

Table 3.9: Crystal Data and Refinement Parameters of **CoN(A)** at 298 K and 113 K.

Molecular Formula	$[Co(H_2O)_3(C_{10}H_8N_2O_2)(NO_3)]$ $NO_3 . (C_{10}H_8N_2O_2) . H_2O$	$[Co_2(H_2O)_6(C_{10}H_8N_2O_2)_2(NO_3)_2]$ $(NO_3)_2 . (C_{10}H_8N_2O_2)_2 . 2H_2O$
Formula weight ($g.mol^{-1}$)	631.38	631.38
Temperature (K)	298	113
Wavelength (Å)	0.71070	0.71070
Crystal System	Triclinic	Triclinic
Space Group	$P\bar{1}$	$P\bar{1}$
a (Å)	7.8139 (2)	12.129 (2)
b (Å)	9.9126 (3)	12.907 (3)
c (Å)	17.1863 (5)	17.896 (4)
α (°)	78.607 (1)	77.49 (3)
β (°)	83.460 (1)	70.25 (3)
γ (°)	85.615 (1)	76.28 (3)
Volume ($Å^3$)	1293.47 (6)	2532.8 (9)
Z	2	4
Calc. Density ($g.cm^{-3}$)	1.620	1.656
μ (mm^{-1})	0.746	0.762
F (000)	650	1300
Crystal Size (mm)	0.08 x 0.15 x 0.30	0.08 x 0.09 x 0.15
θ Range Scanned (°)	2.6 – 27.8	1.2 – 27.1
Index Range	-10 < h < 10, -13 < k < 13, -22 < l < 22	-15 < h < 15, -16 < k < 16, -22 < l < 22
No. Reflections Collected	32831	44753
No. Unique Reflections	6132	11119
Data completeness (%)	87.6	98.9
Refinement Method	Full-matrix L.S. on F^2	Full-matrix L.S. on F^2
Data / Restraints / Parameters	6132 / 0 / 371	11119 / 0 / 749
Goodness-of-fit on F^2	0.998	1.017
Final *R* Indices $[I>2\sigma(I)]$	0.0704, 0.1793	0.0412, 0.0913
R Indices (all data)	0.1355, 0.2094	0.0896, 0.1085
Largest Diff. Peak and Hole ($e.Å^{-3}$)	0.529, -0.475	0.765, -0.460

An interesting feature of this crystal structure is the phase transformation that occurs at ca. 162 K. Figure 3.13(a) and (b) shows the variation in unit cell parameters with temperature, measured on a single crystal. The phase transformation is reversible. Due to the cell we chose, it was impossible to get the relevant transformed α and β angles in terms of the low temperature unit cell, but instead the complimentary angles were obtained. Thus, (180-α) and (180-β) angles were included in the figure.

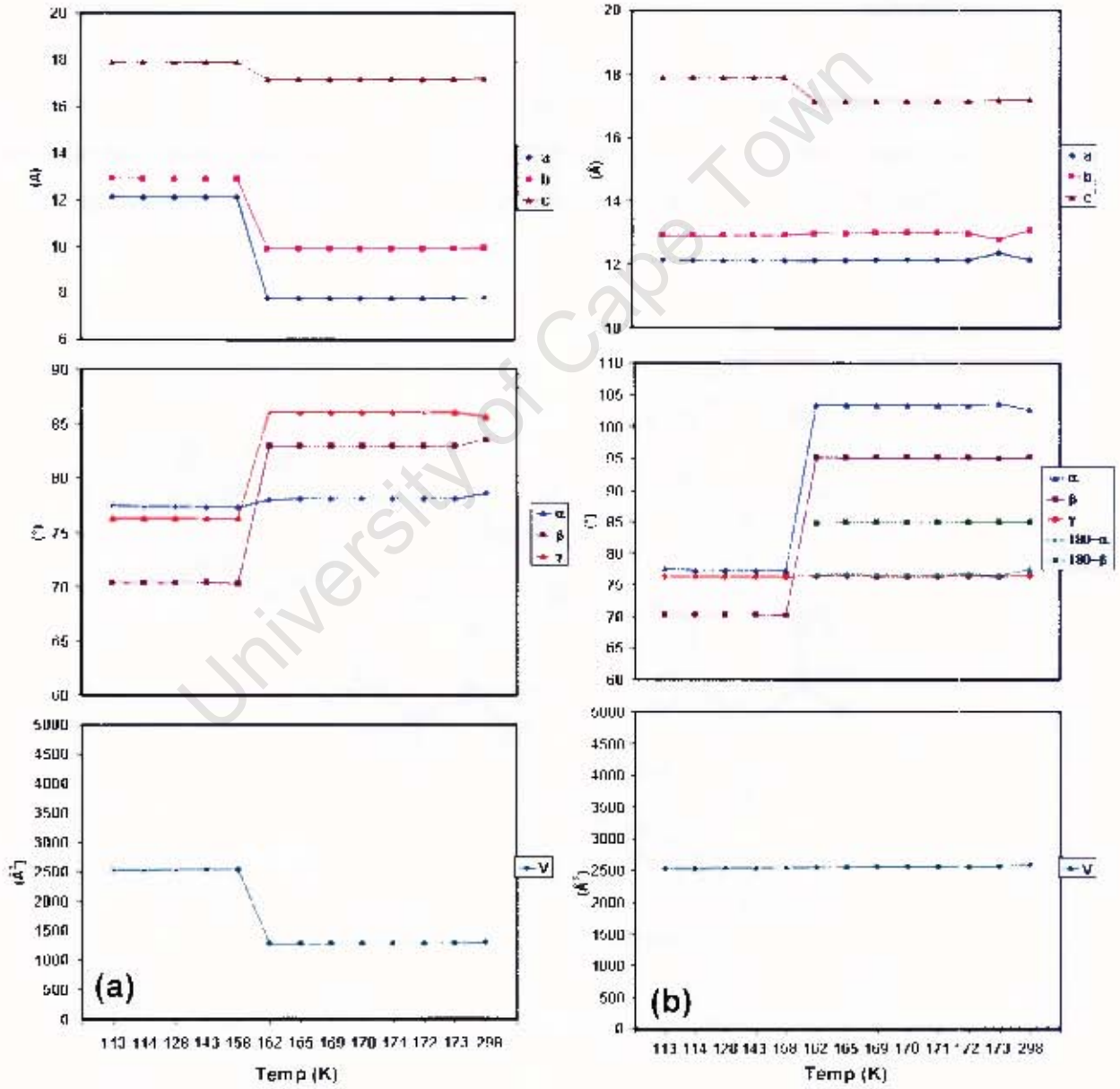

Figure 3.13: **(a)** Variation in unit cell parameters on phase transformation in **CoN(A)**. **(b)** Transformation in terms of low temperature cell showing that the change in volume and cell axes are minor, but the angles alter significantly.

We did not calculate the linear expansion coefficients of the cell axes nor the volume expansion coefficient of the unit cell with temperature, because the data, as shown on the graphs of Figure 3.13(a) and 3.13(b) show that the variations, both before and after the transition points, are practically zero i.e. the graphed functions are flat and invariant with temperature. In a similar study carried out by Caira, Nassimbeni, Su and Weber,[3] they monitored the phase change of the inclusion compound phenylfluorenol from 297 to 193 K, and found linear expansion coefficients of the order of $1x10^{-4}$ K^{-1} for the cell parameter.

Single crystal x-ray data for **CoN(A)** were collected at 298 K and 113 K. In both cases, the space group is triclinic, and the molecular conformations are identical. Figure 3.14 shows the common components of this compound.

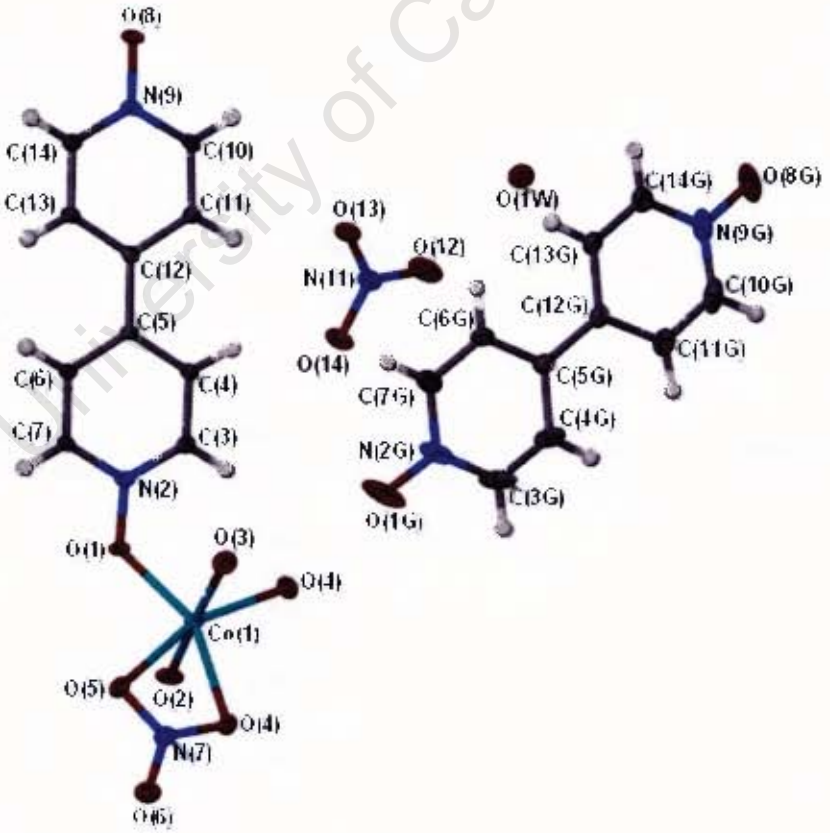

Figure 3.14: Thermal ellipsoid diagram drawn at 50% probability and atomic labelling of **CoN(A)** at room temperature (298 K).

At temperatures above 162 K, the coordination sphere of the $[Co(H_2O)_2(bpdo)(NO_3)]^+$ ion is a distorted octahedron, with the Co–O(nitrate) bond lengths slightly longer (*ca.* 2.2 Å) than Co–O(water or bpdo) (*ca.* 2.0 – 2.1 Å) while O Co O angles are close to 90° except the bite angle of the nitrate ion (58°) and the angle opposite it (105°). In this compound, the bpdo ligand coordinates to the Co(II) through one oxygen, while the other end acts as hydrogen bond acceptor for coordinated waters on two adjacent $[Co(H_2O)_2(bpdo)(NO_3)]^+$ ions (Figure 3.15 (a)).

The bpdo aromatic rings are twisted 3.10° relative to one another. An independent nitrate ion balances the charge, and one molecule each of bpdo and water have been included as guests. Thus, the $[Co(H_2O)_2(bpdo)(NO_3)]^+$ ions form a supramolecular ladder-type framework parallel to the *a*-axis. The void between the frameworks is filled by nitrate ions, water and bpdo guest molecules, stabilised by hydrogen bonds and by $\pi\cdots\pi$ stacking interactions as detailed in Table 3.10 and 3.11.

Table 3.10: Hydrogen bonding details in **CoN(A)** crystal structure.

	D–H (Å)	D···A (Å)	D–H···A (°)	Symmetry operator
O2···O8		2.750 (4)		2-x, 3-y, -z
02···013		2.677 (4)		1+x, y, z
O3···O8		2.761 (4)		1-x, 3-y, -z
O3···O1W		2.647 (5)		x, y, z
O4···O1G		2.616 (5)		x, y, z
O4···O8G		2.607 (5)		2-x, 3-y, 1-z
O1G···O1W		2.729 (5)		1+x, y, z
O1W···O12		2.837 (6)		x, y, z
C6–H6···O13	0.93	3.367 (5)	172	1-x, 2-y, -z
C7–H7···O1	0.93	3.491 (5)	172	2-x, 2-y, -z
C10–H10···O8	0.93	3.257 (5)	164	1-x, 4-y, -z
C13–H13···O13	0.93	3.214 (6)	169	1-x, 2-y, -z
C13G–H13G···O5	0.93	3.480 (6)	163	x, 1+y, z

Table 3.11: $\pi\cdots\pi$ interactions details.

	Distance	Symmetry operator
*Cg(N2–C7)···Cg(N9–C14)	3.912 (4)	1-x, 2-y, -z
Cg(N2–C7)···Cg(N9–C14)	3.898 (4)	2-x, 1-y, -z
Cg(N9–C14)···Cg(N2–C7)	3.921 (4)	1-x, 2-y, -z
Cg(N2G–C7G)···Cg(N9G–C14G)	3.688 (5)	-x, 1-y, 1-z

*Cg = ring centroid

When data for the same crystal is collected at 113 K, the unit cell volume is approximately double that for the data collection at 298 K. At low temperature the asymmetric contents double, with each $[Co(H_2O)_2(bpdo)(NO_3)]^+$, NO_3^- and bpdo having identical molecular geometry to each other and to the geometry observed at room temperature.

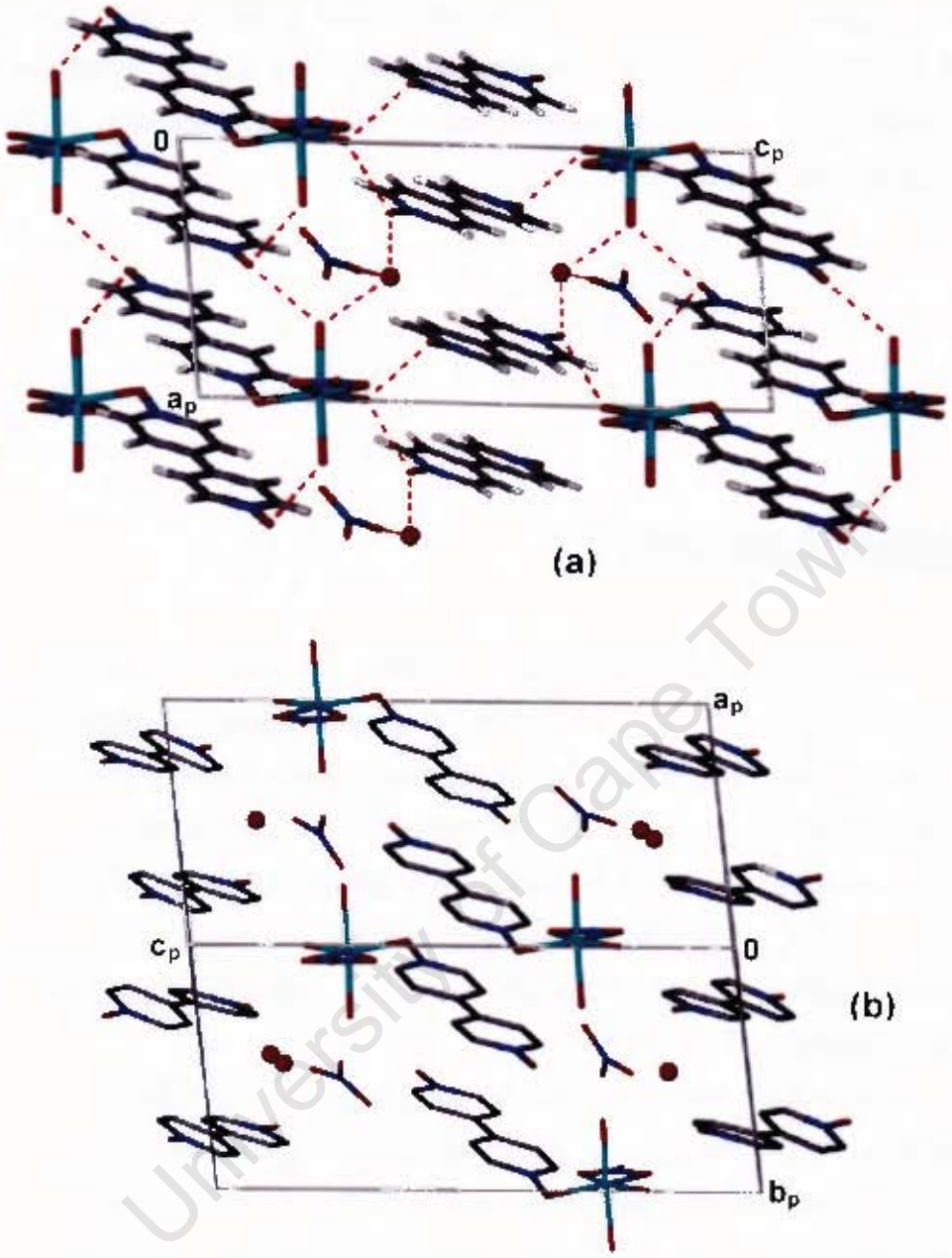

Figure 3.15: **(a)** and **(b)**: Comparison of packing diagrams for **CoN(A)** at **(a) 298 K** and **(b) 113 K**. **(b)** is viewed along [110]. The low temperature induced disorder in O2W disrupts the centrosymmetry and causes a doubling in the unit cell volume.

The only part of the structure to break the centrosymmetry between parts A and B in the asymmetric unit is a disordered water molecule [O(2WA) and O(2WB)] (Figure 3.15(b)). It appears therefore that, in this case, the standard practice of collecting data at low temperature (to minimise thermal motion and crystal decay) has "frozen in" thermal disorder in the crystal structure. As

shown in Figure 3.13(a) and (b), this phenomenon is reproducible occurring at 162 K in each cycle. The *c*-axis is similar in both temperature conditions while the *a*- and *b*-axes differ. The matrix used for comparison between the two cell parameters is as follows:

$$\begin{bmatrix} \bar{a} \\ b \\ \bar{c} \end{bmatrix}_{LT} = \begin{bmatrix} -1 & 1 & 0 \\ 1 & 1 & 0 \\ 0 & 0 & -1 \end{bmatrix} \begin{bmatrix} a' \\ b' \\ c' \end{bmatrix}_{RT}$$

Thermal Analysis

The TG and DSC traces of **CoN(A)** are shown in Figure 3.16 and the results are summarised in the Table 3.12. The TG traces consists of three step mass loss. The first two mass losses are combined (region A and B in Figure 3.16) and were attributed to all water molecules in the compound. Unlike in the previous compounds, the first mass loss corresponded to a guest water molecule (Table 3.12) followed by a sharp second mass loss which was attributed to three coordinated water molecules. The third mass loss shows the decomposition of the compound.

The DSC is characterised by three peaks (Figure 3.16). The first mass loss (endotherm A) corresponds to guest water molecule while the coordinated water molecules are depicted by endotherm B. The third thermal event shows the decomposition of the compound. The onset temperatures (T_{on}) for these peaks are given in Table 3.12.

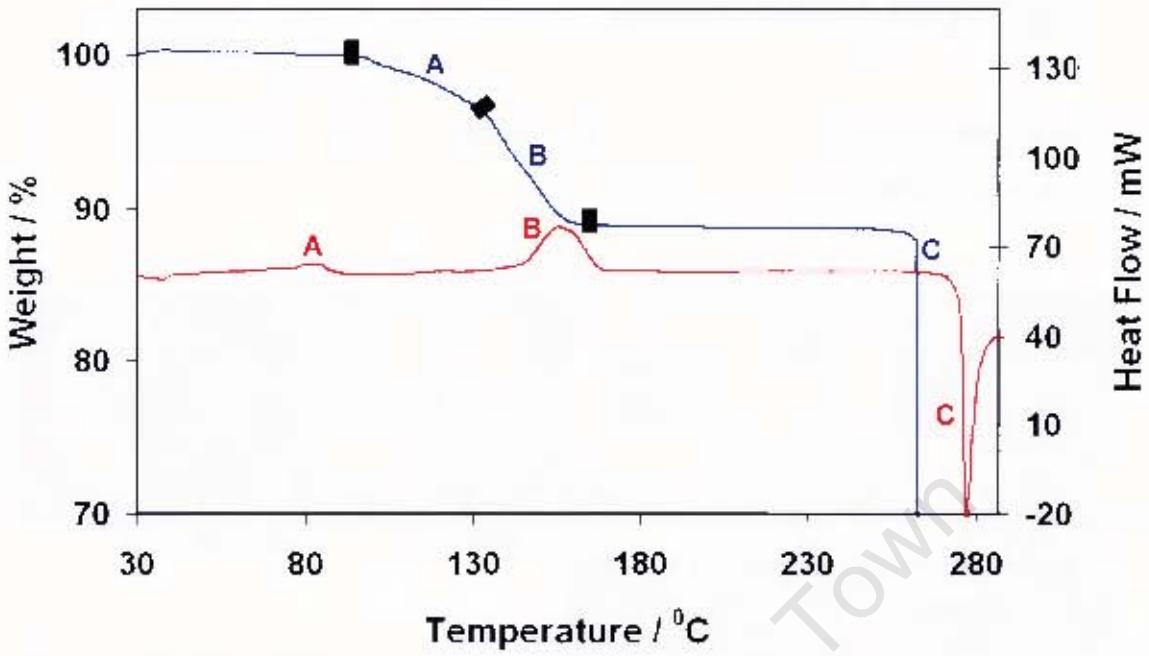

Figure 3.16: TG and DSC traces of **CoN(A)**.

Table 3.12: Thermal analysis results of **CoN(A)**.

	TG Results	
	Calc. % mass loss	Exp. % mass loss
Mass loss A	2.85	3.22
Mass loss B	8.56	7.94
Total H_2O loss	11.41	11.16
complex	**DSC Results**	
	T_{on} (°C) Peak A	T_{on} (°C) Peak B	T_{on} (°C) Peak C
CoN(A)	73.8	139.8	263.9

Hot Stage Microscopy

The crystal of **CoN(A)** compound was observed during thermal decay and photographs are shown in **Figures 3.16**.

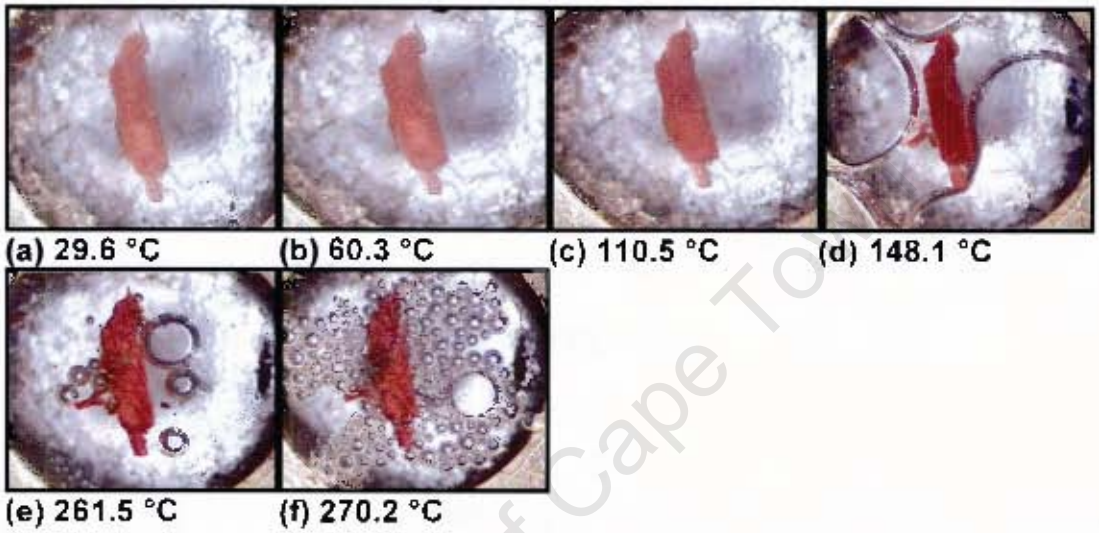

Figure 3.17: Crystals of **CoN(A)** during thermal decay. The crystal colour gradually becomes more intense as a result of guest water molecules escaping from the crystal lattice (Photograph (c), 110.5°C). The coordinated water molecules force themselves out at 148.1 °C and this is observed by bubbles in the silicon oil. The crystal begins to decomposing as shown in photograph (e) 261.5°C and (f) 270.2 °C.

(II) CoN(B)

Table 3.13: Crystal Data and Refinement Parameters of **CoN(B)**.

Molecular Formula	$[Co(H_2O)_2(C_{10}H_8N_2O_2)(NO_3)_2]$
Formula weight ($g.mol^{-1}$)	407.17
Temperature (K)	113
Wavelength (Å)	0.71070
Crystal System	Monoclinic
Space Group	$P2_1/n$
a (Å)	7.5008 (2)
b (Å)	9.6910 (2)
c (Å)	19.574 (4)
α (°)	90.00
β (°)	93.38 (3)
γ (°)	90.00
Volume ($Å^3$)	1420.4 (5)
Z	4
Calc. Density ($g.cm^{-3}$)	1.904
μ (mm^{-1})	1.277
F (000)	828
Crystal Size (mm)	0.02 x 0.05 x 0.12
θ Range Scanned (°)	2.86 – 27.87
Index Range	-9 < h < -9, -12 < k < 12, -25 < l < 24
No. Reflections Collected	23910
No. Unique Reflections	3320
Data completeness (%)	98.5
Refinement Method	Full-matrix L.S. on F^2
Data / Restraints / Parameters	3320 / 0 / 242
Goodness-of-fit on F^2	1.037
Final R Indices $[I>2\sigma(I)]$	0.0381, 0.0778
R Indices (all data)	0.0693, 0.0801
Largest Diff. Peak and Hole ($e.Å^{-3}$)	0.699, -0.455

Single crystal x-ray data for **CoN(B)** were collected at 113 K. The compound crystallises in the monoclinic crystal system, in the space group $P2_1/n$. This crystal structure has four molecules in the unit cell. Thermal ellipsoids and labelling are shown in Figure 3.18.

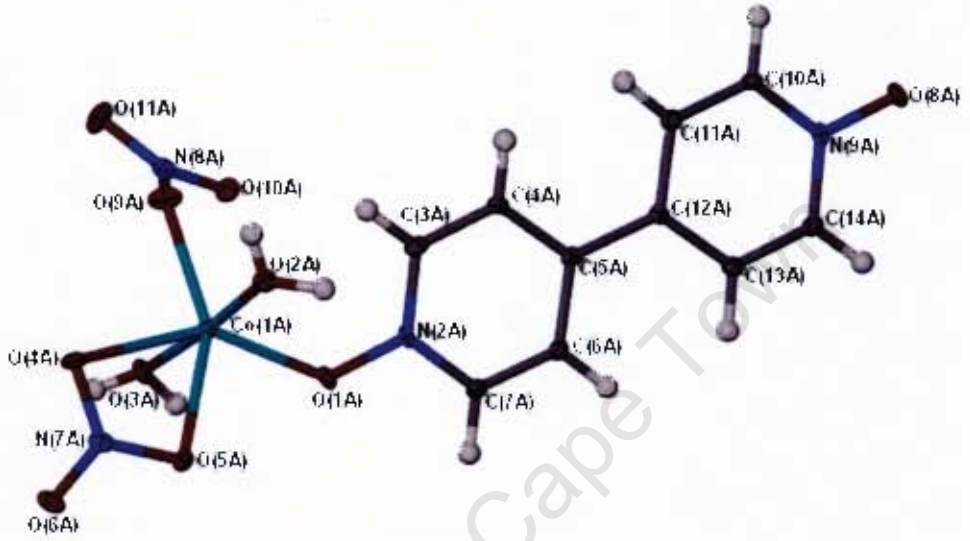

Figure 3.18: Thermal ellipsoid diagram drawn at 50% probability and atomic labelling of **CoN(B)** at 113 K.

The coordination sphere of the $[Co(H_2O)_2(bpdo)(NO_3)_2]$ compound is a irregular octahedron, with the double-coordinated nitrate ends having Co_{1A}–O_{5A}(nitrate) and Co_{1A}–O_{4A}(nitrate) bond lengths slightly longer (*ca.* 2.1 and 2.3 Å, respectively) than the single-coordinated nitrate Co_{1A}-O_{9A}(nitrate) while the Co-O(water or bpdo) are *ca.* 2.0 Å. All the O–Co–O angles are close to 90° except the bite angle of the nitrate ion (58°) and the angle opposite it (122°).

All the coordinated ligands of this compound are involved in hydrogen bonding interactions. Two coordinated water molecules act as hydrogen bond donors for bpdo molecules and nitrate groups to link the adjacent discrete molecules. Details of hydrogen bonding are summarised in Table 3.14 and the illustration can be seen in Figure 3.19. The compound is further stabilised by $\pi\cdots\pi$ stacking interactions (Table 3.15).

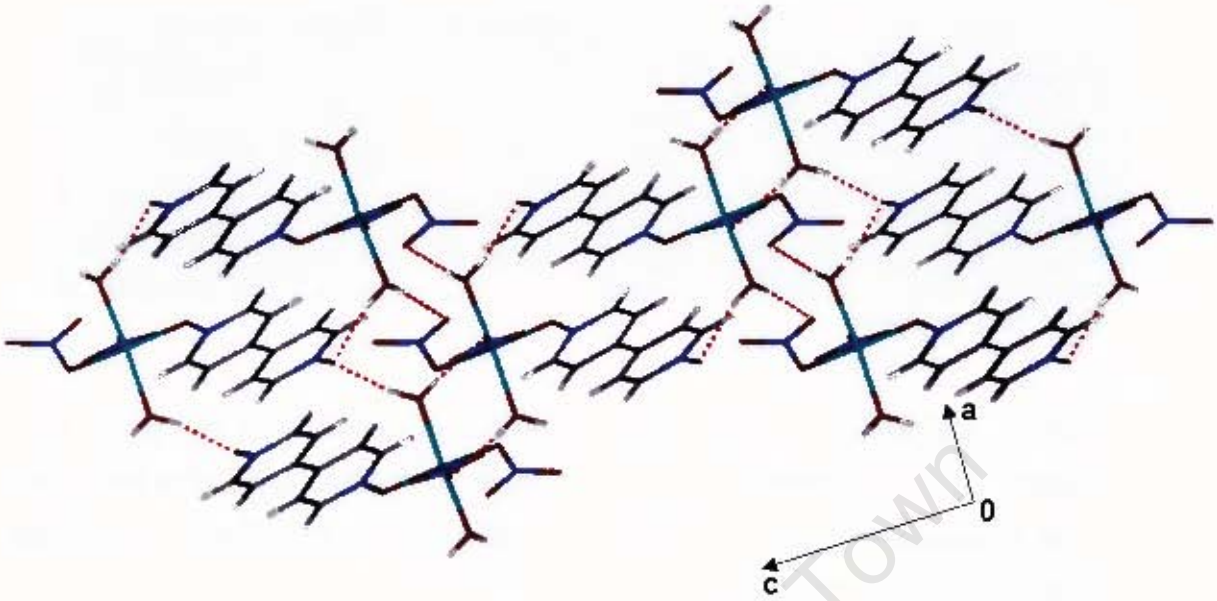

Figure 3.19: Hydrogen bonding interactions in **CoN(B)**.

Table 3.14: Hydrogen bonding details in **CoN(B)** crystal structure.

	D–H (Å)	D···A (Å)	D–H···A (°)	Symmetry operator
O2A–H2A2···O8A	0.87 (3)	2.700 (3)	167 (3)	1-x, -1-y, 2-z
O3A–H3A2···O8A	0.85 (3)	2.750 (2)	168 (3)	-x, -1-y, 2-z
O2A H2A1···O6A	0.75 (3)	2.781 (3)	172 (3)	½-x, - ½+y, 3/2-z
O3A–H3A1···O10A	0.75 (3)	2.860 (3)	172 (3)	-½-x, ½+y, 3/2-z
O3A–H3A1···O11A	0.75 (3)	3.094 (3)	127 (3)	-½-x, ½+y, 3/2-z
C3A–H3A···O4A	0.9500	3.328 (3)	142.00	½-x, -½+y, 3/2-z
C6A–H6A···O5A	0.9500	3.082 (3)	124.00	-x, -y, 2-z
C6A–H6A···O11A	0.9500	3.079 (3)	117.00	½+x, -½-y, ½+z
C7A–H7A···O1A	0.9500	3.526 (3)	174.00	-x, -y, 2-z
C7A–H7A···O5A	0.9500	3.144 (3)	118.00	-x, -y, 2-z
C10A–H10A···O8A	0.9500	3.265 (3)	171.00	1-x, -2-y, 2-z
C11A H11A···O11A	0.9500	3.212 (3)	136.00	½-x, -½+y, 3/2-z
C14A–H14A···O10A	0.9500	3.139 (3)	143.00	-x, -1-y, 2-z

Table 3.15: π···π interactions in **CoN(B)** crystal structure.

	Distance	Symmetry operator
* Cg(N2A–C7A)···Cg(N9A–C14A)	3.812 (2)	-x, -1-y, 2-z
Cg(N2A–C7A)···Cg(N9A–C14A)	3.695 (2)	1-x, -1-y, 2-z
Cg(N9A C14A)···Cg(N2A–C7A)	3.812 (2)	-x, -1-y, 2-z
Cg(N9A–C14A)···Cg(N2A–C7A)	3.695 (2)	1-x, -1-y, 2-z

*Cg = ring centroid

Packing diagrams of **CoN(A)** and **CoN(B)** are similar, but the packing in **CoN(B)** is more compact owing to the absence of free nitrate ions and bpdo guest molecules. Figure 3.20 shows comparison of the packed molecules along [100], [010] and [001].

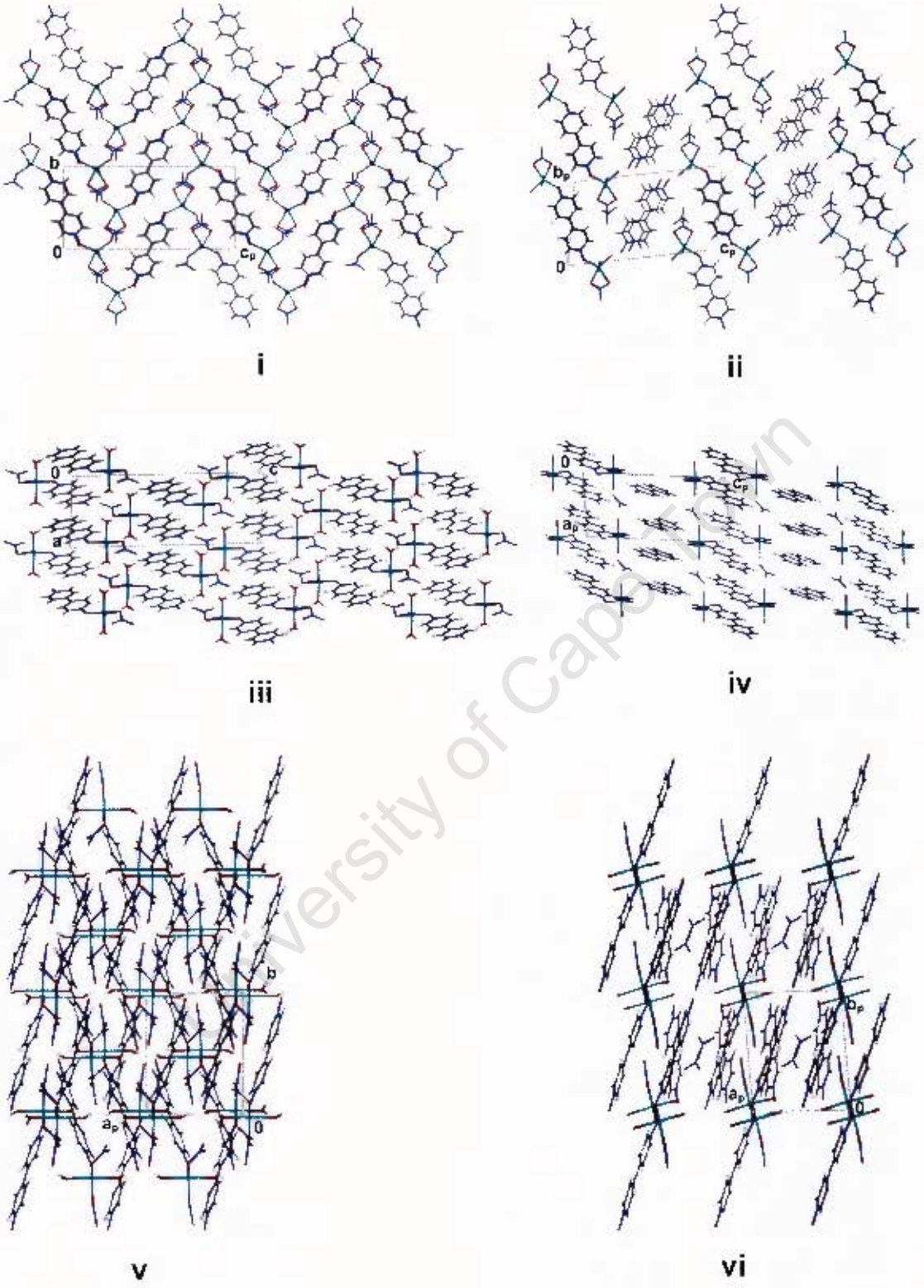

Figure 3.20: Comparison of packed molecules of **CoN(B)** and **CoN(A)** viewed along [100] (**i** and **ii**), [010] (**iii** and **iv**) and [001] (**v** and **vi**), respectively.

CoN(C)

Table 3.16: Crystal Data and Refinement Parameters of **CoN(C)**.

Molecular Formula	$[Co_2(H_2O)_8(C_{10}H_8N_2O_2)_2]\ (NO_3)_4 \cdot 4H_2O$
Formula weight ($g.mol^{-1}$)	471.17
Temperature (K)	113
Wavelength (Å)	0.71073
Crystal System	Monoclinic
Space Group	$P2_1$
a (Å)	7.9362(16)
b (Å)	27.648(6)
c (Å)	8.6441(17)
α (°)	90
β (°)	106.13(3)
γ (°)	90
Volume ($Å^3$)	1822.0(6)
Z	4
Calc. Density ($g.cm^{-3}$)	1.747
μ (mm^{-1})	1.025
F (000)	988
Crystal Size (mm)	0.12 X 0.08 X 0.04
θ Range Scanned (°)	3.30 – 25.67
Index Range	-9 < h < 9, -33 < k < 33, -10 < l < 10
No. Reflections Collected	35282
No. Unique Reflections	6911
Data completeness (%)	100
Refinement Method	Full-matrix L.S. on F^2
Data / Restraints / Parameters	6911 / 0 / 513
Goodness-of-fit on F^2	1.000
Final *R* Indices $[I>2\sigma(I)]$	0.0441, 0.1081
R Indices (all data)	0.0692, 0.1174
Largest Diff. Peak and Hole ($e.Å^{-3}$)	0.605, -0.470

The mean $|E^2 - 1$ value of 0.880 was ambiguous, in-between the expected 0.968 for the centrosymmetric and 0.736 for a non-centrosymmetric crystal structure. Systematic absences suggested that the space group was either $P2_1/m$ or $P2_1$. An attempt to refine the structure in $P2_1/m$ was unsatisfactory, resulting in an *R*-factor of 0.238 and a number of large peaks in the electron density map which could not be incorporated into the model. The structure was then solved in the non-centrosymmetric space group, $P2_1$, and refined well with the *R*-factor of 0.044 and all the atoms except hydrogens were refined anisotropically. The refined Flack parameter was ambiguous, hence the absolute structure could not be determined. Atoms O15A and O1A were refined isotropically. The anisotropic refinement was not possible. The thermal ellipsoid and labelling is shown in Figure 3.21.

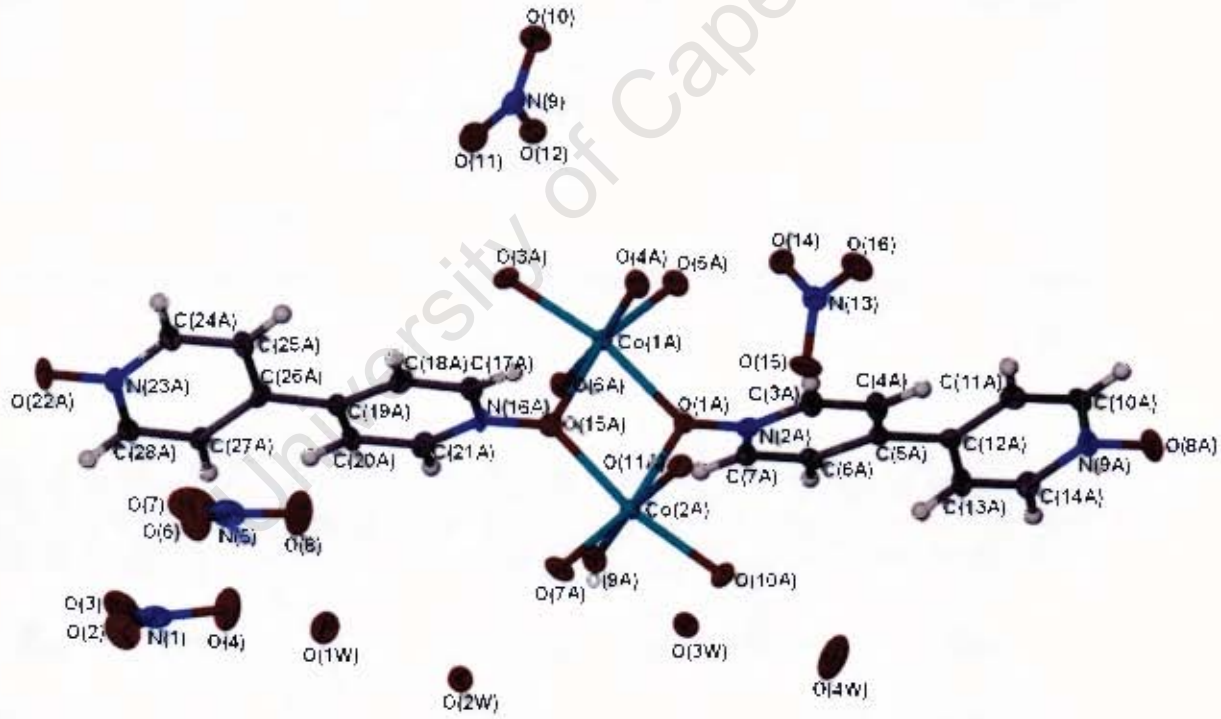

Figure 3.21: Thermal ellipsoid diagram drawn at 50% probability and atomic labelling of **CoN(C)** solved in P2$_1$ space group.

Solving the structure in $P2_1$ revealed two central Co ions with irregular octahedral coordination geometries. Each Co coordinates to four water ligands. In addition, there are two bpdo ligands which bridge between the two

Co ions. All the metal coordinates' bond lengths ranging from 2.051–2.134 Å were within the acceptable value for Co–O length. The metal centres are linked by the bpdo ligand with a metal-metal distance of 3.383 Å. The O–Co–O bond angles, are close to 90° and range between 85.05–93.11 Å, except for the O_{bpdo}–Co–O_{bpdo} (73.46°) and its opposite angle (107.72°).

Four nitrate ions balance the charge and there are four waters included as guests. The atomic displacement parameters of nitrate oxygens are significantly large than those of other atoms. A disorder model was considered but was unsatisfactory.

All the coordinated water and guest molecules are involved in hydrogen bonding interactions with nitrate ions connecting the adjacent discrete molecules. O3W atom accepts H-bonds from coordinated water molecule (O9A) and in return donates H-bonds to both O4W and O16, whereas O2W receives from O7A and donates to O1W and O4. Details of hydrogen bonding are summarised in Table 3.17 and the illustration of classic hydrogen bonds can be seen in Figure 3.22. The compound is further stabilised by weak π···π interactions illustrated Figure 3.23 and stronger C–H···π interactions (details in Table 3.18).

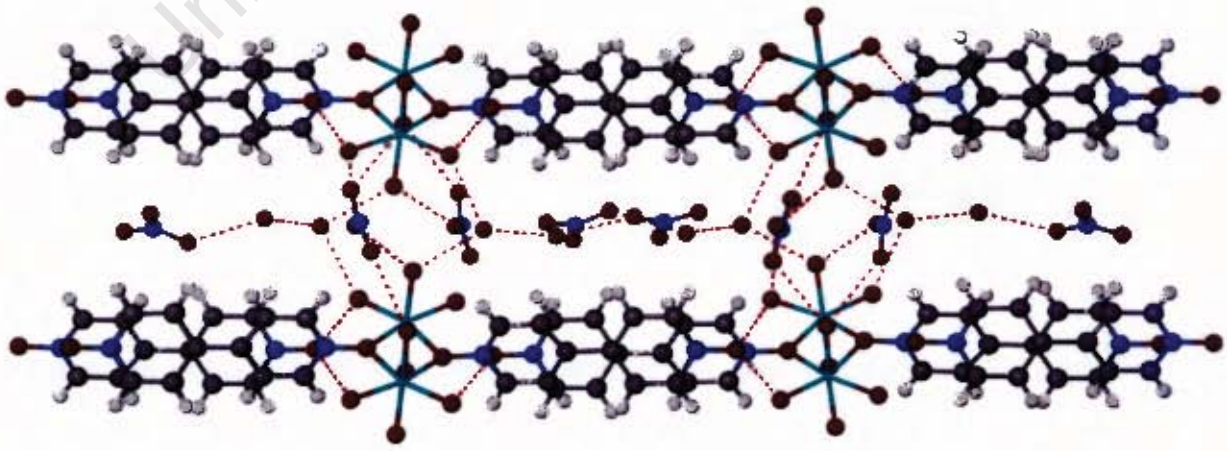

Figure 3.22: Hydrogen bonding interactions in **CoN(C)**.

Table 3.18: C–H$\cdots\pi$ interactions in the **CoN(C)** crystal structures.

	Distance	Symmetry operator
C(4A)–H(4A)$\cdots$ (N23A–C28A)	3.262	1-x, ½+y, -z
C(6A)–H(6A)$\cdots$(N23A C28A)	3.372	-x, ½+y, -z
C(18A)–H(18A)$\cdots$(N9A–C14A)	3.251	1-x, -½+y, -z

The compound forms two distinct layers of hydrophilic molecules (nitrates and water) and the host compound as illustrated in Figure 3.24.

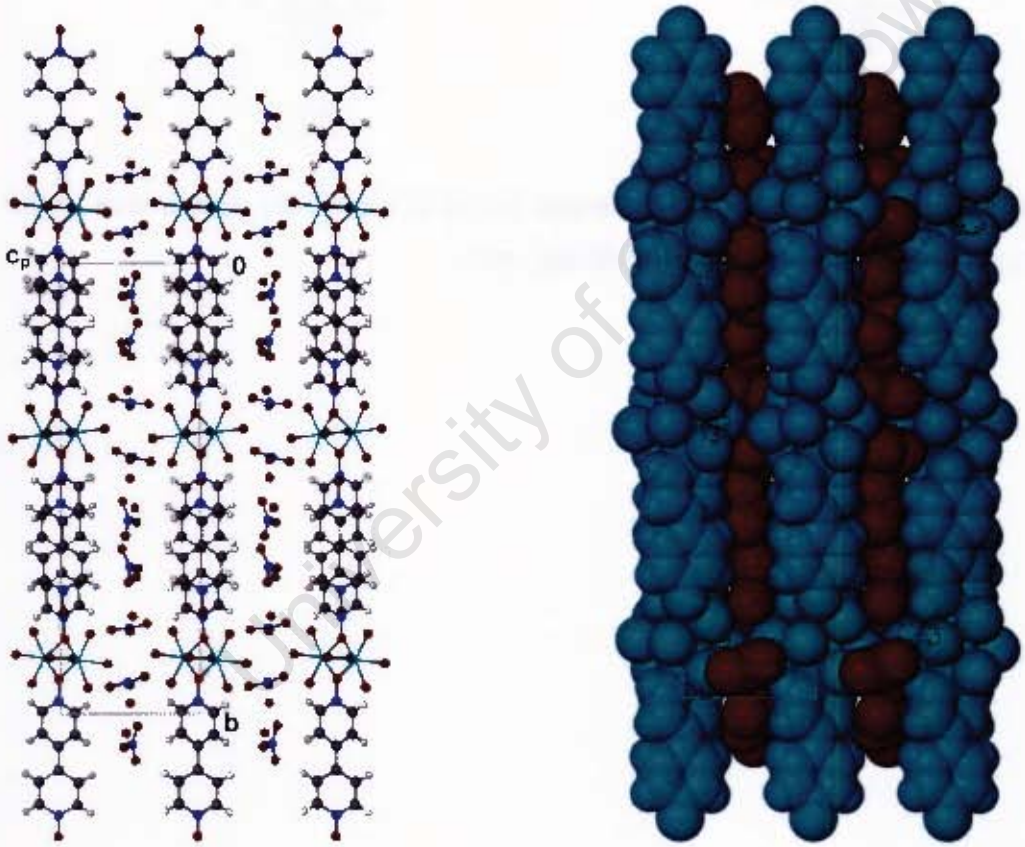

(a) (b)

Figure 3.24: Compound packed along [100] showing two layers formed by guests and host molecules. **(a)** is presented in ball and sticks while **(b)** is van der Waals radii with guests in red and host in blue.

Figure 3.25 shows the packed molecules viewed along [010].

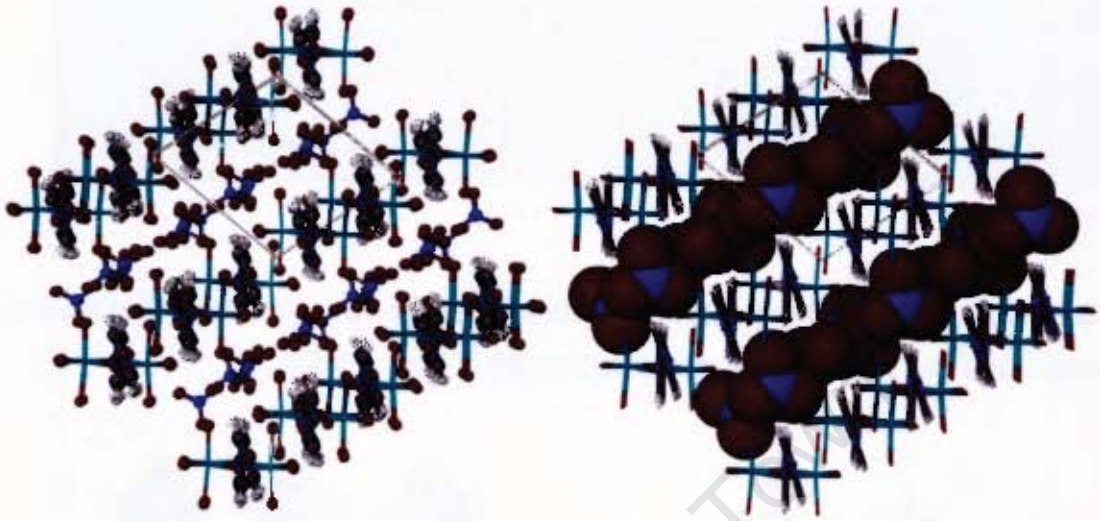

(a) (b)

Figure 3.25: Packing of **CoN(C)** viewed along [010]. In (b) nitrate and water molecules are drawn with van der Waals radii.

CoN(D)

Table 3.19: Crystal Data and Refinement Parameters of **CoN(D).**

Molecular Formula	$[Co(H_2O)_5(C_{10}H_8N_2O_2)]$ $(NO_3)_2$. H_2O
Formula weight ($g.mol^{-1}$)	479.23
Temperature (K)	113
Wavelength (Å)	0.71073
Crystal System	Monoclinic
Space Group	$P2_1/n$
a (Å)	7.286(2)
b (Å)	24.323(5)
c (Å)	10.308(2)
α (°)	90.00
β (°)	90.91(3)
γ (°)	90.00
Volume ($Å^3$)	1826.6(6)
Z	4
Calc. Density ($g.cm^{-3}$)	1.743
μ (mm^{-1})	1.023
F (000)	988
Crystal Size (mm)	0.03 X 0.04 X 0.04
θ Range Scanned (°)	1.67 – 25.35
Index Range	-8 < h < 8, -29 < k < 27, -12 < l < 12
No. Reflections Collected	20260
No. Unique Reflections	3335
Data completeness (%)	100
Refinement Method	Full-matrix L.S. on F^2
Data / Restraints / Parameters	3335 / 0 / 262
Goodness-of-fit on F^2	0.919
Final *R* Indices $[I>2\sigma(I)]$	0.0545, 0.1395
R Indices (all data)	0.1063, 0.1828
Largest Diff. Peak and Hole ($e.Å^{-3}$)	0.557, -0.549

A fourth form of cobalt nitrate with bpdo was refined and elucidated. Single crystal x-ray data were collected at 113 K. The compound crystallised in the space group $P2_1/n$ with four molecules in the unit cell. Atomic labelling and thermal displacements are shown in Figure 3.26.

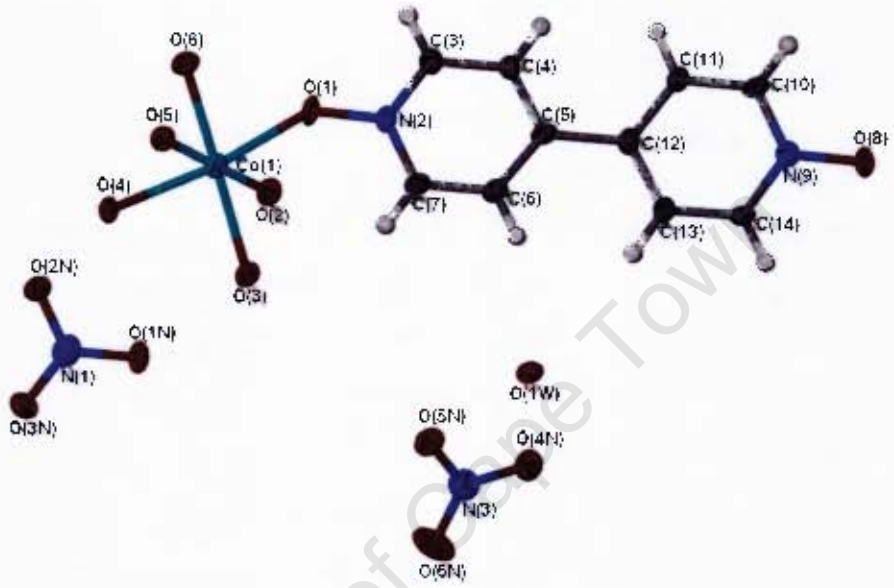

Figure 3.26: Thermal ellipsoid diagram drawn at 50% probability and atomic labelling of compound, **CoN(D)**.

The coordination geometry of **CoN(D)** is an almost perfect octahedron. The Co-O bond lengths ranged from 2.077–2.123 Å, while the O–Co–O bond angles were from 85.06–95.29° (deviating slightly from the ideal value, 90°). The bpdo aromatic rings are twisted by 8.30° relative to one another. One bpdo ligand is coordinated to the central metal and none of the charge balancing nitrates is coordinated. The metal centres are linked by hydrogen bonding (details in Table 3.20) through coordinated waters and oxygens of the bpdo (Figure 3.27). The guest nitrates and water forms layers (Figure 3.28, compound viewed along [100]) of hydrogen bonds connecting the zigzag-shaped discrete molecules which are further held place by $\pi\cdots\pi$ interactions, summarised in Table 3.21.

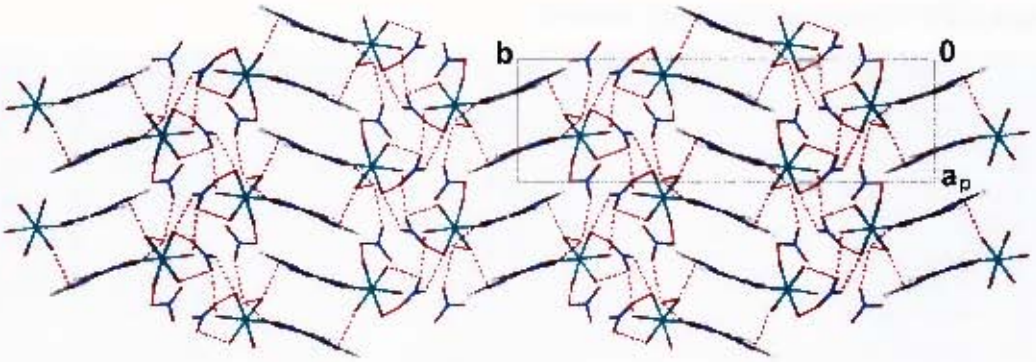

Figure 3.27: Hydrogen bonding illustration.

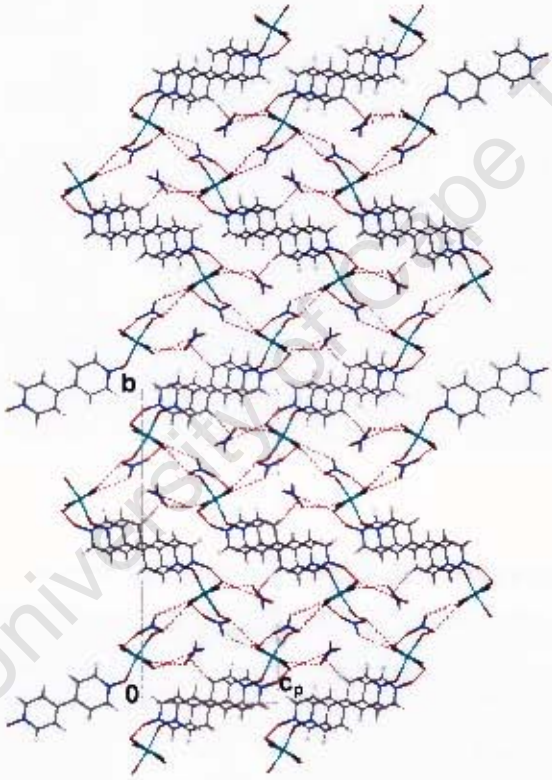

Figure 3.28: Zigzag shaped molecules showing layers organic and inorganic components.

Table 3.20: Hydrogen bonding details.

	D–H (Å)	D···A (Å)	D–H···A (°)	Symmetry operator
O1W–O5N		2.869		x, y, z
O4–O2N		2.850		x, y, z
O3–O1N		2.731		x, y, z
O4–O5N		2.771		x-½, ½-y, ½+z
O6–O4N		2.754		x-1, y, 1+z
O3···O3N		2.792		x-½, ½-y, z-½
O5–O1W		2.695		x, y, 1+z
O2–O2N		2.709		x-½, ½-y, z-½
O5–O8		2.691		1-x, -y, 1-z
C(3) –H(3)···O(8)	0.95	3.425 (8)	170	x, y, 1+z
C(4) H(4)···O(4N)	0.95	3.196 (8)	144	1-x, -y, 1-z
C(6)–H(6)···O(1W)	0.95	3.370 (8)	151	x, y, z
C(7)–H(7)···O(3N)	0.95	3.488 (9)	157	-½+x, ½-y, -½+z
C(11)–H(11)···O(5N)	0.95	3.450 (8)	150	1-x, -y, 1-z
C(14)–H(14)···O(1)	0.95	3.407 (8)	177	x, y, -1+z

Table 3.21: $\pi\cdots\pi$ interactions in **CoN(D)** crystal structure.

	Distance	Symmetry operator
Cg(N2–C7)···Cg(N9–C14)	3.861 (3)	1-x, -y, 1-z
Cg(N9–C14)···Cg(N2–C7)	3.862 (3)	1-x, -y, 1-z
Cg(N2–C7)···Cg(N9–C14)	3.837 (3)	-x, -y, 1-z
Cg(N9–C14)···Cg(N2–C7)	3.836 (3)	-x, -y, 1-z

CoN(E) and CoN(F)

In addition to the four $(CoNO_3)_2$ crystal structures reported in this study, there are two other crystal structures **[CoN(E)** and **CoN(F)]** which were previously reported by Blake *et al.*[4] These structures are briefly discussed here as they form part of this study.

CoN(E) was prepared in aqueous solution and resulted in nitrate counterions and four water molecules coordinated to the central metal completing an octahedral symmetry. Nitrate ions are both monodentate in this structure, while the two bpdo molecules are non-coordinated. The asymmetric unit is composed of half the molecule and the rest is generated by symmetry (Figure 3.29).

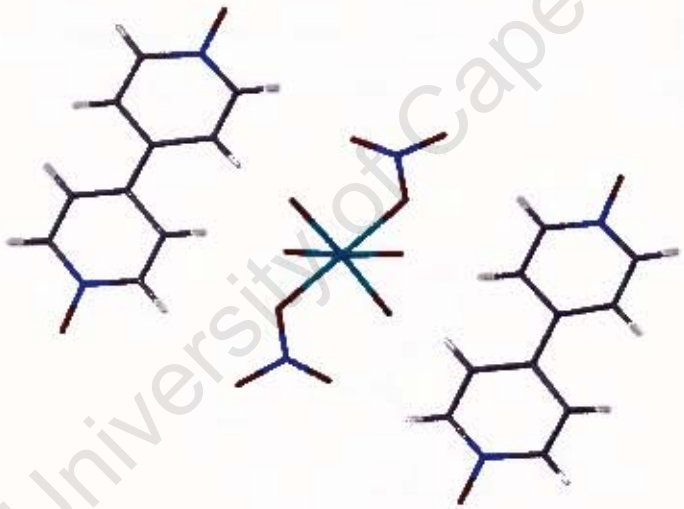

Figure 3.29: **CoN(E)**.

Bpdo acts as H-bond acceptor with eight ligands forming O–H···O_{bpdo} H-bonds with all eight hydrogens atoms of the four coordinated water molecules. The $[Co(NO_3)_2(H_2O)_4]$ unit is bridged by four bpdo molecules forming a H-bonded ring (Figure 3.30).

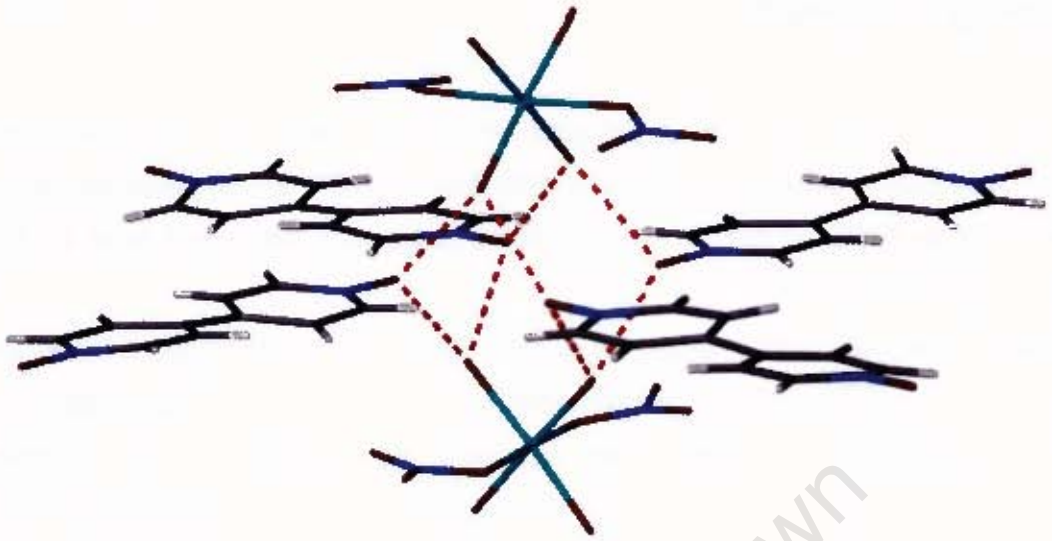

Figure 3.30: $[Co(NO_3)_2(H_2O)_4]$ units bridged by four bpdo molecules.

Crystallisation in the absence of excess water and using methanol only formed **CoN(F)**. In this case, bpdo is adequately competitive as a ligand for the central metal forming six coordinated bpdo ligands and no aquo ligands (Figure 3.31).

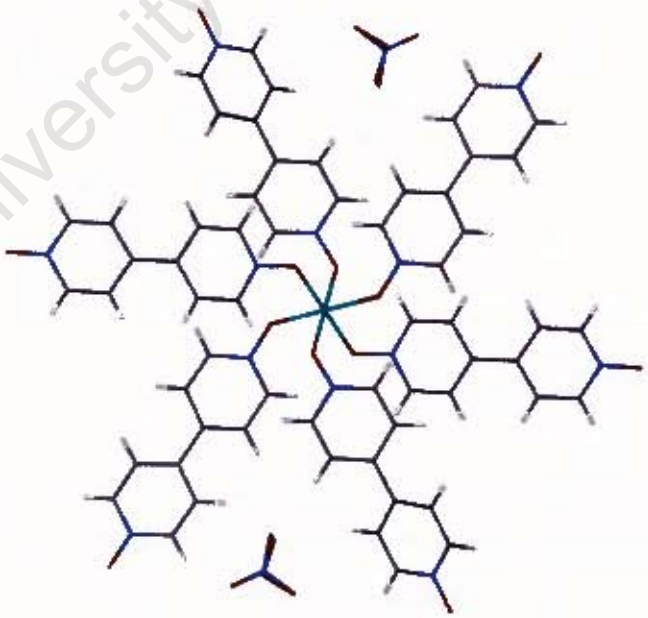

Figure 3.31: **CoN(F)** molecule.

Each metal centre is coordinated by six independent bpdo ligands. These ligands coordinate through only one end (monodentately) of their N-oxide donor leaving the other end to be involved in π···π interactions with other bpdo ligands.

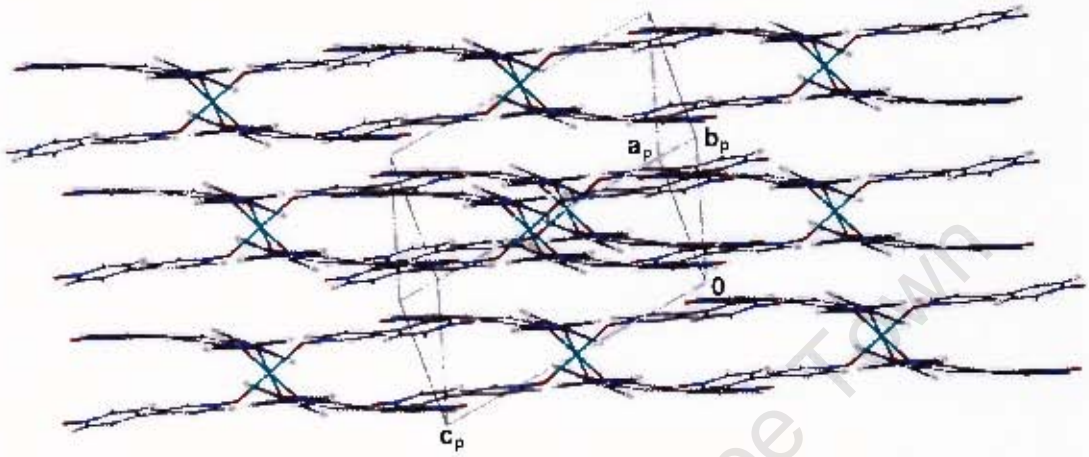

Figure 3.32: Packed molecules showing π···π interactions in the compound.

CoS

Table 3.22: Crystal Data and Refinement Parameters of **CoS**.

Molecular Formula	**$[Co(H_2O)_5(C_{10}H_8N_2O_2)]SO_4 \cdot 2H_2O$**
Formula weight ($g.mol^{-1}$)	469.29
Temperature (K)	113
Wavelength (Å)	0.71073
Crystal System	Monoclinic
Space Group	$P2_1/n$
a (Å)	7.122 (1)
b (Å)	25.319 (5)
c (Å)	10.241 (2)
α (°)	90
β (°)	93.14 (3)
γ (°)	90
Volume ($Å^3$)	1843.8 (6)
Z	4
Calc. Density ($g.cm^{-3}$)	1.691
μ (mm^{-1})	1.113
F (000)	972
Crystal Size (mm)	0.12 x 0.15 x 0.16
θ Range Scanned (°)	3.2 – 26.7
Index Range	-9 < h < 9, -31 < k < 31, -12 < l < 12
No. Reflections Collected	33963
No. Unique Reflections	3883
Data completeness (%)	100.0
Refinement Method	Full-matrix L.S. on F^2
Data / Restraints / Parameters	3883 / 0 / 245
Goodness-of-fit on F^2	1.126
Final *R* Indices $[I>2\sigma(I)]$	0.0369, 0.0882
R Indices (all data)	0.0487, 0.0932
Largest Diff. Peak and Hole ($e.Å^{-3}$)	0.848, -0.477

The data collection was done at 113K. The compound **CoS** crystallises in the monoclinic crystal system, in the space group $P2_1/n$, with four molecules in unit cell. The thermal ellipsoid and atomic labelling is shown in Figure 3.33.

In this compound, the Co(II) ion coordinates one bpdo and five water molecules. Octahedral symmetry is maintained with Co-O bond lengths lying between 2.059 and 2.114 A and O-Co-O angles within 82.99 to 93.49°. The bpdo aromatic rings are twisted 2.84° relative to one another. Only one bpdo oxygen is coordinated to the metal, the other accepts two hydrogen bonds from coordinated waters on two adjacent $[Co(H_2O)_5(bpdo)]^{2+}$ ions. This motif gives rise to an interdigitated layer structure, where each bpdo links adjacent $[Co(H_2O)_5(bpdo)]^{2+}$ ions along [100] (Figure 3.34). Within this layer, offset $\pi\cdots\pi$ interactions also stabilise the structure (Table 3.23).

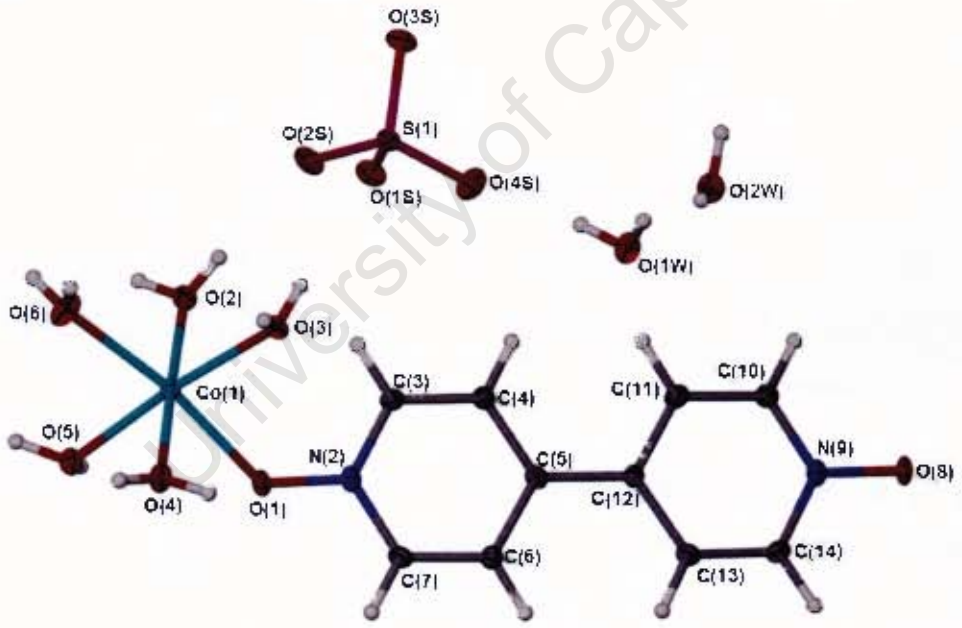

Figure 3.33: Thermal ellipsoid (drawn at 50% probability) and atomic labelling of **CoS** complex.

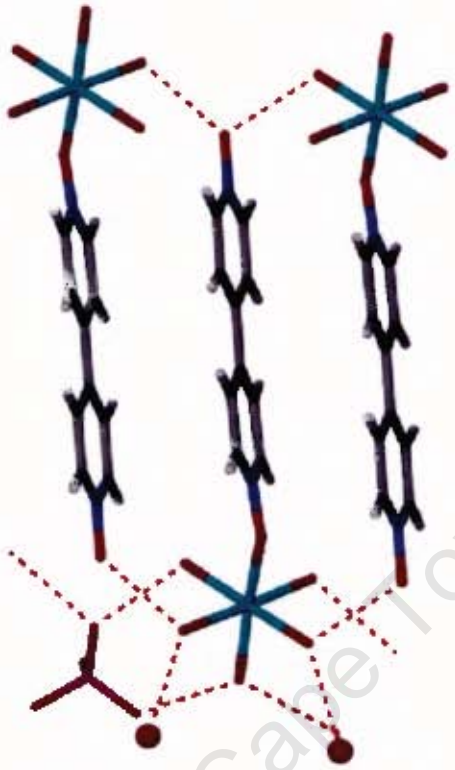

Figure 3.34: Intermolecular interactions.

Table 3.23: π···π interactions in the **CoS** crystal structure.

	Distance	Symmetry operator
Cg(N2–C7)···Cg(N9-C14)	3.687(4)	-x, -y, 1-z
Cg(N2 C7)···Cg(N9-C14)	3.686(4)	1-x, -y, 1-z

*Cg = ring centroid

There is an extensive network of hydrogen bonds (Figure 3.34) between coordinated waters, sulphate and bpdo molecules (details in Table 3.24) which link the structure into a zigzag network along the [100] and approximately parallel to the *b*-axis (Figure 3.35 (a) and (b), respectively). Packing motifs of this compound are comparable to **CoN(D)**.

Table 3.24: Hydrogen bonding details.

	D–H (Å)	D···A (Å)	D–H···A (°)	Symmetry operator
O2–H2A···O2S	0.77 (4)	2.706 (3)	175 (4)	x,y,z
O2–H2B···O3S	0.81 (4)	2.671 (3)	174 (4)	–½+x,½-y,½+z
O3–H3A···O1S	0.74 (4)	2.684 (3)	170 (4)	x,y,z
O3–H3B···O3S	0.88 (4)	2.662 (3)	176 (4)	½+x,½-y,½+z
O4–H4A···OO8	0.82 (5)	2.716 (3)	173 (4)	1-x,-y,1-z
O4–H4B···O1W	0.77 (5)	2.769 (3)	165 (4)	x,y,1+z
O6–H6A···O2S	0.83 (4)	2.757 (3)	175 (4)	½+x,½-y,½+z
O6–H6B···O1S	0.79 (3)	2.809 (3)	167 (4)	–½+x,½-y,½+z
O5–H5A···O2W	0.84 (4)	2.751 (3)	173 (3)	-1+x,y,1+z
O5–H5B···O8	0.77 (4)	2.692 (3)	174 (4)	-x,-y,1-z
O1W–H11W···O4S	0.81 (4)	2.834 (3)	166 (4)	x,y,z
O1W–H12W···O2W	0.85 (5)	2.794 (3)	162 (4)	x,y,z
O2W–H21W···O1S	0.82 (5)	2.839 (3)	174 (3)	½+x,½-y,-½+z
O2W–H22W···O4S	0.84 (5)	2.773 (3)	177 (4)	1+x,y,z
C6–H6···O1W	0.95	3.460 (4)	165	1-x,-y,1-z
C7–H7···O8	0.95	3.248 (3)	176	x,y,1+z
C10–H10···O1	0.95	3.258 (4)	175	x,y,-1+z

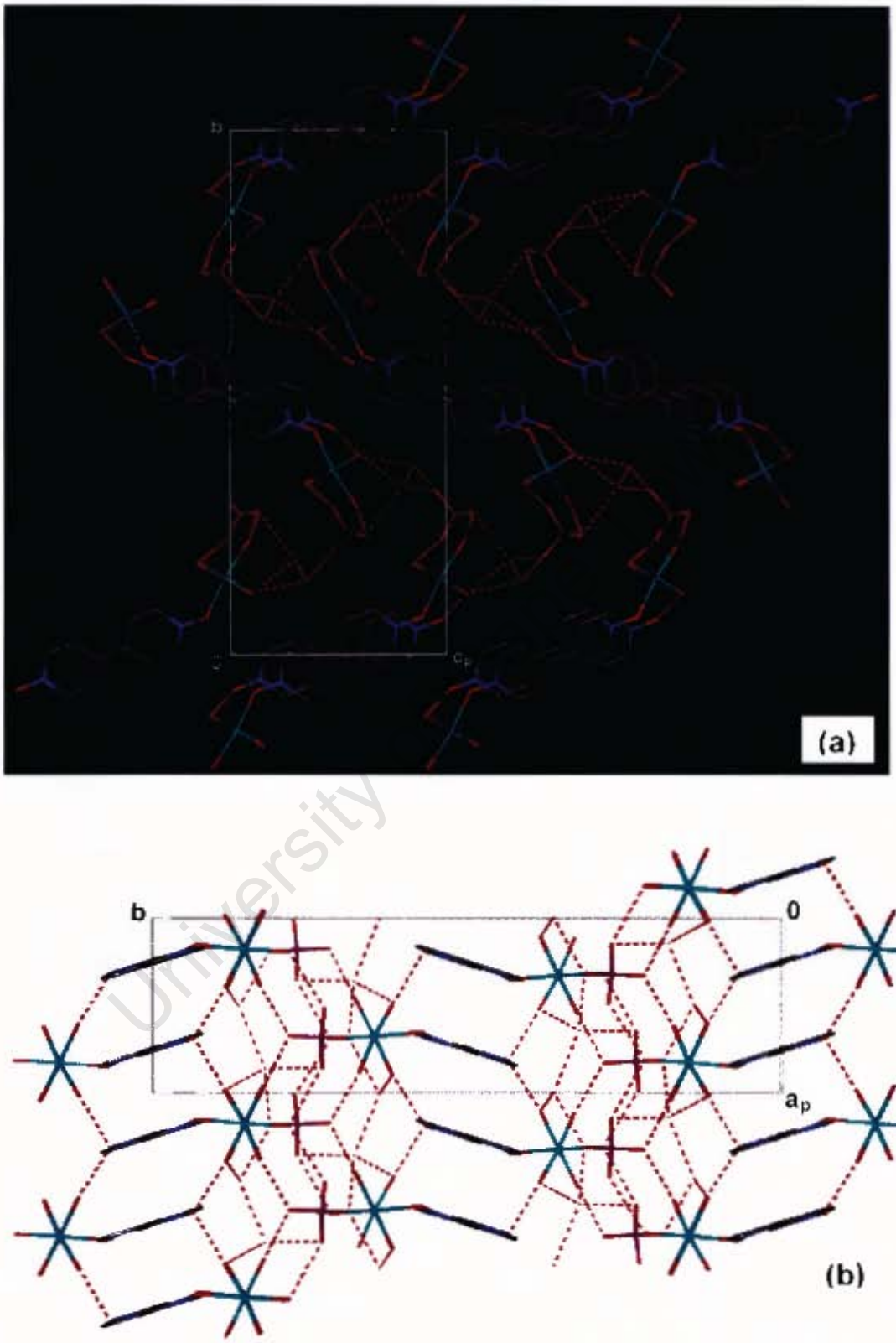

Figure 3.35: Zigzag network structure in **CoS**, showing the hydrophilic regions between Co(II) ions separated by organic layers **(a)** viewed along [100] and **(b)** [001].

Thermal Analysis

The TG and DSC traces **CoS** are shown in Figure 3.36 and the results are summarised in the Table 3.5. The TG of **CoS** is characterised by three step mass losses. The first two mass losses are combined. The first mass loss was attributed to the loss of five coordinated waters (details in Table 3.25), while the second mass loss was due to the two guest water molecules. The third mass loss demonstrated the decomposition.

The DSC traces in Figure 3.36 show endothermic peaks labelled A and B, which corresponds to the loss of coordinated and guest water, respectively. The onset temperatures (T_{on}) for these peaks are given in Table 3.25. The third exotherm indicates the loss of some bpdo ligand, leading to decomposition (exotherm D).

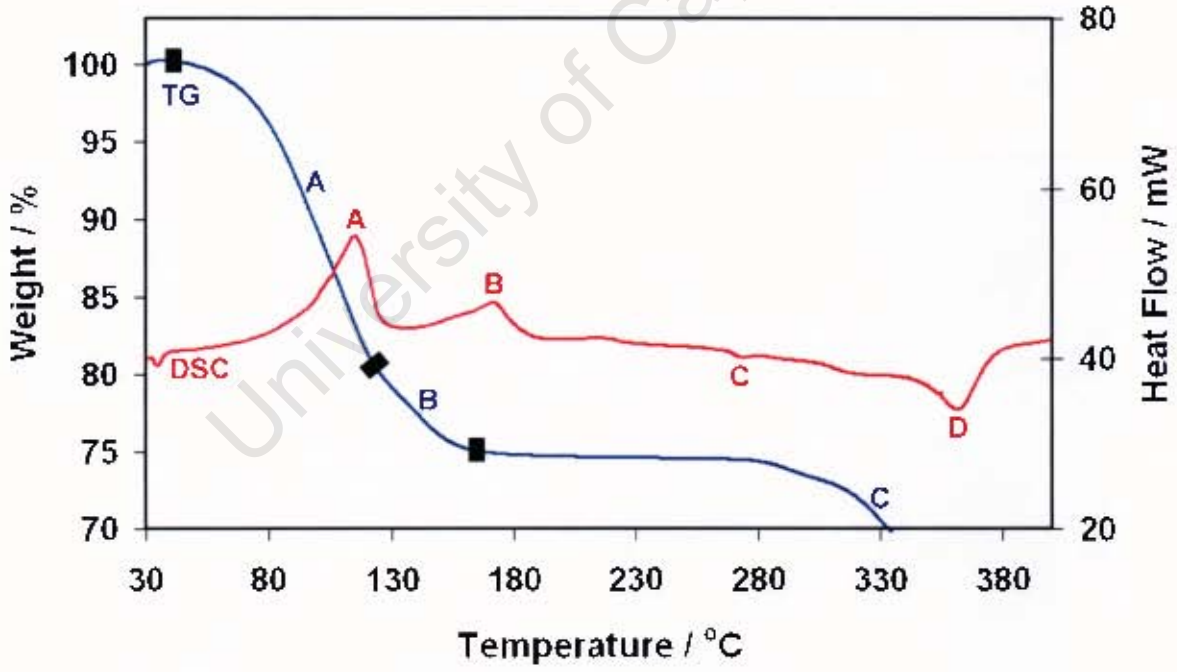

Figure 3.36: TG and DSC traces of **CoS**.

Table 3.25: Thermal analysis results of **CoS**.

	TG Results			
	Calc. % mass loss		Exp. % mass loss	
Mass loss A	19.19		20.27	
Mass loss B	7.68		5.72	
Total H_2O loss	26.87		25.99	
complex	DSC Results			
	T_{on} (°C) Peak A	T_{on} (°C) Peak B	T_{on} (°C) Peak C	T_{on} (°C) Peak D
CoS	98.1	152.6	268.3	350.8

Hot Stage Microscopy

Figure 3.37 shows the photographs of **CoS** complex observed during thermal decay.

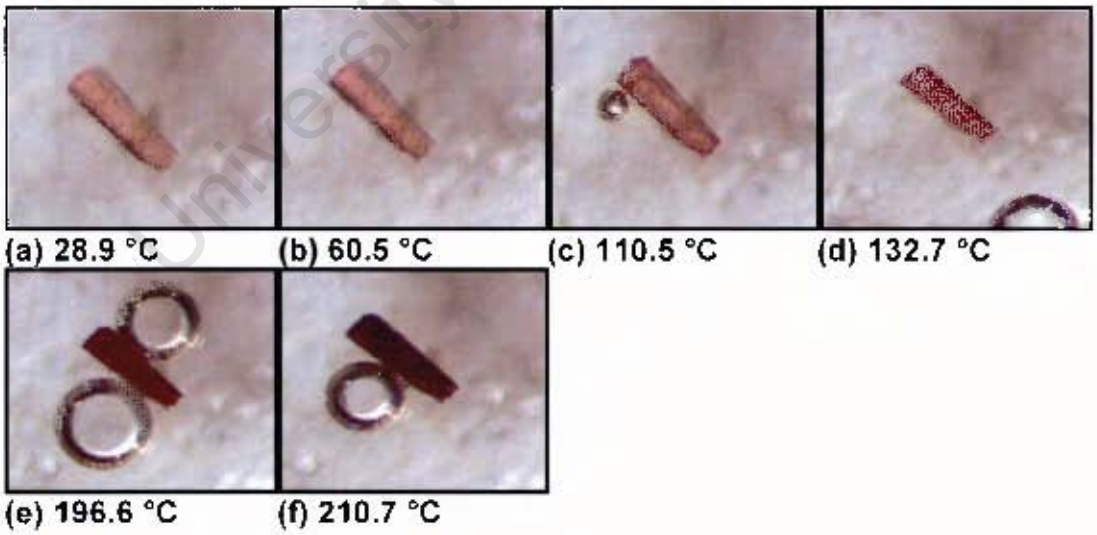

Figure 3.37: Crystals of **CoS** during thermal decay. Photograph (a) the crystal at room temperature, (b) crystal still stable after 60.5 °C, (c) guest water molecules escaping from the crystal lattice, (d) change in colour as a result of water loss, (e) starting to lose bpdo molecule which leads to (f) decomposition of the crystal.

Transformation of Co^{II} complexes to 1D polymer

Within a week dry crystals of compounds **CoB**. $[Co(H_2O)_6]Br_2$. 2(bpdo) . $2H_2O$ and **CoC**, $[Co(H_2O)_6]Cl_2$. 2(bpdo) . $2H_2O$ transform into the 1D coordination polymers described here. We attempted to establish the mechanism to study the Co^{II} compound transformation. but due to the complexity of crystallising **CoB** and **CoC** reproducibly, these experiments were difficult. We attempeted to follow the crystal transformation process on the single crystal diffractometer and using PXRD. but were unable to isolate an intermediate phase.

Structure solution and analysis

CoB-2 and CoC-2

These compounds, **CoB-2** and **CoC-2**, are isostructural with respect to similar molecular shape, similar unit cell parameters and similar atomic coordinates as shown in Table 3.26. The bromide structure will be discussed.

Both compounds crystallise in the monoclinic crystal system, space group *C2/c*. Structure refinement revealed a central Co(II) atom coordinated to two bromides counterions located at the axial positions of the octahedron while two water molecules and two bpdo molecules occupy the equatorial sites. This symmetry is shown in Figure 3.38. The octahedral symmetry is slightly irregular with bonding angles ranging from 86.61-93.42°. The bond lengths of the coordinated bromide (2.686 Å, 2.445 Å for Cl^-) and water molecules (2.111 Å and 2.091 Å, respectively) are within the expected ranges. The literature[1] values are given as 2.085 Å ($Co\text{-}O_{aqua}$). 2.416 Å (Co-Br) and 2.272 ($Co\text{-}Cl^-$). Full bond lengths and angles are given in the Appendix.

Table 3.26: Crystal Data and Refinement Parameters of **CoB-2** and **CoC-2**.

Molecular Formula	$CoBr_2(C_{10}H_8N_2O_2)(H_2O)_2 \cdot H_2O$	$CoCl_2(C_{10}H_8N_2O_2)(H_2O)_2 \cdot H_2O$
Formula weight ($g.mol^{-1}$)	459.97	371.05
Temperature (K)	113	298
Wavelength (Å)	0.71073	0.71073
Crystal System	Monoclinic	Monoclinic
Space Group	*C2/c*	*C2/c*
a (Å)	23.958 (5)	24.114 (5)
b (Å)	5.695 (1)	5.618 (1)
c (Å)	10.862 (2)	10.751 (2)
α (°)	90	90
β (°)	108.60 (3)	109.16 (3)
γ (°)	90	90
Volume ($Å^3$)	1404.5 (5)	1375.7 (5)
Z	4	4
Calculated Density ($g.cm^{-3}$)	2.175	1.792
μ (mm^{-1})	6.931	1.655
F (000)	896	752
Crystal Size (mm)	0.05 x 0.10 x 0.12	0.17 x 0.10 x 0.08
θ Range Scanned (°)	0.79 – 26.05	3.58 – 27.88
Index Range	-29 < h < 29, -7 < k < 7, -13 < l < 13	-31< h < 31, -7 < k < 7, -14 < l < 13
No. Reflections Collected	1379	1646
No. Unique Reflections	1221	1268
Data completeness (%)	99.8	99.9
Refinement Method	Full-matrix L.S. on F^2	Full-matrix L.S. on F^2
Data / Restraints / Parameters	1379 / 0 / 94	1646 / 0 / 92
Goodness-of-fit on F^2	1.121	1.101
Final *R* Indices $[I>2\sigma(I)]$	0.0485, 0.1259	0.0691, 0.2115
R Indices (all data)	0.0567, 0.1296	0.0918, 0.2009
Largest Diff. Peak and Hole ($e.Å^{-3}$)	2.018, -1.059	2.451, -0.572

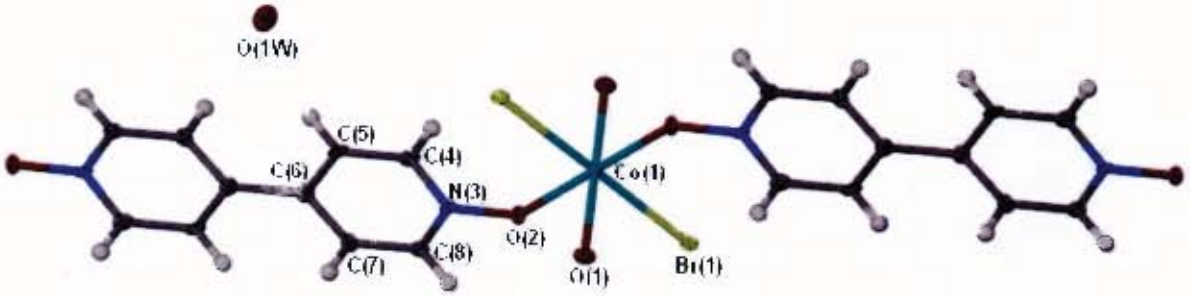

Figure 3.38: **CoB-2** (isostructural to **CoC-2**) coordination polymer showing atomic labelling and thermal displacement diagram drawn at 50% probability.

The bpdo molecule functions as a bridge to connect the two Co atoms, leading to a 1D covalently linked polymer chain as shown in Figure 3.39. The adjacent polymer chains are connected by C–H···O hydrogen bonding through the guest water molecule and dipyridyl rings of the bpdo ligand. Guest water operates as H-bond acceptor in these interactions (Figure 3.39). The hydrogen bonding details are summarised in Table 3.27.

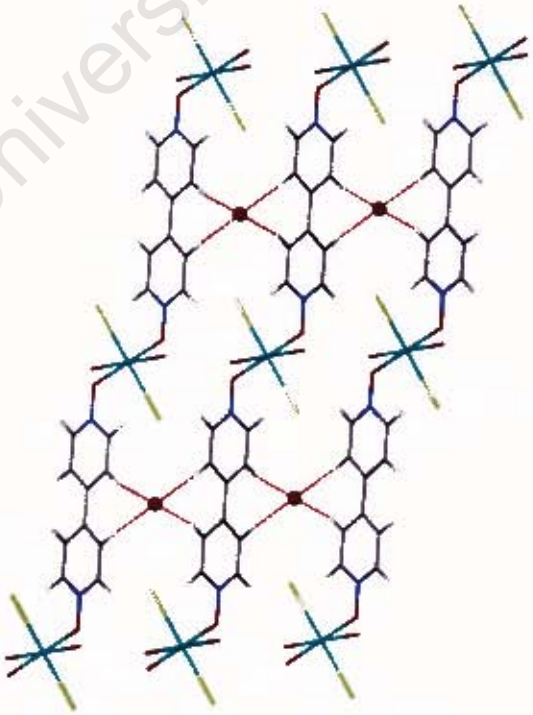

Figure 3.39: Hydrogen bonding interactions.

Table 3.27: Hydrogen bonding details.

CoB-2	D–H (Å)	D···A (Å)	D–H···A (°)	Symmetry operator
C(8)–H(8)···Br(1)	0.95	3.487 (7)	145	½-x, ½+y, 3/2-z
C(5) H(5)···O(1W)	0.95	3.342 (9)	168	-x, y, ½-z
C(5)–H(5)···O(1W)	0.95	3.342 (9)	168	-x, y, ½-z
C(4)–H(4)···Br(1)	0.95	3.532 (7)	156	½-x, -½-y, 1-z
CoC-2				
C(4)–H(4)···Cl(1)	0.93	3.460 (7)	161	½-x, -½-y, -z
C(5)–H(5)···O(1W)	0.93	3.357	169	1-x, y, ½-z
C(5) H(5)···O(1W)	0.93	3.357	169	1-x, y, ½-z
C(8)–H(8)···Cl(1)	0.93	3.476 (7)	148	½-x, ½+y, -½-z

The packing of the molecules looks like an uneven hollow tube when viewed along [001] as shown in Figure 3.40 with pyridyl rings overlapping.

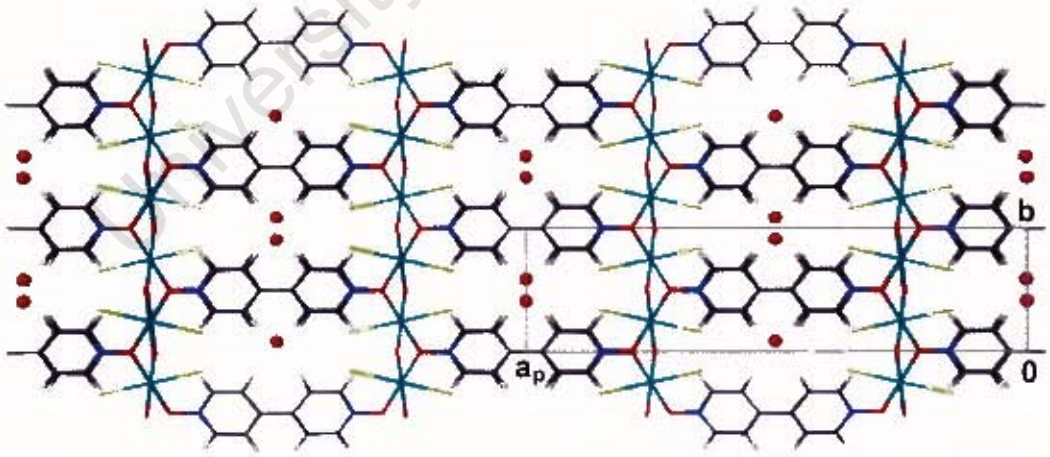

Figure 3.40: Packing of **CoB-2** along [001] showing an overlap in pyridyl rings.

The polymer chains parallel to [010] and [100] as shown in Figure 3.41 (a) and (b).

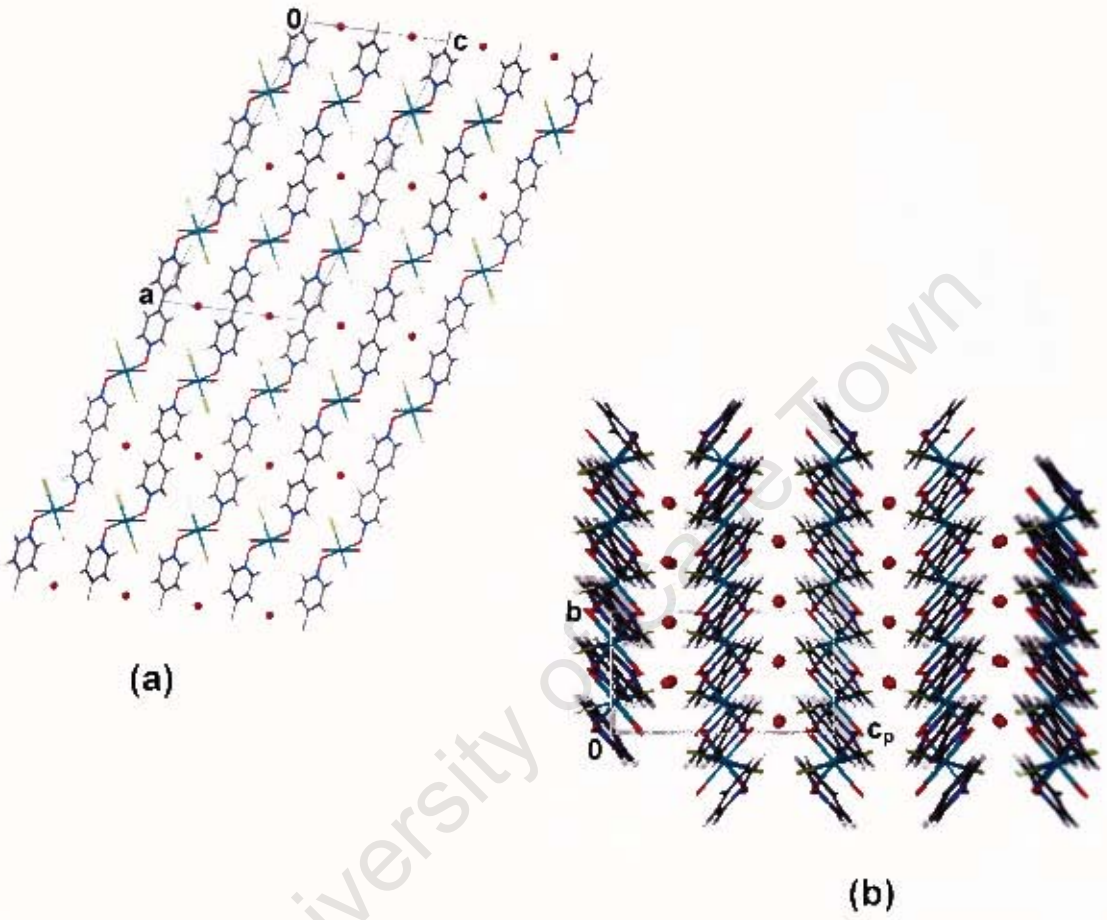

Figure 3.41: **(a) and (b)**: Packing of molecules viewed along [010] and [100] showing polymer chains.

The guest water molecules are trapped into small voids while the coordinated waters are exposed and form layers as shown in Figure 3.42.

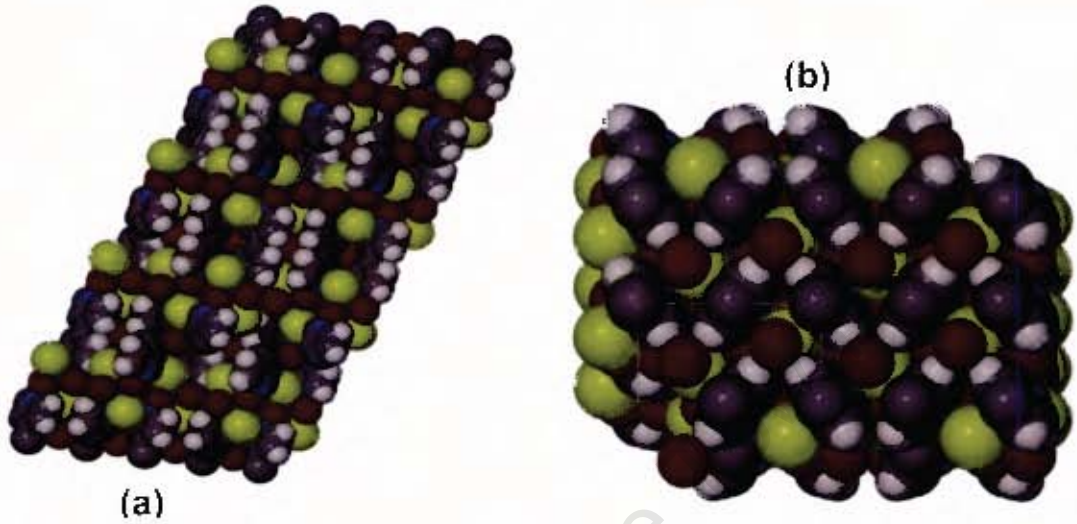

Figure 3.42: **(a) and (b)**: Molecules are packed using van der Waals radii viewed along [010] and [100], respectively.

The voids occupied by guest water molecules were examined using the program SECTION[5] which was used to view sections through the unit cell along [010]. One of these sections is shown in Figure 3.43.

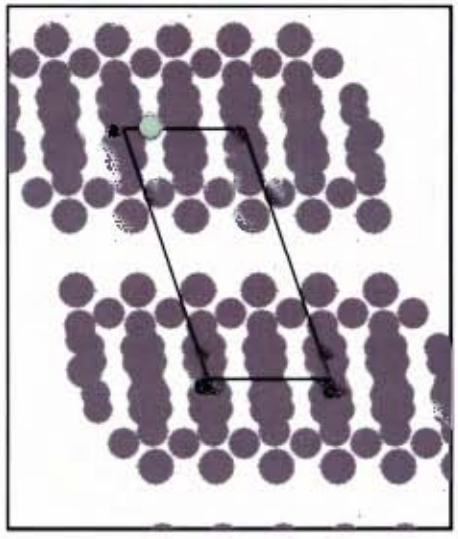

Figure 3.43: SECTION plot of **CoB-2** (guest water molecules omitted) viewed down [010] with the unit cell sectioned at 0.00A along [010]. One of the voids is shown in green circle.

Thermal Analysis

The TG and DSC traces of **CoB-2** and **CoC-2** are shown in Figure 3.44.

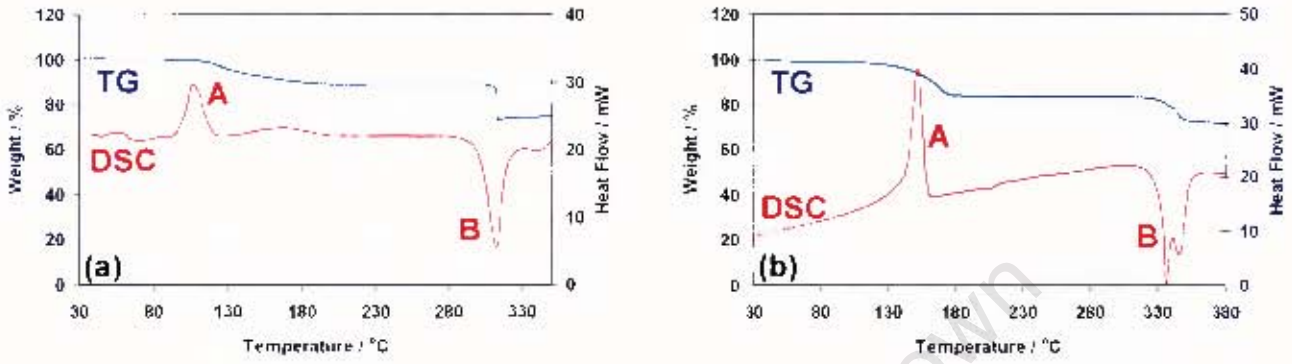

Figure 3.44: TG and DSC traces of **(a) CoB-2** and **(b) CoC-2**.

The TG curves in both graphs show a two step mass loss. The first mass loss in **(a)** and **(b)** is attributed to the loss of three water molecules in the compound i.e. one guest water molecule and two water molecules coordinated to the central metal. The calculated and the experimental mass losses of water molecules corresponded well and the details are shown in Table 3.28. The second step mass loss is due to the decomposition of the compound. The DSC traces in **(a)** and **(b)** are corresponding well with the TG traces shown by endotherm A and exotherm B in Figure 3.44 **(a)** and **(b)**. The onset temperatures for both loss of water molecules and the decomposition events are given in Table 3.29.

Table 3.28: Thermal analysis of **(a) CoB-2** and **(b) CoC-2**.

1D Co^{II} coordination polymers	TG Results (H_2O molecules)		DSC Results	
	Calc. % mass loss	Exp. % mass loss	T_{on} (°C) Peak A	T_{on} (°C) Peak B
CoB-2	11.75	11.34	81.6	299.1
CoC-2	13.56	15.33	161.7	338.4

Hot Stage Microscopy

Crystals of **CoB-2** and **CoC-2** were observed for thermal decomposition using the hot stage microscope. The photographs for thermal events are shown in Figure 3.45 (i) and (ii).

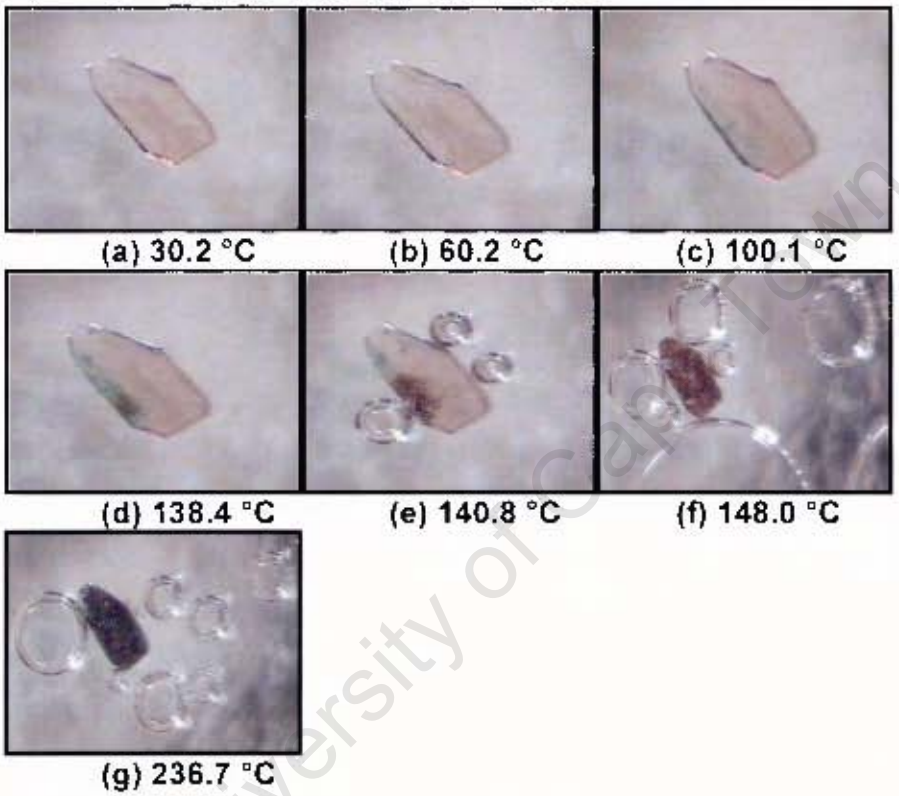

Figure 3.45(i): Thermal decomposition of **CoB-2**. **(a)** Crystal at room temperature, **(b)** crystal quality is still maintained around 60 °C, **(c)** crystal starting to lose the quality and this is shown by decolourisation at the edge of the crystal. This is due to loss of guest water molecules as shown in **(d)**-**(f)** and **(g)** is the beginning of decomposition process.

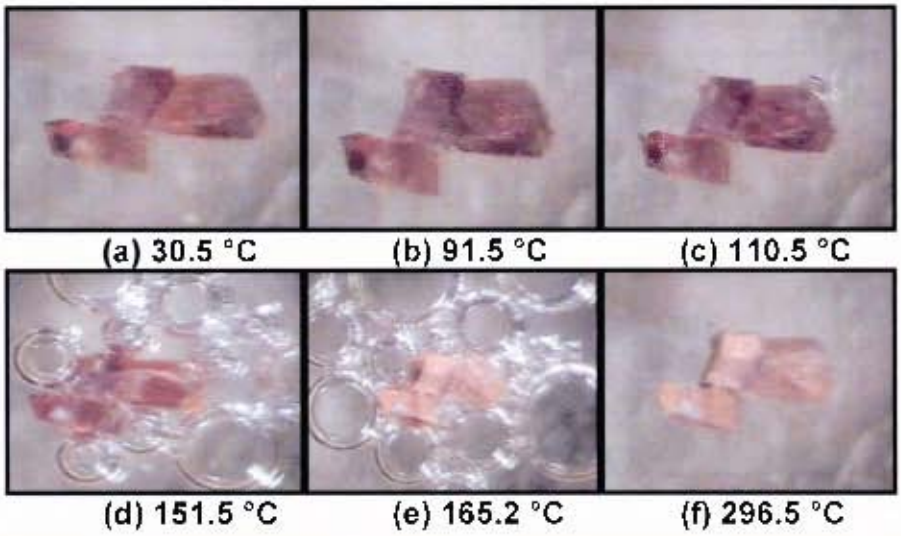

Figure 3.45(ii): Thermal decay in **CoC-2**. **(a)** room temperature, **(b)** crystal still stable, **(c)** bubbling showing loss of water, **(d)** vigorous bubbling with decolourisation **(e)** completes water loss **(f)** decomposition.

Comparison of calculated PXRD patterns of (CoB and CoB-2) and (CoC and CoC-2)

The calculated PXRD patterns of (**CoB** and **CoB-2**) and (**CoC** and **CoC-2**) were compared to show dissimilarity in these compounds. The patterns are shown in Figure 3.46 for (**CoB** and **CoB-2**) and Figure 3.47 for (**CoC** and **CoC-2**). The experimental PXRD pattern is included in Figure 3.46 to confirm that the initial bulk sample was composed of **CoB** compound.

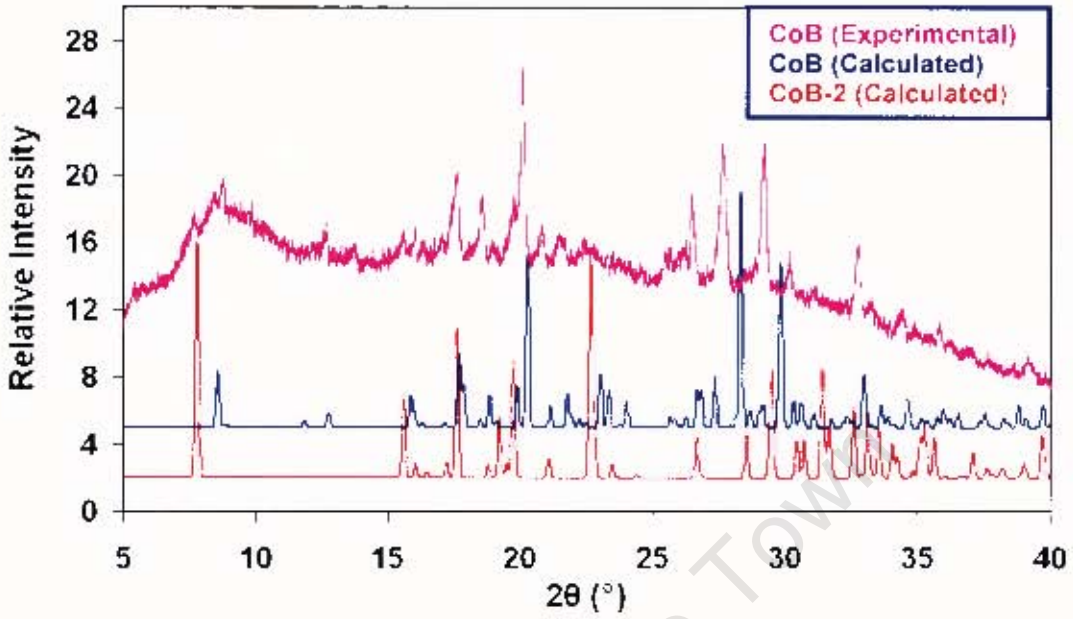

Figure 3.46: Comparison of calculated PXRD patterns of **CoB** and **CoB-2**.

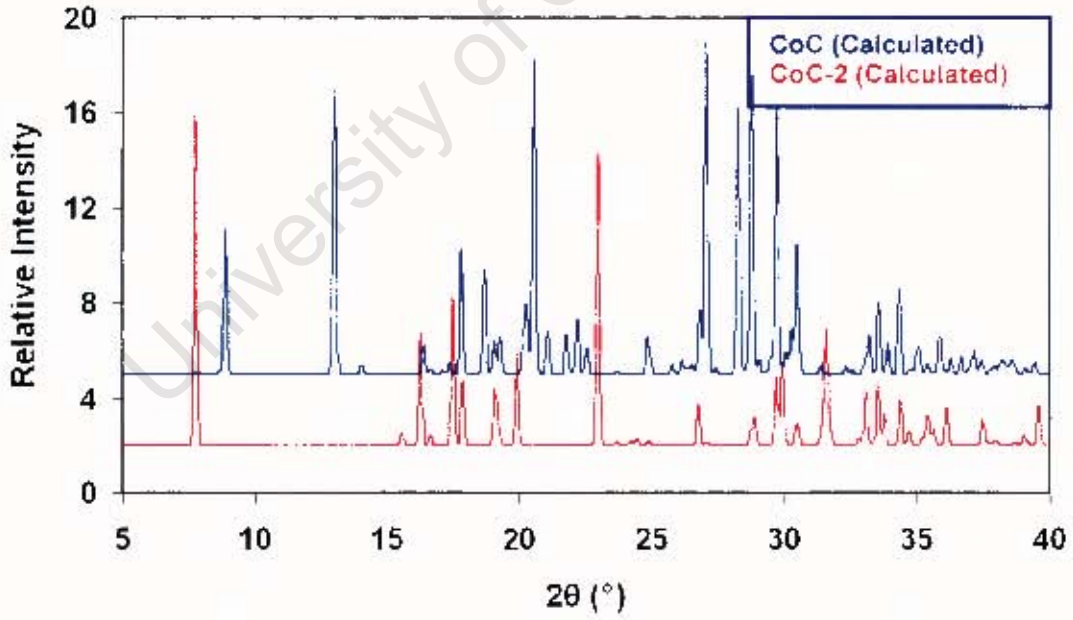

Figure 3.47: Comparison of calculated PXRD patterns of **CoC** and **CoC-2**.

Structural similarities of Co(II) compounds

In this section structural similarities of all Co(II) compounds, discussed in this chapter, will be outlined. The compounds showing these similarities are paired and summarised in Table 3.29 and will be discussed in respective pairs.

Table 3.29: Comparison of Co(II) compounds.

	Structural similarity	
1	CoB	CoC
2	CoI	CoN(E)
3	CoN(A)	CoN(B)
4	CoN(D)	CoS
5	CoN(C)	#
6	CoN(F)	#

no structural similarity with any compound.

CoB and **CoC** are similar with regard to atomic positions and packing of the molecules. **CoI** and **CoN(E)** showed the same packing motifs with four planar bpdo molecules forming a H-bonded ring linking metal centres. **CoN(A)** and **CoN(B)** have the related packing motifs. The only difference between the two is that **CoN(A)** have bpdo as a guest molecule and one nitrate ion not coordinated to the central metal. Both **CoN(D)** and **CoS** have the hydrophilic regions between the Co(II) ions separated by organic layers and their packing motifs are comparable. **CoN(C)** and **CoN(F)** did not show any structural similarity to any of the compounds discussed in this chapter.

Part (B): Temperature (1) and solvent dependent (2) study; Repeatability versus Reproducibility.

Repeatability is the ability to repeat a measurement under an unchanging set of conditions, while reproducibility is the ability to reproduce a measurement whenever a predefined set of conditions is recreated.
In this project, four different complexes of $(CoNO_3)_2$ and bpdo have been prepared. A further two have been reported in the literature.[2] We decided therefore to attempt to elucidate the experimental conditions which favoured the formation of each.

Temperature, solvent mixtures and ratios have proven to be the fundamental experimental parameters which must be controlled in crystal growing procedures for reproducibility of results. Different crystal structures were achieved using alcoholic (MeOH) and aqueous alcoholic (MeOH and H_2O) solutions of cobalt nitrate and bpdo at different temperature. The experiments were set up at 278 K, ambient (295 K – 298 K), 295 K, 298 K and 313 K using chemical quantities discussed previously in Chapter 2.

Compounds were analysed using mainly PXRD and in some cases elemental analyses to confirm homogeneity of the bulk compound. All the results were validated by repetitive experiments and analyses. In all cases, a single crystal was selected for unit cell determination. The insert pictures in PXRD figures illustrate various colours and morphologies of crystals prepared.

Note – Whenever we compare a calculated PXRD pattern to the experimental pattern, we note that the calculated pattern is shifted to the right, i.e. to higher values of 2θ. This is because the calculated pattern is derived from the parameters of the single crystal structure which was elucidated at low temperature. Therefore its unit cell is smaller than that obtained at room temperature, its reciprocal lattice is larger, and hence the pattern shifts to the higher values of 2θ. All X-Ray diffraction patterns were measured at room temperature (298 K).

Crystal structures

The crystal structures have been described in detail in the previous section. Unit cell parameters of the $Co(NO_3)_2$ compounds are summarised in Table 3.30 and the compounds are shown in Figure 3.48.

Table 3.30: Unit cell parameters of **CoN(A)**, **CoN(B)**, **CoN(C)**, **CoN(D)**, **CoN(E)** and **CoN(F)**.

	CoN(A)	CoN(B)	CoN(C)	CoN(D)	CoN(E)	CoN(F)
a (Å)	7.814 (2)	7.501 (2)	7.936 (2)	7.286(2)	19.3116	8.9
b (Å)	9.913 (3)	9.691 (2)	27.648 (6)	24.323(5)	19.3166	11.7
c (Å)	17.186 (5)	19.574 (4)	8.644 (2)	10.308(2)	13.4668	14.0
α (°)	78.61 (1)	90.00	90.00	90.00	90	104.9
β (°)	83.46 (1)	93.38 (3)	106.13 (3)	90.91(3)	90	96.8
γ (°)	85.62 (1)	90.00	90.00	90.00	90	98.3
V (Å^3)	1294.47 (6)	1420.4 (5)	1822.0 (6)	1826.6(6)	5011.1	1383.4

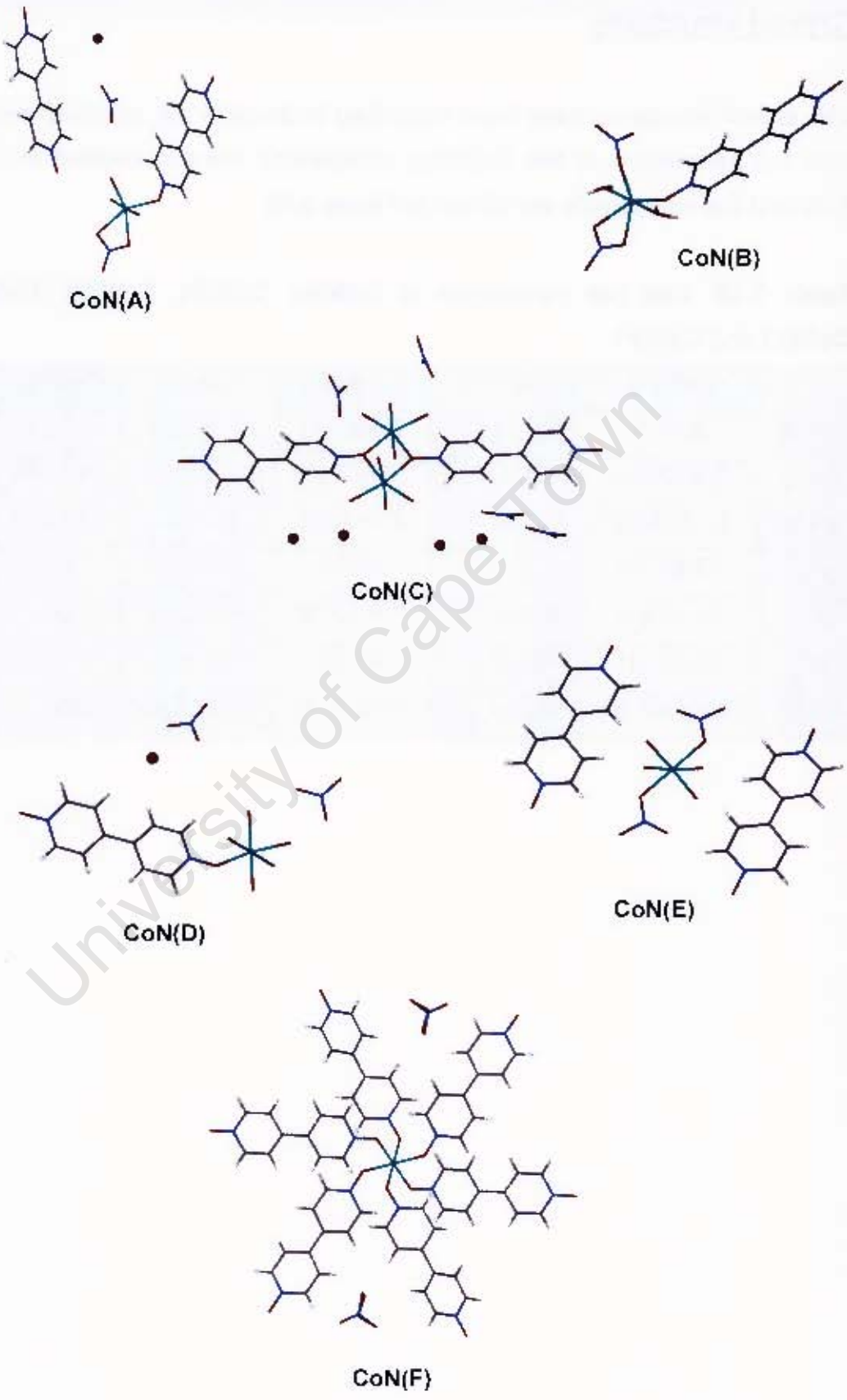

Figure 3.48: Crystal structures of complexes of $Co(NO_3)_2$ with bpdo.

(1) Temperature dependent study using methanol alone

Table 3.31 summarises the results obtained when crystals were prepared from methanolic solutions of $Co(NO_3)_2$ and bpdo. For each selected temperature, two crystallisations were carried out. Microanalysis was only performed on one of the two batches if unit cell measurements and PXRD analyses concluded that the compounds obtained were identical.

At 278 K, the same compound (**CoN(F)**) was prepared in both experimental trials, whereas at ambient temperature (lab bench, estimated 295 K – 298 K) two compounds (**CoN(A)** and **CoN(E)**) of the same elemental composition were obtained. The experiment was repeated under better temperature control using a microvate[6] system. At 298 K, two unit cell parameters for **CoN(B)** and **CoN(D)** were achieved when analysing crystals from the two sets of crystallisations. The same unit cell measurements (for **CoN(B)** and **CoN(D)**) were also obtained at 295 K. Micro and PXRD analyses for the compounds prepared at 295 K could not be obtained as the compounds were too hygroscopic. All the PXRD patterns for samples prepared at ambient and 298 K matched the calculated pattern for **CoN(E)** compound. Microanalysis of the compound formed at 313 K could not be obtained as the compound was hygroscopic. The picture inserted with the PXRD graphs are of the crystals prepared in this study and named in Table 3.31.

Table 3.31: Temperature dependent experiments of Co^{II} complexes.

Temperature	Batch	Unit cell	PXRD	Microanalysis
278 K	1	CoN(F)	CoN(F)	CoN(F)
	2	CoN(F)	CoN(F)	
Ambient (295 K – 298 K)	1	CoN(A)	CoN(E)	CoN(A) or CoN(E)
	2	CoN(E)	CoN(E)	
295 K	1	CoN(B)	Hygroscopic	Hygroscopic
	2	CoN(D)	Hygroscopic	
298 K	1	CoN(B)	CoN(E)	#
	2	CoN(D)	CoN(E)	
313 K	1	CoN(B)	CoN(B)	Hygroscopic
	2	CoN(B)	CoN(B)	

microanalysis not done.

278 K

At 278 K, the compound formed is **CoN(F)**.

Microanalysis (%):

Found: C, 54.11; H, 3.70; N, 13.73

Calculated for **CoN(F)**: C, 54.93; H, 3.69; N, 13.95

The elemental analysis corresponded well with the calculated values.

PXRD:

The pattern of the bulk experimental compound (blue) could generally be compared with the Lazy Pulverix calculated PXRD pattern (red), in Figure 3.49. The PXRD patterns of the metal salt (purple) and bpdo (pink) were measured and included for comparison with the patterns of **CoN(F)** (generated and experimental) in Figure 3.49.

There are two extra peaks at low 2θ values (at approximately 8.5 and 11) in the experimental pattern. Neither corresponds to peaks from the metal salt or the bpdo traces. Thus, the most likely explanation is that the extra peaks could be due to a very small amount of another crystalline compound.

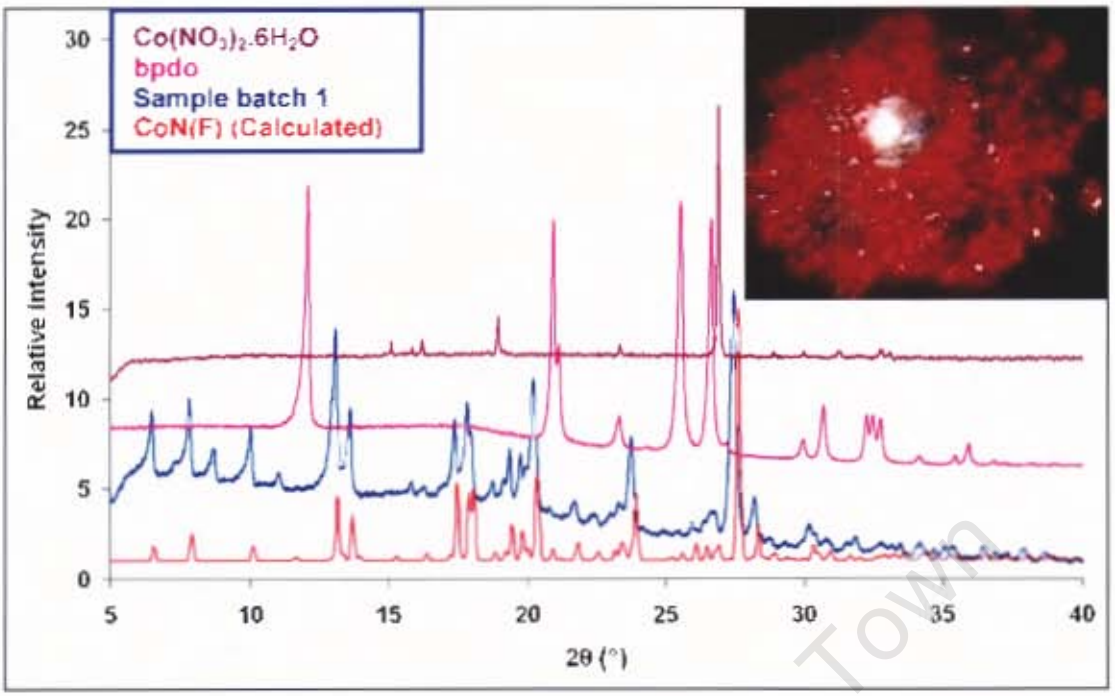

Figure 3.49: Comparison of PXRD patterns of bpdo, cobalt metal salt, experimental (sample batch 1) and calculated Lazy Pulverix PXRD patterns of $[Co(bpdo)_6](NO_3)_2$.

Ambient temperatures (295 K – 298 K)

Two unit cell parameters for **CoN(A)** and **CoN(E)** were obtained when analysing crystals from the two sets of crystallisations. Interestingly, the PXRD of both only matched the pattern for **CoN(E)**.

Microanalysis (%):

Batch 1; Found: C, 37.01; H, 3.08; N, 13.09

Batch 2: Found: C, 37.09; H, 3.49; N, 13.17

Calculated for **CoN(A)**: C, 38.05; H, 3.83; N, 13.31

Calculated for **CoN(E)**: C, 38.05; H, 3.83; N, 13.31

The elemental analysis corresponds to the calculated values, but with relatively large discrepancies. This could represent either **CoN(A)** or **CoN(E)** as they have similar molecular entities and can both be prepared at ambient temperature. One single crystals was removed from each batch: one had unit cell parameters corresponding to **CoN(A)** and the other to **CoN(E)**.

PXRD:

The PXRD patterns of each compound are shown in Figure 3.50 and 3.51. Crystal colours and morphologies were similar in both sample batch 1 and 2. The insert picture representing both compounds is shown in Figure 3.51.

The calculated PXRD of **CoN(A)** and the experimental sample batch 1 patterns are a mismatch. Calculated PXRD pattern of **CoN(E)** has been included in Figure 3.50 and it was a good match of sample batch 1 pattern.

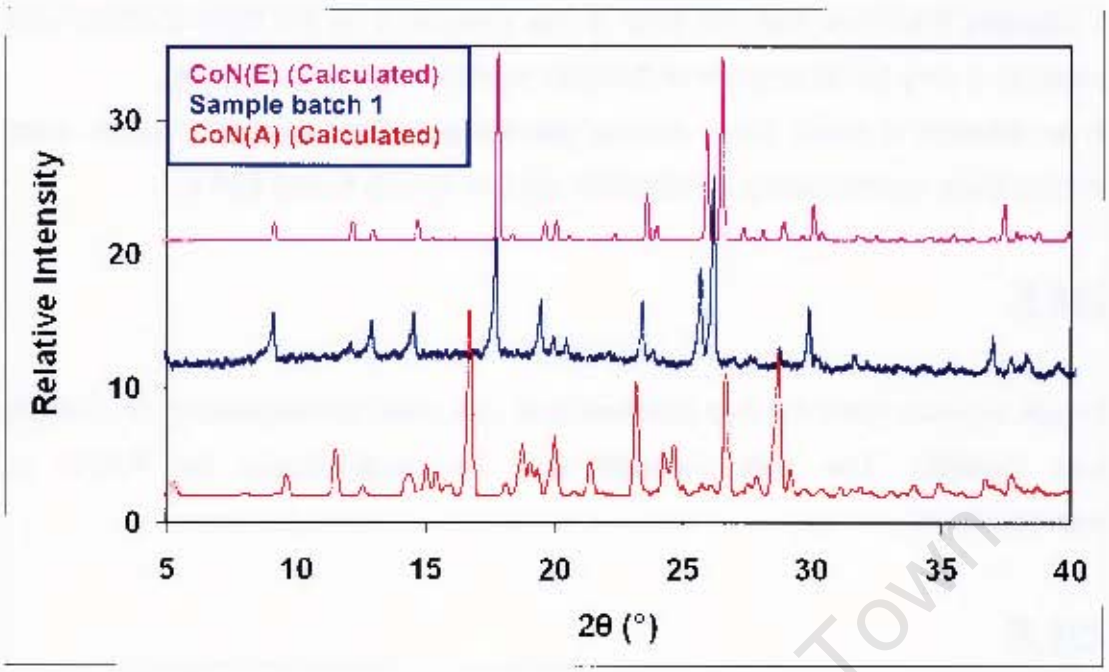

Figure 3.50: Comparison of calculated PXRD pattern for **CoN(A)** and **CoN(E)** with experimental pattern for sample batch 1.

The PXRD pattern of both calculated **CoN(E)** and sample batch 2 are also a good match.

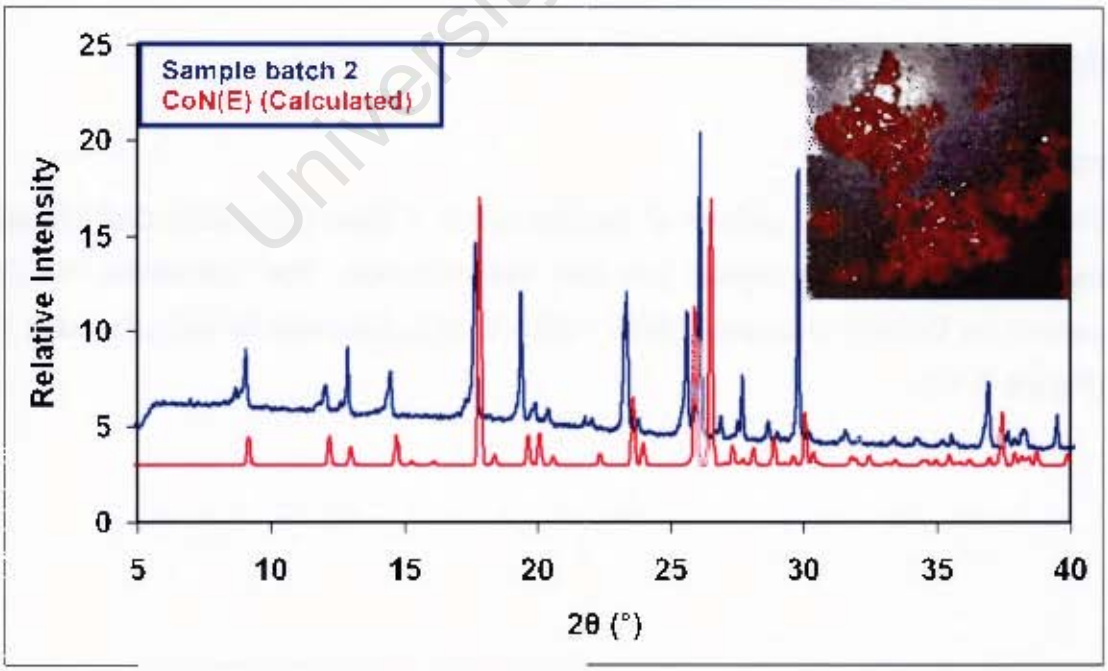

Figure 3.51: Overlay of calculated PXRD pattern of **CoN(E)** and experimental pattern of sample batch 2.

It appears therefore that the bulk of the sample is of the form **CoN(E)** with possibly a very small amount of **CoN(A)** crystallising concomitantly.
In an attempt to clarify these results, we repeated the experiment under strict temperature control using a microvate system at 295 K and 298 K.

295 K

Single crystals from the two batches had unit cells corresponding to **CoN(B)** and **CoN(D)**. The bulk material was too hygroscopic for PXRD or microanalysis.

298 K

Two unit cell parameters for **CoN(B)** and **CoN(D)** were obtained when analysing crystals from the two sets of crystallisations. The PXRD of both matched the pattern for **CoN(E)** suggesting that the bulk material is of the form **CoN(E)**. Because PXRDs showed mixtures of compounds, microanalysis was expected to be inconclusive and was therefore not done.

Sample batch 1

PXRD:
The measured PXRD pattern of sample batch 1 does not match **CoN(B)** as expected from single crystal unit cell determination. The calculated PXRD pattern for **CoN(E)** showed a better match to that observed for sample batch 1 (Figure 3.52).

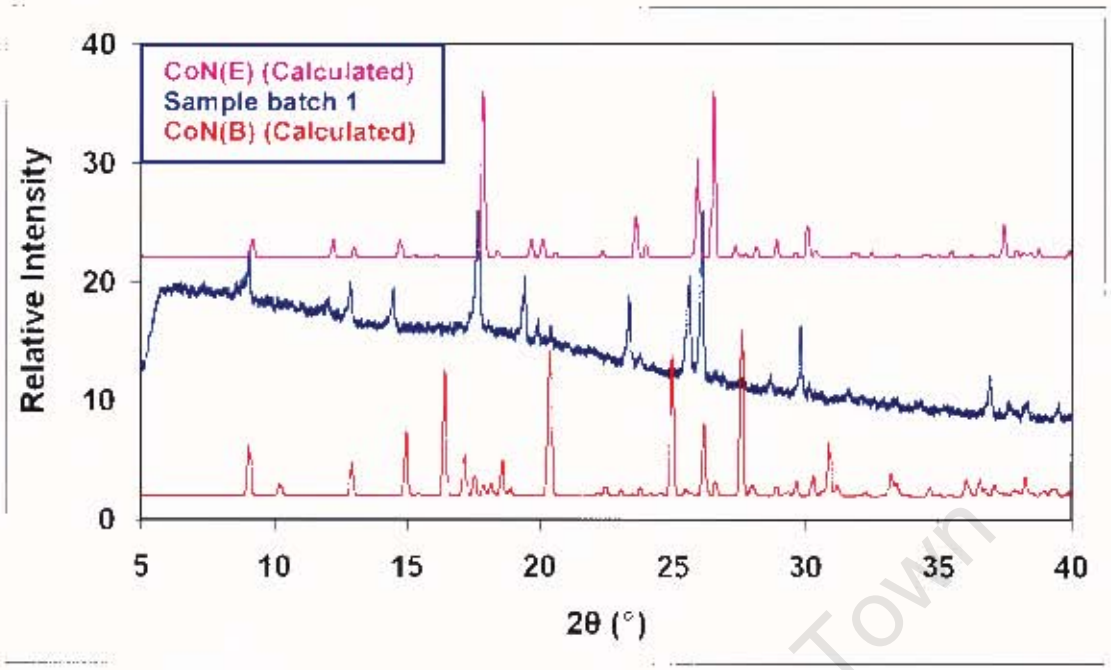

Figure 3.52: Comparison of calculated PXRD pattern for **CoN(B)** and **CoN(E)** with experimental pattern for sample batch 1.

Sample batch 2

PXRD:

Similarly, the measured PXRD pattern of sample batch 2 does not match the expected compound (**CoN(D)**) determined from single crystal unit cell. The calculated PXRD pattern for **CoN(E)** showed a better match to that observed for sample batch 2 as shown in Figure 3.53.

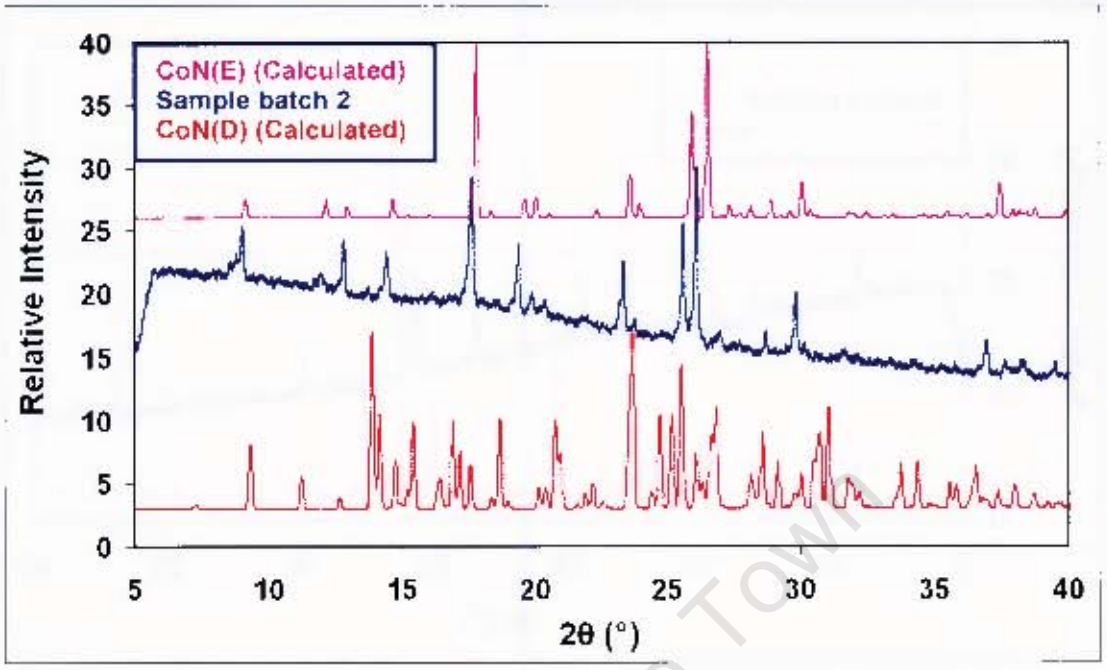

Figure 3.53: Comparison of calculated PXRD pattern for **CoN(D)** and **CoN(E)** with experimental pattern for sample batch 2.

313 K

At 313 K, the compound formed is **CoN(B)**.

Microanalysis could not be obtained as the sample was too hygroscopic.

PXRD:

The PXRD pattern matched that of **CoN(B)**. Due to the reproducibility of the PXRD patterns for both batch 1 and 2, only one pattern is shown here (Figure 3.54).

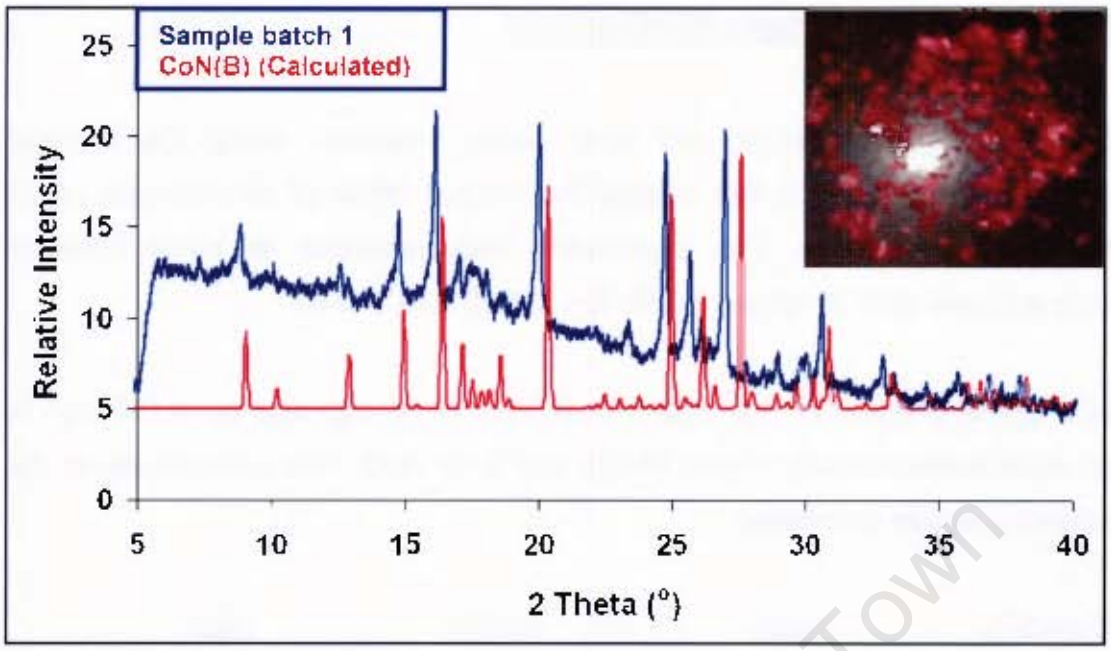

Figure 3.54: Overlay of experimental and calculated patterns of sample batch 1 and **CoN(B)**

Summary

At 278 K, the preparation of the **CoN(F)** compound was reproducible as confirmed by XRD methods and elemental analysis.

At ambient temperature, reproducibility proved impossible to attain. Single crystals chosen had unit cells corresponding to four compounds: **CoN(A)**, **CoN(B)**, **CoN(D)** and **CoN(E)**. The bulk material of all samples that were crystallised have PXRD patterns which are similar to those calculated for **CoN(E)**, suggesting that multiple compounds are formed under these conditions.

At 313 K, only the **CoN(B)** was produced. Elemental analysis was unreliable due to the hygroscopic nature of the compound, but the PXRD was a good match.

The prepared crystals are different colours which helps identification with the naked eye in confirming that different compounds were obtained.

(2) Solvent ratio study (MeOH:H_2O)

Compounds of $Co(NO_3)_2$ and bpdo were prepared, using the method described in Chapter 2, but varying the relative ratios of the solvents used: methanol and water. The experiment was repeated at three different temperatures (278 K, ambient (295 K – 298 K) and 313 K).

In a typical preparation we mixed $Co(NO_3)_2$ (72.76 mg) and bpdo (35 mg) in an equivolume mixture of 5 mL MeOH and 5 mL H_2O. This corresponds to the following values in mmoles:

$Co(NO_3)_2$	:	bpdo	:	MeOH	:	H_2O
0.40	:	0.19	:	123	:	278

Thus the ratio of $Co(NO_3)_2$: bpdo is 2 : 1 and the ratio for of MeOH : H_2O is 1 : 2.3, but the solvent is in great excess to the $Co(NO_3)_2$ and bpdo.
Similarly for other various solvent ratios.

278 K

Table 3.32 shows the solvent ratios used, the unit cell parameters of the single crystal selected from each batch of crystals, PXRD and microanalysis results where possible. Microanalysis of compounds prepared using solvent ratios 1:1 and 2:1 were unreliable as different compounds of different elemental compositions were obtained.
Interesting PXRD results using a 2:1 solvent ratios showing a combination of compound patterns, led to performance of three experimental trials. The 1:0 solvent ratio results have been discussed in Part B (1) and were included in Table 3.32 for comparison.

Table 3.32: Results for the Co^{II} complexes using different solvent ratios.

Temp.	Batch	MeOH:H_2O	Unit cell	PXRD match	Micro-analysis
278 K	1	1:0	CoN(F)	CoN(F)	CoN(F)
	2	1:0	CoN(F)	CoN(F)	
	1	1:1	CoN(E)	CoN(E)	#
	2	1:1	CoN(E)	CoN(B)	
	1	1:2	CoN(E)	CoN(E)	CoN(E)
	2	1:2	CoN(E)	CoN(E)	
	1	2:1	CoN(C)	CoN(B) + CoN(C)	#
	2	2:1	CoN(D)	CoN(B)	
	3	2:1	CoN(E)	CoN(B)	

microanalysis not done

1:1 ratio

Similar unit cell parameters to those for **CoN(E)** were obtained in both sample batches, but the PXRD patterns matched both **CoN(B)** and **CoN(E)**

Sample batch 1

Because PXRDs showed mixtures of compounds, microanalysis was expected to be inconclusive and was therefore not done.

PXRD:

PXRD patterns for both sample batches are presented here since they differed from each other (Figure 3.55 and 3.56).

The PXRD pattern of both calculated **CoN(E)** and sample batch 1 are a good match.

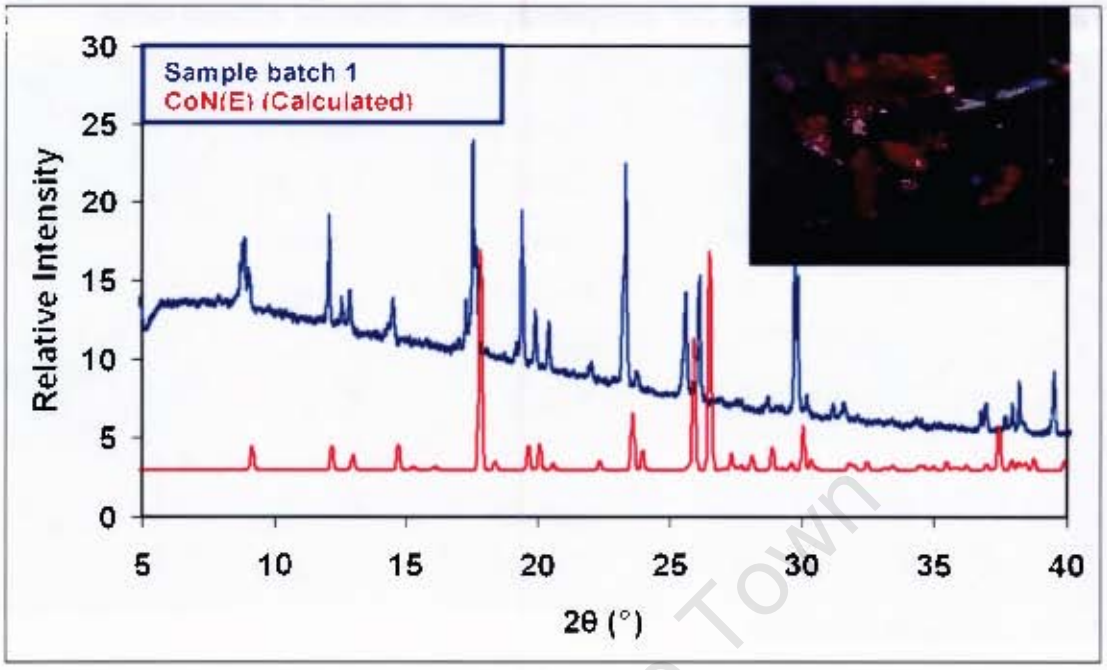

Figure 3.55: Overlay of calculated PXRD pattern of **CoN(E)** and experimental pattern of sample batch 1 using 1:1 solvent ratio.

Sample batch 2

Because PXRDs showed mixtures of compounds, microanalysis was expected to be inconclusive and was therefore not done.

PXRD:

The calculated PXRD for **CoN(E)** and the experimental (sample batch 2) pattern are a mismatch. The experimental PXRD is better match for the calculated pattern of **CoN(B)** and this identification was further strengthened by the colour of crystals as shown by the photo in Figure 3.56.

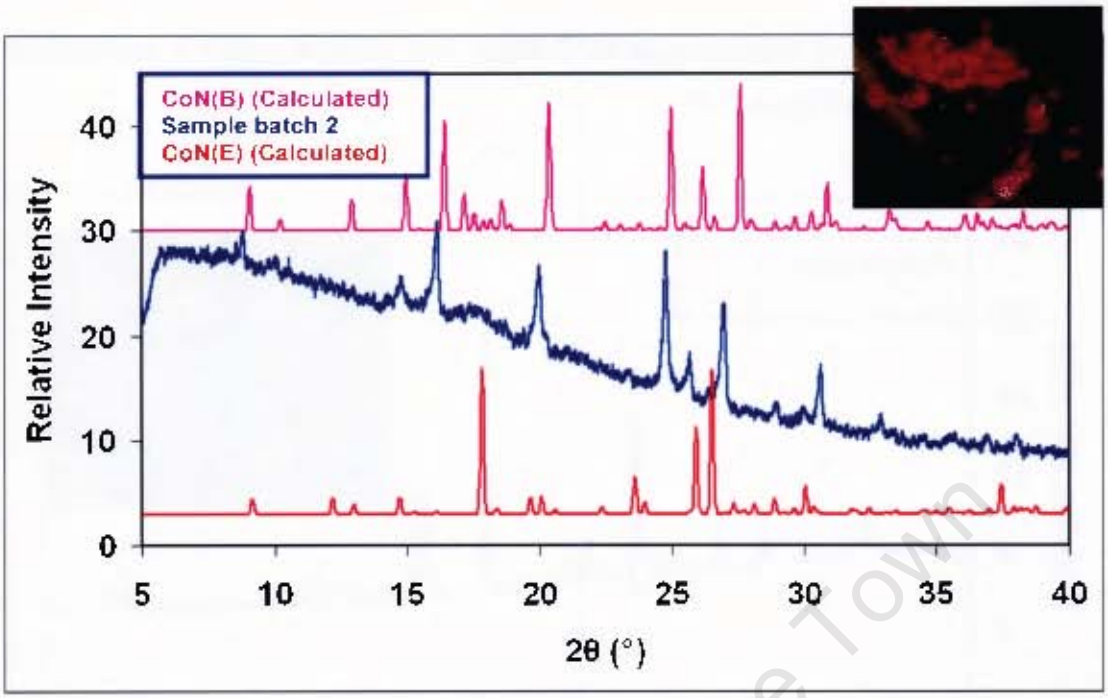

Figure 3.56: Overlay of calculated PXRD pattern of **CoN(E)** and experimental pattern of sample batch 2 using 1:1 solvent ratio. Calculated PXRD of **CoN(B)** compound is included in the figure for comparison.

1:2 ratio

CoN(E) is formed when using 1:2 solvent ratio for both sample batches.

Sample batch 1

Microanalysis (%):

Microanalysis was done for sample batch 1 only since **CoN(E)** was reproduced in both sample batches.

Found: C, 38.38; H, 3.64: N, 12.76

Calculated for **CoN(E)**: C, 39.81; H. 4.01; N, 13.93

The elemental analysis corresponds to the calculated values, but with relatively large discrepancies.

PXRD:

The PXRD pattern of both calculated **CoN(E)** and sample batch 1 are a good match as shown in Figure 3.57.

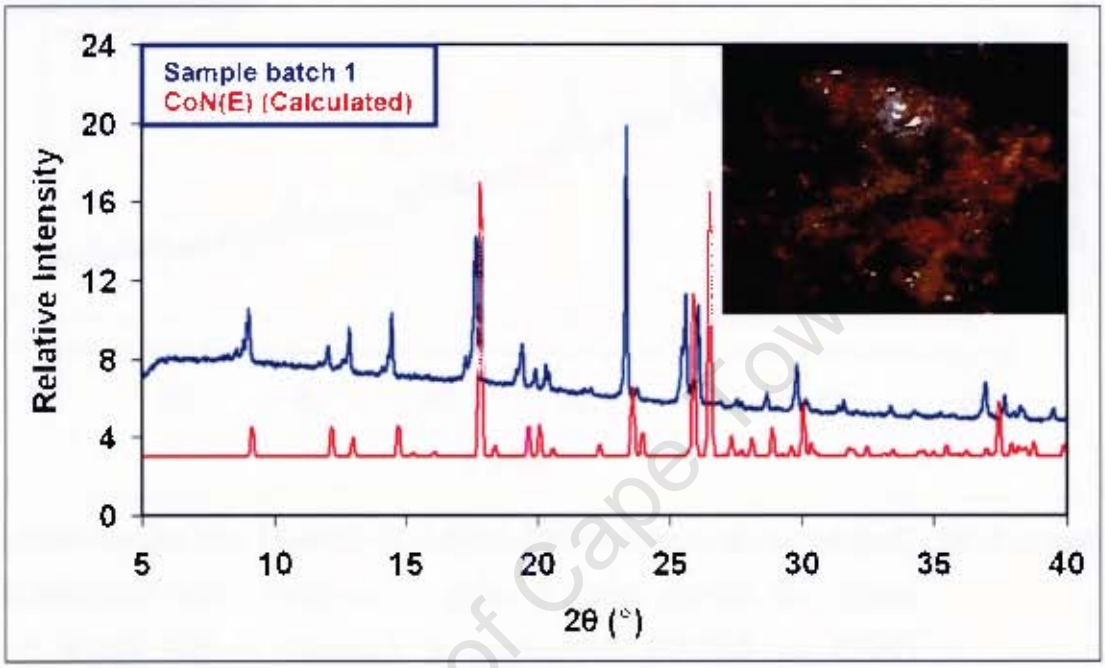

Figure 3.57: Overlay of calculated PXRD pattern of **CoN(E)** and experimental pattern of sample batch 1 using 1:2 solvent ratio.

Sample batch 2 was not included here since the results for both batches were reproducible.

2:1 ratio

Three different unit cell parameters matching **CoN(C)**, **CoN(D)** and **CoN(E)** compounds were measured for single crystals from sample batch 1, 2 and 3 respectively. According to the unit cell parameters determination, the PXRD pattern of sample batch 2 was expected to match the one of **CoN(D)**, but the results proved otherwise, as it was matching **CoN(B)** pattern (Figure 3.59).

The PXRD patterns of sample batch 1 and 3 were expected to match the calculated PXRD's of **CoN(C)** and **CoN(E)**, but the patterns were a complete mismatch, suggesting a mixture of compounds as shown in Figure 3.58 and 3.60.

Sample batch 1

Because PXRDs showed mixtures of compounds, microanalysis was expected to be inconclusive and was therefore not done.

PXRD:

The general PXRD patterns match **CoN(C)**, except peak at low 2θ (approximately 6.5) which suggest a compound mixture. Figure 3.58 shows an overlay of the patterns for sample batch 1 and calculated **CoN(C)**. The calculated pattern of **CoN(B)** is included in this figure for comparison as it could be part of the mixture. The suggestion of **CoN(B)** is validated by PXRD pattern observed in sample batch 2 (Table 3.32).

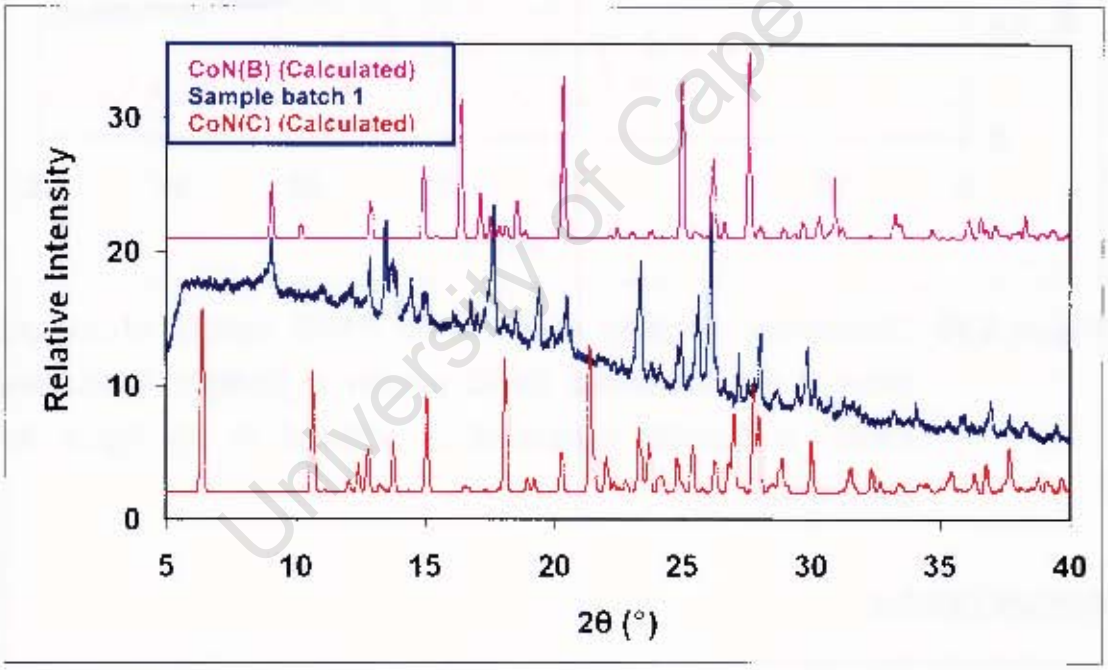

Figure 3.58: Overlay of experimental sample batch 1 and calculated **CoN(C)** PXRD patterns. Calculated PXRD of **CoN(B)** compound is included in the figure for comparison.

Sample batch 2

Because PXRDs showed mixtures of compounds, microanalysis was expected to be inconclusive and was therefore not done.

PXRD:

The measured PXRD of sample batch 2 does not match **CoN(D)** as expected from single crystal unit cell determination. The calculated PXRD pattern of **CoN(B)** showed a better match to that observed for sample batch 2, see Figure 3.59.

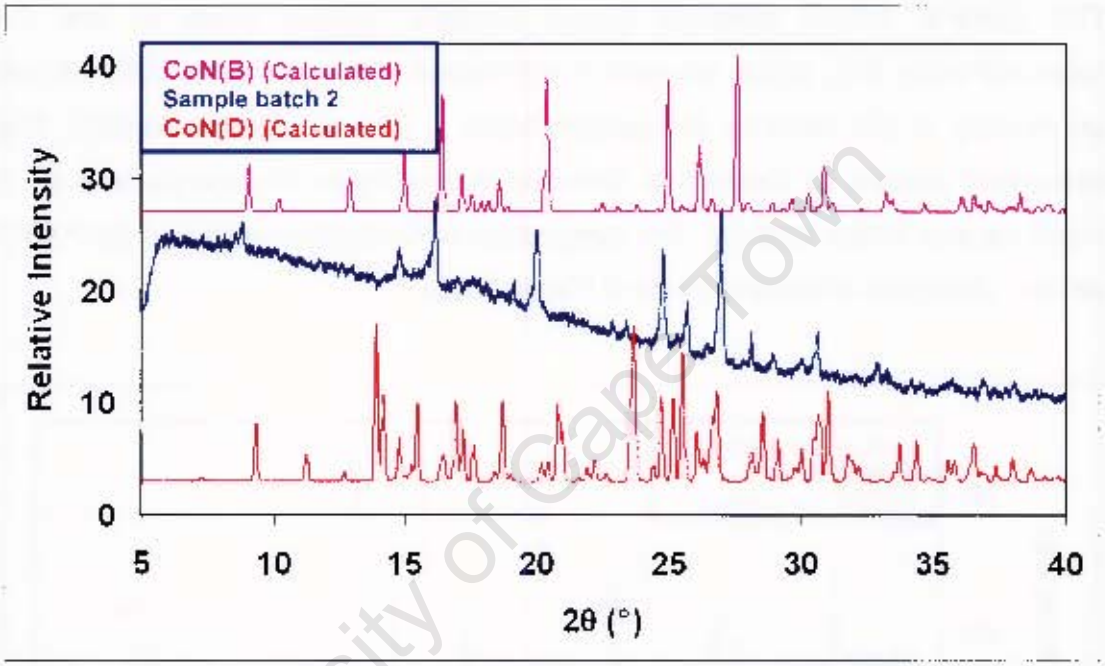

Figure 3.59: Comparison between experimental PXRD pattern of sample batch 2 and calculated PXRD pattern of **CoN(D).** Calculated PXRD of **CoN(B)** compound is included in the figure for comparison.

Sample batch 3

Because PXRDs showed mixtures of compounds, microanalysis was expected to be inconclusive and was therefore not done.

PXRD:

The calculated PXRD of **CoN(E)** and sample 3 patterns are a mismatch. Calculated PXRD pattern of **CoN(B)** is included in Figure 3.60 for comparison as it showed some peaks which are similar to those observed for PXRD pattern of sample batch 3. This PXRD pattern may shows a new phase that

has not been characterised by single crystal methods, or it may be a mixture of several phases.

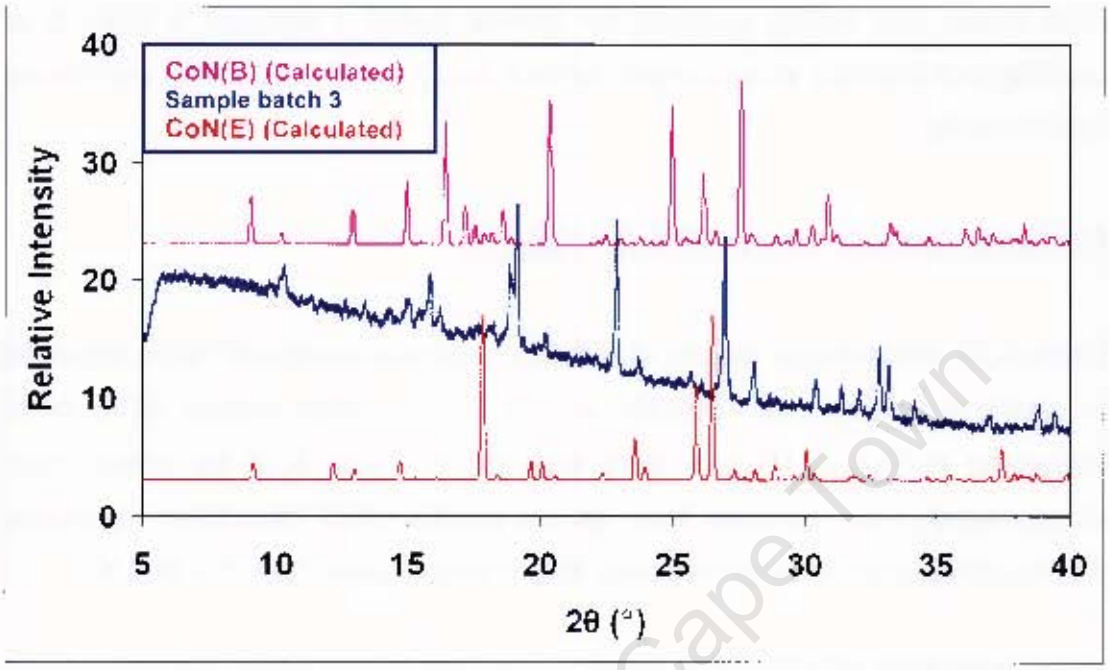

Figure 3.60: Comparison between experimental PXRD pattern of sample batch 3 and calculated PXRD pattern of **CoN(E)**. Calculated PXRD of **CoN(B)** compound is included in the figure for comparison.

Summary

Using a 1:1 ratio at 278 K results in **CoN(E)** with the possibility of some **CoN(B)** being formed. One of the PXRD patterns showed a trace of **CoN(B)** while the other sample matched only **CoN(E)**. Single crystals taken from both batches corresponded to **CoN(E)**, suggesting that concomitant crystallisation had occurred.

Reproducible results for the unit cell parameters and the PXRD patterns were obtained for **CoN(E)** when using the aqueous methanol mixture with a ratio of 1:2 concluding in the formation of **CoN(E)** crystals.

Three different unit cells for the **CoN(C)**, **CoN(D)** and **CoN(E)** compounds were obtained using a ratio of 2:1. The PXRD patterns of each of the three sample batches did not correspond to the unit cell parameters determined in each case. The PXRD patterns for sample batch 1 showed a mixture of **CoN(B)** and **CoN(C)**, while sample batch 2 and 3 matched **CoN(B)** compound considerably.

Ambient temperature (295 K – 298 K)

Table 3.33 summarises results of different aqueous methanol ratios obtained at ambient temperature. Results of 1:0 solvent ratio results have been discussed in Part B (1) and were included in Table 3.33 for comparison. Microanalysis was not done here, as the results could have been unreliable due to compound mixtures prepared at this temperature (295 K – 298 K).

Table 3.33: Results for Co^{II} complexes using different solvent ratios.

Temp.	Batch	MeOH:H_2O	Unit cell	PXRD match
ambient	1	1:0	CoN(A)	CoN(E)
	2	1:0	CoN(E)	CoN(E)
	1	1:1	CoN(C)	CoN(E)
	2	1:1	CoN(B)	CoN(B)
	1	1:2	CoN(E)	CoN(B) + CoN(E)
	2	1:2	CoN(E)	CoN(B) + CoN(E)
	1	2:1	CoN(E)	CoN(E)
	2	2:1	CoN(E)	CoN(B) + CoN(E)

1:1 ratio

Two different unit cell parameters for **CoN(C)** and **CoN(B)** were obtained from single crystals in sample batches 1 and 2, respectively. The PXRD pattern suggested that there is a mixture of compounds in sample batch 1 (**CoN(C)** and **CoN(E)**), while in sample batch 2, **CoN(B)** was formed. Calculated PXRD patterns of **CoN(C)**, **CoN(B)** and **CoN(E)** are shown in Figure 3.61 for

comparison. There is a possibility of concurrent crystallisation of **CoN(B)** in sample batch 1 since it was the sole product in sample batch 2, hence the inclusion of its calculated PXRD in Figure 3.61 for comparison.

Sample batch 1

PXRD:

The PXRD patterns for sample batch 1 does not match that calculated for **CoN(C)**. The PXRD pattern of sample batch 1 is a better match to the calculated pattern for **CoN(E)**. **CoN(B)** is another possibility owing to the similarity of its pattern to **CoN(E)**, as explained before.

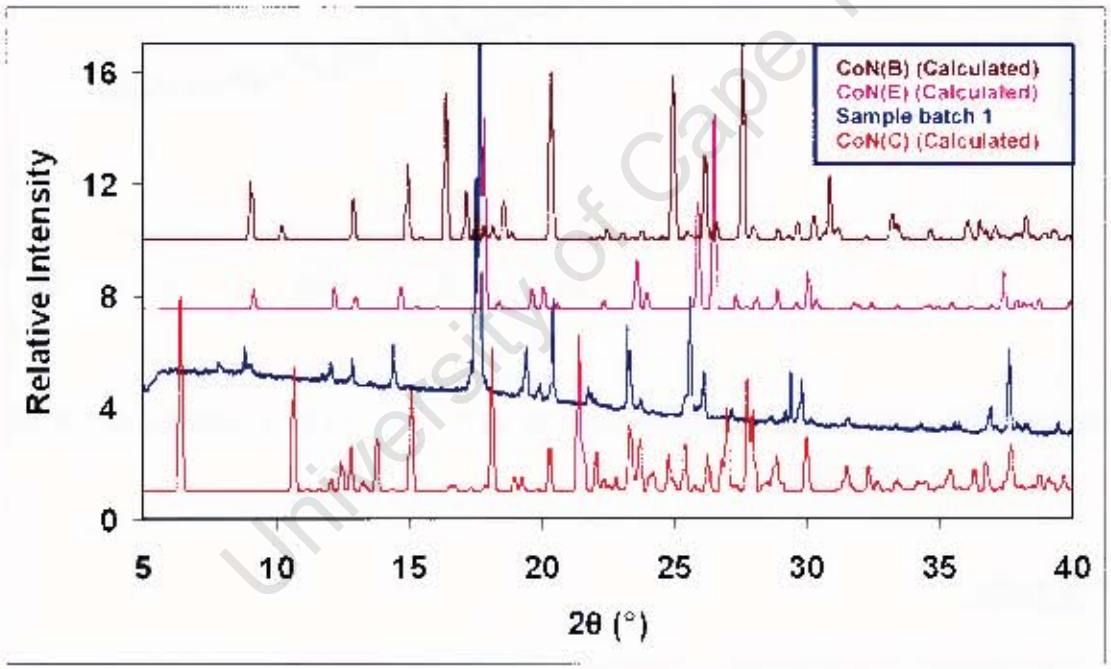

Figure 3.61: Comparison between experimental PXRD pattern of sample batch 1 and calculated PXRD pattern of **CoN(C)** compound. Calculated PXRD of **CoN(B)** and **CoN(E)** compound are included in this figure for comparison.

Sample batch 2

PXRD:

The PXRD patterns between the calculated **CoN(B)** and the sample batch 2 matches as shown in Figure 3.62, suggesting that the bulk material is **CoN(B)**.

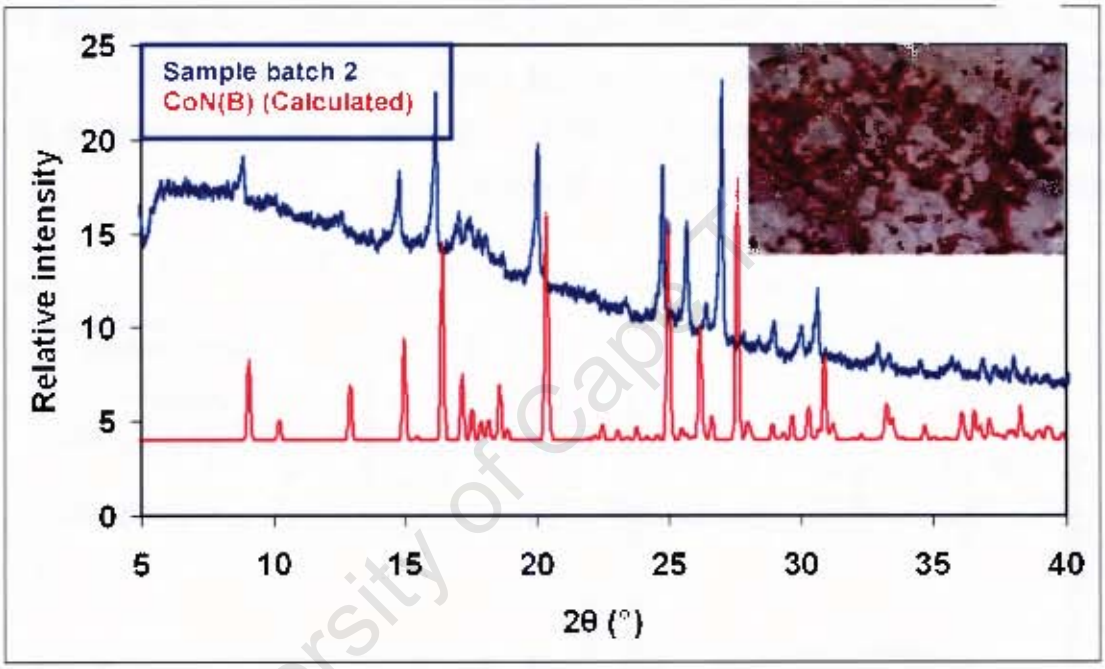

Figure 3.62: Overlay of experimental (sample batch 2) and calculated PXRD of **CoN(B)**.

1:2 ratio

Using 1:2 solvent ratio, the two unit cell parameters from each sample batch were measured. They were both similar and corresponded to **CoN(E)**. Nonetheless, PXRD patterns revealed that both batches were not homogenous, but were a mixture of **CoN(B)** and **CoN(E)** in both cases. Only sample batch 1 PXRD is shown to illustrate the two sample batches results.

Sample batch 1

PXRD:

The calculated PXRD of **CoN(E)** and experimental pattern of sample batch 1 partially match, suggesting a compound mixture (**CoN(B)** and **CoN(E)**). Most PXRD peaks of sample batch 1 corresponds to those of calculated **CoN(B)** and it is therefore included in Figure 3.63 for comparison.

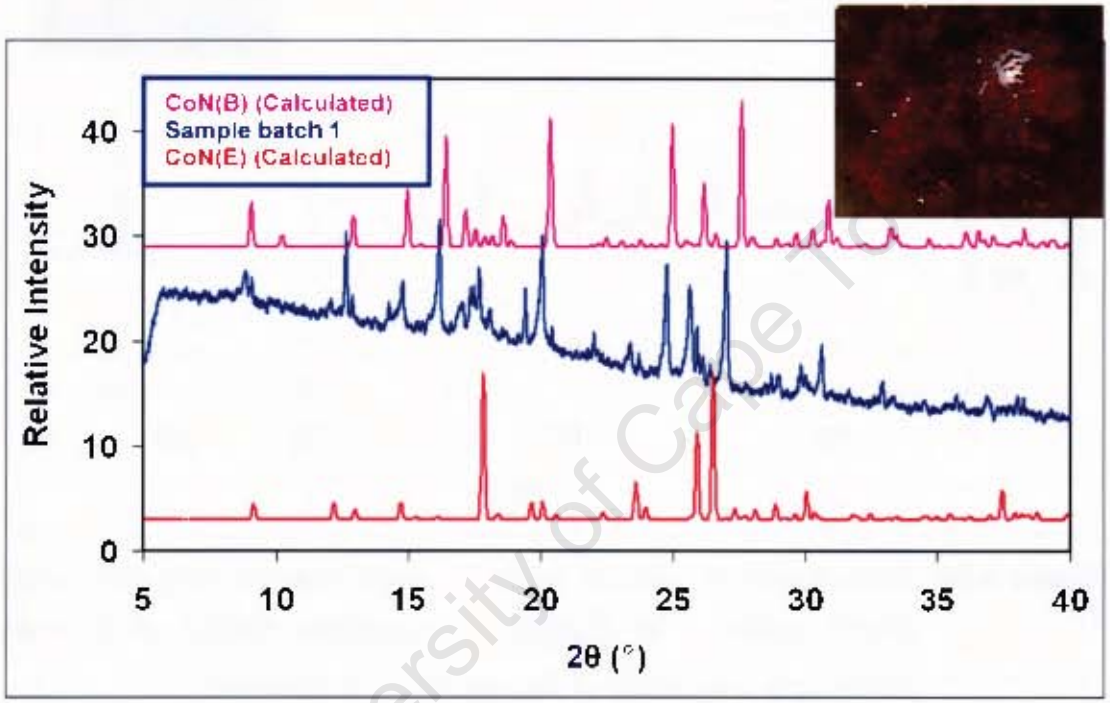

Figure 3.63: Overlay of the calculated PXRD pattern of **CoN(E)** and experimental (sample batch 1) pattern. Calculated PXRD of **CoN(B)** compound is included in this figure for comparison.

2:1 ratio

Unit cell measurements were carried out for sample batch 1 and 2 and confirmed in both cases the formation of the **CoN(E)** compound only. PXRD of sample batch 1 corresponded well with calculated PXRD (Figure 3.64). However, the PXRD patterns of sample batch 2 showed the possibility of concurrent crystallisation of **CoN(B)** (Table 3.33), thus the calculated PXRD pattern of **CoN(B)** was included in Figure 3.64 for comparison.

Sample batch 1

PXRD:

PXRD patterns of sample batch 1 and **CoN(E)** are a match.

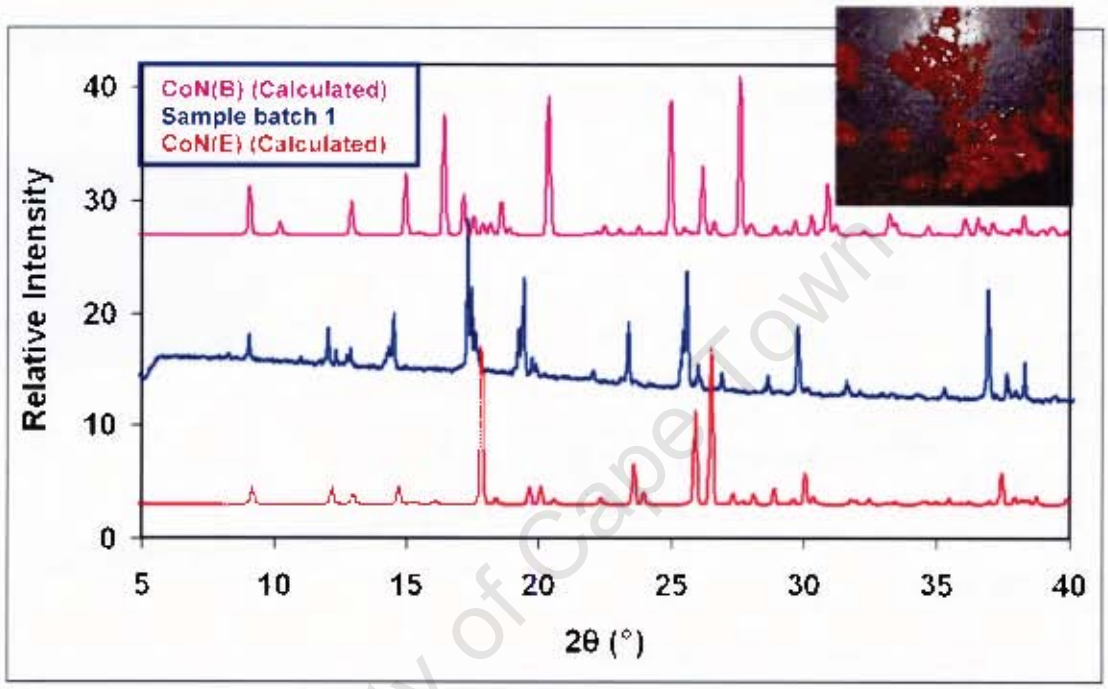

Figure 3.64: Comparison of sample batch 1 (experimental) and calculated PXRD patterns of **CoN(E).** Calculated PXRD of **CoN(B)** compound is included in the figure for comparison.

Sample batch 2

PXRD:

The PXRD patterns partially match, suggesting a compound mixture. The bulk sample of sample batch 2 is composed of **CoN(B)**. This is shown by a number of peaks observed in the experimental **CoN(B)** trace which corresponds to the calculated **CoN(B)** trace in Figure 3.65 and this is further confirmed by the colour of the crystals, which is different from sample batch 1, but similar to the **CoN(B)** compound shown previously in this section (Figure 3.62).

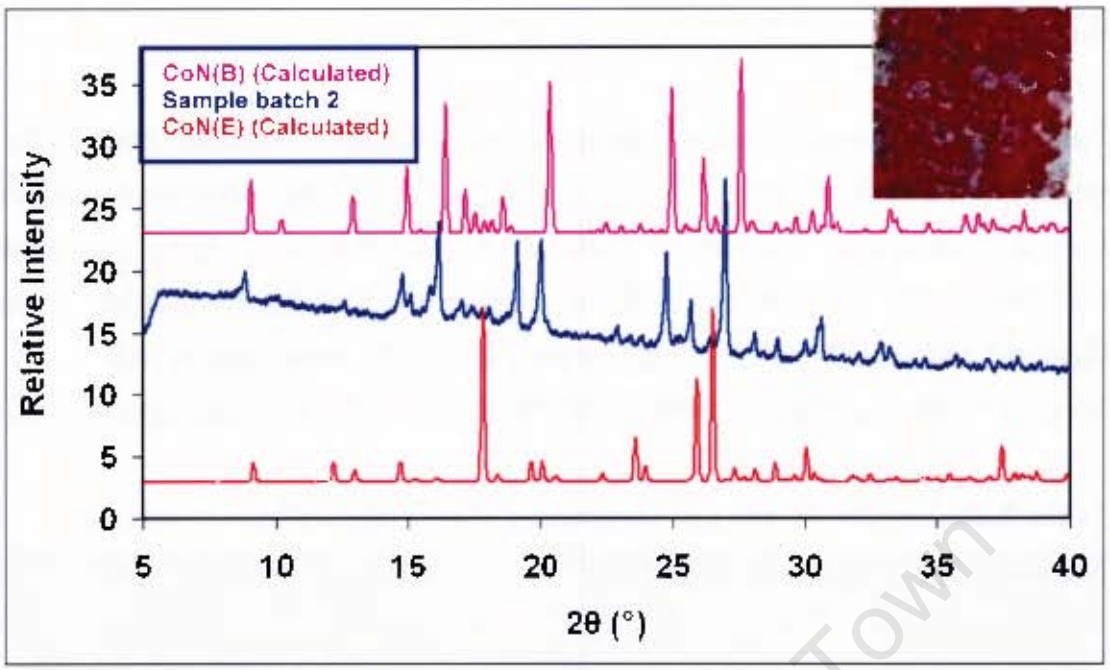

Figure 3.65: The calculated PXRD pattern of **CoN(E)** matched the experimental pattern of sample batch 2. Calculated PXRD of **CoN(B)** compound is included in the figure for comparison.

Summary

Elemental analysis was not an ideal method to confirm which compounds were prepared at ambient temperature (295 K – 298 K) since we obtained compound mixtures in unknown ratios.

313 K

Table 3.34 shows compounds prepared using different aqueous methanolic solutions at 313 K. Results of 1:0 solvent ratio results have been discussed in Part B (1) and were included in Table 3.34 for comparison. Using a solvent ratio of 1:1, two different unit cells for **CoN(A)** and **CoN(E)** compounds were obtained, while 1:2 and 2:1 ratios formed the **CoN(B)** compound alone. Microanalysis could not be obtained as the compounds were too hygroscopic.

Table 3.34: Results for the Co^{II} complexes using different solvent ratios.

Temperature	Batch	MeOH:H_2O	Unit cell	PXRD match
313 K	1	1:0	CoN(B)	CoN(B)
	2	1:0	CoN(B)	CoN(B)
	1	1:1	CoN(A)	CoN(A) + CoN(B)
	2	1:1	CoN(E)	CoN(B) + CoN(E)
	1	1:2	CoN(B)	CoN(B)
	2	1:2	CoN(B)	CoN(B)
	1	2:1	CoN(B)	CoN(B)
	2	2:1	CoN(B)	CoN(B)

1:1 ratio

Sample batch 1

PXRD:

The single crystal from sample batch 1 gave in the unit cell parameters of **CoN(A)**. When comparing the generated PXRD pattern of **CoN(A)** with the experimental pattern, it was a mismatch. The PXRD pattern suggests a compound mixture composed mostly of **CoN(B)** compound and a small amount of the **CoN(A)** crystallising concomitantly, as shown in Figure 3.66. Crystal colours and morphologies were similar in all prepared crystals and thus only one photograph is shown in Figure 3.66.

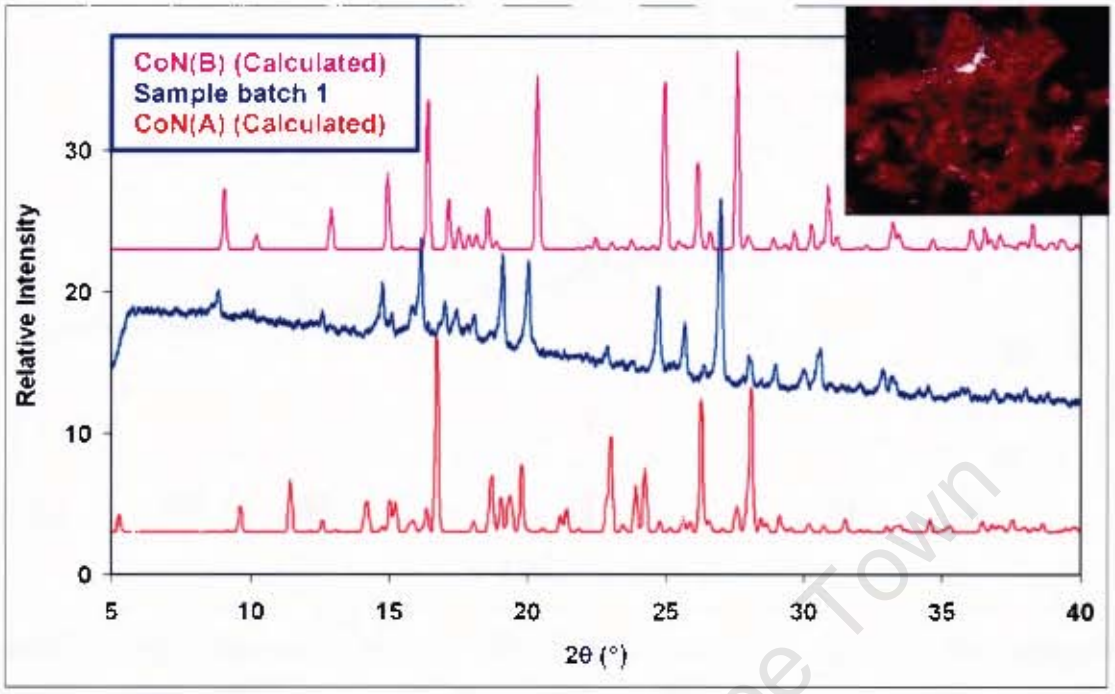

Figure 3.66: Overlay of experimental (sample batch 1) and calculated (**CoN(A)**) PXRD patterns. Calculated PXRD of **CoN(B)** compound is included in the figure for comparison.

Sample batch 2

PXRD:

The PXRD patterns of calculated **CoN(E)**, which was suggested by the unit cell measurement, and sample batch 2 partially match, suggesting that the compound is a mixture of **CoN(B)** and **CoN(E)** as shown in Figure 3.67.

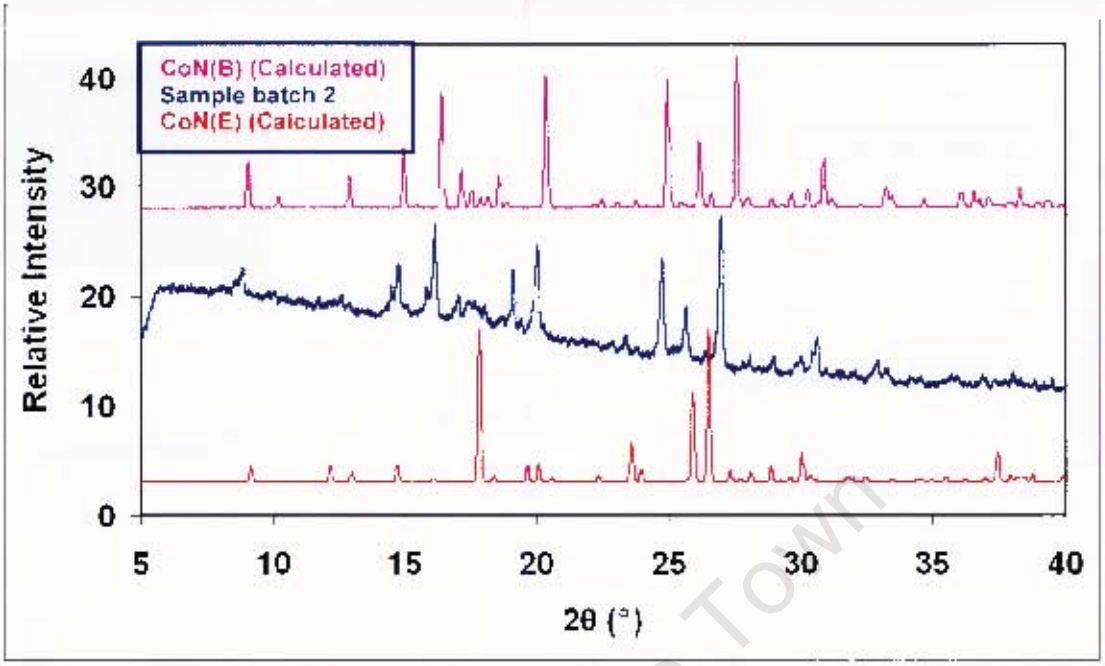

Figure 3.67: Overlay of experimental PXRD pattern of sample batch 2 and calculated **CoN(E).** Calculated PXRD of **CoN(B)** compound is included in the figure for comparison.

1:2 ratio

CoN(B) compound is formed from sample batch 1 and 2.

Sample batch 1

PXRD:

PXRD patterns are a match in both sample batches and the PXRD pattern of sample batch 1 is shown (Figure 3.68), to illustrate the general result.

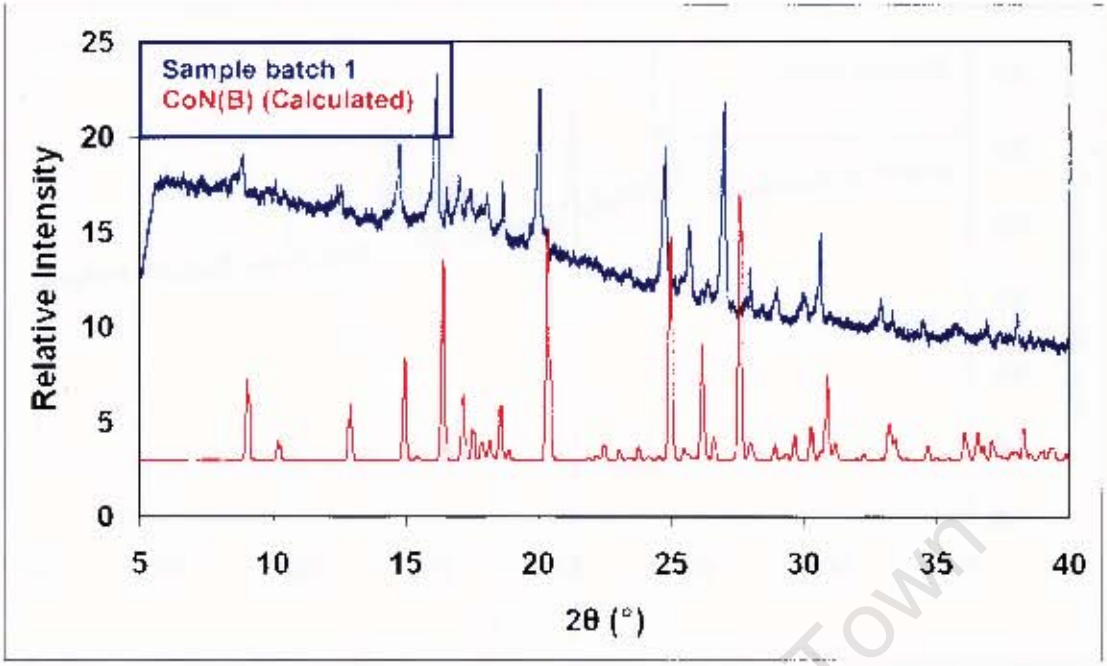

Figure 3.68: Calculated PXRD pattern of **CoN(B)** is matched with experimental pattern of sample batch 1.

2:1 ratio

CoN(B) compound is formed from sample batch 1 and 2.

Sample batch 1

PXRD:

PXRD patterns are a match in both sample batches and the PXRD pattern of sample batch 1 is shown (Figure 3.69), to illustrate the general results.

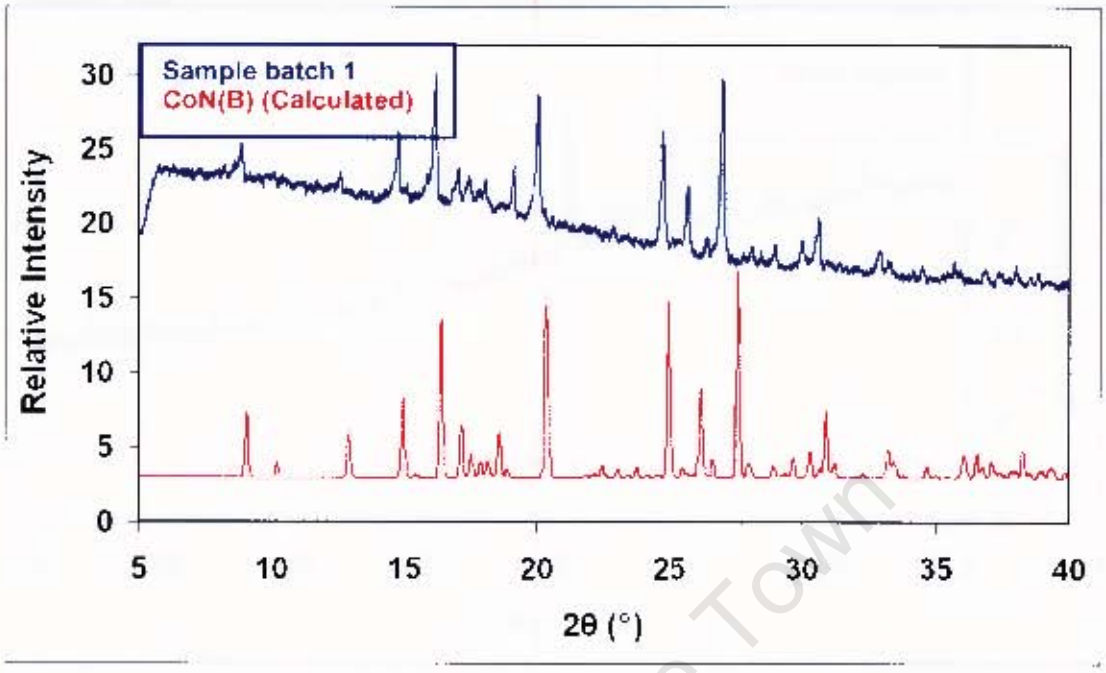

Figure 3.69: Calculated PXRD pattern of **CoN(B)** is matched with experimental pattern of sample batch 1.

Summary

At 313 K, using the solvent ratio 1:1 resulted in two different unit cell parameters: **CoN(A)** and **CoN(E)** from sample batch 1 and 2, respectively. PXRD patterns suggest compound mixtures, composed mostly of the **CoN(B)** compound and small amounts of **CoN(A)** and **CoN(E)** crystallising concomitantly in batch 1 and 2, respectively.

CoN(B) is formed when using ratios 1:2 and 2:1. The PXRD patterns showed footprints of **CoN(B)** when compared with the calculated pattern.

Co-grinding of physical mixtures of $Co(NO_3)_2$ and bpdo

The results of the variable solvent crystallisation study, just described, prompted the question of what compounds would form in the absence of solvent. Braga and Grepioni[7] have carried out a number of studies on the preparation of coordination compounds by co-grinding mixtures of metal salts and ligands.

The physical mixtures of $Co(NO_3)_2$ and bpdo were prepared and analysed using PXRD. Two experiments were done; the first experiment was prepared using chemical quantities discussed previously in Chapter 2 while in the second experiment a metal:bpdo molar ratio of 1:6 was used. Co-grinding was done for two hours in each experiment. The first experiment was done to establish which of the prepared and elucidated Co(II) complexes, discussed in this chapter, forms by physical mixture without using a solvent. The PXRD pattern of the mixture (sample batch 1) completely matched the calculated PXRD for **CoN(E)** as shown in Figure 3.70.

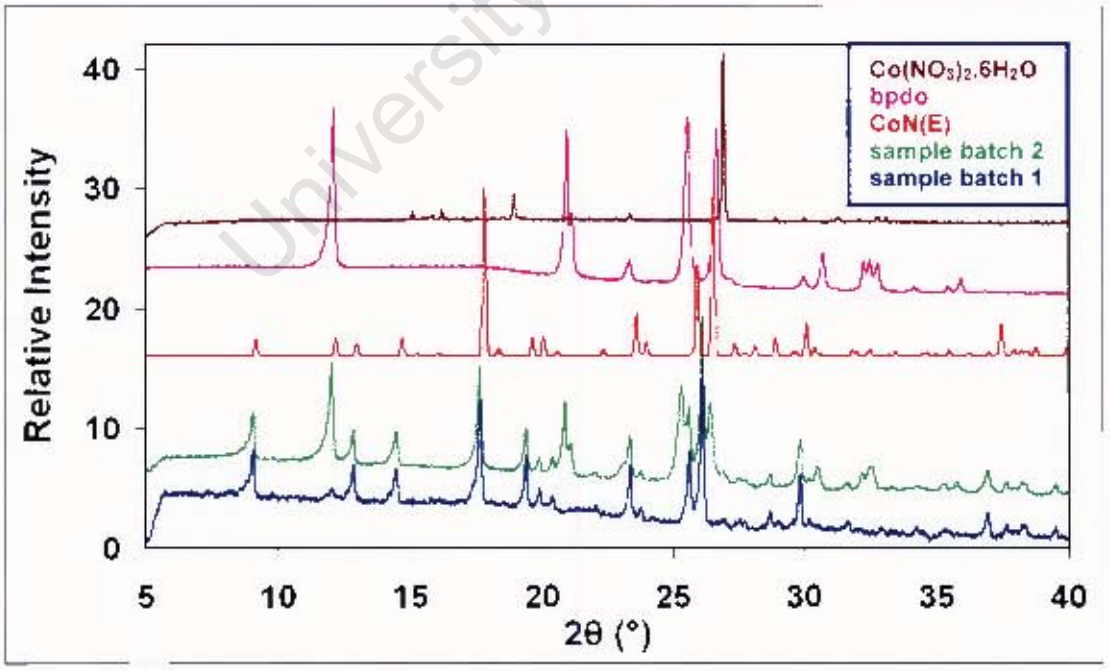

Figure 3.70: Comparison of PXRD patterns of sample batch 1 and 2, calculated **CoN(E)**, bpdo and $Co(NO_3)_2$.

In the second experiment, an excess of the bpdo ligand was used in a physical mixture. It was expected that the bpdo would sufficiently compete to coordinate to all the binding sites of the central metal to form the **CoN(F)** compound. Instead, the PXRD trace obtained (sample batch 2) matched the calculated PXRD for **CoN(E)** (Figure 3.70). The experimental PXRD pattern showed extra peaks which corresponded to the PXRD pattern of bpdo ligand.

Discussion and conclusion

Part A: Compounds discussed in this chapter illustrate a variety of supramolecular networks. It is evident from the range of structures refined and elucidated that by changing the metal ligands while using the same spacer ligand (bpdo) has an effect on the type of crystal structures obtained.
As long as the axially coordinated ligand is bidentate, it is expected that the product should be polymeric, but this was not the case in the cobalt metal complexes which often form supramolecular polymers through hydrogen bonding.

In **CoB** and **CoC**, the hydrogen-bonded salt structures give rise to inorganic-organic layered structures. **CoI** forms a high symmetry 3-dimensional supramolecular network, while **CoN(A)**, **CoN(D)** and **CoS** form interdigitated layers in which hydrophilic regions between the Co(II) ions are separated from one another by organic regions. **CoN(B)** has both nitrate counterions and two water molecules coordinated to the central metal displaying an irregular octahedral symmetry while in **CoN(C)**, Co(II) ions are bridged by bpdo ligands.
In addition to coordinated water molecules, all crystal structures (except **CoI**) contained guest water molecules which are linked to the host compound by hydrogen bonding.

A common feature in all these nine structures is the presence of strong $\pi\cdots\pi$ interactions. This representation is shown in Figure 3.71, in which the selected sections of each structure have been chosen to illustrate the interactions which appear to be a strong structure-directing influence.

Compounds of **CoB** and **CoC** were transformed from discrete molecules to 1 dimensional coordination polymers with guest water molecules bridging the two polymer chains through hydrogen bonding. Unlike in discrete molecules of **CoB** and **CoC**, bpdo molecule is directly coordinated to the central metal resulting in the loss of water.

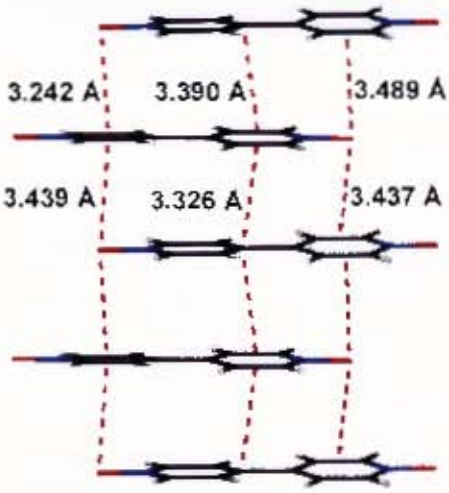

CoB and CoC

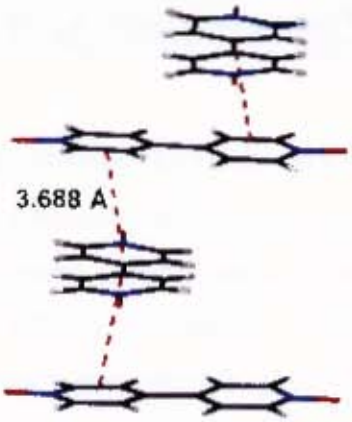

CoI

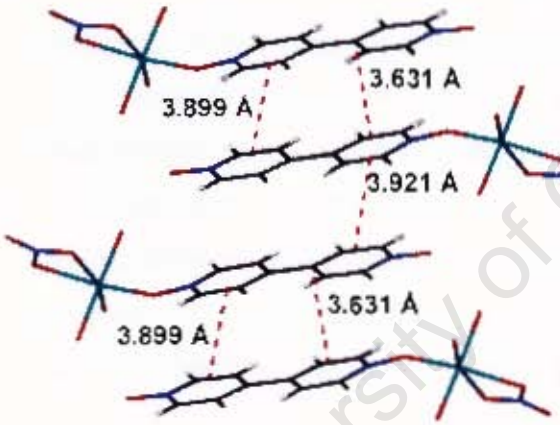

Host

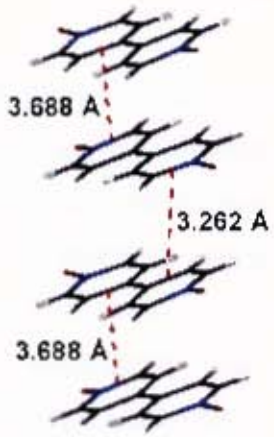

Guest

CoN(A)

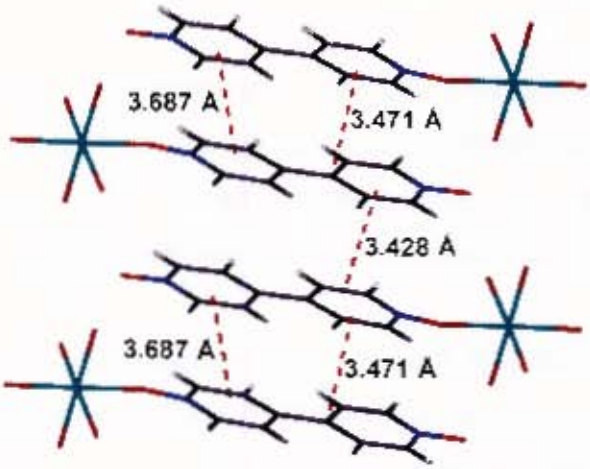

CoS

Figure 3.71: Conservation of the π interactions in structures.

A search of the CSD[2] (Version 5.27, November 2005) for cobalt compounds with bpdo found five structures to have been reported previously. In $[Co(bpdo)_4(H_2O)_2](PF_6)_2.2H_2O$, a 3D diamondoid network is formed in which double bpdo spacers bridge two adjacent metal centres.[8] Cobalt perchlorate has been used to produce both $[Co(H_2O)_4(bpdo)](ClO_4)_2.2(bpdo)$[9] and $[Co(bdpo)_2(N(CN)_2)_2(H_2O)_2]$.[10] In the former one bpdo bridges two cobalt ions, giving a 1D covalently linked chain along [100] while an uncoordinated bpdo links two cobalts along the cell diagonal via hydrogen bonds, leaving a triangular channel containing ClO_4^- anions. Uniquely among these structures, there are no $\pi\cdots\pi$ interactions in this case. In the latter case, crystallisation from ethanol rather than water, and the use of a competing ligand, eliminates perchlorate from the final structure to produce $[Co(bdpo)_2(N(CN)_2)_2(H_2O)_2]$. Both bpdo and dicyanamide act as terminal ligands and as hydrogen bond acceptors to coordinated aqua ligands.

Using $Co(NO_3)_2$ and bpdo as the starting material has been reported[4] to produce two different structures to the four (**CoN(A), CoN(B), CoN(C), CoN(D)**) reported in this study. When the metal salt and bpdo are mixed in aqueous solution the resulting material is $[Co(NO_3)_2(H_2O)_4].2(bpdo)$ (**CoN(E)**) which is most like **CoI** solved in this study, in that the hydrated metal salt and bpdo molecules form a hydrogen bonded network with similar tetragonal symmetry. Crystallisation from a mixture of methanol and water gave the discrete molecule $[Co(bpdo)_6](NO_3)_2$ (**CoN(F)**), in which each bpdo coordinates via one N-oxide donor while the other end of each ligand engages in $\pi\cdots\pi$ interactions with other molecules in a 2D supramolecular net.[4] Four intermediate crystal structures of $Co(NO_3)_2$ produced in this work may be related to the different crystallisation conditions employed, i.e. crystals were grown in sole alcoholic solutions and aqueous alcoholic solutions, at various temperatures.

According to the CSD[2], only one coordination polymer of Co(II) using bpdo and different counterions have been reported.[4] This is $[Co(H_2O)_4(bpdo)](ClO_4)_2.2(bpdo)$. The compound has been discussed in this section and it is

similar to coordination polymers {**CoB-2** and **CoC-2**} discussed in this study. They both form 1D covalently bonded chains joined through hydrogen bonding forming two dimensional sheets. From our experience and CSD[2] search, it is fairly improbable that coordination polymers of Co(II) metal salts will form using bpdo ligand.

In **Part B**, we demonstrated that temperature and solvent mixtures can play a huge role in deciding the topology of crystal structures. Experiments in this work were performed at different temperatures, and different crystal structures were prepared. In some cases, compound mixtures were obtained. However, reproducible results were achieved in some crystallisations by controlling the experimental temperature.

Crystallisation using methanolic solutions afforded consistent preparation of **CoN(F)** and **CoN(B)** at 278 K and 313 K respectively, while at ambient (295 K – 298 K) temperatures, two compounds (**CoN(A)** and **CoN(E)**) of the same elemental composition suggesting compound mixtures were prepared. Nonetheless, PXRD patterns of samples prepared at 295 K – 298 K were consistent of **CoN(E)** compound. Unit cell parameters for **CoN(B)** and **CoN(D)** were obtained at 298 K, but PXRD patterns of samples prepared have patterns similar to those calculated for **CoN(E)**. Crystallisation in the absence of excess water revealed that the bpdo ligand becomes sufficiently competitive for the central metal as it was demonstrated by **CoN(F)**. This compound can only be prepared at 278 K.

Introduction of water in compound preparations changed the whole trend observed when using methanolic solutions and reproducibility of results. Most preparations using aqueous solution produced compound mixtures.
At 278 K, consistent preparation of **CoN(E)** compound was observed when using 1:2 solvent ratio. The same compound was correspondingly common in all single crystal cell determinations, except in sample batch 1 of 2:1 solvent ratio.

At 295 K – 298 K, crystallisation mostly produced compound mixtures. **CoN(E)** compound was again common in terms of unit cell determination, except in batches 1 and 2 of solvent ratio 1:1. Microanalysis of these compounds was not done due to compound mixtures and therefore results would be unreliable.

Slight heating of the solutions to 313 K gave rise to formation of **CoN(B)**. This is confirmed by the PXRD patterns of the prepared sample batches which corresponded to calculated PXRD of **CoN(B)**. Unit cell dimensions corresponding to **CoN(B)** are common at 313 K, except in sample batch 1 (**CoN(A)**) and sample batch 2 (**CoN(E)**) using 1:1 solvent ratio. This resulted in compounds mixtures of sample batch 1 and 2. However, due to general behaviour of these compounds, the possibility of having a compound mixture in other crystallisation vials should not be neglected although the PXRD confirmed their homogenity. The physical mixture of $Co(NO_3)_2$ and bpdo gave PXRD patterns that matched the calculated PXRD pattern for **CoN(E)**.

The experiments repeated using the same measurements did not show reproducible results, except when using methanol only at 278 K and 313 K.

In conclusion it is evident that by using one metal ion and one ligand, a range of crystal structures can be constructed. This study also provides further evidence that crystallisation conditions are important when preparing metal-organic frameworks. Ligand and counterion may compete for the metal's coordination sites. This behaviour was illustrated by the formation **CoN(B)**, **CoN(E)** and **CoI** compounds using bpdo as was discussed in this chapter.

References

1. F.H. Allen, O. Kennard, D.G. Watson, L. Brammer, A.G. Orpen, R. Taylor, 1987, *J. Chem. Soc. Perkin.* 2, pp. S1-19.
2. F.H. Allen, *Acta Crystallogr.*, 2002, **B58**, 380.
3. M. Caira, L.R. Nassimbeni, H. Su, E. Weber, *CrystEngComm.*, 2003, **5**, 351.
4. A.J. Blake, M.T. Brett, N.R. Champness, A.N. Khlobystov, D-L. Long, C. Wilson, M. Schröder, *Chem. Commun.* 2001, 2258.
5. L.J. Barbour, SECTION, A computer program for the graphic display of cross sections through a unit cell, *J Appl. Cryst.*, 1999, **32**, 353.
6. Microvate: Device for high-through-put crystallisation, React Array solo RS12, Version 0.9.0.0, Barnstead STEM™, © 2005 Anachem Limited.
7. D. Braga, S.L. Giaffreda, F. Grepioni, A. Pettersen, L. Maini, M. Curzi, M. Polito, *Dalton Trans.*, 2006, 1249.
8. B.Q. Ma, H-L. Sun, S. Gao, *Inorg. Chem.* 2005, **44**, 837.
9. B.Q. Ma, S. Gao, H-L. Sun, G-X. Xu, *J. Chem. Soc., Dalton Trans.* 2001, 130.
10. A. Nedelcu, Z. Žak, A.M. Madalan, J. Pinkas, M. Andruh, *Polyhedron*, 2003, **22**, 789.

Chapter 4

Synthesis and crystal structures of $Cu_2Cl_4(bpdo)_3(H_2O)_2 \cdot 2(CH_3)_2SO$ and $[PbX_2(bpdo)]_n$ (X= Br, Cl and I) complexes.

This chapter describes compounds of Cu(II) and Pb(II) metal salts prepared using the same starting materials (DMSO, CH_2Cl_2 or $CHCl_3$ and bpdo) at ambient (295 K – 298 K) temperatures. The presence of DMSO has provided some interesting study on the effect of driving crystal structure construction. The crystal structures refined and elucidated adopted different structural topologies.

The Cu(II) complex is a z-shaped discrete molecule with a DMSO molecule hydrogen bonded to the host through coordinated water molecule. The central metals are linked by hydrogen bonds through coordinated water and oxygens of the bpdo ligand. Crystallisation of $PbBr_2$, $PbCl_2$ and PbI_2 with bpdo afforded 2D coordination polymers. The adjacent metal centres of these polymers are bridged by coordinated Br^-, Cl^- or I^- anions. These polymers possess no conventional hydrogen bonds and the crystal structures are isostructural.
Thermal and elemental analysis of compounds prepared has been carried out and crystal structures have been elucidated.

For each of the crystal structures described in this chapter the crystallographic data, experimental and refinement parameters are given in Table 4.2 and 4.6. The final atomic coordinates, bond lengths and angles, torsion angles, thermal angles, thermal parameters and tables of observed and calculated structure factors for each of the crystal structures are given in the appendices.

Complex preparation

Suitable crystals were grown by solvent layering at ambient temperatures (295 K – 298 K). The complexes were obtained by crystallisation of either Cu(II) or Pb(II) metal salts covered, but not fully dissolved. by either CH_2Cl_2 or $CHCl_3$ and carefully layered under the solution of bpdo in DMSO. Solvent combinations used resulted in a Cu(II) discrete molecule and 1D polymers of Pb(II) metal salt.

The compounds obtained are abbreviated as follows:

$Cu_2Cl_4(bpdo)_3(H_2O)_2 \cdot 2(CH_3)_2SO$: **CuC**

$[PbCl_2(bpdo)]_n$: **PbC**

$[PbI_2(bpdo)]_n$: **PbI**

$[PbBr_2(bpdo)]_n$: **PbB**

Microanalysis

Table 4.1 shows elemental analysis results. The experimental and calculated percentages corresponded well.

Table 4.1: Elemental analysis results for **CuC, PbC, PbI** and **PbB** compounds.

Complex	Found %				Calculated %			
	C	H	N	S	C	H	N	S
CuC	39.77	3.78	8.16	6.23	39.81	3.54	8.19	6.25
PbC	25.57	1.57	5.86	–	25.76	1.73	6.01	–
PbI	18.02	1.22	3.76	–	18.48	1.24	4.32	–
PbB	21.61	1.40	4.86	–	21.63	1.45	5.05	–

PXRD

The calculated (red trace) and experimental (blue trace) PXRD patterns for Cu(II) and Pb(II) complexes are shown in Figure 4.1(a) (d). PXRDs of all

these compounds are a complete match suggesting that the samples prepared were homogenous.

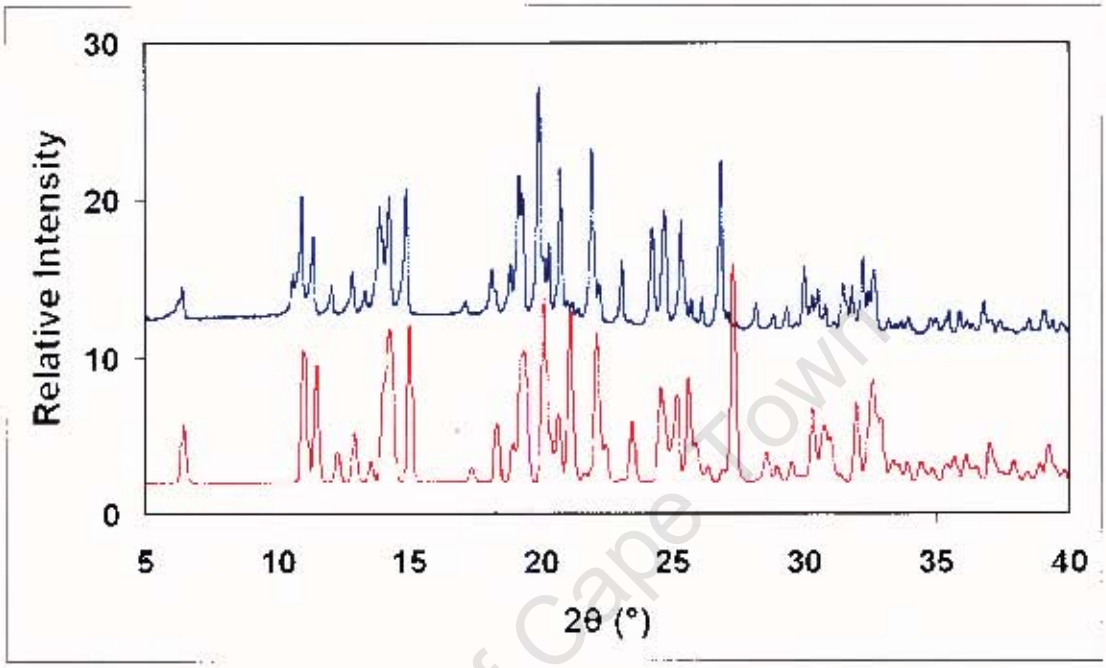

Figure 4.1(a): Comparison of experimental and calculated PXRD patterns for **CuC**.

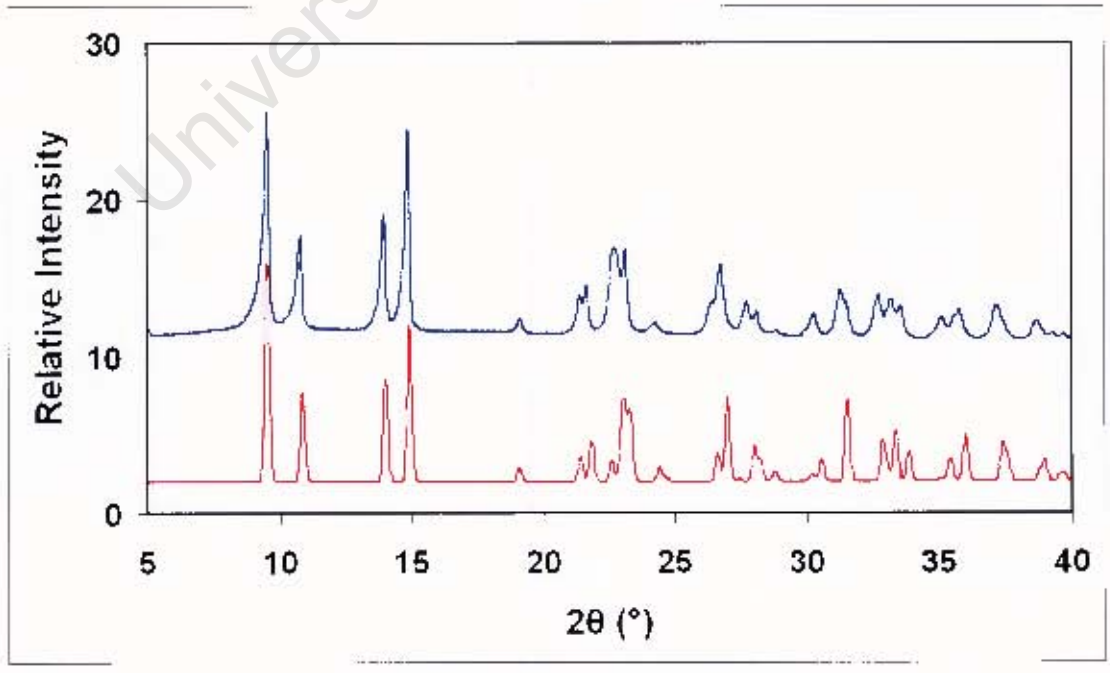

Figure 4.1(b): Comparison of experimental and calculated PXRD patterns for **PbC**.

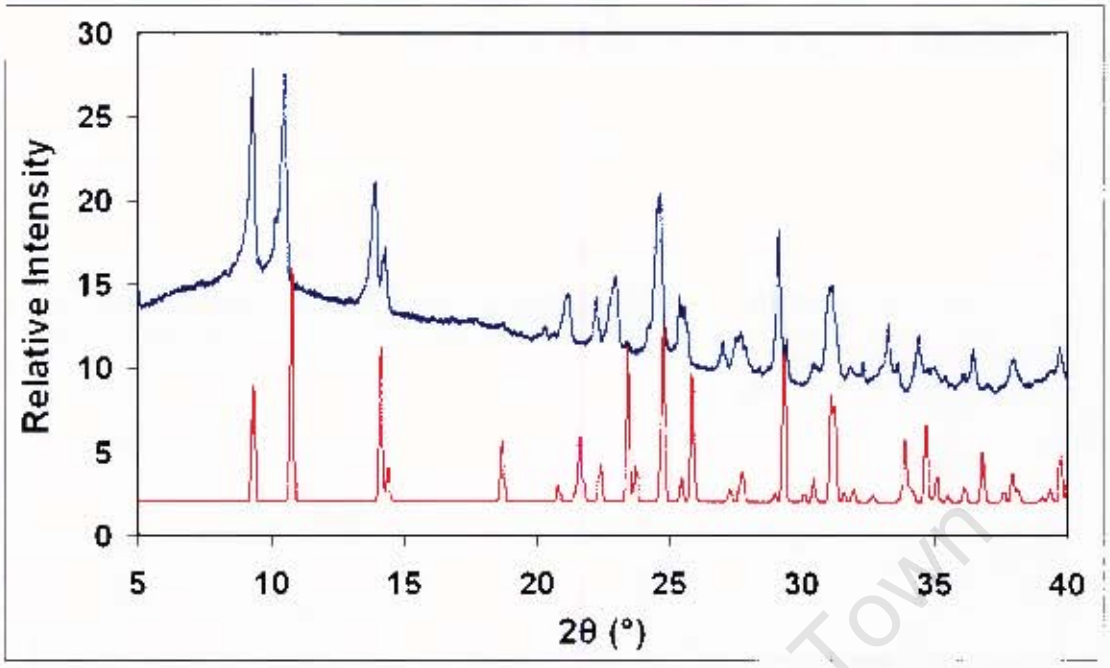

Figure 4.1(c): An overlay of **PbI** experimental and calculated PXRD patterns.

The PXRD patterns of **PbB** are a match as shown in Figure 6.5.

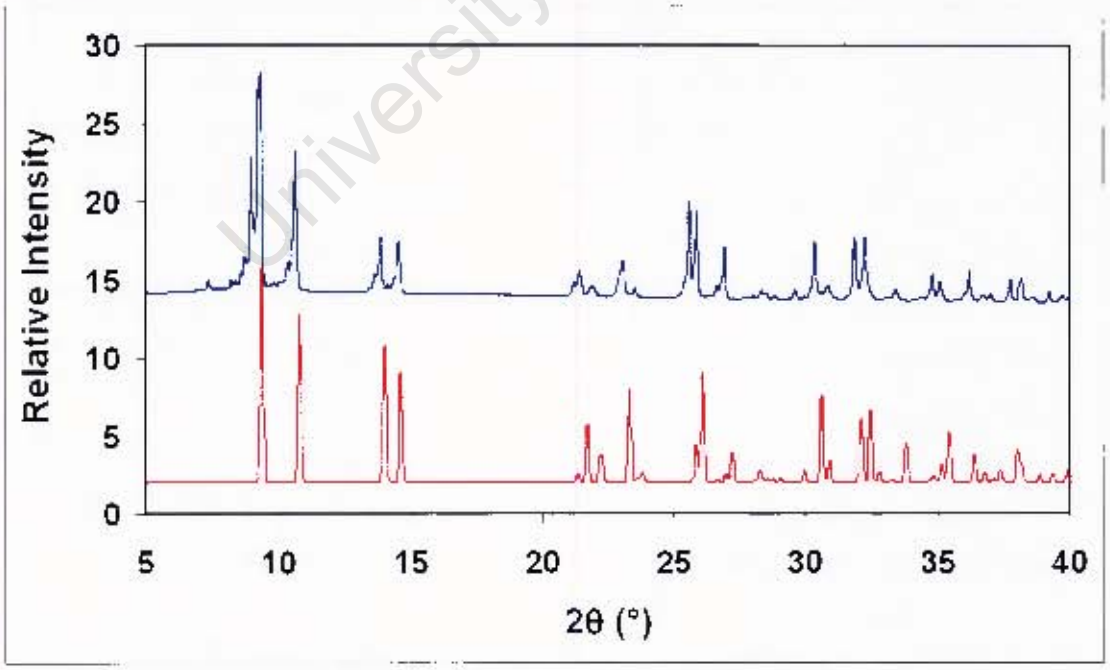

Figure 4.1(d): An overlay of **PbB** experimental and calculated PXRD patterns.

Structure solution and analysis

CuC

Table 4.2: Crystal Data and Refinement Parameters of **CuC**.

Molecular Formula	$Cu_2Cl_4(C_{10}H_6O_2N_2)_3(H_2O)_2 \cdot 2(CH_3)_2SO$
Formula weight ($g.mol^{-1}$)	1025.72
Temperature (K)	113
Wavelength (Å)	0.71073
Crystal System	Triclinic
Space Group	$P\bar{1}$
a (Å)	8.731 (2)
b (Å)	8.943 (2)
c (Å)	14.408 (3)
α (°)	102.85 (3)
β (°)	97.49 (3)
γ (°)	109.77 (3)
Volume ($Å^3$)	1005.9 (3)
Z	1
Calculated Density ($g.cm^{-3}$)	1.693
μ (mm^{-1})	1.491
F (000)	524
Crystal Size (mm)	0.15 x 0.15 x 0.20
θ Range Scanned (°)	0.21–26.37
Index Range	-11 < h < 11, -10 < k < 11, -18 < l < 18
No. Reflections Collected	29349
No. Unique Reflections	4211
Data completeness (%)	99.9
Refinement Method	Full-matrix L.S. on F^2
Data / Restraints / Parameters	4211 / 0 / 271
Goodness-of-fit on F^2	1.110
Final *R* Indices $[I>2\sigma(I)]$	0.0255, 0.0598
R Indices (all data)	0.0334, 0.0632
Largest Diff. Peak and Hole ($e.Å^{-3}$)	0.75, -1.07

The compound, **CuC**, could be solved in space group *P* $\bar{1}$ with two molecules in the unit cell. The thermal displacement and labeling of the asymmetric unit is shown in Figure 4.2. Only the asymmetric unit has been labeled.

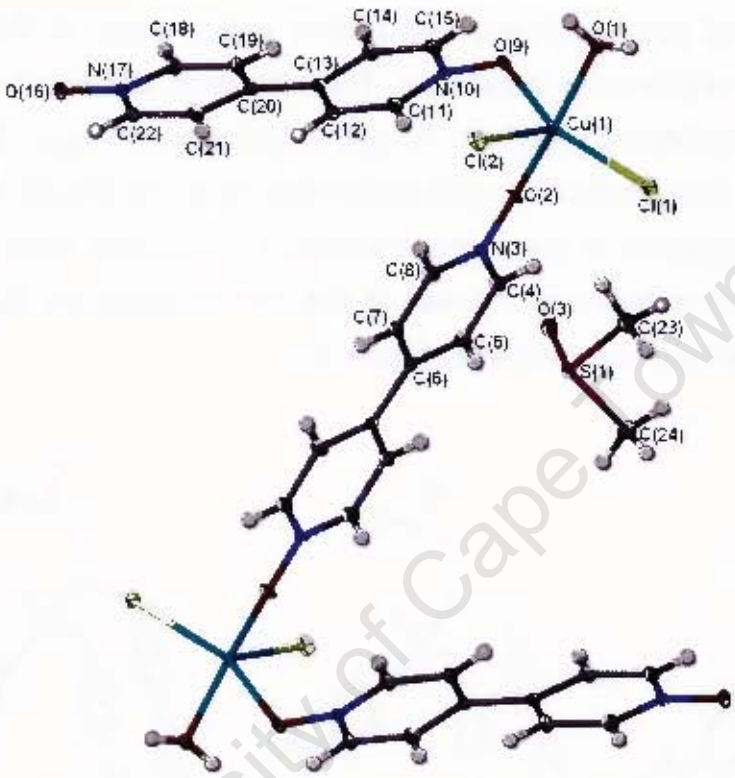

Figure 4.2: Part of the **CuC** molecule is showing atomic labeling. Thermal ellipsoid diagram is drawn at 50% probability.

This structure shows irregular trigonal bipyramidal coordination geometry. The literature[1] Cu–O and Cu–Cl bond lengths in the absence of distortion are 2.11 and 2.40 Å respectively on the bases of the ionic radii and they were comparable to experimental distances; 1.99 Å (Cu–O) and 2.41 Å (Cu–Cl), of the crystal structures obtained. The structure shows an enlarged Cl1–Cu–O9 bond angle of 148.88°, two inclined angles of 101.38° (Cl2–Cu–O9) and 109.42° (Cl1–Cu–Cl2), as opposed to the expected trigonal planar bond angles of 120° each. Similarly, the bond angles between the trigonal and bipyramidal planes were expected to be 90°, but due to the same distortion effect, the bond angles ranged from 79.93°–98.02°. The bpdo molecule is

planar but flexible, hence the two aromatic rings were twisted by 6.30 Å in **CuC**. Full bond lengths and angles are given in the Appendix.

The crystal structure shows a z-shaped molecule with two Cu metals joined by three bpdo molecules as shown in Figure. 3.68.
The compound packs with top and bottom bpdo "arms" of the z-shape in parallel with neighbouring molecules. The molecules are linked by hydrogen bonding of coordinated water and oxygen of bpdo ligand [$O_{aqua}\cdots O_{bpdo}$ = 2.717 Å], forming a supramolecular zigzag polymeric structure (Figure 4.3). There is a center of inversion at the centroid between the parallel arms. The DMSO guest molecule is hydrogen bonded to the host molecule by its oxygen and the coordinated water as shown in Figure 4.3.

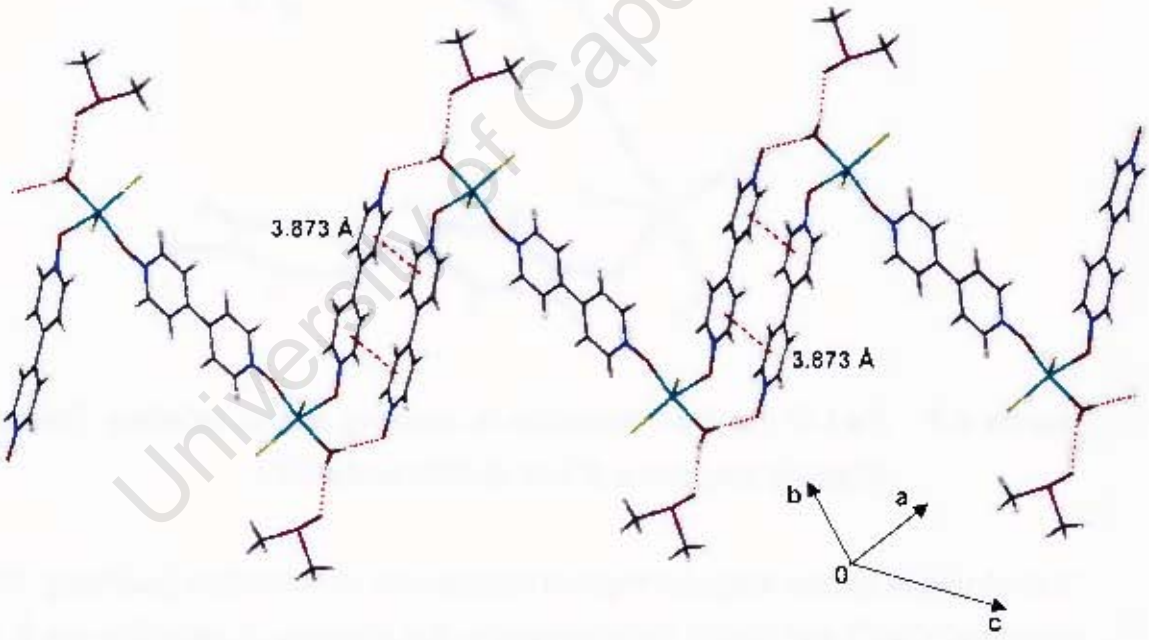

Figure 4.3: Hydrogen bonding and π-π interactions in **CuC** complex.

The packing of the molecules adopts a zigzag chain due to hydrogen bonding, with molecules almost superimposed to each other in a z-shape as shown by the schematic diagram in Figure 4.4. Detailed hydrogen bonding data is summarised in Table 4.3.

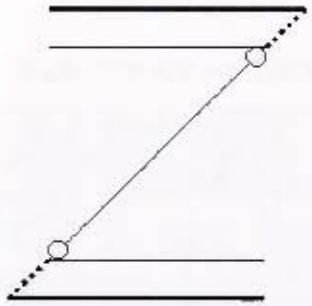

Figure 4.4: Schematic representation of the z-shaped molecules. Circles represent the copper metal. Less dense lines represent Z-shaped molecule where metal centres are joined by bpdo ligands. Dense lines showing molecule "arms" linked by hydrogen bonding (dashed lines) and bpdo ligands.

Table 4.3: Hydrogen bonding details in **CuC** crystal structure.

	D–H (Å)	D···A (Å)	D–H···A (°)	Symmetry operator
O(1)–H(1W)···O(16)	0.80	2.718 (2)	175	-1-x, -1-y, -z
O(1)–H(2W)···O(3)	0.77	2.704 (2)	165	x, 1+y, z
C(5)–H(5)···Cl(2)	0.95	3.402 (1)	141	-x, -y, 1-z
C(8)–H(8)···O(16)	0.95	2.959 (2)	134	-1-x, -2-y, -z
C(12)–H(12)···O(3)	0.95	3.443 (2)	154	-1+x, y, z
C(14)–H(14)···O(2)	0.95	3.474 (2)	156	-x, -1-y, -z
C(15)–H(15)···O(16)	0.95	3.221 (2)	170	1+x, 1+y, z
C(22)–H(22)···O(9)	0.95	3.170 (2)	164	-1+x, -1+y, z
C(23)–H(23B)···Cl(2)	0.98	3.666 (2)	147	1+x, y, z

The molecule is stabilised by a series of π···π stacking interactions (details summarised in Table 4.4) of bpdo rings as shown in Figure 4.3. There are also C–H···π interactions. Full bond lengths and angles are given in the Appendix. The crystal packing of the structure viewed along [010] is shown in Figure 4.5.

Table 4.4: π interactions in **CuC** crystal structure.

	Distance	Symmetry operator
*Cg(N10–C15)···Cg(N17–C22)	3.873 (1)	-1-x, -1-y, -z
Cg(N17–C22)···Cg(N10–C15)	3.873 (1)	-1-x, -1-y, -z
Cg(N17–C22)···Cg(N17–C22)	3.607 (1)	-1-x, -2-y, -z
C(21)–H(21)···Cg(N10–C15)	3.356	-1-x, -1-y, -z
C(24)–H(24A)···Cg(N3–C8))	2.881	1+x, y, z

*Cg = ring centroid

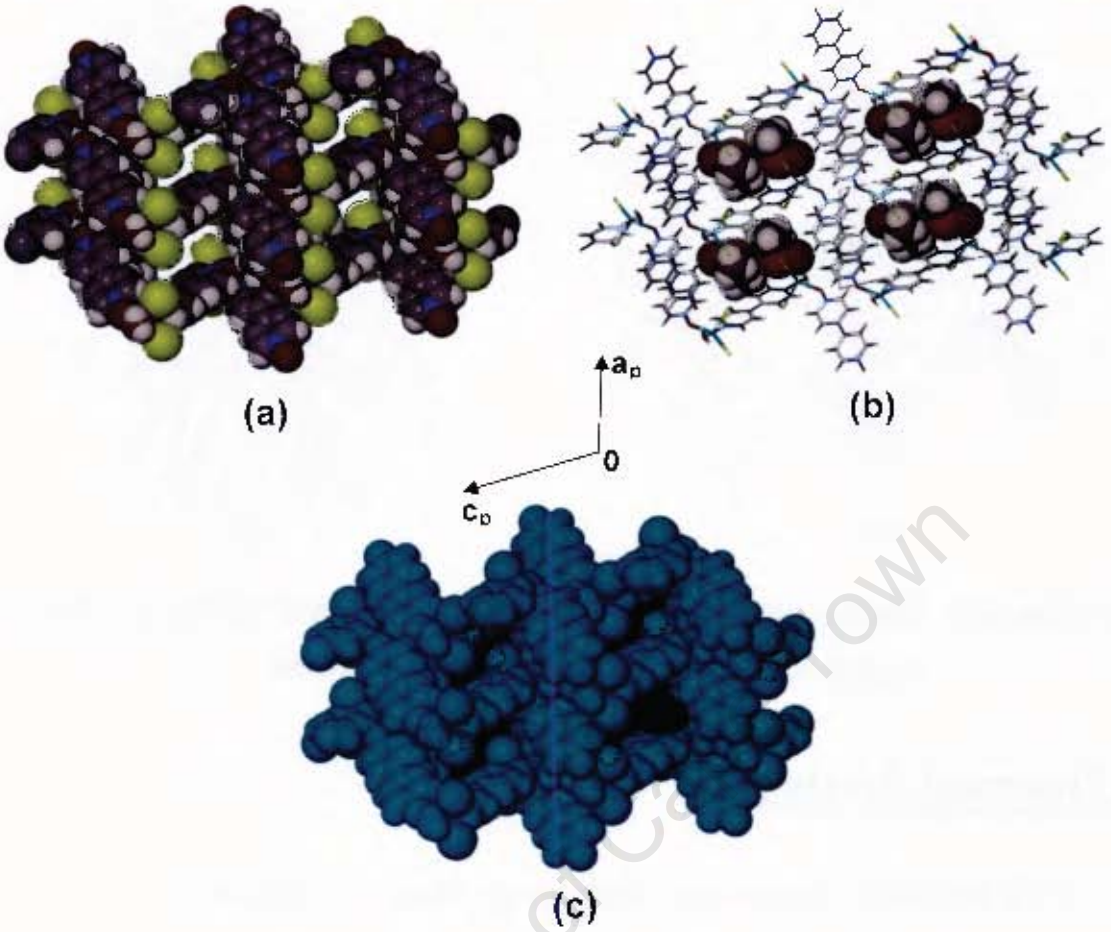

Figure 4.5: Crystal packing of **CuC** viewed along [010]. **(a)** shows an empty host lattice represented in van der Waals radii, **(b)** shows DMSO guest molecules (van der Waals radii) located in cavities of the host. (c) demonstrates how guest molecules reside in and are enclosed in the voids.

Viewing the compound packing along [100] shows the zigzag patterns, while the packing diagram along [001] illustrates the $\pi\cdots\pi$ stacks (Figure 4.6).

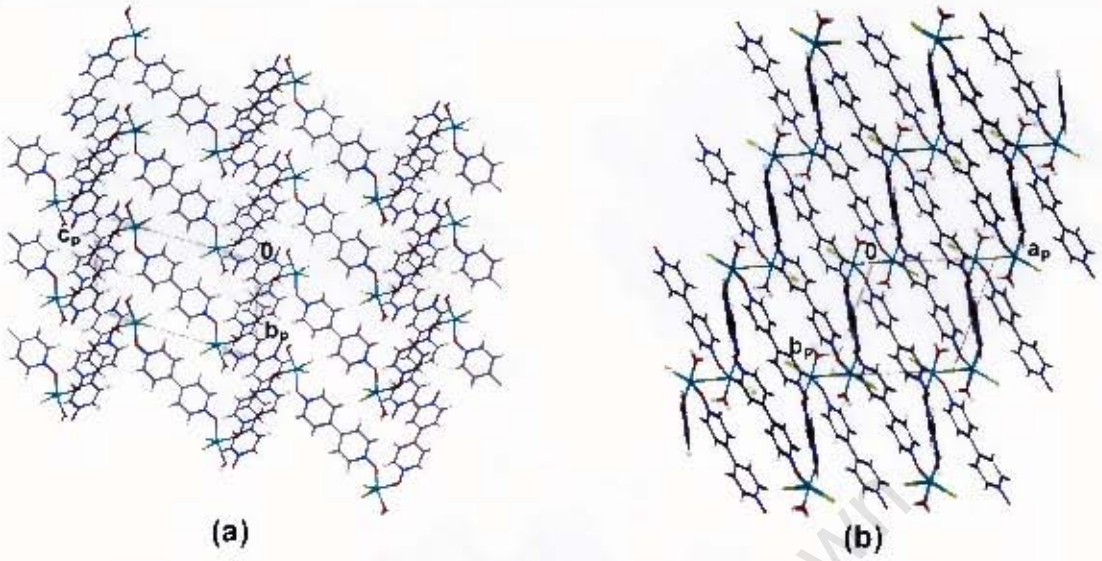

Figure 4.6: Packed diagrams viewed along [100] and [001]: (a) shows zigzag shapes while (b) illustrates $\pi\cdots\pi$ stacks.

Thermal Analysis

The TG and DSC traces of **CuC** complex are shown in Figure 4.7.

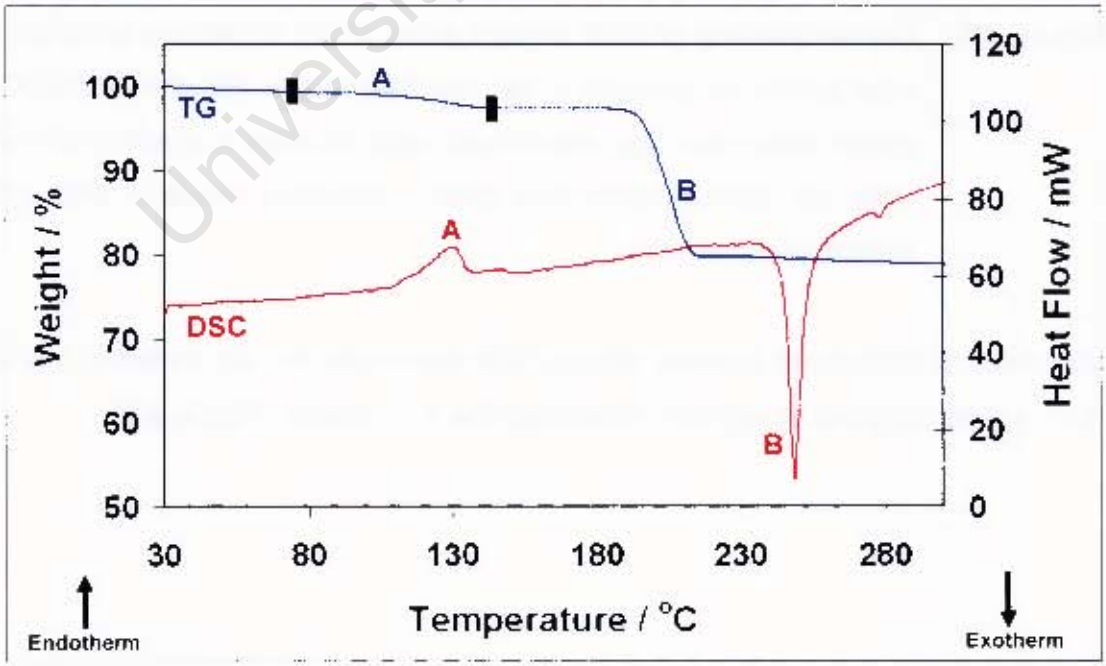

Figure 4.7: TG and DSC traces for **CuC** complex.

The TG trace shows a two step mass loss (region A and B). The first step mass loss in Figure 4.7 of **CuC** compound is attributed to loss of a coordinated water molecule. The experimental mass loss (region A; 2.35%) was accounted for only about 67% of the water molecule, as compared to the calculated value of 3.51%. The remaining percentage of coordinated water was released in the second step mass loss, which was essentially for the release of DMSO (details in Table 4.5). The two step mass losses in the TG trace correspond to endotherm A and exotherm B in the DSC trace. The TG and DSC results are summarised in the Table 4.5.

Table 4.5: Results on thermal analysis of **CuC**.

Guests	TG Results		DSC Results
	Calc. % mass loss	Exp. % mass loss	T_{on} (°C)
H_2O	3.51	2.35	**Peak A**; 110.9
DMSO	15.23	16.97	**Peak B**; 244.6

Hot Stage Microscopy

The crystal of Cu(II) complex was observed during thermal decay using the hot stage microscopy. The photographs for thermal events are shown in Figure 4.8.

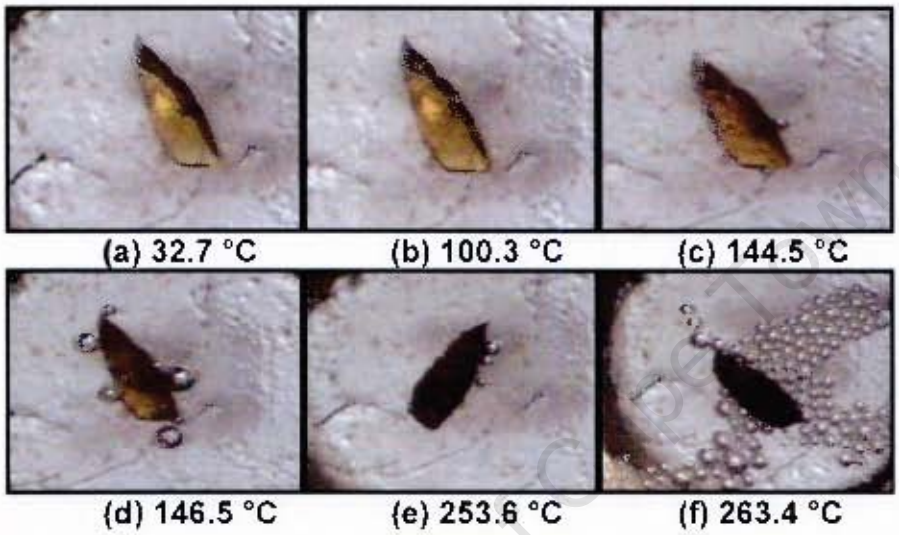

Figure 4.8: Thermal decay for **CuC** compound.

Photographs: **(a)** crystal at room temperature, **(b)** crystal retains its rigidity at the normal boiling point of water, owing to the strength of the coordination bond. **(c)** coordinated water molecule is released at 144.5 °C and this is further demonstrated by loss in color of a crystal **(d)**. **(e)** depicts loss of DMSO guest molecule and the bubbles are vigorous in **(f)** after which the crystal decompose.

PbC, PbI and PbB

Table 4.6: Crystal Data and Refinement Parameters for **PbC**, **PbI** and **PbB**.

Molecular Formula	$[PbCl_2(C_{10}H_8N_2O_2)]_n$	$[PbI_2(C_{10}H_8N_2O_2)]_n$	$[PbBr_2(C_{10}H_8N_2O_2)]_n$
Formula weight (g.mol^{-1})	466.27	649.17	555.19
Temperature (K)	113	113	173
Wavelength (Å)	0.71073	0.71073	0.71073
Crystal System	Monoclinic	Monoclinic	Monoclinic
Space Group	*C2/c*	*C2/c*	*C2/c*
a (Å)	16.327 (7)	16.438 (3)	16.403 (3)
b (Å)	4.071 (1)	4.538 (9)	4.2412 (8)
c (Å)	18.615 (8)	18.973 (4)	18.846 (4)
α (°)	90	90	90
β (°)	93.73 (1)	91.04 (3)	92.59 (3)
γ (°)	90	90	90
Volume (Å^3)	1234.60 (8)	1415.1 (5)	1309.7 (4)
Z	4	4	4
Calc. Density (g.cm^{-3})	2.509	3.047	2.816
μ (mm^{-1})	14.087	16.277	18.974
F (000)	856	1144	1000
Crystal Size (mm)	0.03 x 0.05 x 0.09	0.08 x 0.16 x 0.18	0.03 x 0.08 x 0.14
θ Range Scanned (°)	0.21 – 27.10	1.00 – 27.48	1.00 – 25.67
Index Range	-19 < h < 19, -4 < k < 4, -22 < l < 22	-21 < h < 21, -5 < k < 5, -24 < l < 24	-19 < h < 19, -4 < k < 5, -22 < l < 22
No. Reflections Collected	12454	9843	8122
No. Unique Reflections	1159	1603	1246
Data completeness (%)	99.8	99.6	99.9
Refinement Method	Full-matrix L.S. on F^2	Full-matrix L.S. on F^2	Full-matrix L.S. on F^2
Data / Restraints / Parameters	1159/ 0 / 79	1603 / 0 / 78	1246 / 0 / 79
Goodness-of-fit on F^2	1.062	1.066	1.066
Final *R* Indices $[I>2\sigma(I)]$	0.0252, 0.0545	0.0340, 0.0759	0.0348, 0.0774
R Indices (all data)	0.0379, 0.0593	0.0487, 0.0813	0.0490, 0.0827
Largest Diff. Peak and Hole (*e*.Å^{-3})	1.120, -1.086	1.511, -1.954	1.961, -1.558

PbC, **PbI** and **PbB** are isostructural, so their description will mainly be outlined with reference to **PbC**, but crystallographic interactions will be tabulated for all prepared crystal structures.

PbC crystallises in the monoclinic crystal system, *C2/c*, with four molecules in the unit cell. The ligand is situated on a centre of inversion, *-1*, at Wyckoff position *d* and the metal is on a diad at Wyckoff position *e*. The thermal displacement and atom labeling of the asymmetric unit is shown Figure 4.9. The four coordinated chloride ligands form the equatorial position while the bpdo is on the axial positions. Full bond lengths and angles for **PbC**, **PbI** and **PbB** are given in the Appendix.

Figure 4.9: Part of the polymeric chain structure of **PbC** is showing the atom labeling. Atoms of the asymmetric unit are labeled. Displacement ellipsoids are drawn at 50% probability.

The metal octahedral symmetry is almost perfect, with Pb–O and Pb–Cl distances of 2.496 to 2.897 Å respectively and Cl–Pb–Cl angles of the square planar were ranging from 89.64–90.75° while Cl–Pb–O ranges from 85.74–94.26°. Pb–Cl–Pb bond angles are 89.64°, 89.97° and 90.75°, resulting in symmetrical adjacent octahedra.

The coordinated chlorides function as bridging ligands between metals of adjacent chains forming an extended two dimensional sinusoidal shape coordination polymer (Figure 4.10). The polymer chains are joined by oxygens of bpdo ligand. There are no conventional hydrogen bonds in these crystal

structures. The chains are held by weak hydrogen bonding through (aromatic)C–H···O(bpdo) and (aromatic)C–H···Cl(ligand); Table 4.7.

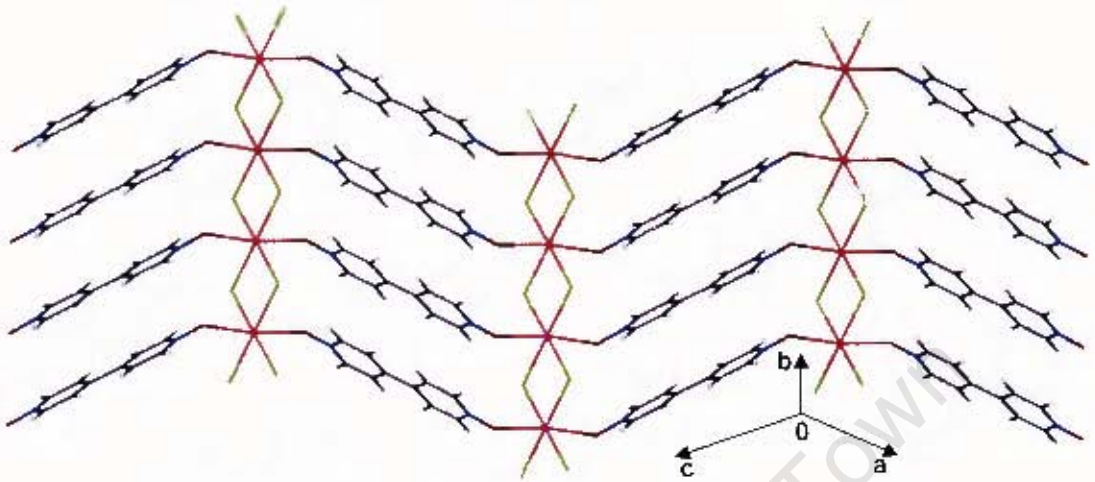

Figure 4.10: 2D coordination polymer showing sinusoidal shape. **PbC** compound is represented by sticks showing chloride ions bridging metal atoms.

The compound is a layered polymer, in which layers of metal centres are separated by organic layers as shown in Figure 4.11.

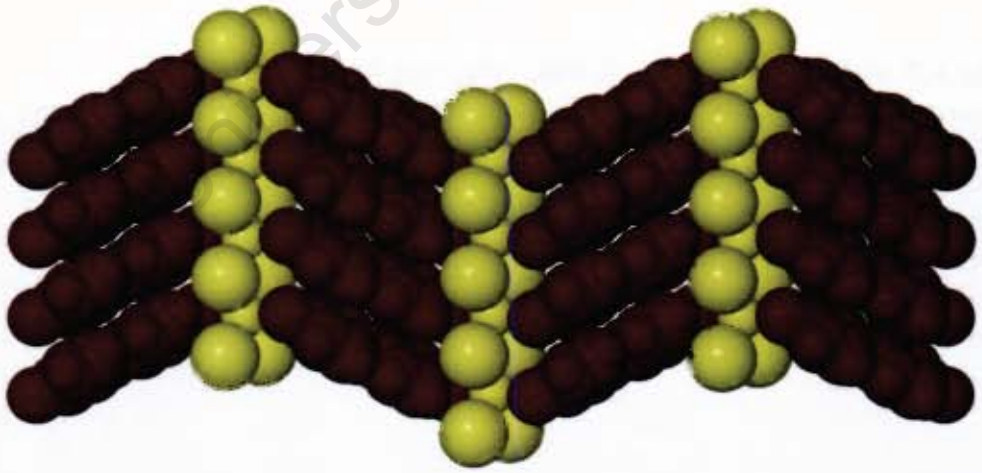

Figure 4.11: Layers formed by organic (maroon) and inorganic (yellow) components. Atoms are represented in van der Waals radii.

Figure 4.12 shows a packed diagram viewed along [010] showing 2D coordination polymer in **PbC**.

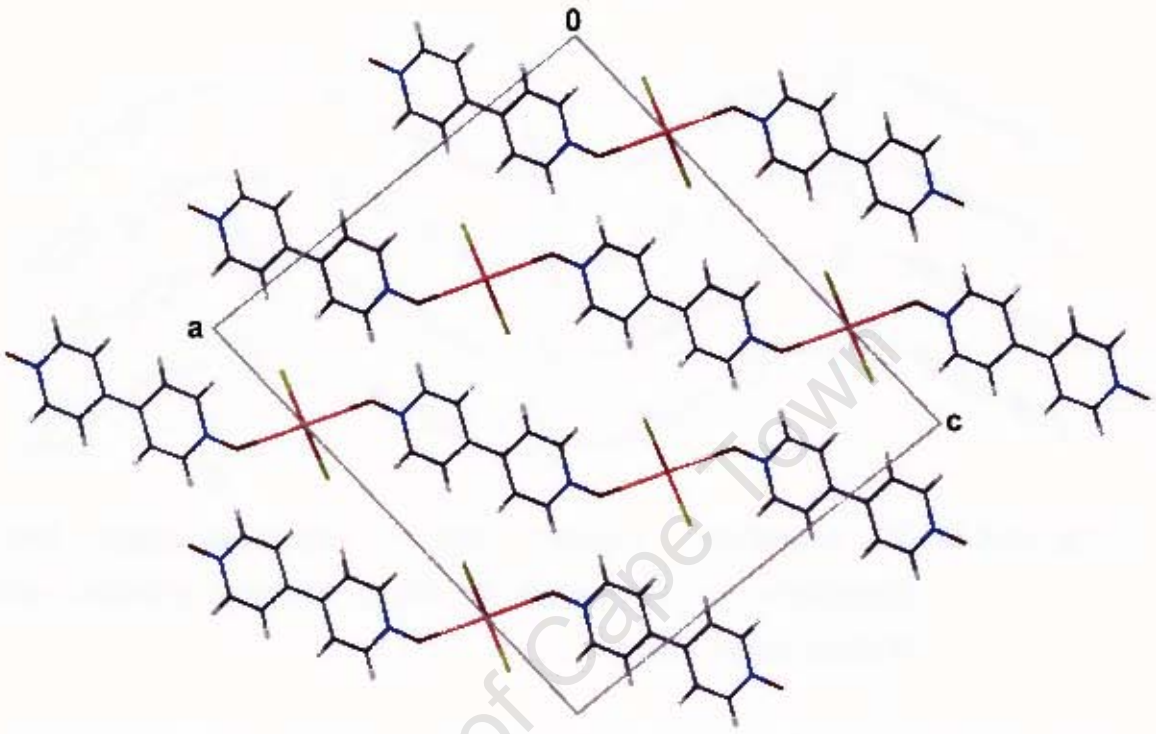

Figure 4.12: Packed **PbC** compound viewed along [010] showing the 2D coordination polymer.

Table 4.7: Hydrogen bonding in **PbC**, **PbI** and **PbB** polymers.

	D–H (Å)	D···A (Å)	D–H···A (°)	Symmetry operator
PbC				
C(3)–H(3)···O(1)	0.95	3.173 (9)	160	-½-x, -½+y, ½-z
C(6)–H(6)···Cl(1)	0.95	3.721 (7)	163	-x, -y, 1-z
PbI				
C(7)–H(7)···O(1)	0.95	3.236 (9)	158	½-x, -½+y, 3/2-z
C(4)–H(4)···I(1)	0.95	3.961 (8)	167	-x, -y, 1-z
PbB				
C(3)–H(3)···O(1)	0.95	3.210 (11)	162	½-x, -½+y, ½-z
C(6)–H(6)···Br(1)	0.95	3.832 (9)	168	1-x, -y, 1-z

PbC, **PbI** and **PbB** compounds are very flat polymers with short axes of 4.07 Å, 4.538 Å and 4.22 Å respectively and this can be seen when viewing the compounds along [001] as shown in Figure 4.13 for **PbC**.

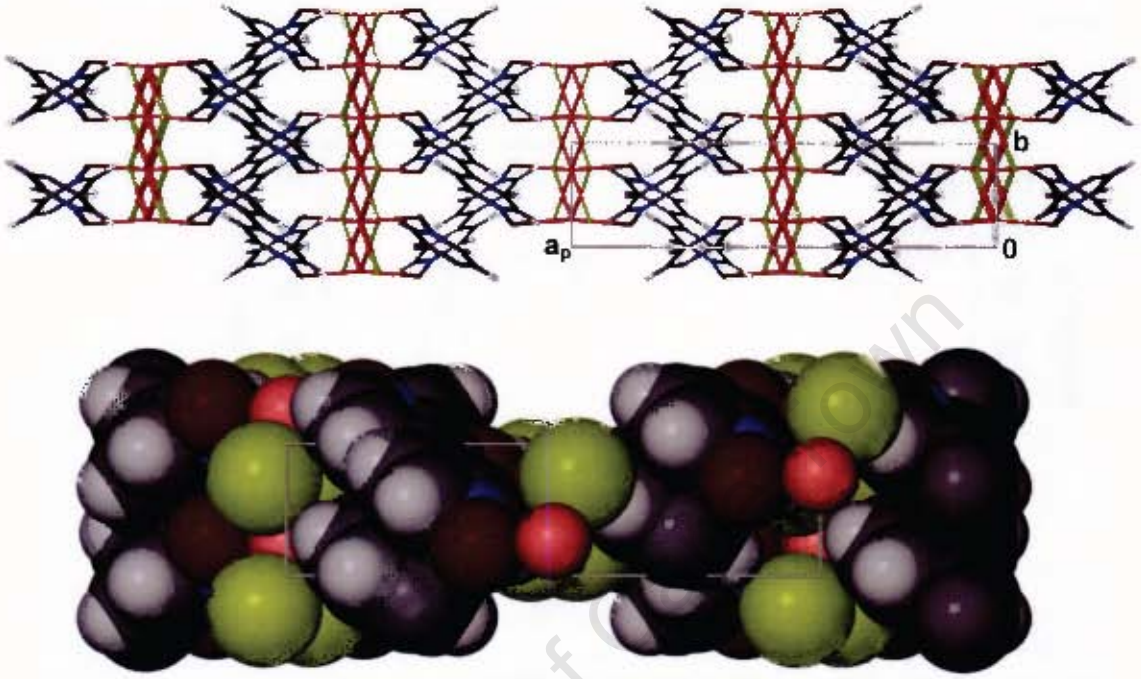

Figure 4.13: Packed molecule of compound **PbC** viewed along [001] represented by sticks and van der Waals radii.

Thermal Analysis

The TG and DSC traces of lead complexes are shown in Figure 4.14 (a) and (b). TG trace for **PbB** polymer is comparable to **PbC**, hence it is not shown here.

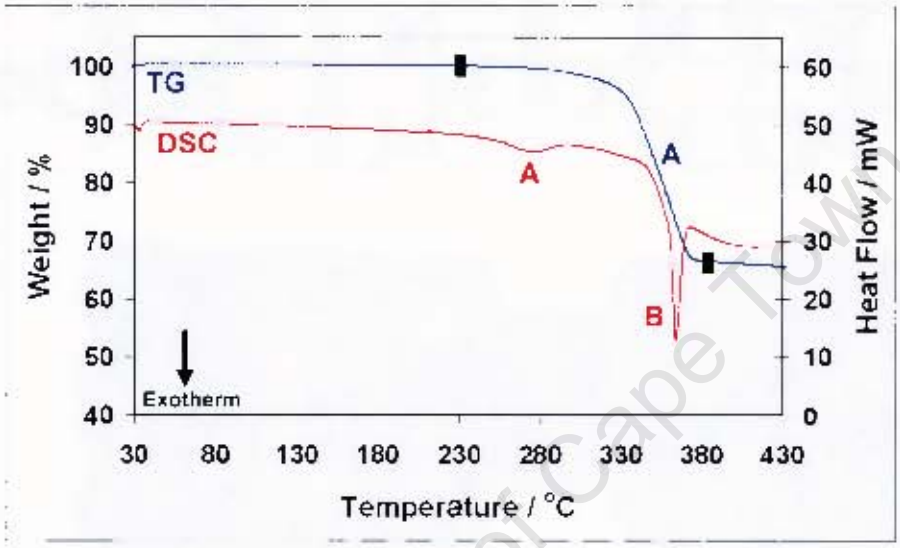

Figure 4.14(a): TG and DSC traces for **PbC**.

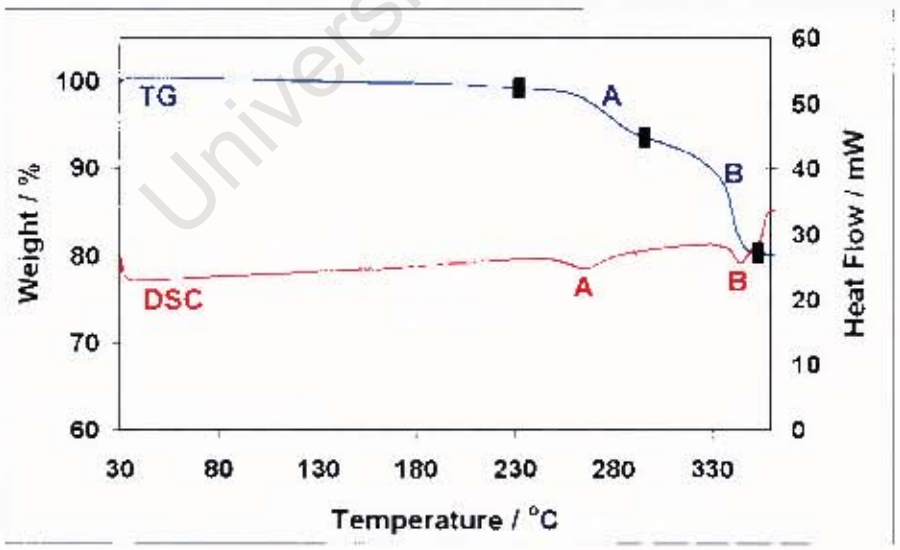

Figure 4.14(b): TG and DSC traces for **PbI**.

TG/DSC traces for **PbC**, **PbI** and **PbB** are stable up to >200 °C. The TG trace for **PbC** shows a one step mass loss (area A in Figure 4.14(a)) while **PbI** showed two step mass losses (area A and B in Figure 4.14(b)) which, in both

cases, represented decomposition of the polymers. The thermal events are further shown in Figure 4.15 (hot stage photographs).

The mass losses corresponded well to exotherms A and B in the DSC trace (Figure 4.14(a) and (b)) and their onset temperatures are given in Table 4.8.

Table 4.8: DSC results for **PbC**, **PbI** and **PbB**.

Coordination polymer	DSC Results	
	T_{on} (°C) Peak A	T_{on} (°C) Peak B
PbC	253.5	360.2
PbI	255.6	336.2
PbB	236.7	375.3

Hot Stage Microscopy

The thermal decomposition photographs of **PbC**, **PbI** and **PbB** polymers using the hot stage microscopy are shown in Figure 4.16(a-c).

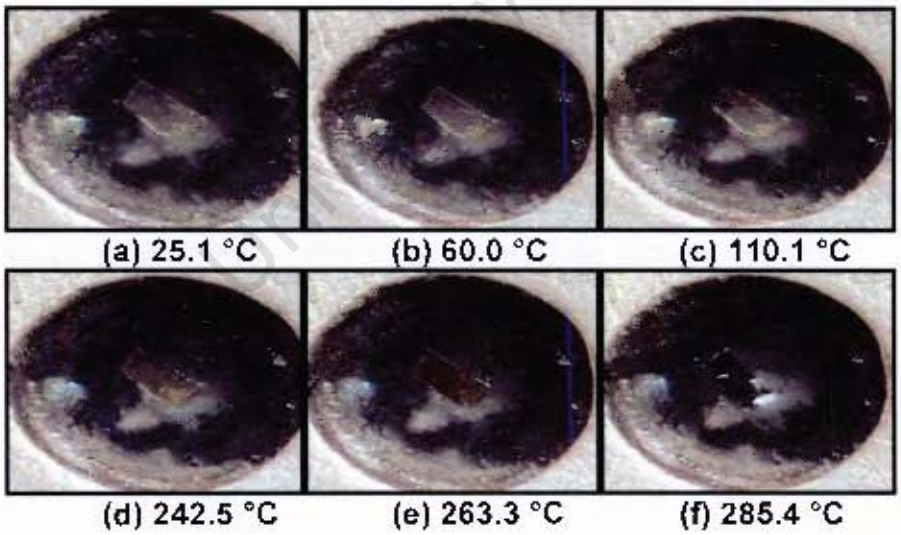

Figure 4.15(a): Thermal decomposition of **PbC**. **(a)** room temperature, **(b)** and **(c)** demonstrated that a crystal is still maintaining its quality and crystallinity, **(d)** and **(e)** a crystal losing its color to black depicting the start of the decomposition while **(f)** is a melt showing decomposition.

(a) 25.9 °C (b) 273.2 °C (c) 295.5 °C

Figure 4.15(b): Thermal decay of **PbI**. **(a)** room temperature, **(b)** crystal losing its color to brown showing decomposition of the compound. **(c)** shows complete decomposition.

(a) 30.5 (b) 110.8 (c) 235.4

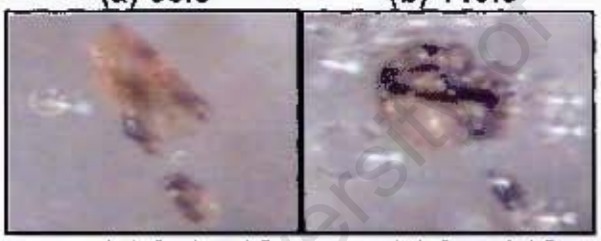

(d) 356.5 °C (e) 395.1 °C

Figure 4.15(c): Thermal decomposition of **PbB**. **(a)** room temperature, **(b)** the crystal still stable, **(c)** crystal losing some bpdo which continues until the crystal lost color **(d)** showing the start of decomposition, **(e)** is a melt showing complete decomposition.

Isostructurallity

PbC, **PbI** and **PbB** are isostructural with respect to their similar molecular shape, unit cell parameters and atomic coordinates as shown in Table 4.6. The thermal ellipsoids and atom labeling of **PbI** and **PbB** are shown in Figure 4.16(i) and (ii) respectively. A summary of hydrogen bonding interactions is shown in Table 4.7.

Figure 4.17 shows packed molecules of **PbI** and **PbB** polymers viewed along [010], showing packing similarities of all the Pb(II) compounds prepared in this study.

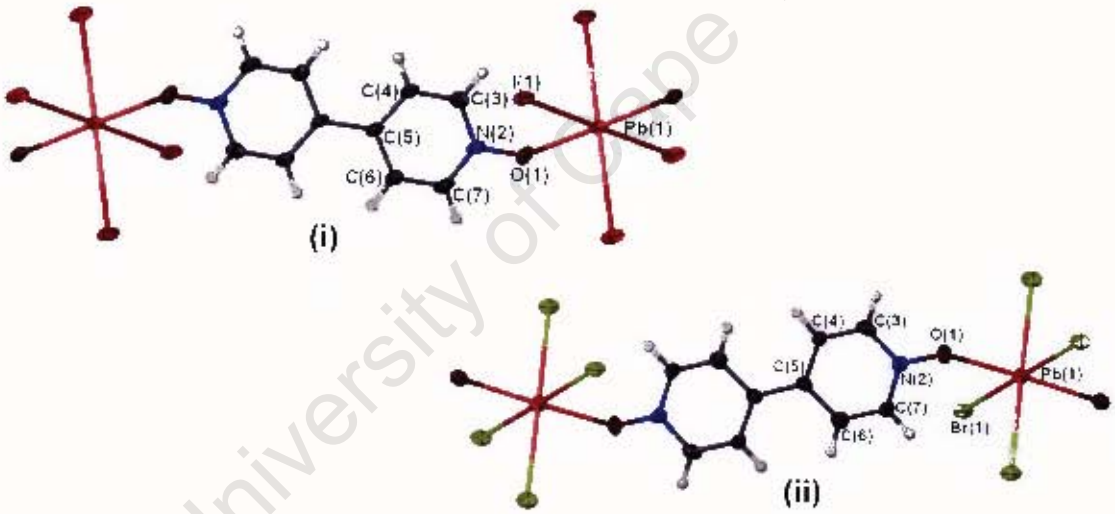

Figure 4.16: Part of the 2D coordination polymer structure of **(i) PbI** and **(ii) PbB** are showing the atom labeling. Atoms of the asymmetric unit are labeled and the thermal ellipsoids are drawn at 50% probability.

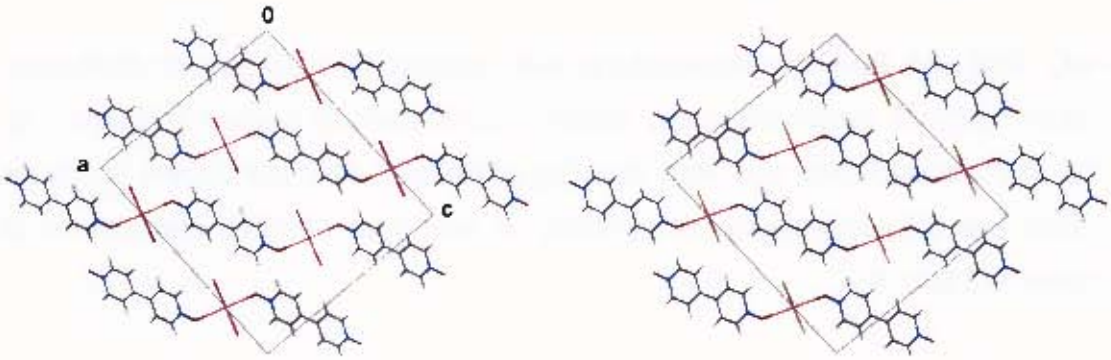

Figure 4.17: Packing diagrams of **PbI** and **PbB** respectively viewed along [010], showing isostructurality in these polymers.

Discussion and conclusion

Compounds of Cu(II) and Pb(II) were studied and their crystal structures have been refined and elucidated. The compounds obtained from these two metal salts were prepared by using the same synthetic route, but afforded crystal structures of different topologies. The compounds were either supramolecular 1D (**CuC**) or coordination 2D polymers (**PbC**, **PbI** and **PbB**). Thermal analysis of these compounds was carried out to determine their thermal stability and decomposition profiles.

CuC is a z-shaped molecule with metal centres linked by a bpdo ligand. The molecule showed an irregular trigonal bipyramidal coordination geometry. Discrete molecules are connected through hydrogen bonding via coordinated water molecule and oxygens of the bpdo ligand forming a supramolecular chain. This chain is also held by π interactions making the compound fairly rigid .

In our experience, knowledge and CSD[2] (Version 5.27, November 2005) search, this trigonal bipyramidal coordination geometry shown by **CuC** is rare when using bpdo as a bridging ligand making this compound to be the first of its kind. Two compounds with a coordination number of five have been previously reported.[3,4] These compounds are ([Cu(bpdo)$_2${N(CN)$_2$}$_2$(H2O)] and [{L((μ-OH)Cu$_2$}(bpdo) {Cu$_2$(μ-OH)L}(ClO$_4$)$_4$·1.33H$_2$O), where L=2.6-bis[*N*-(2-pyridylethyl)formimidoyl] -4-methyl-phenolato. Both adopted for a square pyramidal coordination geometry than the trigonal bipyramidal observed in the **CuC** complex reported in this study.

The most common reported coordination geometry for copper complexes with bpdo is an octahedron.[5,6] Crystallisation of bpdo and $CuCl_2$ or $CuClO_4$ in aqueous solutions produced [Cu(H$_2$O)$_6$]Cl$_2$ · 2bpdo · 2H$_2$O, [Cu(bpdo)$_6$][ClO$_4$], [Cu$_3$(bpdo)$_8$(H$_2$O)$_8$][ClO$_4$]$_8$ · 2bpdo·6H$_2$O, [Cu(bpdo)(H$_2$O)$_4$][ClO$_4$]$_2$·2bpdo and [Cu(bpdo)(L)][ClO$_4$]$_2$ · 2H$_2$O · bpdo, L=*4,4'*-bipyridine. The latter compound is a 2D coordination polymer which accomodated bpdo and ClO_4 into its

channels while the rest are discrete molecules governed mainly by hydrogen bonding and π interactions.

In addition to the coordination entities, Tian *et al.*[7] reported a rare square planar copper complex ($[Cu_2(L)_2][bpdo]$, L=3,5-pyrazoledicarboxylic acid). Each Cu^{II} charge in the $[Cu_2(L)_2]$ unit is balanced by two coordinated L^{2-} ligands in chelating fashion through the carboxylic oxygens as well as adjacent nitrogen atoms. Hydrogen bonding via bpdo and carbonyl oxygen atom joins adjacent molecules giving rise to two dimensional structure.

PbC, **PbI** and **PbB** coordination polymers are isostructural. These compounds are 2D polymers with two bpdo ligands occupying the axial positions and four halide ligands (Br^-, Cl^- or I^-) on the equatorial positions completing an octahedral coordination symmetry. The adjacent polymer chains are bridged by halide ligands forming a 2D sinusoidal shapes. There are no conventional hydrogen bonding in these coordination polymers. These polymers are stable up to >200 °C as was confirmed by thermal analysis.

To the best of our knowledge and the CSD[3], no Pb(II) crystal structures using bpdo have been reported so far. An analogues dipyridyl ligand, bpy (*4,4*-bipyridine), formed $[PbBr_2(bpy)]_n$ coordination polymer[8] which is related to the Pb(II) coordination polymers reported in this study. This polymer was prepared using the hydrothermal (393 K) reaction of $Pb(O_2CCH_3)$, NaBr and bpy. The 2D layers are formed by connecting metal centres through bridging Br and bpy ligands. Nordell *et al.*[9] later reported $[PbCl_2(bpy)]_n$ coordination polymer prepared hydrothermally at 403 K. The compound; $[(PbBr_2)_2(pyz)]_n$, was prepared by layering an aqueous methanolic solution of pyz on top of aqueous HBr solution of $PbBr_2$.[10]

The selection of DMSO as a solvent allowed the preparation of crystal structures of thel form of **PbC** ambient temperature (295 K – 298 K). Our attempts to prepare polymers via solvent layering of alcoholic bpdo solution and chlorinated solvents have to date been unsuccessful. It is evident from literature and CSD[2] search that irrespective of the synthetic route and/or

solvents applied in crystallisation of $PbBr_2$, $PbCl_2$ and PbI_2 complexes with either bpdo, bpy or pyrazine[10] (pyz), the product crystal structure obtained is a typical 2D coordination polymer bridged by halides.

References

1. F.H. Allen, O. Kennard, D.G. Watson, L. Brammer, A.G. Orpen, R. Taylor, *J. Chem. Soc. Perkin Trans.*, 1989, S1-S83.
2. F.H. Allen, *Acta Crystallogr.*, 2002, **B58**, 380.
3. A. Nedelcu, Z. Zak, a.M. Madalan, J. Pinkas, M. Andruh, *Polyhedron*, 2003, **22**, 789.
4. D. Visinescu, G. I. Pascu, M. Andruh, J. Magull, H. Roesky, *Inorg. Chim. Acta*, 2002, **340**, 201.
5. B.Q. Ma, H-L. Sun, S. Gao, *Inorg. Chem.* 2005, **44**, 837.
6. B.Q. Ma, S. Gao, H-L. Sun, G-X. Xu, *J. Chem. Soc., Dalton Trans.* 2001, 130.
7. J-L. Tian, S-P. Yan, D-Z. Liao, Z-H. Jiang, P. Cheng, *Inorg. Chim. Acta*, 2003, **6**, 1025.
8. Y. Cui, J. Ren, G. Chen, W. Yu, Y. Qian, *Acta Crystallogr.*, 2000, **C56**, e552.
9. K.J. Nordell, K.N. Schultz, K.A. Higgins, M.D. Smith. *Polyhedron*, 2004, **23**, 2161.
10. Y-J. Shi, X-T. Chen, C-X. Cai, Y-Z. Zhang, Z. Xue, X-Z. You, S-M. Peng, G.H. Lee, *Inorg. Chem. Commun.*, 2002, **5**, 621.

Chapter 5

Constructing Zn(II) complexes of bpdo by means of solvent evaporation and layering.

Crystallisation of $ZnBr_2$ and bpdo by slow evaporation and solvent layering methods afforded three different crystal structures, a 2D coordination polymer and two discrete molecules. The polymer obtained had a double strand polymer chain through coordinated bpdo ligands and no conventional hydrogen bonds. The discrete molecules had two independent Zn(II) atoms with different coordination geometries (octahedral and tetrahedral). The discrete molecules in both complexes are joined through hydrogen bonding of coordinated waters, bpdo ligands and guest water molecules. Replacement of bromide with thiocynate afforded a zigzag chain with adjacent chains linked through hydrogen bonding.

The complexes were characterised by thermal analysis, microanalysis and elucidated by single x-ray diffractometry.

Crystallographic data, experimental and refinement parameters are given in Table 5.2, 5.6, 5.10 and 5.13. Final atomic coordinates, bond lengths and angles, torsion angles, thermal parameters and tables of observed and calculated structure factors for each of the crystal structure are given in the appendices.

Preparation of complexes

Suitable crystals for data collection were obtained by slow evaporation and solvent layering at ambient temperatures over a period of a week using methods discussed in Chapter 2. These complexes were crystallised using alcoholic solvents for discrete molecules ($[Zn_3Br_6(bpdo)_4(H_2O)_2] \cdot (bpdo)$ and $[ZnBr_4][\ Zn(H_2O)_5(bpdo)] \cdot 2(bpdo) \cdot (H_2O)$) and layering of alcoholic solutions on top of chlorinated solvents for the coordination polymer ($Zn_2Br_4(bpdo)_2$ and $[Zn(NCS)_2(bpdo)(H_2O)_2]_n \cdot H_2O$).

The compounds obtained as well as their abbreviations are as follows:

$Zn_2Br_4(bpdo)_2$:	**ZnB1**
$[Zn_3Br_6(bpdo)_4(H_2O)_2] \cdot (bpdo)$:	**ZnB2**
$[ZnBr_4][\ Zn(H_2O)_5(bpdo)] \cdot 2(bpdo) \cdot (H_2O)$:	**ZnB3**
$[Zn(NCS)_2(bpdo)(H_2O)_2]_n \cdot H_2O$:	**ZnN**

Microanalysis

Elemental analysis results are given in Table 5.1 and they corresponded well with the calculated elemental mass percentages. Elemental composition analysis for **ZnB1** and **ZnN** were not done. **ZnB1** was unstable to atmospheric conditions and lost solvent when removed from the mother liquor, while **ZnN** was very hygroscopic making preparatory measures for microanalysis impossible. **ZnB2** and **ZnB3** were very stable and their elemental analysis is given in Table 5.1.

Table 5.1: Elemental analysis results for **ZnB2**.

Element	ZnB2		ZnB3	
	Found %	Calc. %	Found %	Calc. %
C	36.62	36.34	32.39	32.09
H	2.67	2.68	2.90	3.23
N	8.39	8.48	6.99	7.48

PXRD

The calculated (red) and experimental (blue) PXRD patterns for **ZnB1**, **ZnB2** and **ZnB3** are shown in Figures 5.1 – 5.3. Experimental PXRD analysis for **ZnN** was not done due to insufficient sample being available. Only the calculated PXRD of this compound is shown In Figure 5.4.

The patterns for **ZnB1** do not match well. This could be due to a mixture of compounds or phases in the bulk material or the loss of some solvent in the compound as discussed later in this study.

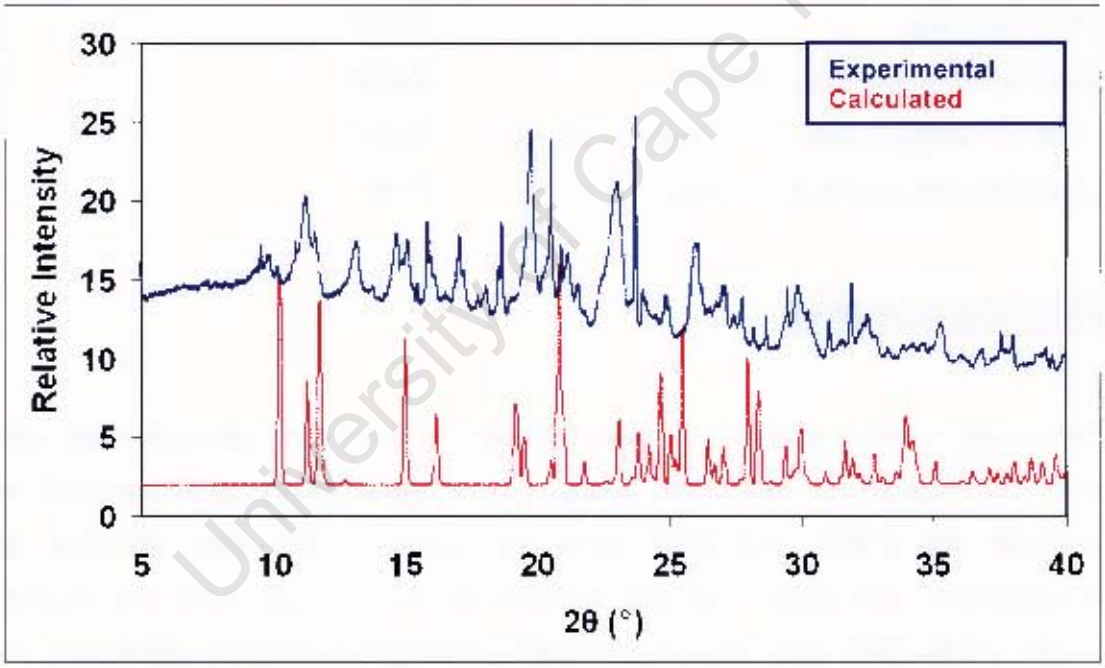

Figure 5.1: PXRD patterns for **ZnB1** compound.

The general PXRD pattern for **ZnB2** is a match confirming that the prepared sample was homogenous (Figure 5.2).

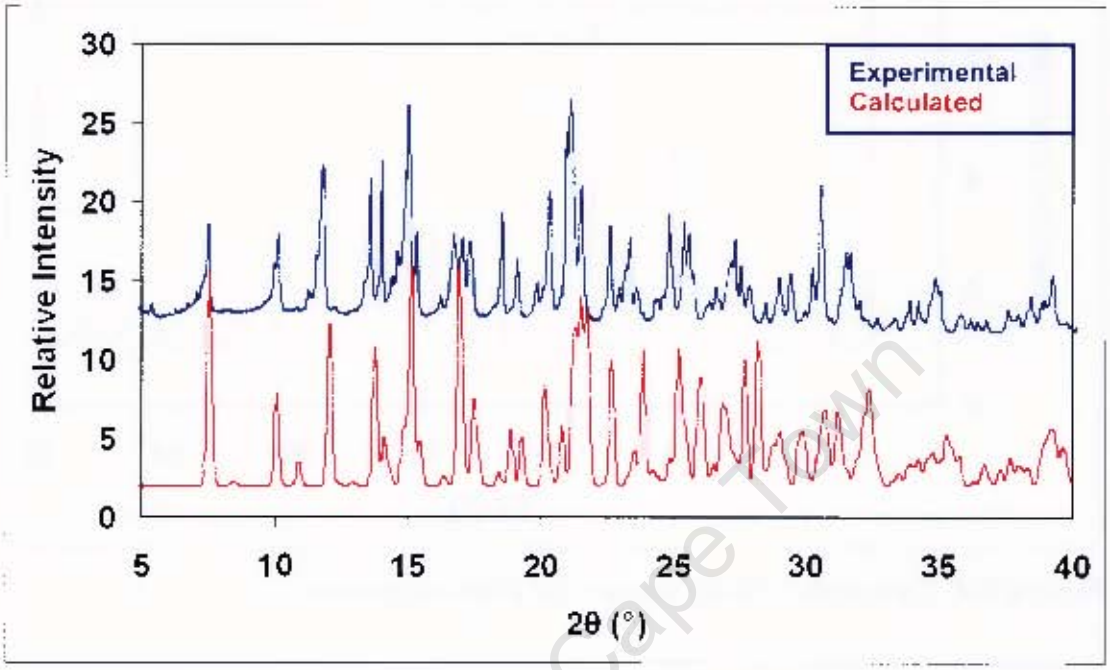

Figure 5.2: PXRD patterns of **ZnB2** compound.

The general PXRD pattern for **ZnB3** matches the calculated pattern.

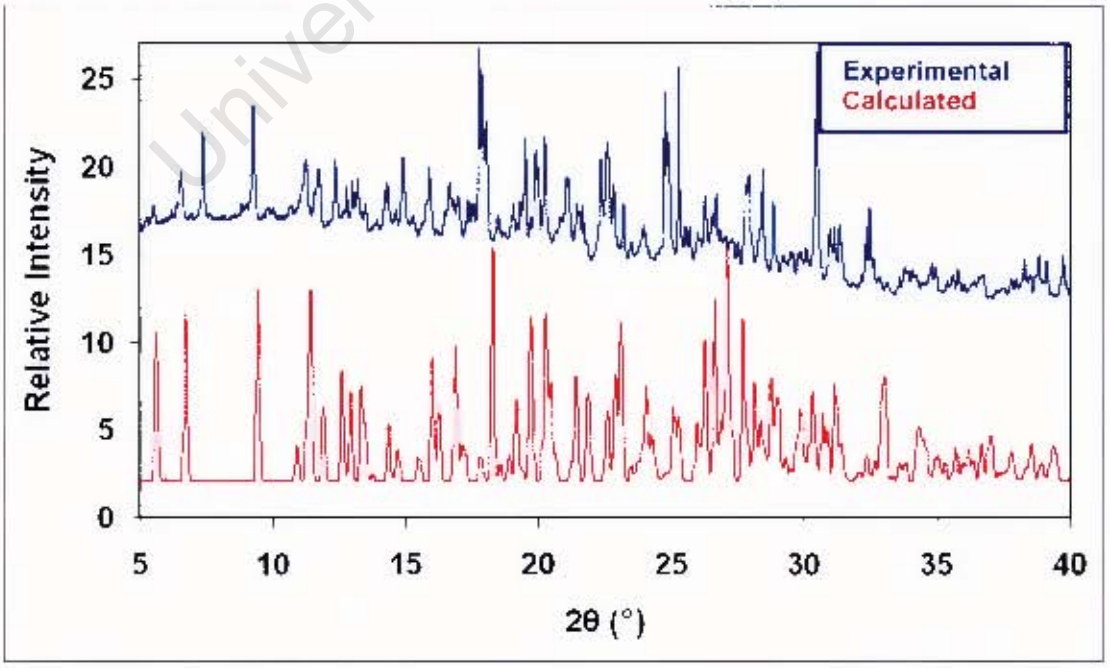

Figure 5.3: Calculated PXRD pattern for **ZnB3** compound.

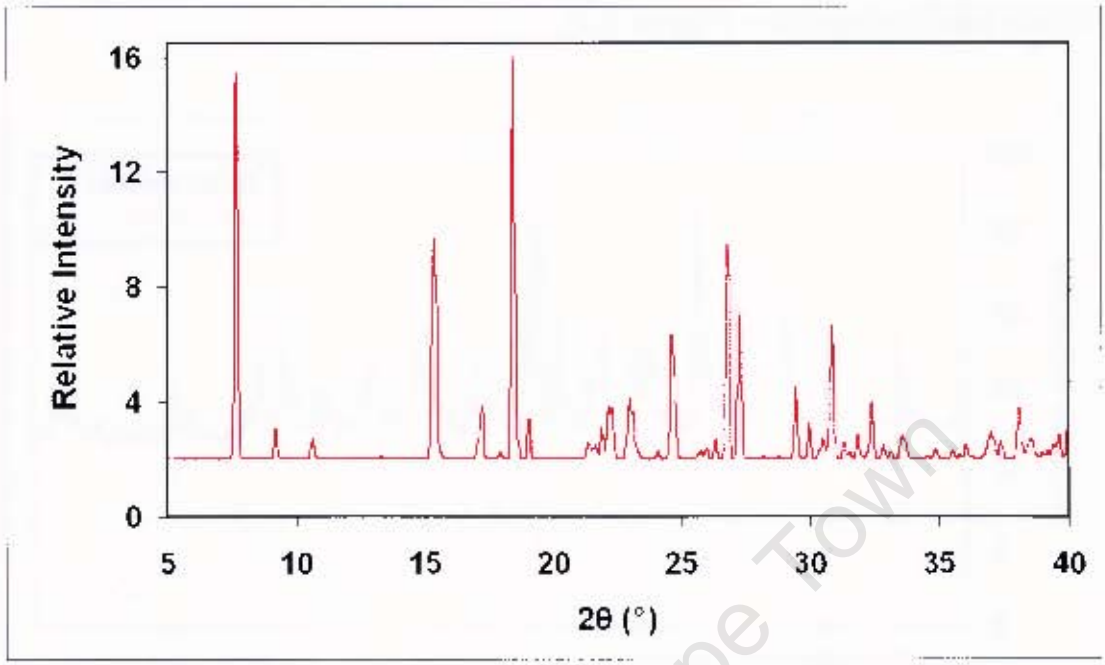

Figure 5.4: Calculated PXRD pattern for **ZnN** compound.

Structure solution and analysis

ZnB1

Table 5.2: Crystal Data and Refinement Parameters of **ZnB1**.

Molecular Formula	$Zn_2Br_4(C_{10}H_8N_2O_2)_2$
Formula weight (g.mol^{-1})	826.74
Temperature (K)	113
Wavelength (Å)	0.71073
Crystal System	Triclinic
Space Group	$P\bar{1}$
a (Å)	8.2359 (2)
b (Å)	9.3216 (2)
c (Å)	9.4713 (3)
α (°)	66.6032 (11)
β (°)	84.5784 (12)
γ (°)	66.6732 (15)
Volume (Å^3)	611.09 (3)
Z	1
Calc. Density (g.cm^{-3})	2.247
μ (mm^{-1})	8.537
F (000)	396
Crystal Size (mm)	0.15 x 0.1 x 0.05
θ Range Scanned (°)	1.02 – 27.88
Index Range	-10 < h < 10, -12 < k < 12, -12 < l < 12
No. ref. Collected	16797
No. Unique Reflections	2917
Data completeness (%)	100.0
Refinement Method	Full-matrix L.S. on F^2
Data / Restraints / Parameters	2917 / 0 / 155
Goodness-of-fit on F^2	1.037
Final R Indices [$I>2\sigma(I)$]	0.026, 0.0502
R Indices (all data)	0.0428, 0.0541
Largest Diff. Peak and Hole (e.Å^{-3})	0.71, -0.56

ZnB1 compound crystallises in the triclinic crystal system in the space group $P\bar{1}$ with two molecules in the unit cell. The thermal ellipsoids of this compound and atom labelling are illustrated in Figure 5.3.

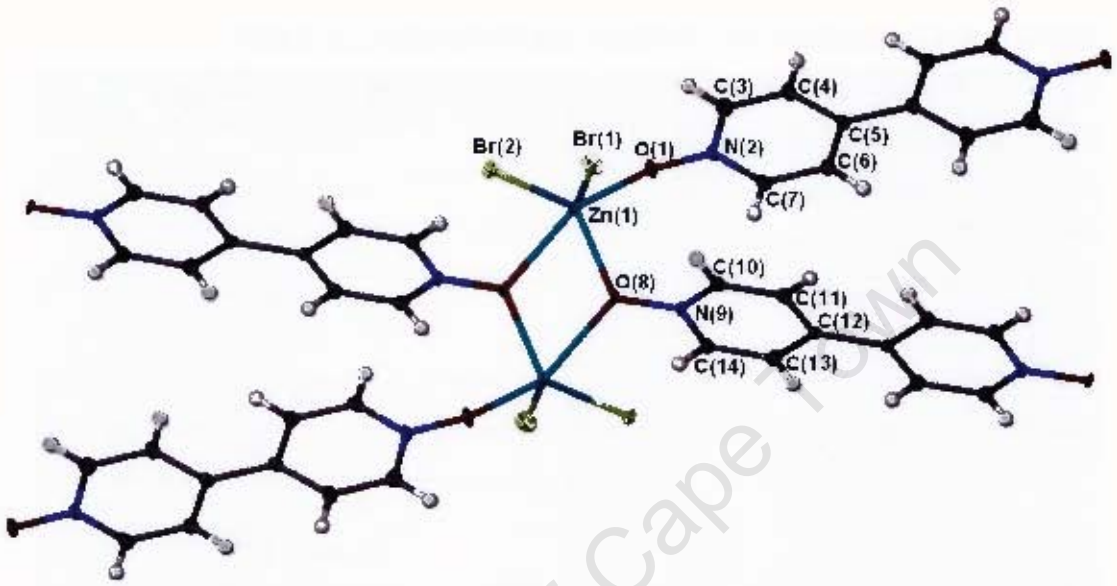

Figure 5.3: Part of the polymeric double-strand chain structure of **ZnB1** showing the atom labeling. Displacement ellipsoids are drawn at 50% probability. Atoms of the asymmetric unit are labeled.

The crystal structure shows Zn(II) metal centres with irregular trigonal bipyramidal coordination geometry. The Zn–Br(1) and Zn–Br(2) bond lengths are 2.382 and 2.373 Å, respectively. These values corresponded well with the range literature value[7] of 2.390 Å. The Zn–O_{npdo} bond lengths have a range from 2.039–2.353 Å. The maximum bond length value (2.353 Å, Zn–O_{npdo}) determined deviated slightly from the average literature value of 2.076 Å. The distortion effects caused the structure angles to either decline or enlarge from the expected 90° (bipyramidal plane) and 120° (trigonal plane). The bond angles determined for trigonal plane; Br(1)–Zn–Br(2), Br(1)–Zn–O(8) and Br(2)–Zn–O(8) are 122.68°, 111.81° and 121.3° respectively, while the bipyramidal bond angles ranged from 67.34°–106.66°. Full bond lengths and angles are given in the Appendix.

In **ZnB1** , individual metal centres are connected by bpdo ligands to form zig-zag chains as shown in Figure 5.4.

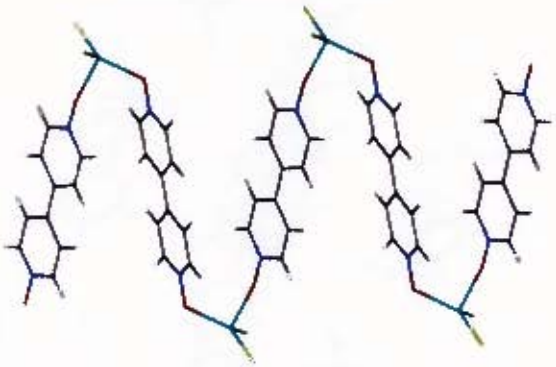

Figure 5.4: Zig-zag chains showing the linkages between zinc centres.

These chains then form 2D coordination polymer chains shown in Figure 5.5. The bridged zinc metals are separated from each other by a distance of 3.659 Å and the bridging O–O terminals are 2.449 Å apart. The bridging angle Zn–O–Zn is 112.66°.

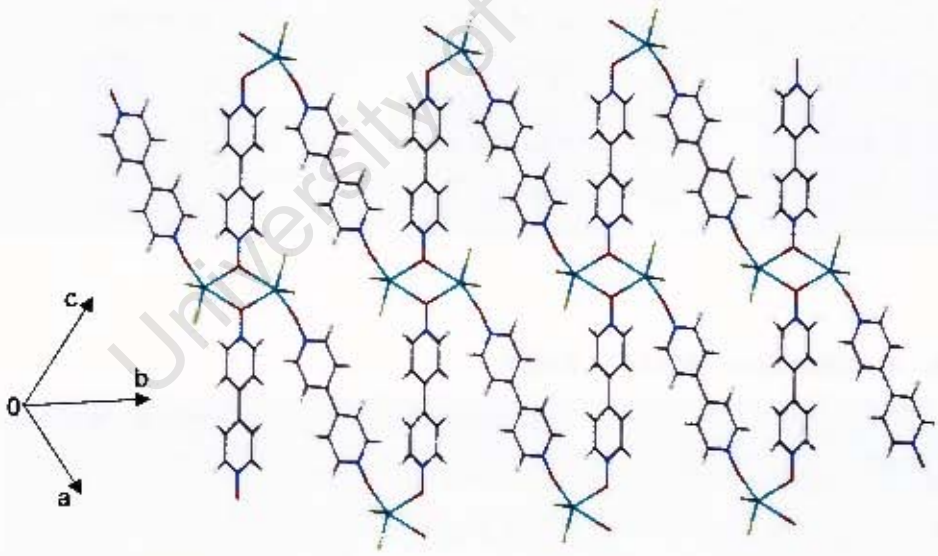

Figure 5.5: 2D coordination polymer of **ZnB1**.

There are no classic hydrogen bonding interactions in **ZnB1**. The adjacent polymers are linked through weak hydrogen bonds (Figure 5.6) and are held into place by π interactions. Summarised hydrogen bonding and π interactions results are given in Table 5.3 and 5.4 respectively.

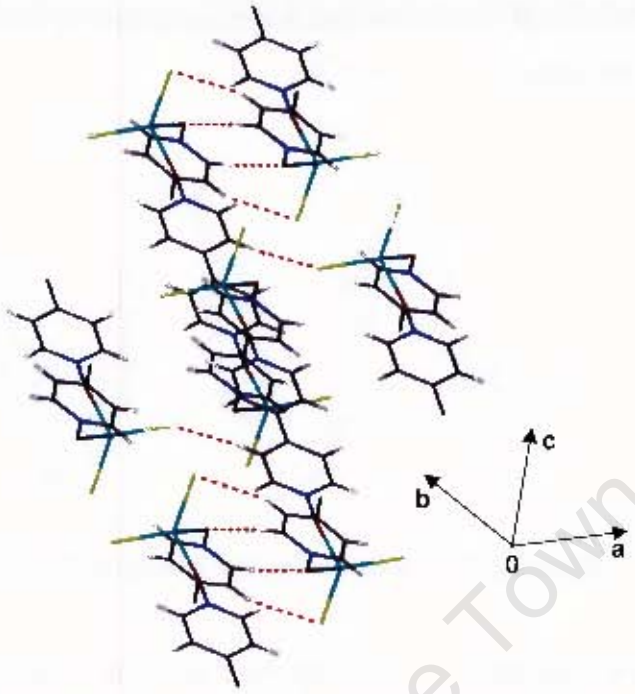

Figure 5.6: Hydrogen bonding interactions in **ZnB1** polymer.

Table 5.3: Results on hydrogen bonding in **ZnB1** polymer.

	D–H (Å)	D···A (Å)	D–H···A (°)	Symmetry operator
C(13)–H(13)···Br(1)	0.95	3.650 (3)	156	1+x, -1+y, z
C(7)–H(7)···O(1)	0.95	3.326 (3)	174	1-x, -y, 2-z
C(6)–H(6)···Br(2)	0.95	3.670 (3)	141	1-x, -y, 2-z

Table 5.4: π interaction details in **ZnB1**.

	Distance	Symmetry operator
* Cg(N2–C7)···Cg(N9–C14)	3.846 (1)	x, y, z
Cg(N9–C14)···Cg(N2–C7)	3.846 (1)	x, y, z
C(7)–H(7)···Cg(N9–C14)	3.037	x, y, z

*Cg = ring centroid

There is a centre of inversion at the centroid between the two bridged metals. The crystal packing of the structure viewed along [010] is shown in Figure 5.7 illustrating this centre of inversion and the $\pi\cdots\pi$ interactions. The polymer chains are running parallel to (1 0 -1).

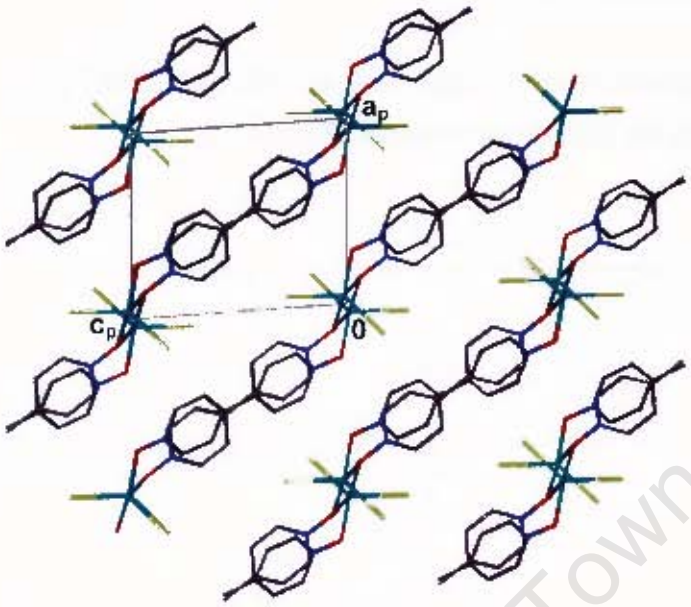

Figure 5.7: Crystal packing of **ZnB1** viewed along [010] illustrating the centre of inversion and π interactions.

The space-filling diagrams viewed along [100], [010] and [001] are shown in Figure 5.8. This was to demonstrate that **ZnB1** polymer is compact and does not have channels.

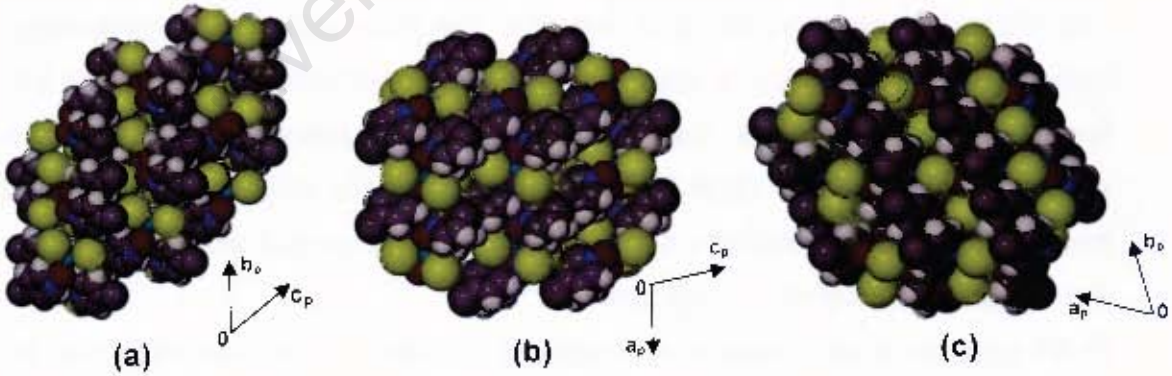

Figure 5.8: Packing diagrams viewed along (a) [100], (b) [010] and (c) [001] showing close packing. Molecules are represented in van der Waals radii.

Thermal Analysis

The zinc compounds were analysed by TG and DSC and the respective TG/DSC curves for **ZnB1** are shown in Figure 5.9.

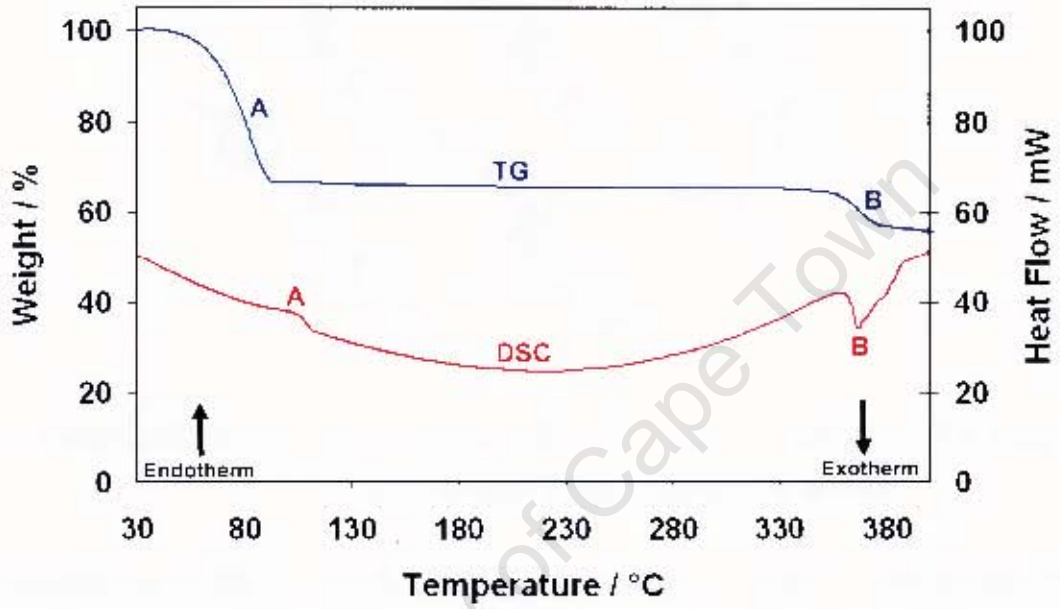

Figure 5.9: TG and DSC traces for **ZnB1**.

The TG trace was very difficult to describe. The trace shows a two step mass loss. It would be unlikely to lose the coordinated bromide ligands during the first step. Similarly, the loss of bpdo·Br salt, although matching the experimental mass loss of 34.76 % (calculated: 32.45), is unlikely. This mass loss could be due the lost of 1.5bpdo (34.14 %). The second step mass loss is the decomposition of the compound.

ZnB1 polymer is not stable to atmospheric conditions. This was shown by an immediate loss in quality of a clear crystal to opaque when exposed to surroundings. The fading of clear crystal suggests the loss of some moiety from the crystal lattice.

The DSC trace was characterised by an endotherm (peak A) and exotherm (peak B) which corresponds to the TG trace. The onset temperatures of the DSC are given in Table 5.5.

Table 5.5: Thermal analysis results for **ZnB1** polymer.

polymer	DSC Results	
	T_{on} (°C) Peak A	T_{on} (°C) Peak B
ZnB1	91.4	362.7

Hot Stage Microscopy

The crystals of **ZnB1** polymer were observed during thermal decomposition using the hot stage microscopy. The photographs for thermal events are shown in Figure 5.10.

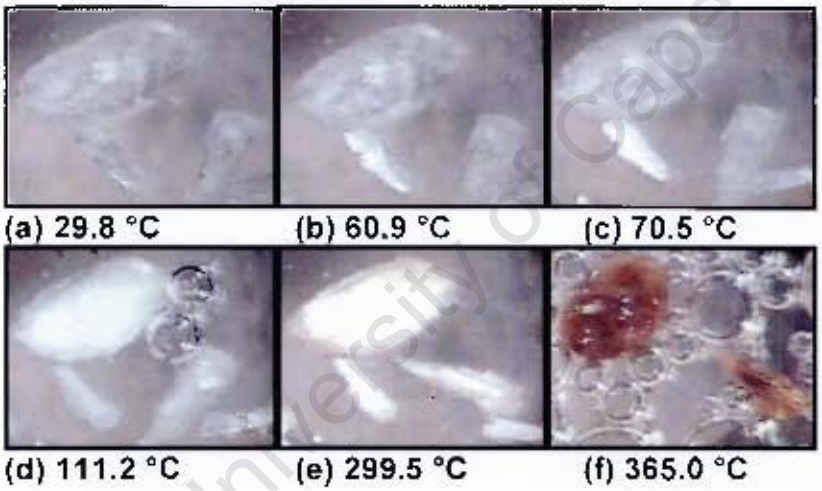

Figure 5.10: Thermal decomposition of **ZnB1**. Photographs (a) shows clear crystal submerged in oil at room temperature. (b) Crystal was starting to lose its quality. (c) An opaque crystal was observed indicating loss of some bpdo. Bubbling in (d) signifies further release of some bpdo. (e) Crystal has reached decomposition as shown by the beginning of brown color and upon decomposition the crystal melts as shown in photograph (f).

ZnB2

Table 5.6: Crystal Data and Refinement Parameters of **ZnB2**.

Molecular Formula	$Zn_3Br_6(C_{10}H_8N_2O_2)_4(H_2O)_2 \cdot (C_{10}H_8N_2O_2)$
Formula weight ($g.mol^{-1}$)	1652.52
Temperature (K)	113
Wavelength (Å)	0.71073
Crystal System	Triclinic
Space Group	$P\bar{1}$
a (Å)	7.244 (1)
b (Å)	12.017 (2)
c (Å)	16.630 (3)
α (°)	99.90 (3)
β (°)	95.97 (3)
γ (°)	95.21 (3)
Volume ($Å^3$)	1409.60 (5)
Z	1
Calc. Density ($g.cm^{-3}$)	1.947
μ (mm^{-1})	5.588
F (000)	810
Crystal Size (mm)	0.35 x 0.25 x 0.25
θ Range Scanned (°)	1.02 – 27.88
Index Range	-9 < h < 9, -15 < k < 15, -21 < l < 21
No. ref. Collected	39535
No. Unique Reflections	6747
Data completeness (%)	100.0
Refinement Method	Full-matrix L.S. on F^2
Data / Restraints / Parameters	6747 / 0 / 368
Goodness-of-fit on F^2	1.011
Final *R* Indices $[I>2\sigma(I)]$	0.0315, 0.0644
R Indices (all data)	0. 0502, 0. 0698
Largest Diff. Peak and Hole ($e.Å^{-3}$)	1.169, -0.560

The structure was solved in the space group $P\bar{1}$ with one full molecule in the unit cell. The thermal ellipsoids of **ZnB2** and atom labels are give in Figure 5.11.

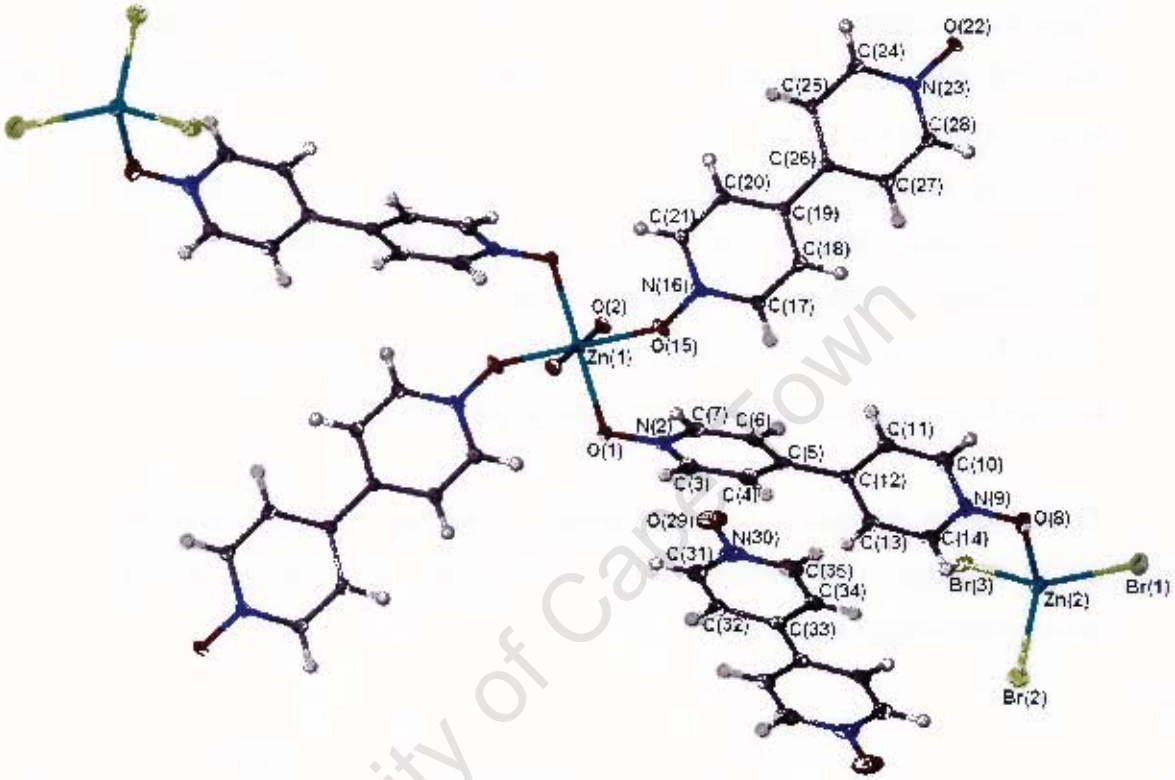

Figure 5.11: Displacement ellipsoids for **ZnB2** compound are drawn at 50% probability. Atoms of the asymmetric unit are labeled.

Structural characterisation by single crystal x-ray diffraction revealed that the product formed consisted of a molecule with two different zinc environments. These are labelled Zn(1) and Zn(2) and have different coordination geometries: octahedral and tetrahedral. **ZnB2** exists as a discrete molecular unit $[Zn_3Br_6(bpdo)_4(H_2O)_2] \cdot (bpdo)$, in which the three zinc atoms are connected by two bpdo ligands. The central Zn(1) ion is coordinated by two axial H_2O molecules and four *trans*-coordinated equatorial bpdo ligands resulting in a slightly irregular cationic octahedral coordination geometry, while the terminal Zn(2) is coordinated by three bromide counterions and a bpdo ligand forming an irregular tetrahedral coordination geometry. All the bond lengths were within the expected literature values.[1]

The coordinated bpdo ligands were twisted by a minimum of 15.2° and maximum 27.8° while the guest bpdo molecule was co-planar rings.

At Zn(1) environment, Zn(1)–O_{aqua} bond length is 2.080 Å, while the Zn(1)–O_{bpdo} bond lengths are 2.072 Å and 2.110 Å. These values corresponded well with the literature[1] values of 2.090 Å and 2.076 Å, respectively. The bond angles ranged from 86.85°–93.15°.

At Zn(2) environment, Zn(2)–Br(1), Zn(2)–Br(2), Zn(2)–Br(3) and Zn(2)–$O(8)_{bpdo}$ bond lengths are 2.374 Å, 2.390 Å, 2.427 Å and 2.011 Å, respectively. These bond lengths corresponded well with literature values of 2.390 Å (Zn–Br) and 2.076 Å (Zn–O). The expected bond angles was 109.5°, but the bond angles determined ranged from 100.49°–117.11°.[2]

The discrete molecules are connected by strong hydrogen bonding (Figure 5.12) through coordinated water molecules and the oxygens of the coordinated bpdo ligands.

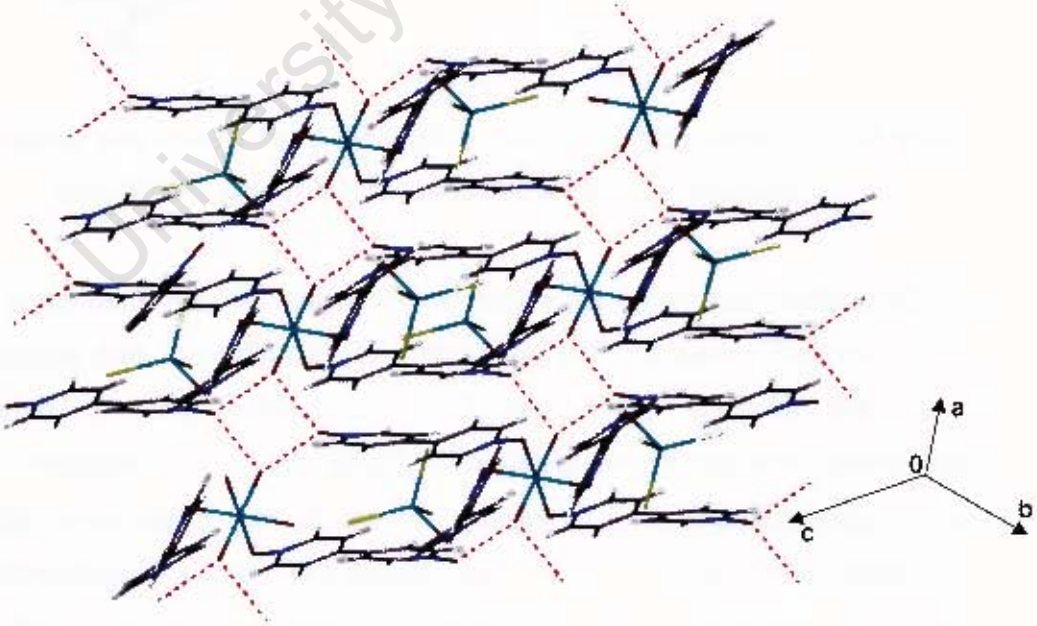

Figure 5.12: Hydrogen bonding interaction connecting adjacent discrete molecules.

ZnB2 also has weak, C–H···O, hydrogen bonds and π interactions further stabilising the structure. The hydrogen bonding details and π interactions are summarised in Table 5.7 and 5.8, respectively.

Table 5.7: Summary of hydrogen bonds in **ZnB2**.

	D–H (Å)	D···A (Å)	D–H···A (°)	Symmetry operator
O(2)···O(22)		2.724		2-x, 2-y, -z
O(2)···O(22)		2.658		2-x, 2-y, -z
C(3)–H(3)···O(22)	0.95	3.249 (4)	157	-1+x, -1+y, z
C(4)–H(4)···O(29)	0.95	3.173 (4)	132	-1+x, y, z
C(6)–H(6)···Br(3)	0.95	3.698 (3)	142	2-x, 2-y, 1-z

Table 5.8: Summary of π interactions in **ZnB2**.

	Distance	Symmetry operator
* Cg(N2–C7)···Cg(N30–C35)	3.633 (2)	x, y, z
Cg(N9-C14)···Cg(N9-C14)	3.932 (2)	1-x, 2-y, 1-z
Cg(N16–C21)···Cg(N23–C28)	3.979 (2)	1-x, 2-y, -z
Cg(N23–C28)···Cg(N16–C21)	3.979 (2)	1-x, 2-y, -z
Cg(N30–C35)···Cg(N2–C7)	3.633 (2)	x, y, z
C(17)–H(17)···Cg(N2–C7)	3.010	x, y, z
C(20)–H(20)···Cg(4)	3.314	2-x, 2-y, -z
C(25)–H(25)···Cg(3)	3.146	1-x, 2-y, -z
C(35)–H(35)···Cg(N30–C35)	3.148	2-x, 1-y, 1-z

*Cg = ring centroid

The host framework, networked by hydrogen bonds, is arranged in supramolecular chains forming channels which accommodated bpdo guest molecules. The packed molecules viewed along [100] are shown in Figure 5.13.

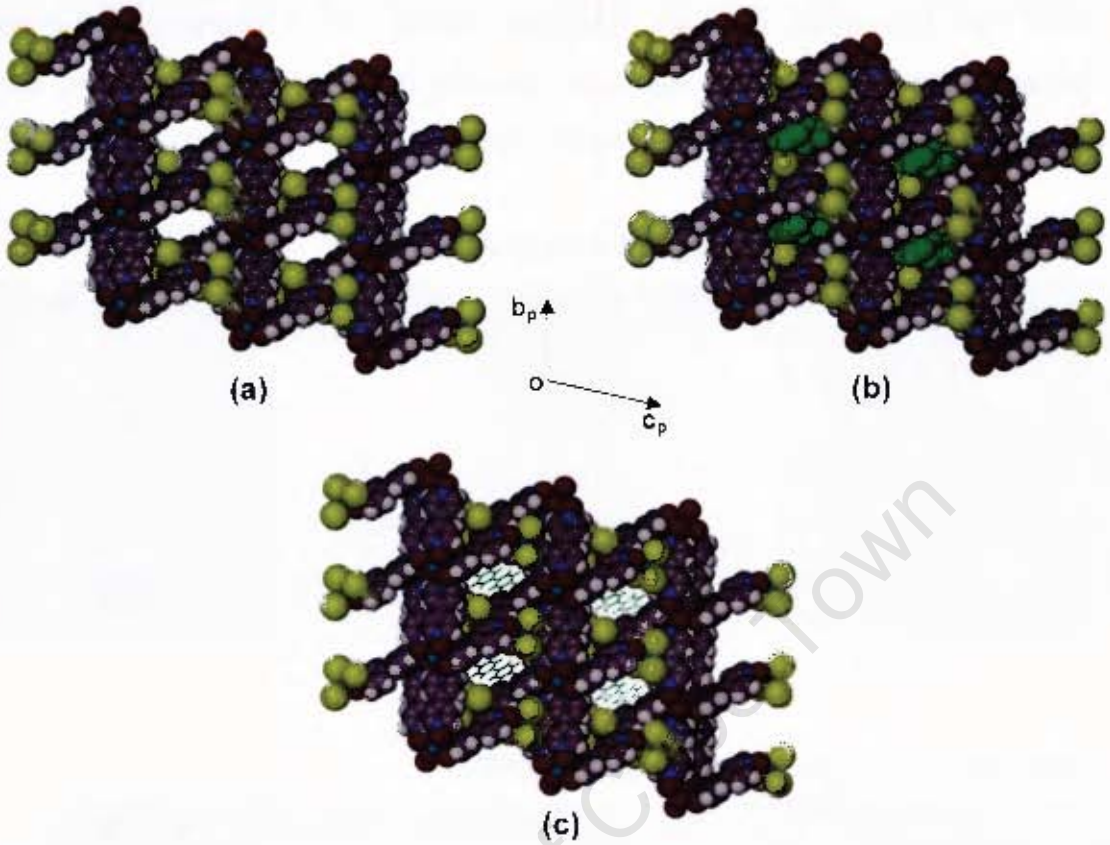

Figure 5.13: Packing of **ZnB2** viewed along [100]. (a) Shows a host compound with guest molecules omitted. (b) Host compound and the guest (green) are represented by van der Waals radii. (c) Guest molecules are illustrated in sticks.

Thermal Analysis

TG and DSC traces of **ZnB2** are shown in Figure 5.14.

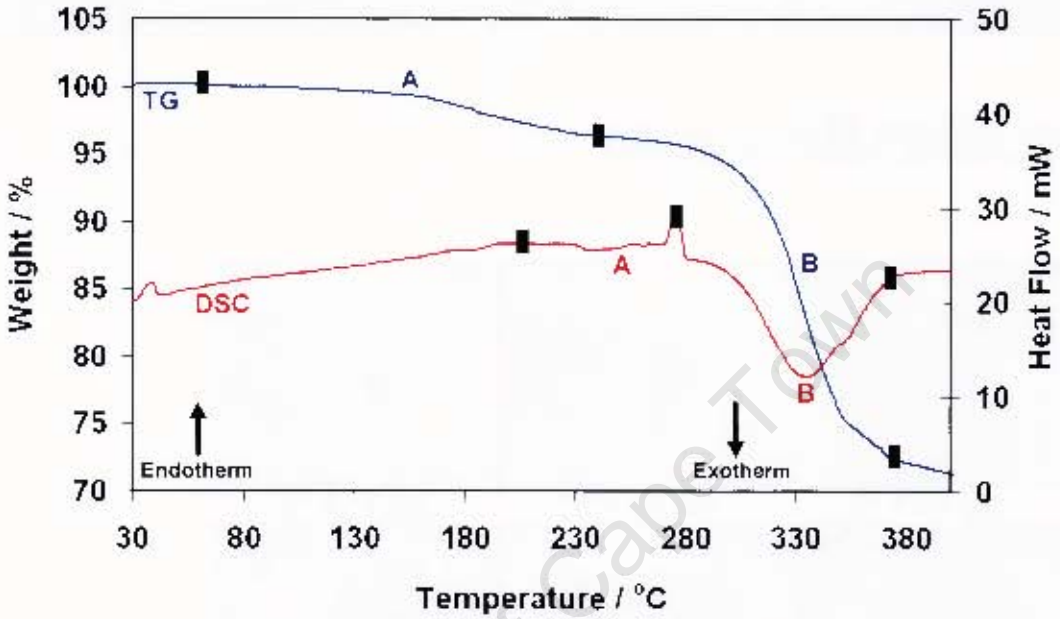

Figure 5.14: TG and DSC traces for **ZnB2**.

TG trace showed a two step mass loss. The first step (region A in Figure 5.14) is attributed to the release of coordinated water molecules, occurring over a wide temperature range (Table 5.9). The second step mass loss was attributed to loss of bpdo ligands (region B) and this stage can be observed clearly in hot stage microscopy (color change to brown). Bpdo loss depicted continues until the decomposition stage.

Exotherm A (in the DSC) corresponds to the end of the water loss observed in the TG. The poor temperature correlation can be attributed to the different instrumental conditions. The decomposition of **ZnB2** is marked by a large exotherm, B.

Table 5.9: Thermal analysis results on TG and DSC.

complex	TG Results		DSC Results	
	Calculated mass loss	Experimental mass loss	T_{on} (°C) Peak A	T_{on} (°C) Peak B
ZnB2	2.18	3.00	254.8	304.9

Hot Stage Microscopy

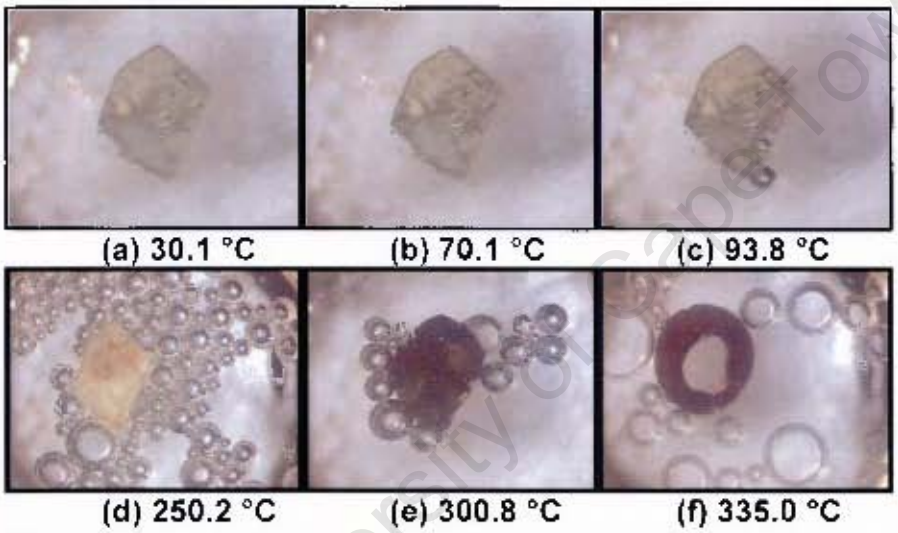

Figure 5.15: Thermal decomposition of **ZnB2**. Photographs (a) crystal at room temperature, (b) crystal still stable, (c) crystal bubbling demonstrating the loss of water molecule, (d) vigorous bubbling and slight colour change depicting the loss of the bpdo ligand, (e) crystal has reached initial stages of decomposition and (f) upon complete decomposition the crystal melts.

ZnB3

Table 5.10: Crystal Data and Refinement Parameters of **ZnB3**.

Molecular Formula	$[ZnBr_4][Zn(H_2O)_5(C_{10}H_8N_2O_2) \cdot 2(C_{10}H_8N_2O_2) \cdot (H_2O)$
Formula weight ($g.mol^{-1}$)	1123.03
Temperature (K)	113
Wavelength (Å)	0.71073
Crystal System	Triclinic
Space Group	$P\bar{1}$
a (Å)	7.712 (2)
b (Å)	15.768 (3)
c (Å)	16.639 (3)
α (°)	70.99 (3)
β (°)	87.77 (3)
γ (°)	85.63 (3)
Volume ($Å^3$)	1907.3 (7)
Z	2
Calc. Density ($g.cm^{-3}$)	1.955
μ (mm^{-1})	5.515
F (000)	1108
Crystal Size (mm)	0.04 x 0.08 x 0.12
θ Range Scanned (°)	1.00 – 25.68
Index Range	$-9 < h < 9, -19 < k < 19, -20 < l < 20$
No. ref. Collected	49973
No. Unique Reflections	7211
Data completeness (%)	100
Refinement Method	Full-matrix L.S. on F^2
Data / Restraints / Parameters	7211 / 0 / 5524
Goodness-of-fit on F^2	1.020
Final *R* Indices $[I>2\sigma(I)]$	0.0345, 0.0761
R Indices (all data)	0.0572, 0.0853
Largest Diff. Peak and Hole ($e.Å^{-3}$)	0.982, -0.629

Interestingly, a different complex, **ZnB3**, was formed when performing crystallisation in ethanolic solution instead of methanolic, as was the case in preparation of **ZnB2** complex. Single crystal diffraction data revealed that the structure could be solved in $P\bar{1}$ with two molecular units in the unit cell. Figure 5.16 shows thermal ellipsoids of **ZnB3** and their atomic labeling.

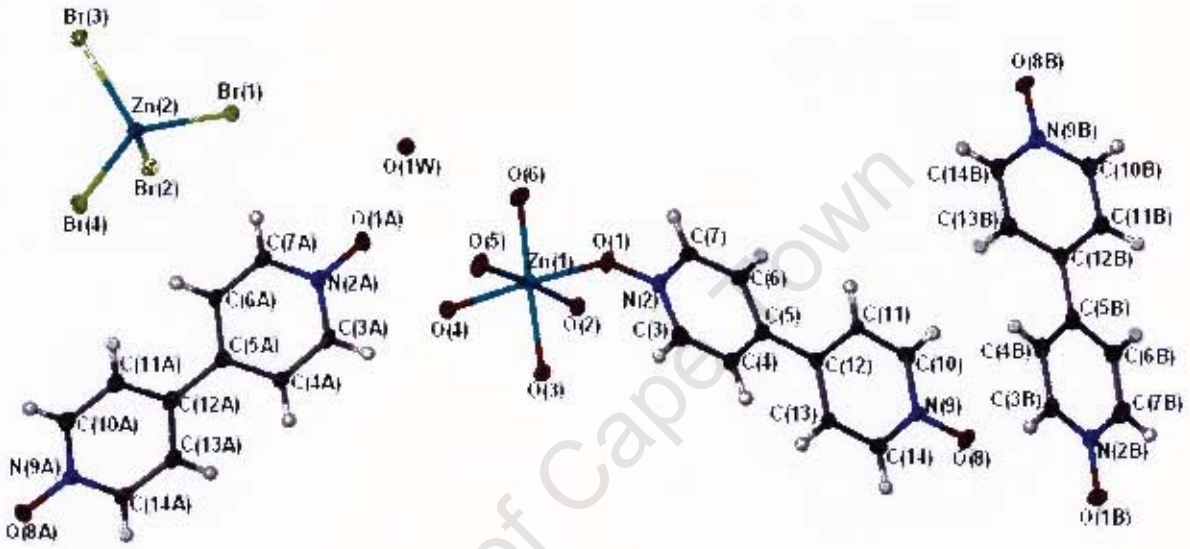

Figure 5.16: Atomic labeling of the asymmetric unit of **ZnB3**. Thermal ellipsoids are drawn at 50% probability.

Like the **ZnB2** complex, **ZnB3** has two independent zinc atoms with different coordination geometries, this time in separate molecular entities. Zn(1) ion is coordinated to one bpdo ligand and five water molecules forming an octahedral coordination geometry $[Zn(bpdo)(H_2O)_5]^{2+}$ while Zn(2) is coordinated to four bromide counterions adopting a tetrahedral coordination geometry $[ZnBr_4]^{2-}$. The other two bpdo ligands are not coordinated. The bpdo ligands are twisted by a minimum of 15.3° and maximum 17.9°. Bekaert *et al.*[2] reported a related Zn(II) complex, $([Zn(C_3H_7NO_2)_3][ZnBr_4])$, which also demonstrated two independent zinc atoms consisting of both tetrahedral and octahedral coordination geometry.

The Zn–O_{aqua} bond lengths ranged from 2.044–2.129 Å while Zn–O_{bpdo} was 2.092 Å. The bond angles slightly deviated from the actual value of 90°.[1] Angles measured were ranging from 84.75–93.06°.

At Zn(2) environment, Zn–Br bond lengths were all ~2.4 Å and these values were within the expected value (2.39 Å). Br–Zn–Br bond angles deviated very slightly from the expected value of 109.5° with the smallest and highest measured value of 108.29° and 110.35°.

Discrete $[Zn(bpdo)(H_2O)_5]^{2+}$ are linked by a network of hydrogen bonding through coordinated water molecules, bpdo and guest water molecule as shown in Figure 5.17

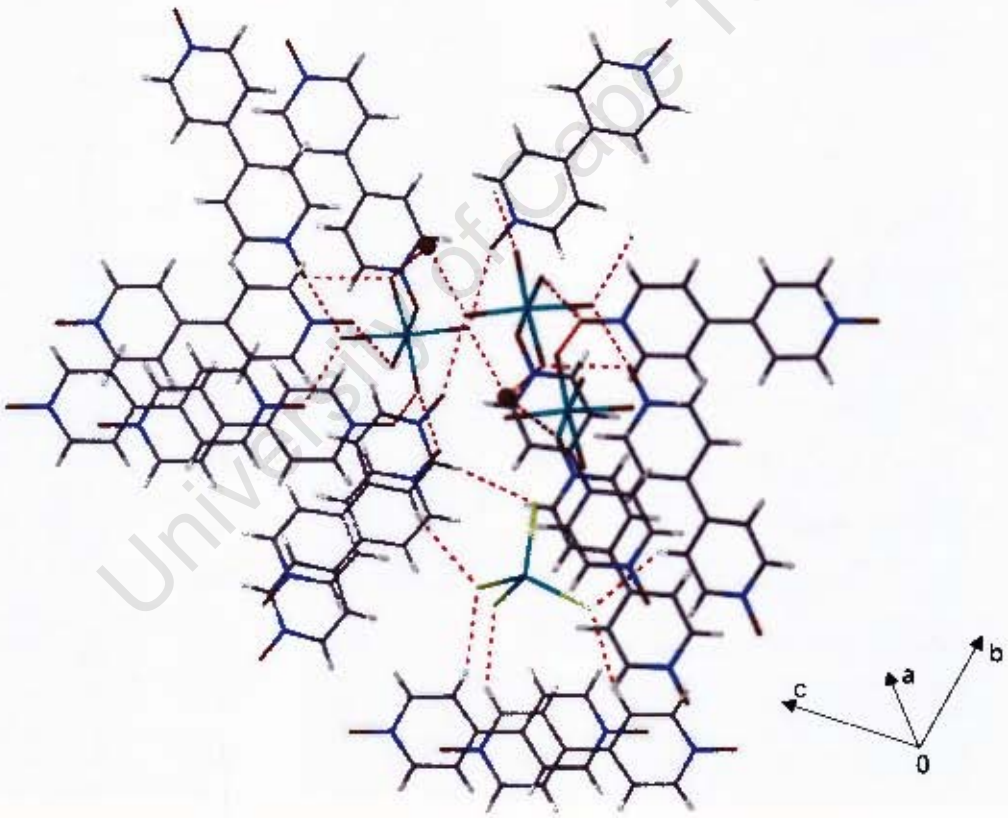

Figure 5.17: Hydrogen bonding networks in **ZnB3**.

The guest water molecule is the intermediary between the discrete molecules by receiving and donating hydrogen bonds to link adjacent molecules. In addition to conventional hydrogen bonds, the structure contains C–H···O,

C–H···Br and π interactions for further stability of the compound. Summary of hydrogen bonding and selected (interactions is given in Table 5.11 and 5.12).

Table 5.11: Hydrogen bonding results.

	D–H (Å)	D...A (Å)	D–H...A (°)	Symmetry operator
O(2)···O(1W)		2.753		1-x, 1-y, 1-z
O(2)···O(8)		2.774		1-x, 1-y, 2-z
O(3)···O(8B)		2.661		x, y-1, z
O(3)···O(8)		2.680		1-x, 1-y, 2-z
O(4)···O(8A)		2.737		1-x, -y, 1-z
O(4)···O(1B)		2.676		1-x, 1-y, 2-z
O(5)···O(1A)		2.659		x, y, z
O(5)···O(1B)		2.675		-x, 1-y, 2-z
O(6)···O(8A)		2.732		x, 1+y, z
O(6)···O(1W)		2.770		x, y, z
O(1W)···O(1)		2.765		-x, 1-y, 1-z
C(3A)–H(3A)···O(8B)	0.95	3.306 (6)	148	x, -1+y, z
C(3B)–H(3B)···O(3)	0.95	3.142 (5)	126	-x, 1-y, 2-z
C(10A)–H(10A)···O(1B)	0.95	3.321 (6)	155	x, -1+y, -1+z
C(4)–H(4)···Br(3)	0.95	3.561 (5)	126	x, y, 1+z
C(4B)–H(4B)···Br(3)	0.95	3.726 (5)	165	-x, 1-y, 1-z
C(6B)–H(6B)···Br(4)	0.95	3.642 (5)	145	x, y, 1+z
C(14B)–H(14B)···Br(2)	0.95	3.572 (5)	145	-x, 1-y, 1-z
C(14A)–H(14A)···Br(1)	0.95	3.772 (5)	170	1-x, -y, 1-z
C(13A)–H(13A)···Br(4)	0.95	3.840 (5)	162	1-x, -y, 1-z

Table 5.12: Summary of π interactions.

	Distance	Symmetry operator
* Cg(N2A–C7A)···Cg(9A–C14A)	3.677 (2)	1-x, -y, 1-z
Cg(9A–C14A)···Cg(N2A–C7A)	3.677 (2)	1-x, -y, 1-z
C(6B)–H(6B)···Cg(N9B–C14B)	3.188	1-x, 2-y, 2-z
C(11A)–H(33)···Cg(N2A–C7A)	3.054	-x, -y, 1-z
Zn(2)–Br(1)···Cg(N2–C7)	3.645 (2)	-x, 1-y, 1-z
N(9)–O(8)···Cg(N2B–C7B)	3.097 (4)	x, y, z
N(9B)–O(8B)···Cg(N2B–C7B)	3.836 (4)	-x, 2-y, 2-z

ZnB3 forms channels which accommodate bpdo guest molecules. These bpdo molecules are hydrogen bonded to the host framework. The channels are readily observed when packing the molecules along [100] as shown in Figure 5.18.

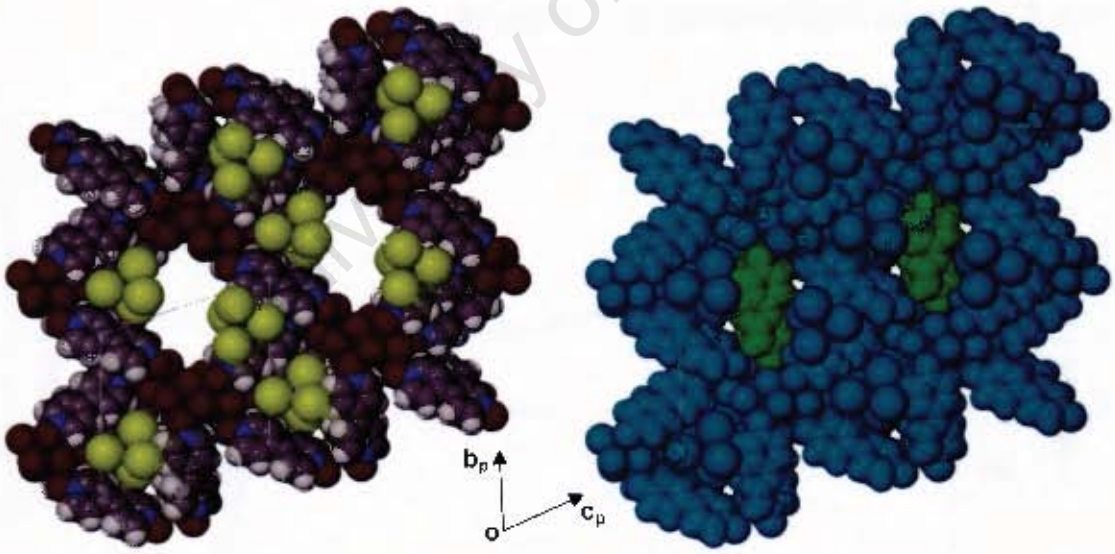

Figure 5.18: Packed molecules of **ZnB3** viewed along [100]. (a) Shows and empty host and (b) shows bpdo guest (green colour) molecules in channels.

Supramolecular chains run along [010] and [001]. Figure 5.19 shows packed molecules of **ZnB3** viewed along [010].

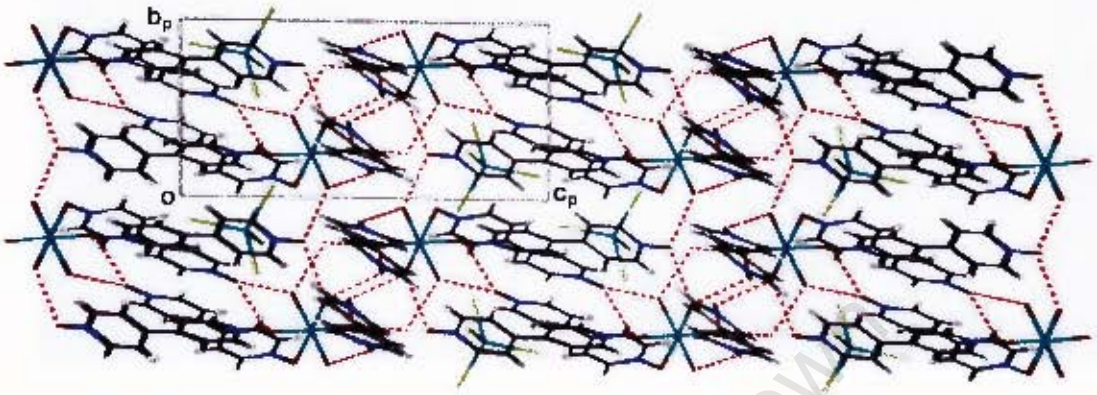

Figure 5.19: A packed **ZnB3** crystal structure viewed along [010] showing supramolecular chains.

Thermal analysis

The TG trace for **ZnB3** is shown in Figure 5.20.

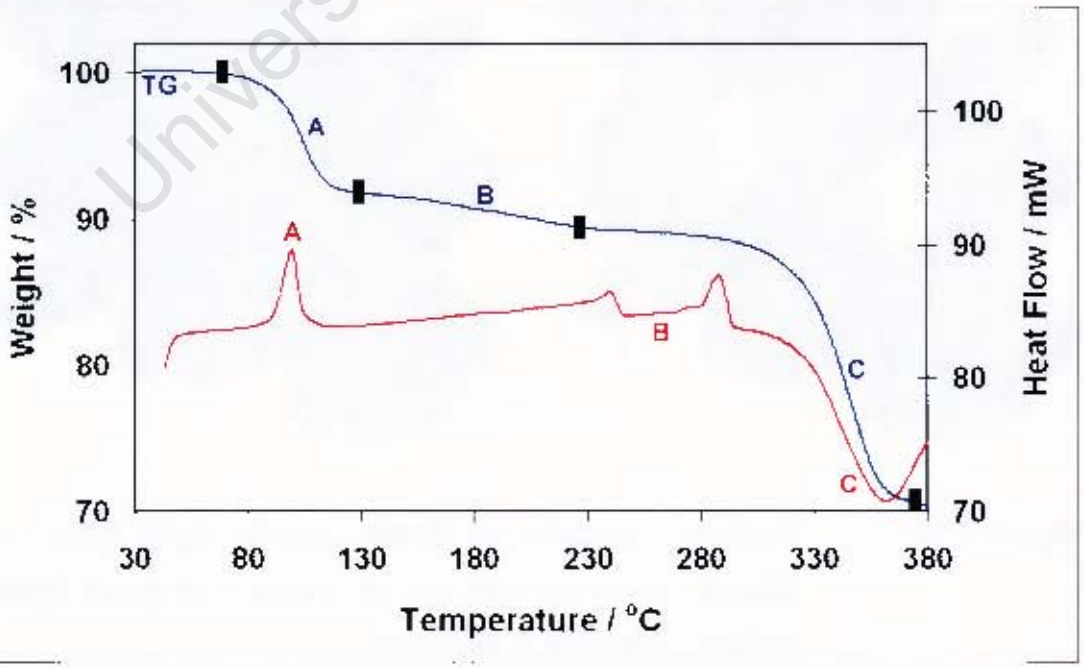

Figure 5.20: TG trace for **ZnB3** compound.

The TG trace is characterised by a three step mass loss shown by area A, B and C in Figure 5.20. Steps A and B are attributed to water mass loss. The experimental mass percentage for both steps (10.31 %) accounts for five coordinated water molecules and the guest water (calculated mass loss is 9.63). The bpdo is released in step C which was accompanied by decomposition of the compound (third step mass loss). DSC trace corresponds with the TG. Endotherm A (T_{on} = 90.8 °C) is due to loss of water molecules while exotherm B (T_{on} = 241.3 °C) and C (T_{on} = 327.00 °C) are attributed to compound decomposition.

Hot Stage Microscopy

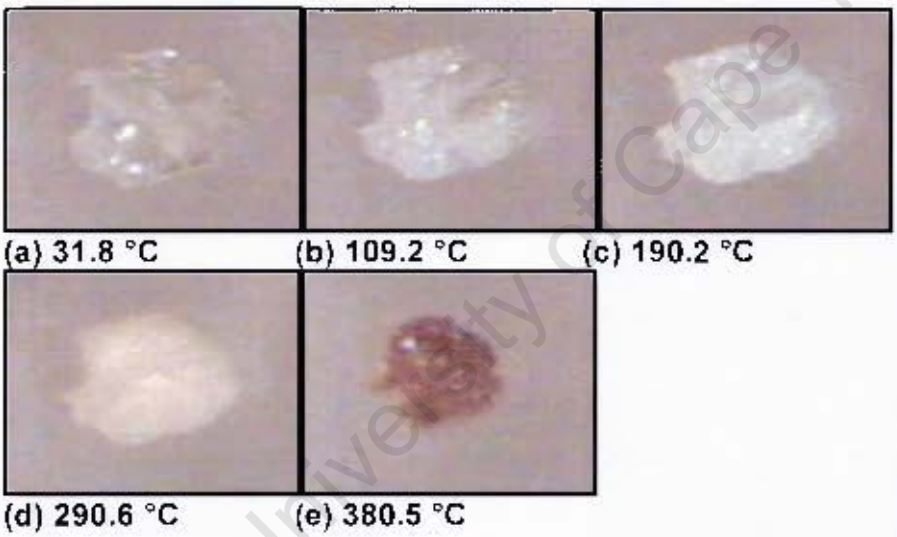

Figure 5.21: Thermal decomposition of **ZnB3**. Unlike other compounds, hot stage of **ZnB3** was not characterised by bubbles. (a) Crystal at room temperature. (b) At 109.2 °C, the crystal loses its colour to opaque signifying the loss of water molecules. (c) The opaque color became denser depicting release of bpdo. (d) Initial stages of compound decomposition shown by faint brown colour and (e) shows the complete compound decomposition.

ZnN

Table 5.13: Crystal Data and Refinement Parameters of **ZnN**.

Molecular Formula	**$Zn(NCS)_2(C_{10}H_8N_2O_2)(H_2O)_2 \cdot H_2O$**
Formula weight ($g.mol^{-1}$)	423.78
Temperature (K)	113
Wavelength (Å)	0.71073
Crystal System	Triclinic
Space Group	$P\bar{1}$
a (Å)	7.311 (2)
b (Å)	9.863 (2)
c (Å)	12.013 (2)
α (°)	77.29 (3)
β (°)	79.67 (3)
γ (°)	88.12 (3)
Volume ($Å^3$)	831.3 (3)
Z	2
Calc. Density ($g.cm^{-3}$)	1.693
μ (mm^{-1})	1.759
F (000)	432
Crystal Size (mm)	0.09 x 0.15 x 0.20
θ Range Scanned (°)	1.00 – 23.37
Index Range	$-9 < h < 9, -12 < k < 12, -14 < l < 14$
No. ref. Collected	32479
No. Unique Reflections	3356
Data completeness (%)	100.0
Refinement Method	Full-matrix L.S. on F^2
Data / Restraints / Parameters	3356 / 0 / 242
Goodness-of-fit on F^2	1.096
Final *R* Indices $[I>2\sigma(I)]$	0.0232, 0.0575
R Indices (all data)	0.0283, 0.0595
Largest Diff. Peak and Hole ($e.Å^{-3}$)	0.33, -0.40

Solving the structure in space group $P\bar{1}$ revealed that the central Zn ion is coordinated by two NCS^- counterions on the axial positions, while the equatorial positions are occupied by two water molecules and two bpdo ligands, resulting in octahedral coordination geometry. The atomic labels and thermal displacements are given in Figure 5.22.

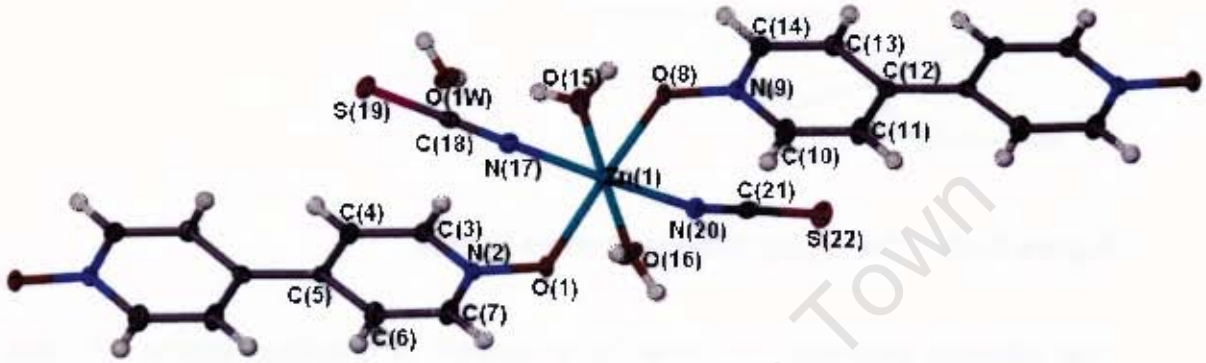

Figure 5.22: Labeled asymmetric unit of **ZnN** compound. The thermal ellipsoid diagram was drawn at 50% probability.

All bond lengths and angles were within the expected range. The Zn–N_{NCS^-} bond length is 2.034 Å, while Zn–O_{bpdo} and Zn–O_{acua} are 2.154 Å and 2.169 Å respectively. These bond distances are comparable with literature[1] values of 1.988 Å (Zn–N_{NCS^-}), 2.076 Å (Zn–O_{bpdc}) and 2.090 Å (Zn–O_{aqua}), correspondingly. Details of bond lengths and angles are given in the Appendix.

This compound is a 1D zigzag-like coordination polymer (Figure 5.23).

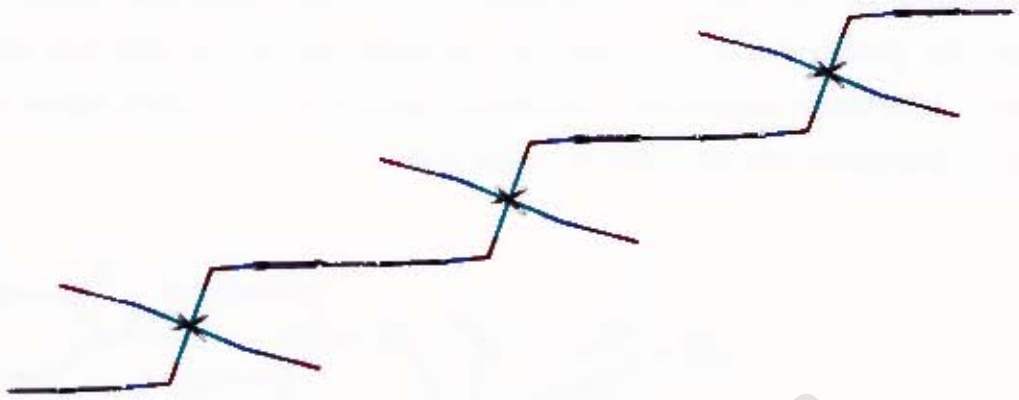

Figure 5.23: The zigzag polymeric chain in **ZnN**.

The adjacent polymers are linked by a network of hydrogen bonds. The two coordinated water molecules are involved in hydrogen bonding as donors. Coordinated water (O16) donates hydrogen bonds {O(16)–H(16A)···$O(1)_{bpdo}$ and O(16)–H(16B)···$O(8)_{bpdo}$} to the terminal oxygens of the coordinated bpdo ligand with the $O(16)_{aqua}$···$O(1)_{bpdo}$ distances of 2.839 Å and 2.853 Å, respectively. The *trans*-coordinated water molecule donates hydrogen bonds (O(15)–H(15B)···O(1W)) to guest water molecule with the O(15)···$O(1W)_{guest}$ distance of 2.662 Å. The guest water molecule in return donates hydrogen bonds, O(1W)–H(1W1)···O(8) and O(1W)–H(1W2)···O(1), to two coordinated bpdo ligands linking the adjacent chains with the O···O distance of 2.793 Å for $O(1W)_{aqua}$···$O(8)_{bpdo}$ and 2.848 Å for $O(1W)_{aqua}$···$O(1)_{bpdo}$. The hydrogen bond network is illustrated in Figure 5.24. A summary of hydrogen bonding results and π...S close contacts are given in Table 5.14 and 5.15.

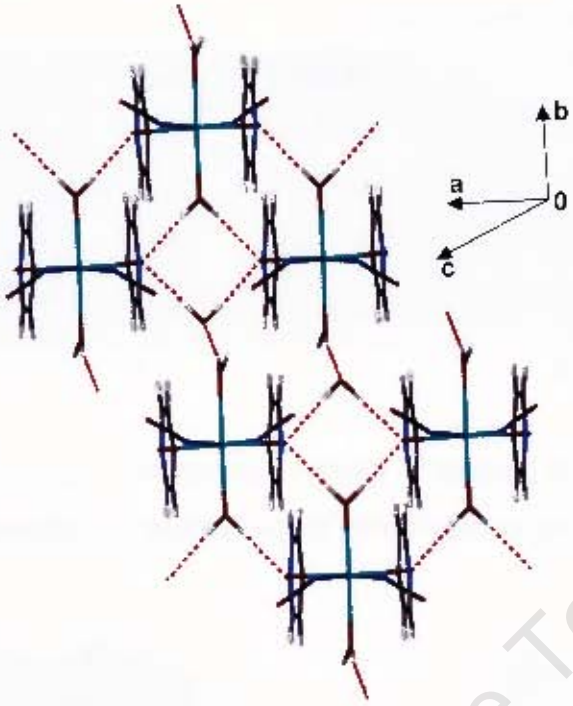

Figure 5.24: Hydrogen bonding networks.

Table 5.14: Hydrogen bonding details.

	D–H (Å)	D···A (Å)	D–H···A (°)	Symmetry operator
O1W–H1W1···O8	0.77 (3)	2.793 (2)	175	1-x, 1-y, 1-z
O1W–H1W2···O1	0.82 (3)	2.847 (2)	176	-x, 1-y, 1-z
O15–H15A···S19	0.83 (2)	3.377 (2)	164	1-x, 1-y, 1-z
O15–H15B···O1W	0.78 (2)	2.662 (2)	170	x, y, z
O16–H16A···O1	0.84 (3)	2.839 (2)	175	-x, 2-y, 1-z
O16–H16B···O8	0.78 (3)	2.853 (2)	178	1-x, 2-y, 1-z
C3–H3···O1W	0.95	3.089 (2)	134	x, y, z
C7–H7···N20	0.95	3.468 (2)	163	-x, 2-y, 1-z
C10–H10···N17	0.95	3.439 (2)	160	1-x, 2-y, 1-z

Table 5.15: π interactions in **ZnN**.

	Distance	Symmetry operator
*C18–S19···Cg(N2–C7)	3.908 (1)	x, y, z
C18–S19···Cg(N2–C7)	3.645 (1)	1+x, y, z
C21–S22···Cg(N2–C7)	3.616 (1)	-1+x, y, z
C21–S22···Cg(N2–C7)	3.905 (1)	x, y, z

*Cg = ring centroid

Polymer chains run parallel to [001] as shown in Figure 5.25(a) and the guest water molecules are encapsulated in the compound cavities (Figure 5.25(b)).

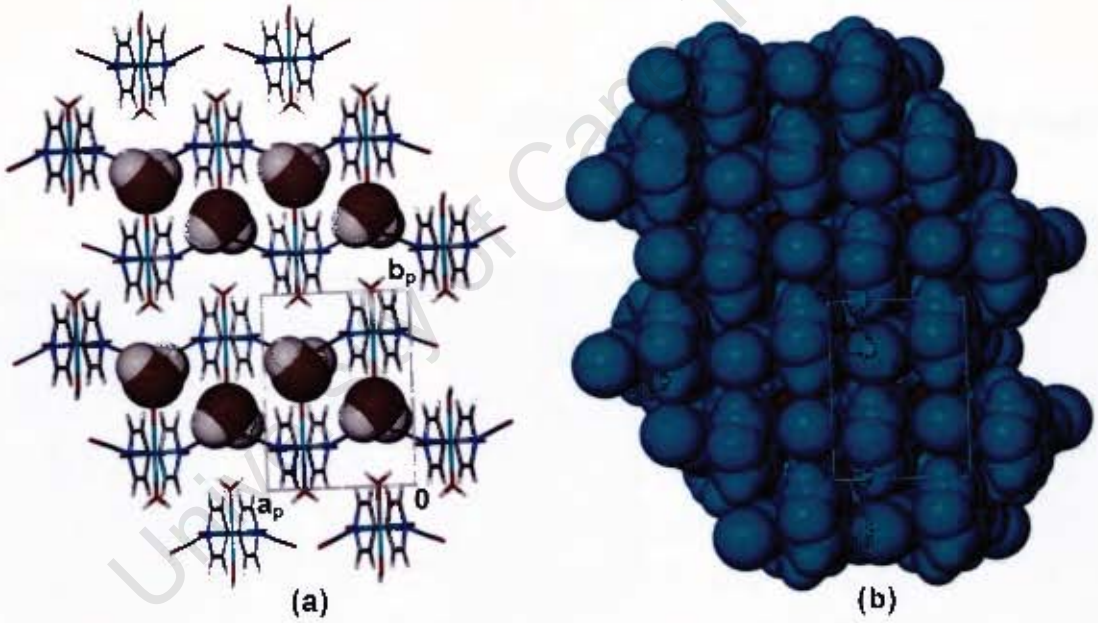

Figure 5.25: Packed molecules viewed along [001], showing **ZnN** polymer. (a) Water guest molecules and host are represented in van der Waals radii while in (b) both guest (maroon) and host (blue) are shown in van der Waals radii.

The packing diagrams viewed along [100] and [010] are shown in Figure 5.26.

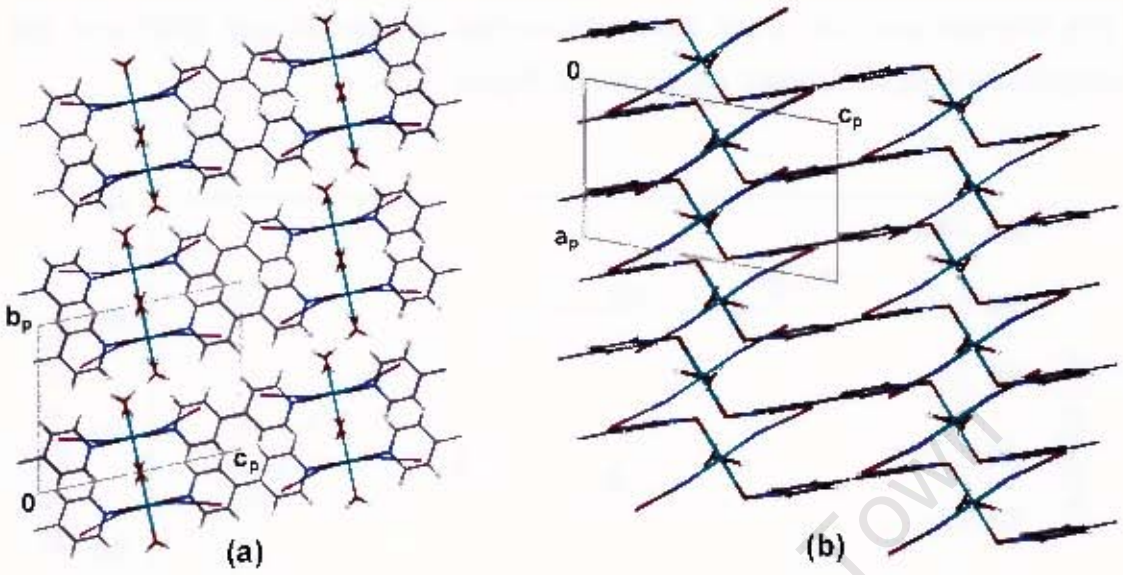

Figure 5.26: Molecules are packed along [100] and [010]. (a) Shows sheets of organic and inorganic components while (b) shows π···π stacks and zigzag shapes.

Thermal Analysis

The thermal analysis of the **ZnN** was carried out by TG and DSC and the respective TG/DSC curves are shown in Figure 5.27.

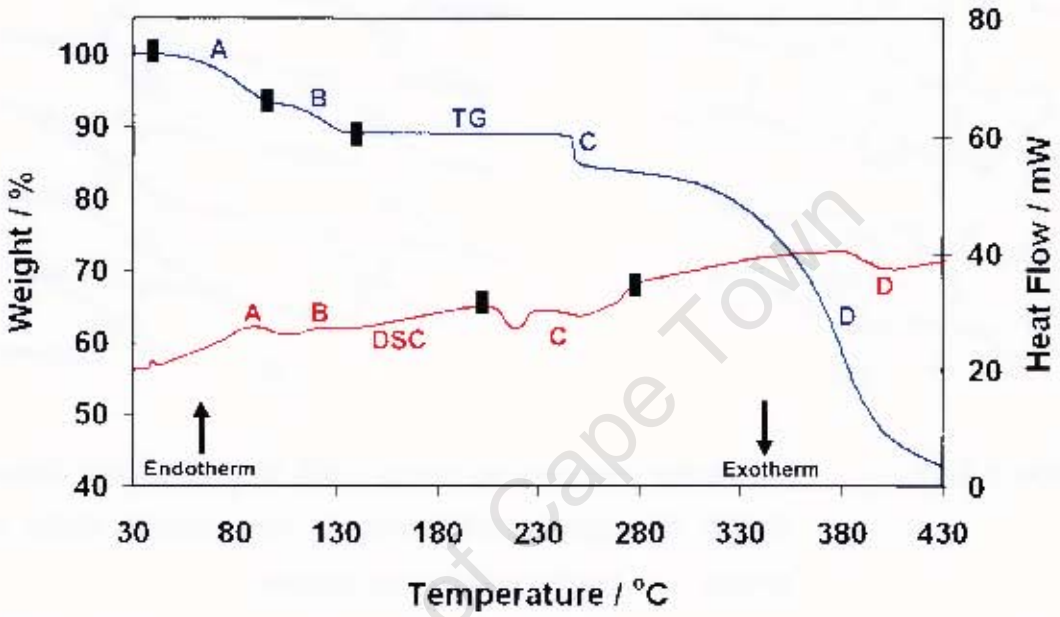

Figure 5.27: TG and DSC traces for **ZnN**.

The TG trace shows a four step mass loss. The guest and two coordinated water molecules are removed in steps A and B (Figure 5.27). Collectively, the percentage mass loss calculated for these water molecules is 10.96% which was lower than the actual mass loss observed (details are given in Table 5.16). The difference could be due to the hygroscopic nature of **ZnN**. The third step mass loss (C) is unusually sharp. The hotstage (discussed below in this section) illustrates that at this temperature the crystal melts (Figure 5.28(d)). The fourth step mass loss is the decomposition of **ZnN**.

The mass losses observed in the TG trace corresponded well with the DSC trace (Figure 5.27). The first two endotherms, A and B, were due to water molecules. The third, exothermic peak (region C) was due to the melting with the decomposition while peak D continues decomposition stage. Summary of onset temperatures is given in Table 5.16.

Table 5.16: Thermal analysis results on TG and DSC.

	TG Results			
	Calc. % mass loss		Exp. % mass loss	
Mass loss A	6.75		8.50	
Mass loss B	4.21		4.25	
Total H_2O loss	10.96		12.75	
complex	DSC Results			
	T_{on} (°C) Peak A	T_{on} (°C) Peak B	T_{on} (°C) Peak C	T_{on} (°C) Peak D
ZnN	75.0	111.1	209.8	384.1

Hot Stage Microscopy

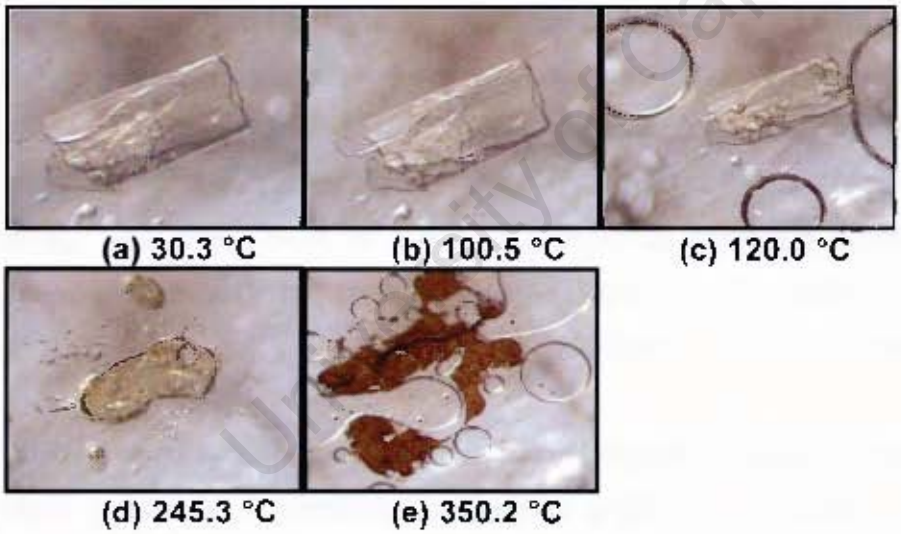

Figure 5.28: **ZnN** compound during thermal decay. (a) shows crystal at room temperature, (b) crystal still stable, (c) bubbling due to loss of water molecules. (d) crystal changed colour to brown and melted. (e) Compound decomposition is observed at 350.2 °C.

Discussion and conclusion

ZnB1, **ZnB2** and **ZnB3** were prepared using the same starting materials ($ZnBr_2$ and bpdo) but different crystallisation methods (solvent layering and slow evaporation), while **ZnN** was prepared by slow evaporation using $Zn(NCS)_2$. The compounds were characterised by thermal analysis and the crystal structures have been elucidated using single crystal diffractometry. The zinc compounds prepared in this study crystallised in the triclinic space group $P\bar{1}$, but were not isostructural.

ZnB1 is a double-strand one dimensional polymeric structure with metal centres bridged through oxygens of the bpdo ligand. The compound adopts the trigonal bipyramidal coordination geometry. There is no conventional hydrogen bonding in **ZnB1**. A literature and CSD[3] (Version 5.27, November 2005) search revealed that crystallisation using $ZnBr_2$ and bpdo has not been fully explored which makes this study to be more interesting. However, Hu *et al.*[4] reported compounds prepared using either $ZnBr_2$ or $ZnCl_2$ using bpy (4,4'-bypyridine; an analogue of bpdo). Crystallisation produced one dimensional zigzag coordination polymers ($[ZnX_2(bpy)]_n$, X=Cl^- or NCS^-) with bpy ligand bridging ZnX_2 moeities with an essentially tetrahedral coordinated geometry. Moreover, these polymers are dissimilar to **ZnB1**.

ZnB2 is a *trans*-coordinated discrete molecule composed of four bpdo ligands and two water molecules completing octahedral coordination symmetry. Both coordinated waters are involved in hydrogen bonding interactions, linking $Zn_3Br_6(bpdo)_4(H_2O)_2$ discrete molecules. An interesting characteristic of **ZnB2** is the presence of two metal centres of different coordination geometry. To the best of our knowledge and literature search related to this study, this form of compound is unique. **ZnB2** is an inclusion compound accommodating bpdo molecules into its channels. In comparison to **ZnB2**, Long *et al.*[5] reported a Zn(II) crystal structure composing of discrete $[Zn(bpdo)_6]^{2+}$ cation and uncoordinated nitrate anions (guest molecules). The Zn(II) centres are octahedral and the structure is governed uniquely by $\pi\cdots\pi$ interactions.

Replacement of nitrate anion by fluorosilicate (SiF_6) resulted in an environmentally unstable compound, $[Zn(MeOH)_2(bpdo)_4]$ $(SiF_6) \cdot 3MeOH$.[5]

In **ZnB3** there are also two independent Zn(II) environment with different coordination geometries. However, the octahedral geometry is formed by coordination of five water molecules and bpdo ligand to the central Zn(II) metal, while the tetrahedral symmetry is coordinated by four bromide counterions, in two separate entities. The discrete molecules are linked by a network of hydrogen bonds. **ZnB3** forms channels which accommodates bpdo molecules.

ZnN forms a one dimensional zigzag-like polymer. The adjacent chains of **ZnN** are linked by hydrogen bonding through coordinated water, guest water molecule and bpdo ligands. The metal centre forms octahedral coordination symmetry. This structure is different to thiocyanide structure reported by Hu *et al.*[4], $[Zn(NCS)_2(bpy)]_n$ (discussed above in this section). One dimensional polymer, $\{[Zn(H_2O)_4(bpdo)_2] \cdot (ClO_4)_2 \cdot 2(bpdo)\}_n$,[6] prepared from $Zn(ClO_4)_2$ and bpdo was reported by Ma *et al.*[6] This is a zigzag shape polymer with adjacent chains connected through hydrogen bonding between the coordinated water molecules and the bridging bpdo ligands leading to a two dimensional sheet. These two dimensional sheets are linked three dimensionally through hydrogen bonding produced by a single hydroxyl group of each coordinated water with one uncoordinated bpdo guest molecule. None of these compounds is isostructural or closely related to **ZnN**.

In conclusion, an overall comparison of Zn(II) polymers provide an insight about the role of an anion and crystallisation methods in construction of metal-organic frameworks. Thus for an example, the bromide anion afforded a one dimensional polymer (**ZnB1**) prepared by solvent layering and two discrete molecular structures (**ZnB2** and **ZnB3**) prepared by solvent evaporation, while the thiocyanide anion afforded a one dimensional polymer (**ZnN**) and $[ZnNCS_2(bpy)]_n$ by solvent evaporation,[4] while nitrate and fluorosilicate anions afforded $[Zn(bpdo)_8](NO_3)_2$ discrete molecule and $[Zn(MeOH)_2(bpdo)_4]$ $(SiF_6) \cdot 3MeOH$ coordination polymer by solvent evaporation, respectively.[5] The

perchlorate anion afforded one dimensional polymer $\{[Zn(H_2O)_4(bpdo)_2] \cdot (ClO_4)_2 \cdot 2(bpdo)\}_n$ by solvent evaporation. [6]

References

1. F.H. Allen, O. Kennard, D.G. Watson, L. Brammer, A.G. Orpen, R. Taylor, *J. Chem. Soc. Perkin Trans.*, 1989, S1-S83.
2. A. Bekaert, P. Lemoine, J. D. Brion, B. Viossat, *Acta Cryst.*, 2005, **C61**, m76.
3. F.H. Allen, *Acta Crystallogr.*, 2002, **B58**, 380.
4. C. Hu and U. Englert, *CrystEngComm*, 2001, **23**, 1.
5. D-L. Long, A.J. Blake, N.R. Champness, and M. Schröder, *Chem. Commun.*, 2000, 2273.
6. B-Q. Ma, S. Gao, H-L Sun and G-X Xu, *J. Chem. Soc., Dalton Trans.*, 2001, 130.

Chapter 6

Crystal structures of Au(III) complexes: Protonation of dipyridyl ligands

Crystal structures of Au(III) with dipyridyl ligands (bpdo, BPE and DPE) were constructed and characterised by thermal analysis (TG, DSC and HSM), elemental analysis, and XRD. Crystal structures have been refined and elucidated using single crystal diffractometry.

The experiments were performed in acidic media of $H[AuCl_4]$ whereby in all crystallisation preparations, the dipyridyl ligand was protonated. The bpdo was protonated on one end of the bidentate sites, while protonation in BPE and DPE was observed on both terminals of the ligand. It is through this protonation that the structures acquired conventional hydrogen bonding interactions connecting the discrete ions of the crystal structure. The Au(III) metal centres are linked through C H···Cl interactions and the structure is further stabilised through interionic Au···Cl and intermolecular Cl···Cl contacts.

Crystallographic data, experimental and refinement parameters are given in Table 6.2, and 6.3. Final atomic coordinates, bond lengths and angles, torsion angles, thermal parameters and tables of observed and calculated structure factors for each of the crystal structure are given in the appendices.

Complex preparation

Good quality crystals for single crystal data collection were obtained by slow evaporation at ambient temperatures (295 K – 298 K) within a week. The method was discussed in Chapter 2.

The abbreviations for the discrete gold complexes in this chapter are as follows:

$AuCl_4$(bpdo·H) : **Au1**

$AuCl_4$(BPE·2H) · Cl : **Au2**

$AuCl_4$(DPE·2H) · Cl : **Au3**

Microanalysis

Elemental analysis results are given in Table 6.1 and they corresponded well with the calculated elemental mass percentages.

Table 6.1: Elemental analysis results for Au(III) complexes.

Complex	Calculated %			Found %		
	C	H	N	C	H	N
Au1	22.75	1.72	5.31	23.12	1.52	5.29
Au2	25.72	2.52	5.00	25.83	2.56	4.83
Au3	25.81	2.17	4.76	25.84	2.16	4.85

PXRD

PXRD patterns for **Au1**, **Au2** and **Au3** are shown in Figure 6.1(a-c). The patterns generally match, except two peaks at low 2θ (approximately 6 and 8) for calculated **Au1**. This observation could be due to preferred orientation i.e. the morphology of the crystallites causes some peaks to have enhanced intensities while others are practically unobserved. In this case, **Au1** crystals typically form long needles so it is likely that the crystallites will retain this morphology when crushed.

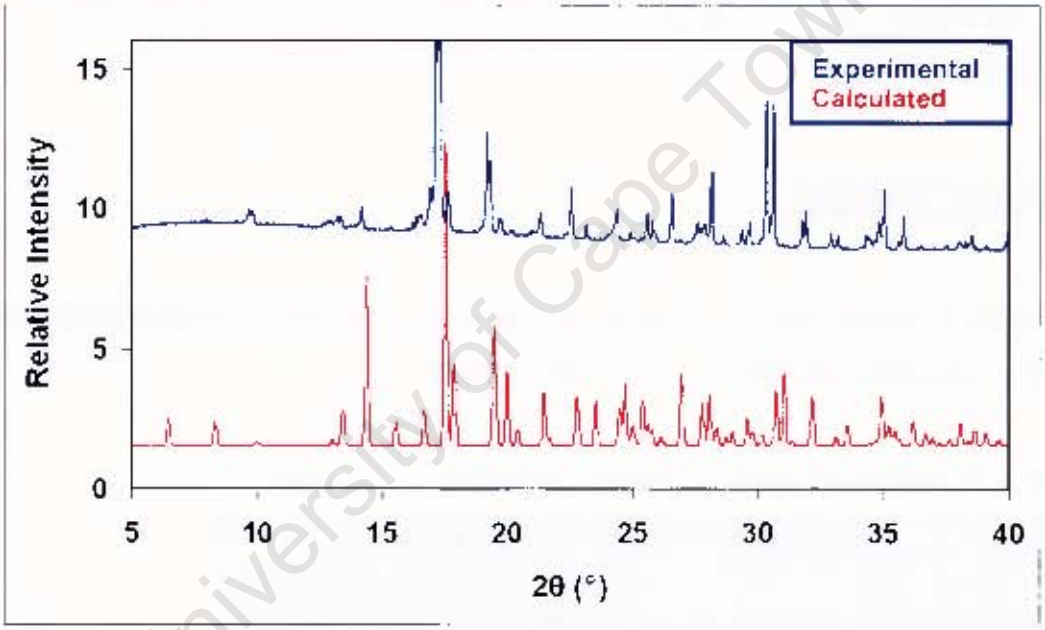

Figure 6.1(a): Calculated PXRD pattern for **Au1**.

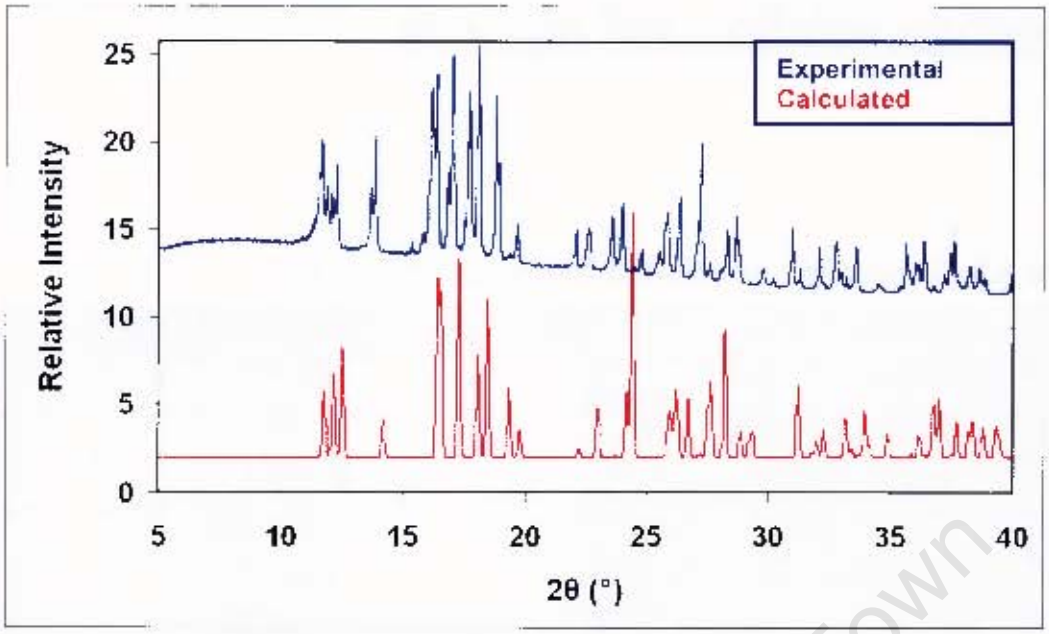

Figure 6.1(b): Calculated PXRD pattern for **Au2**.

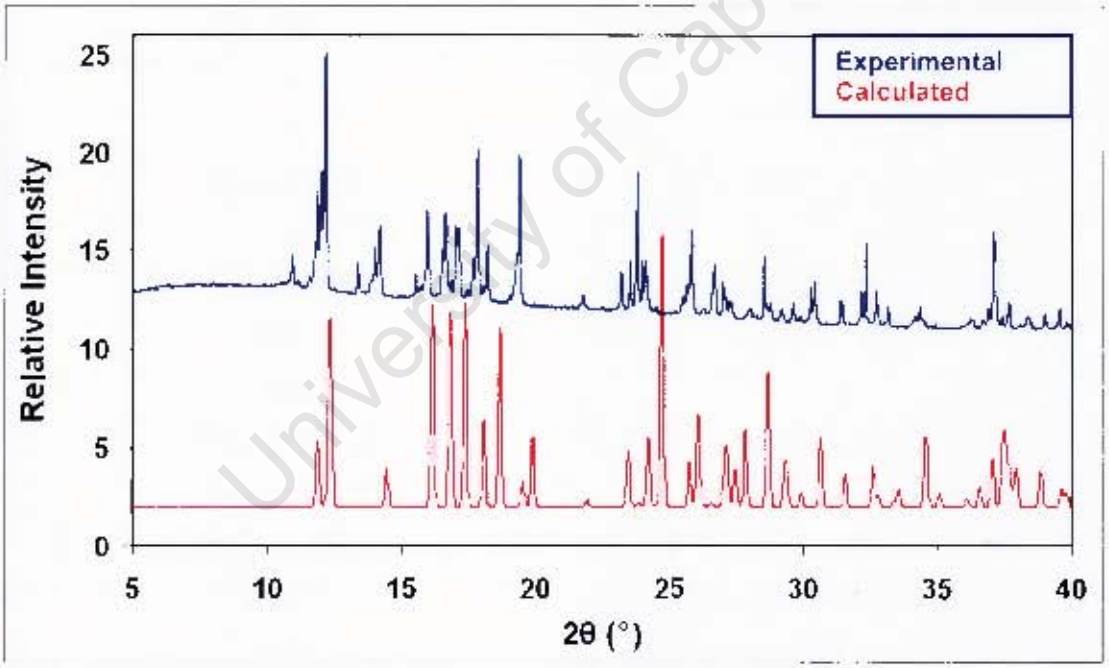

Figure 6.1(c): Calculated PXRD pattern for **Au3**.

Structure solution and analysis

Au1

Table 6.2: Crystal Data and Refinement Parameters of **Au1**.

Molecular Formula	$AuCl_4(C_{10}H_9N_2O_2)$
Formula weight ($g.mol^{-1}$)	527.96
Temperature (K)	113
Wavelength (Å)	0.71073
Crystal System	Orthorhombic
Space Group	*Cmc2₁*
a (Å)	17.756 (4)
b (Å)	21.268 (4)
c (Å)	7.556 (2)
α (°)	90
β (°)	90
γ (°)	90
Volume ($Å^3$)	2853.5 (10)
Z	8
Calculated Density ($g.cm^{-3}$)	2.458
μ (mm^{-1})	11.056
F (000)	1968
Crystal Size (mm)	0.05 x 0.09 x 0.10
θ Range Scanned (°)	2.99 - 25.67
Index Range	-21 < h < 21, -25 < k < 25, -9 < l < 9
No. Reflections Collected	17669
No. Unique Reflections	2779
Data completeness (%)	99.9
Refinement Method	Full-matrix L.S. on F^2
Data / Restraints / Parameters	2779 / 0 / 177
Goodness-of-fit on F^2	1.080
Final *R* Indices *[I>2σ(I)]*	0.0216, 0.0422
R Indices (all data)	0.0240, 0.0428
Largest Diff. Peak and Hole ($e.Å^{-3}$)	0.768, -1.175

Crystal data refinement revealed that **Au1** could be solved in the space group $Cmc2_1$, with 8 molecules in the unit cell. The crystal structure is composed of two Au(III) metal centres located on the mirror plane and having site occupancy factors of 0.5 and each is coordinated by four chloride ions forming almost perfect square planar coordination geometry. In the asymmetric unit, the chlorine atoms of Au(1)are also located on the mirror planes so they have site occupancies of 0.5 while the chlorines for Au(2) are present at 100%. Thus the $[AuCl_4]^-$ ions are oriented perpendicular to one another along the mirror plane. Thermal ellipsoids and asymmetric labels are shown in Figure 6.2.

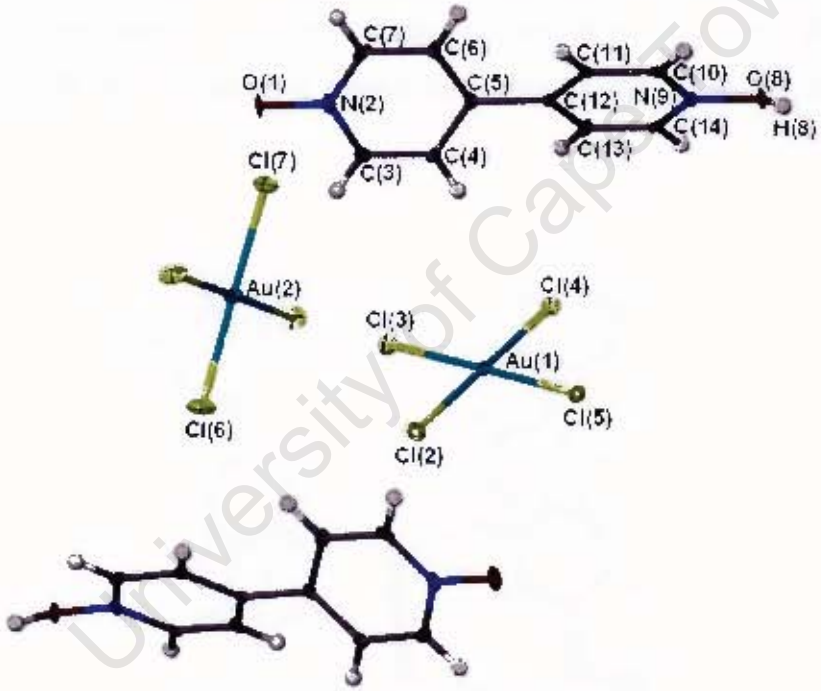

Figure 6.2: The asymmetric unit for **Au1** is labeled and thermal ellipsoids are drawn at 50% probability.

Au–Cl bonds have an average length of 2.285 Å and are all close to the expected value of 2.301 Å. Coordination bond angles ranged from 88.62° to 90.90°, deviating slightly from the expected value of 90°. One end of the bpdo molecule is protonated due to the Au(III) solution. H(8) was located on a difference electron density map and found to have a bond distance of 0.98 Å

which is an equivalent of a typical O–H bond. The hydrogen atom (attached to oxygen of the bpdo) was included in the structural refinement. The O–H bond connectivity gave rise to strong O–H···O hydrogen bonding with short O···O distance of 2.425 Å, which is within the usual range observed for short hydrogen bonds. Similar short O···O contacts of ~2.4 Å were reported by Asaji[2,3] and Hussain.[4,5,6] The bpdo molecules are linked by hydrogen bonding through protonated terminal and the oxygen of the opposite end forming H-bonded chain. The Au(III) metal centres are connected to the bpdo through C–H···Cl interactions. Hydrogen bonding interactions are demonstrated in Figure 6.3 and summarised in Table 6.2. The $[AuCl_4]^-$ square planes adopt alternating orientations giving rise to interionic Au···Cl interactions separated by 3.908 Å. The bpdo molecule has planar rings, but these are twisted by an angle of 31.15°. Full bond lengths and angles are given in the Appendix.

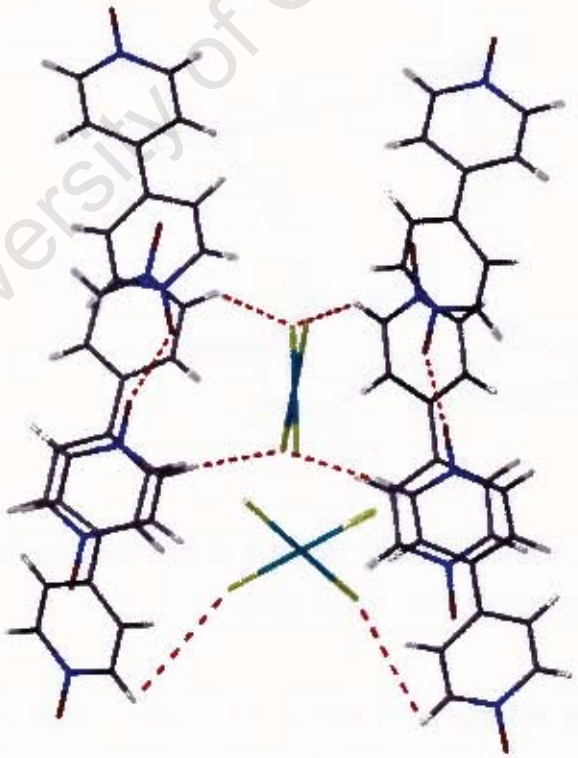

Figure 6.3: Hydrogen bonding interactions in **Au1**.

Table 6.2: Summarised hydrogen bonding interactions in **Au1**.

	D–H (Å)	D···A (Å)	D–H···A (°)	Symmetry operator
O(8) H(8)···O(1)	0.98	2.433 (5)	172	3/2-x, ½+y, z
C(7)–H(7)···Cl(2)	0.95	3.660 (5)	160	3/2-x, 3/2-y, -½+z
C(10)–H(10)··· Cl(6)	0.95	3.413 (5)	138	-½+x, ½+y, z
C(14)–H(14)··· Cl(5)	0.95	3.495 (5)	132	x, y, -1+z

The mirror planes are easily seen when the compound is packed along [010] and [001] (Figure 6.4).

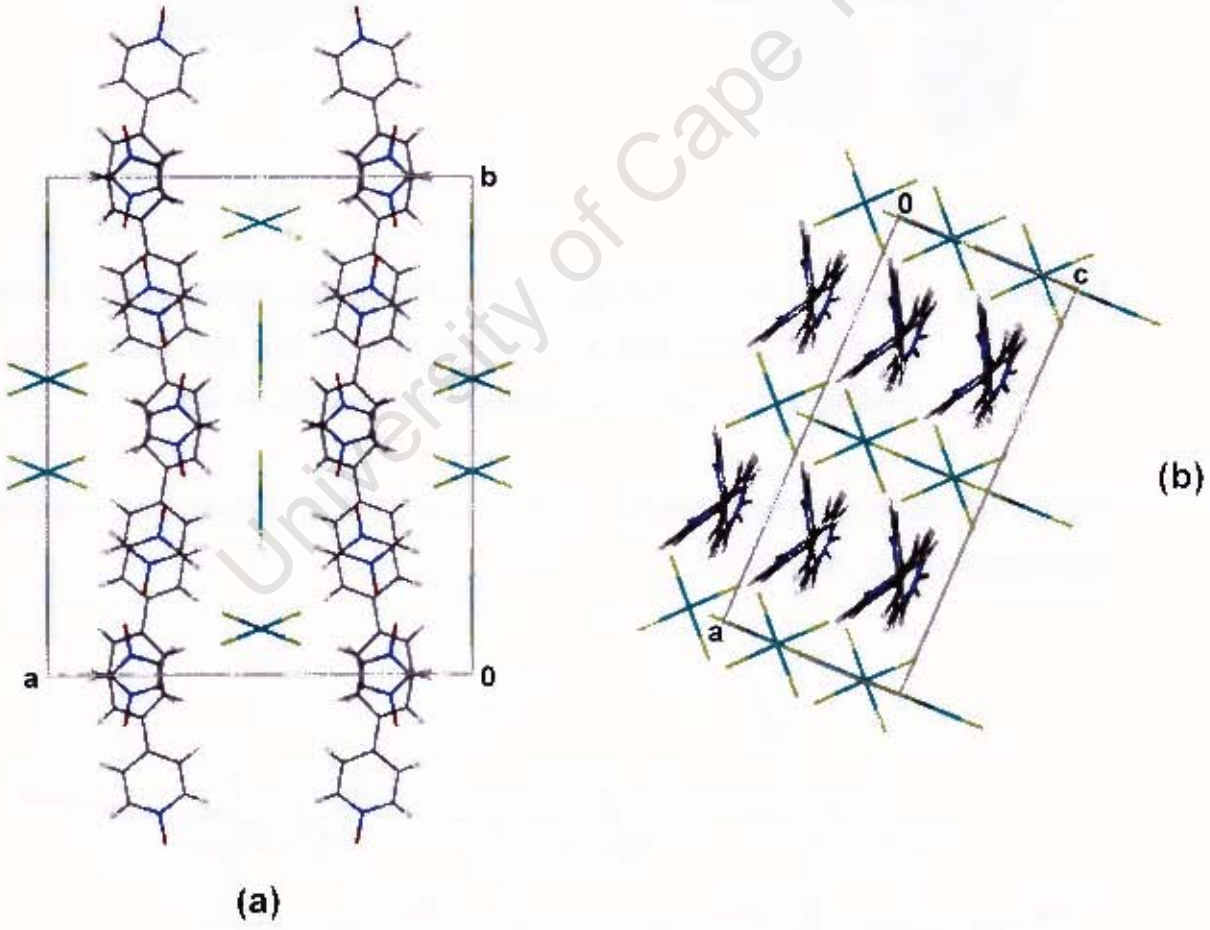

Figure 6.4: Packing diagrams in **Au1** along **(a)** [001] and **(b)** [010].

The **Au1** compound forms distinct layers of the $[AuCl_4]^-$ anions and H–bpdo$^+$ cations as illustrated in Figure 6.5.

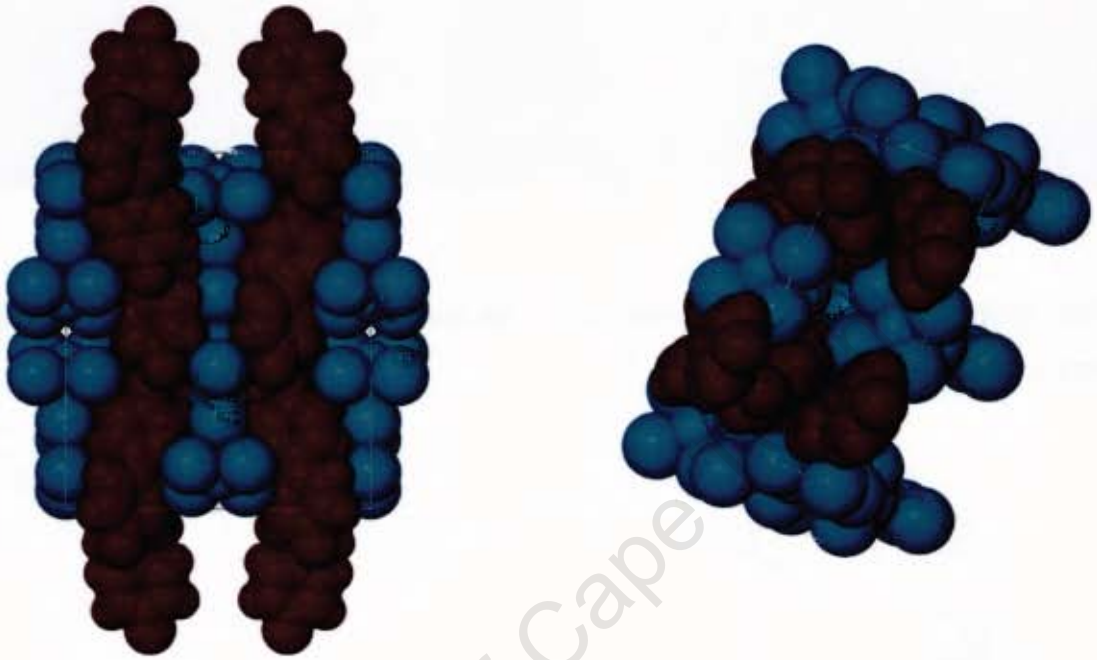

Figure 6.5: Packing diagrams in **Au1** compound viewed along **(a)** [001] and **(b)** [010]. Molecules are represented by van der Waals radii. $[AuCl_4]^-$ are in blue, while bpdo molecules are in red.

Figure 6.6 shows packed diagram viewed along [100] showing the twofold screw axis in the compound.

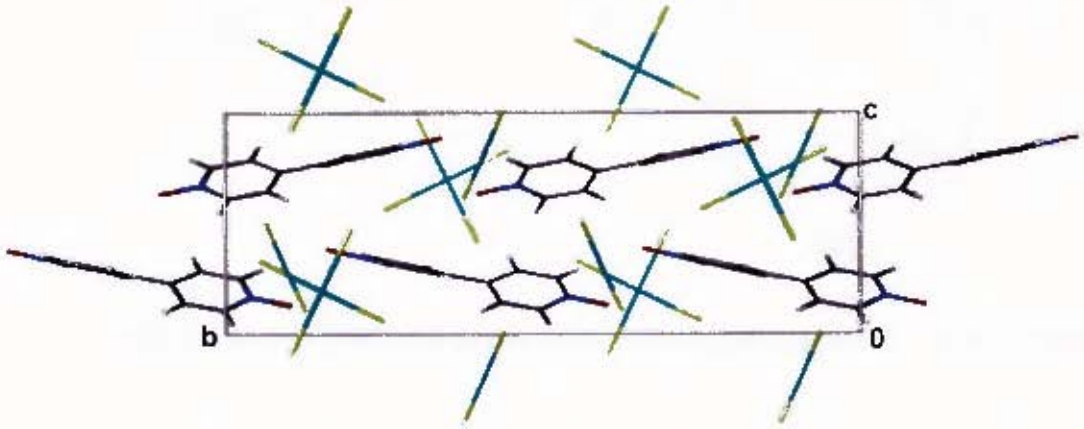

Figure 6.6: Packing of **Au1** viewed along [100] showing twofold screw axis.

Thermal Analysis

The TG and DSC traces of **Au1** are shown in Figure 6.7.

In **Au1**, TG trace consists of one step mass loss (Figure 6.7, region A). The compound is stable up to greater than 200 °C. This step indicates the decomposition of the compound. The DSC trace showed an exotherm (Figure 6.7, peak A with T_{on} = 248.2 °C) which corresponded to the TG mass loss.

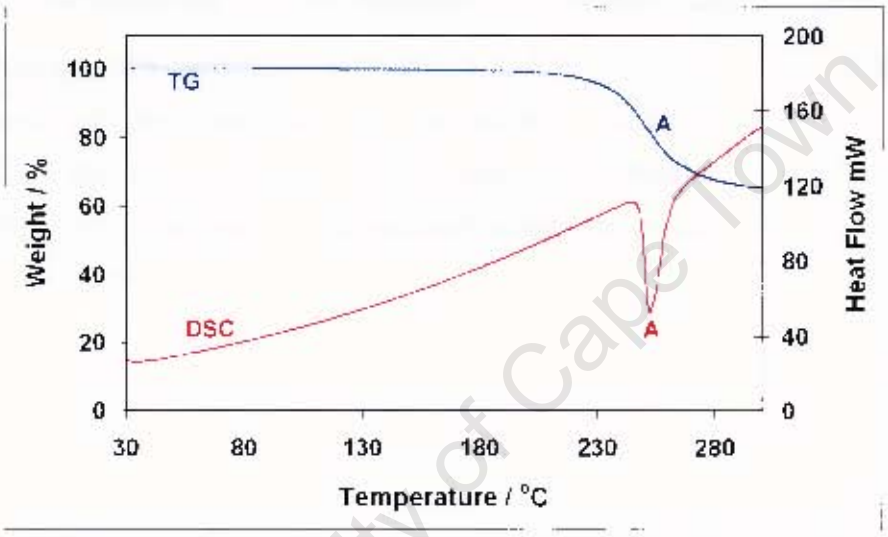

Figure 6.7: TG and DSC traces of **Au1**.

Hot Stage Microscopy

The thermal decay observed in **Au1** is shown in Figure 6.8.

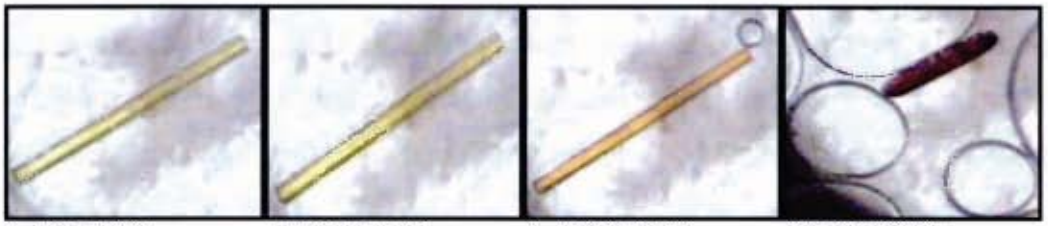

(a) 29.5 °C **(b) 110.9 °C** **(c) 245.4 °C** **(d) 275.0 °C**

Figure 6.8: Crystals of **Au1** during thermal decay. Photograph (a) the crystal is stable at room temperature, (b) crystal still stable, (c) crystal decay begins which continues until complete decomposition was observed at (d) 275.0 °C.

Structure solution and analysis

Au2 and Au3

Table 6.3: Crystal Data and Refinement Parameters of **Au2** and **Au3**.

Molecular Formula	$AuCl_4(C_{12}H_{14}N_2) \cdot Cl$	$AuCl_4(C_{12}H_{12}N_2) \cdot Cl$
Formula weight ($g.mol^{-1}$)	560.46	558.46
Temperature (K)	113	113
Wavelength (Å)	0.71073	0.71073
Crystal System	Triclinic	Triclinic
Space Group	$P\bar{1}$	$P\bar{1}$
a (Å)	7.339 (2)	7.280 (2)
b (Å)	7.503 (2)	7.562 (2)
c (Å)	7.928 (2)	7.796 (2)
α (°)	108.47 (3)	73.18 (3)
β (°)	90.31 (3)	89.43 (3)
γ (°)	96.27 (3)	81.95 (3)
Volume ($Å^3$)	411.22 (14)	406.53 (14)
Z	1	1
Calculated Density ($g.cm^{-3}$)	2.263	2.281
μ (mm^{-1})	9.746	9.858
F (000)	264	262
Crystal Size (mm)	0.06 X 0.08 X 0.10	0.03 x 0.06 x 0.07
θ Range Scanned (°)	3.27 - 26.10	2.73 - 26.43
Index Range	-9 < h < 9, -9 < k < 9, -9 < l < 9	-9 < h < 9, -9 < k < 9, -9 < l < 9
No. Reflections Collected	9811	9740
No. Unique Reflections	1624	1668
Data completeness (%)	99.1	99.6
Refinement Method	Full-matrix L.S. on F^2	Full-matrix L.S. on F^2
Data / Restraints / Parameters	1624 / 0 / 95	1668 / 0 / 95
Goodness-of-fit on F^2	1.092	1.053
Final *R* Indices $[I>2\sigma(I)]$	0.0179, 0.0377	0.0217, 0.0401
R Indices (all data)	0.0184, 0.0379	0.0232, 0.0406
Largest Diff. Peak and Hole ($e.Å^{-3}$)	0.767, -0.896	0.713, -1.032

Au2 and **Au3** are isostructural with respect to their similar molecular shape, similar unit cell parameters and atomic coordinates as shown in Table 6.3. Both compounds crystallise in the triclinic crystal system, space group $P\bar{1}$. The ligand, metal and the chloride ion are situated on a centre of inversions, *-1*, at Wyckoff positions *e*, *a* and *d*, respectively. In the crystal structure, the BPE (**Au2**) and DPE (**Au3**) dipyridyl ligands are found to be protonated on both nitrogen terminals. **Au2** structure will be discussed in detail. Thermal displacement and labeling of the asymmetric unit is shown in Figure 6.9. Only the asymmetric unit has been labeled.

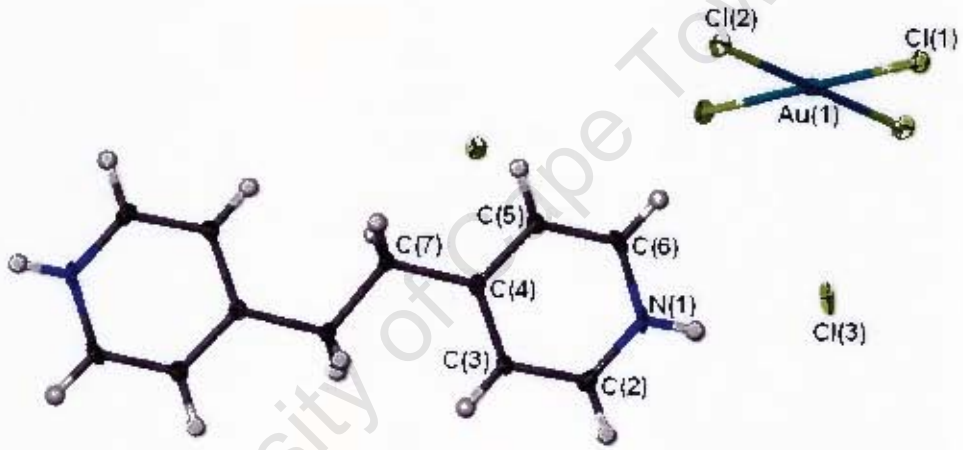

Figure 6.9: Thermal ellipsoids are drawn at 50% probability. The asymmetric unit for **Au2** is labeled.

All H-atoms were found on the difference electron density map, but the geminal atoms H(7A) and H(7B) and aromatic H-atoms were positioned geometrically with C–H = 0.99 Å (geminal), and 0.95 Å (aromatic ring) and all these H-atoms were refined with $U_{iso}(H) = 1.2U_{eq}(C)$. The N–H bond length found on the difference map was 1.01 Å. This hydrogen was refined with a fixed bond length and U_{iso}.

The metal environment in the complex is square planar with Au–Cl bond lengths at an average of 2.28 Å and Cl–Au–Cl bond angles of 89.68° and 90.32° (89.84° and 90.16° for **Au3**). The protonated ends of the dipyridyl are involved in N–H···Cl hydrogen bonding interactions linking the BPE molecules

forming a supramolecular chain. The Au(III) metal centres are connected through C–H···Cl interactions *via* BPE molecule. Hydrogen interactions are demonstrated in Figure 6.10 and results are summarised in Table 6.4.

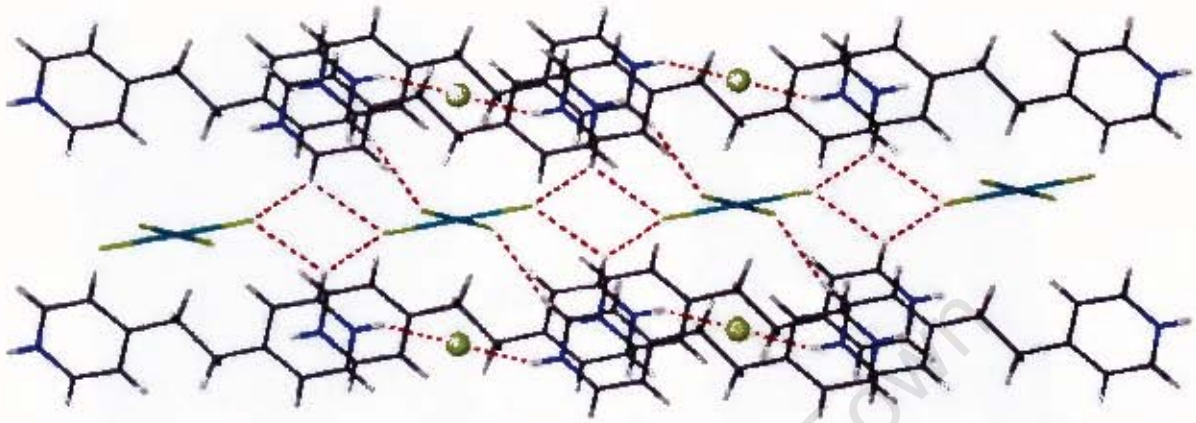

Figure 6.10: Illustration of H-bonds observed in **Au2** (similar for **Au3**).

Table 6.4: Summarised hydrogen bonding interactions for **Au2 and Au3**.

	D–H (Å)	D···A (Å)	D–H···A (°)	Symmetry operator
Au2				
N(1)–H(1)···Cl(3)	0.88	3.021 (2)	153	x, y, z
C(2)–H(2)···Cl(1)	0.95	3.557 (4)	145	1-x, -y, -z
C(6)–H(6)···Cl(2)	0.95	3.654 (3)	156	x, y, z
Au3				
N(1)–H(1)···Cl(4)	0.88	3.004 (3)	161	x, y, z
C(2)–H(2)···Cl(2)	0.95	3.575 (4)	154	1+x, 1+y, z
C(6)–H(6)···Cl(3)	0.95	3.657 (4)	163	-x, 1-y, -z

The crystal structure refinement revealed that there is a conventional Au(1)···Cl(3) interactions with interionic distances of 3.670 Å. Au···Cl interactions were also observed in some tetrachloroaurate(III) complexes reported by Asaji *et al.* (average interaction distances of 3.54 Å).[3,4] The $[AuCl_4]^-$ planes and the uncoordinated chloride ion forms supramolecular ladder shapes (Figure 6.11) with channels occupied by the BPE molecules (Figure 6.11 (b)). The presence of intermolecular Cl···Cl interaction with

distances of 4.48 Å seems to contribute to connect the $[AuCl_4]^-$ planes. The square planes form the upright while the chlorine atoms are the rungs of the ladder.

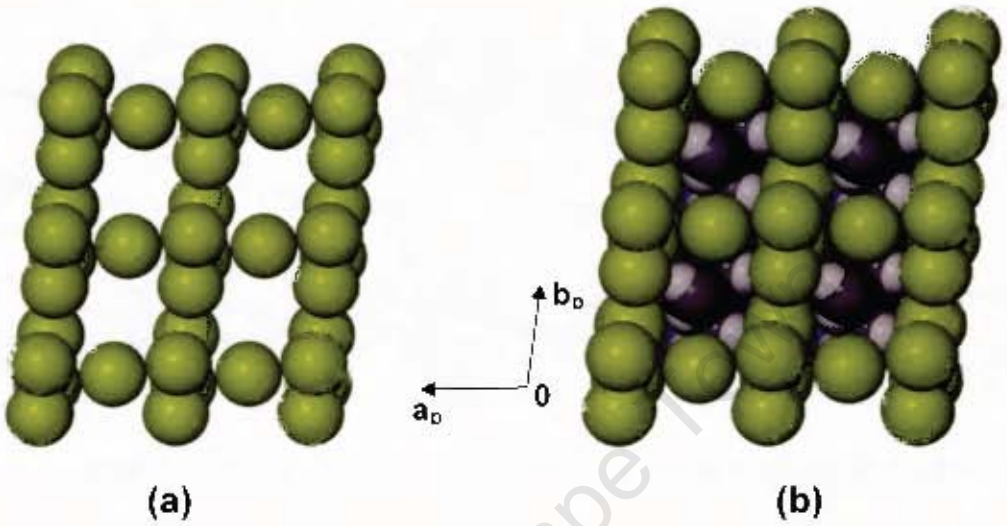

Figure 6.11: Crystal packing of **Au2** viewed along [001]. **(a)** Supramolecular ladder. BPE molecules are not shown. **(b)** BPE molecules are shown residing in channels.

The square planar and the chlorine sheets are running parallel to [100] as shown in Figure 6.12.

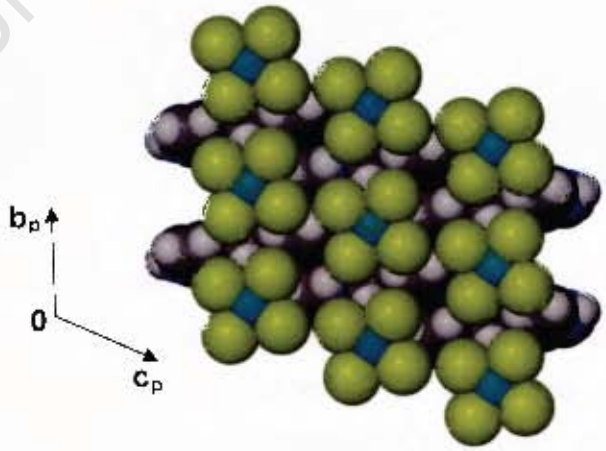

Figure 6.12: Packing of **Au2** viewed along [100] showing square planar and chlorine atom layers running parallel to [100].

Figure 6.13 shows packing diagrams of **Au2** and **Au3** viewed along [001], [010] and [001]. The crystal packings demonstrate similarities in **Au2** and **Au3** crystal structures. It is evident from the crystal packing diagrams (Figure 6.11) that the crystal structures consists of well separated centrosymmetric $[AuCl_4]^-$ anions, $[H_2(BPE)]^+$ cations and uncoordinated chloride ions.

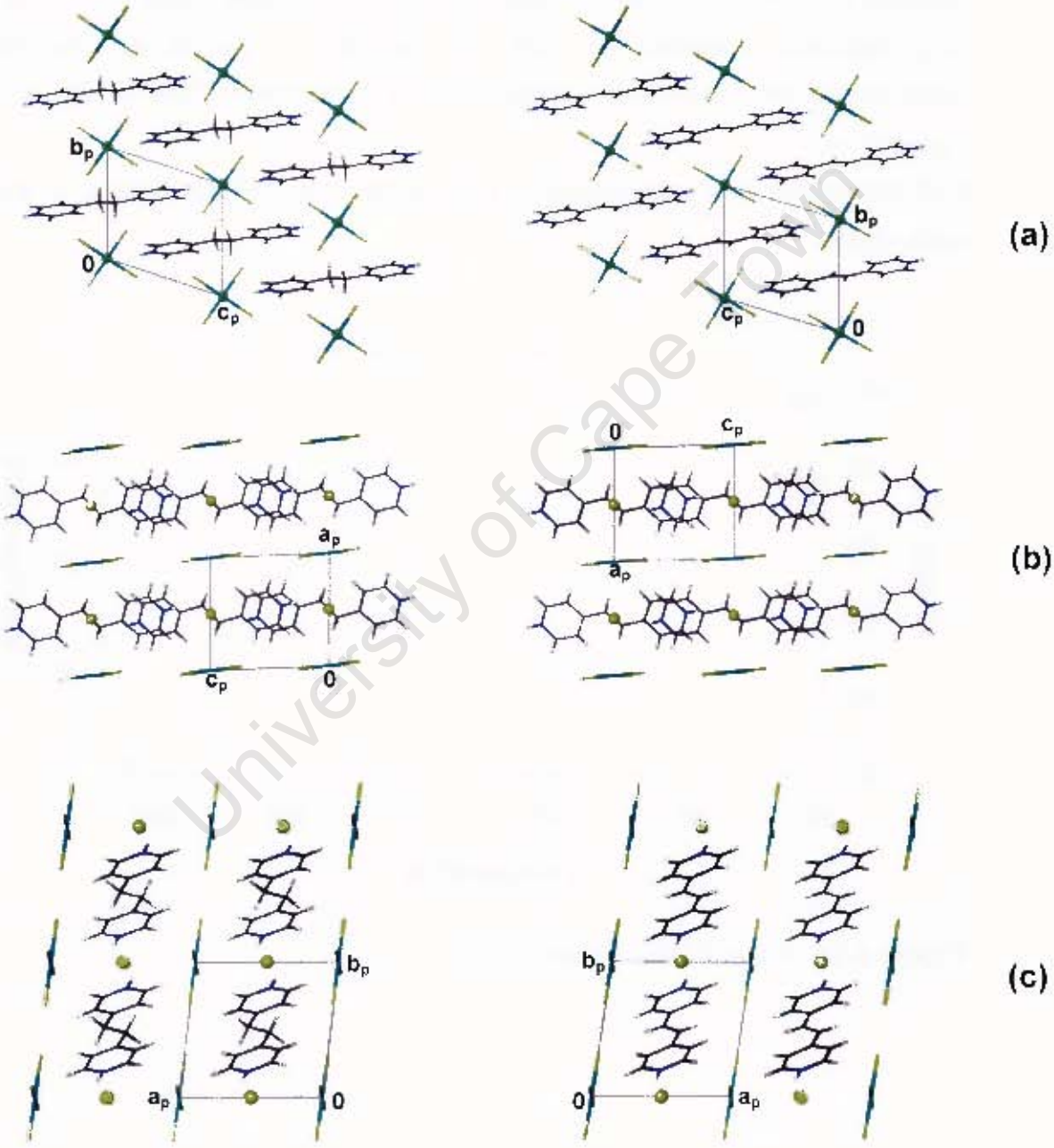

Figure 6.13: Packing diagrams for **Au1** (left) and **Au2** (right) showing packing similarities. Crystals structures are packed along **(a)** [001], **(b)** [010] and **(c)** [001].

Thermal Analysis

TG trace observed in **Au2** consists of three step mass loss. All the mass losses are consecutive and hence difficult to separate accurately. The most likely decomposition mechanism for this compound involves loss of BPE followed (or concurrent with) by loss of HCl (the calculated mass loss of 39.5 % corresponds reasonably well with that observed in Figure 6.14). The DSC trace shows two endotherms followed by an exortherm. This is shown in Figure 6.14.

Au3 compound was comparable to **Au2**, hence only TG/DSC traces of **Au2** were shown.

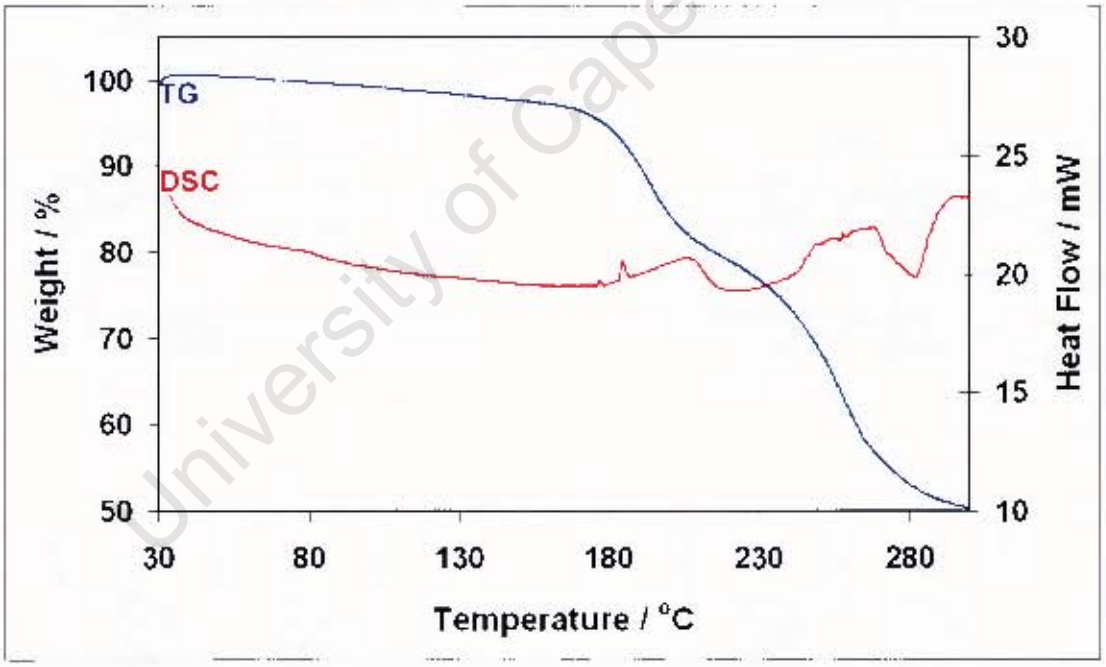

Figure 6.14: TG and DSC traces of **Au2**.

Hotstage microscopy

The thermal decomposition observed in **Au2** (similar for **Au3**) is shown in Figure 6.15.

(a) 31.4 °C **(b) 135.5 °C** **(c) 218.1 °C** **(d) 235.2 °C**

Figure 6.15: Crystals of **Au2** during thermal decomposition. Photograph (a) the crystal is stable at room temperature, (b) and (c) bubbles depicting release of HCl and BPE (d) decomposition was complete by 235.2 °C.

Infrared (IR) spectroscopy

IR analysis was performed to confirm the protonation of dipyridyl ligands. IR spectra were run for (A) dried ligands, (B) ligand kneaded with a small amount of HCl and (C) crystalline material, all as KBr disks. DPE spectra were not included as they are comparable to BPE.

Figure 6.16 shows the IR spectra of bpdo only (A: red), bpdo·HCl (B: blue) and **Au1** (C: pink). The broad bands centred around 800 cm^{-1} which were observed in B and C are indicative of a short O–H···O hydrogen bond, similar to that observed in protonated pyridine N-oxide.[5] υ(N–O) is seen at 1231 cm^{-1} in C, compared to 1241 cm^{-1} in dry bpdo and 1205 cm^{-1} in bpdo·HCl. The broad band near 3400 cm^{-1} in all the three is probably due to moisture.[7]

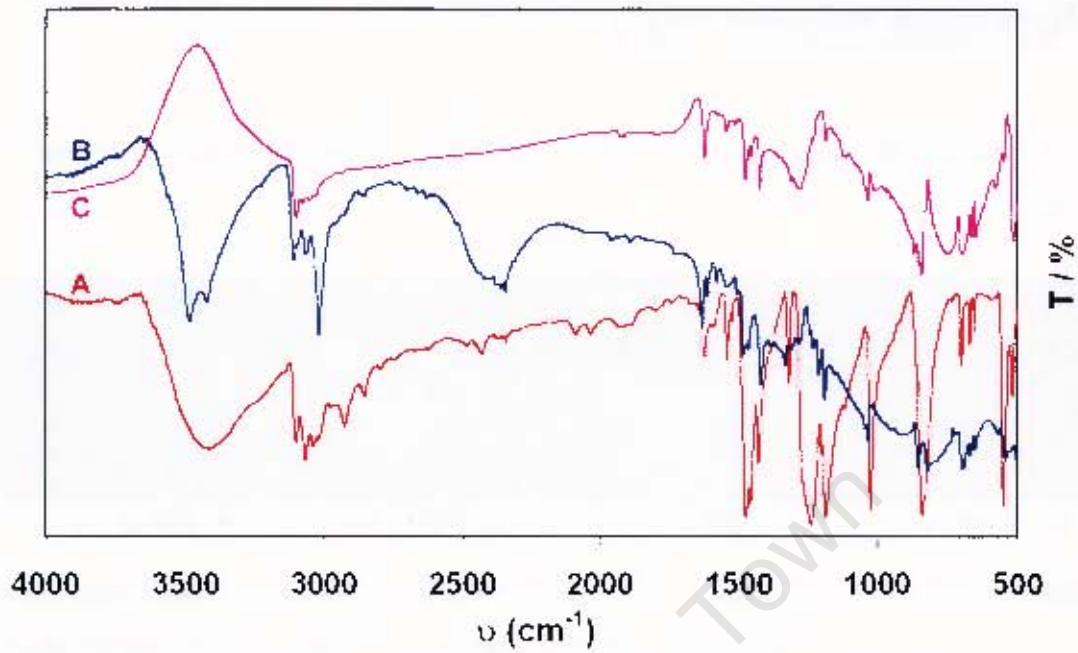

Figure 6.16: The IR spectrum of bpdo only (red) and protonated bpdo (blue).

Figure 6.17 shows an overlaid IR spectra of dry BPE (A: red), BPE·HCl (B: blue) and **Au2** (C: pink). υ(N H), expected between 3100 – 3000 cm^{-1}, is obscured by the broad bands in each case.

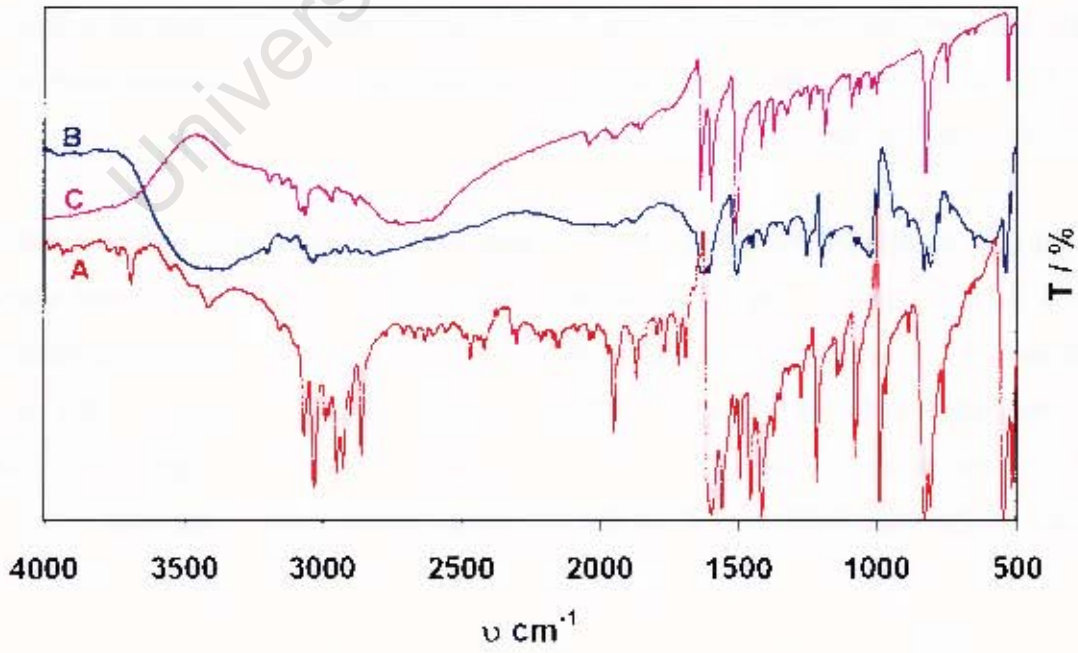

Figure 6.17: The IR spectrum of BPE only (red) and protonated BPE (blue).

Discussion and conclusion

Crystal structures refined and elucidated in this chapter showed square planar metal geometries ($[AuCl_4]^-$) and cationic dipyridyl ligands.

Au1 is composed of distinct layers of $[AuCl_4]^-$ anions and bpdo molecules. One terminal of bpdo was protonated allowing hydrogen bonding to occur. These are short hydrogen bonding interactions that connect the bpdo cations into supramolecular chains. The metal centres are connected to these chains through C–H···Cl interactions.

Au2 and **Au3** have supramolecular ladders formed by the $[AuCl_4]$ and chloride ions. These ladders form channels which are occupied by BPE or DPE cations. The BPE and DPE are protonated on both ends giving rise to hydrogen bonding interactions which link dipyridyl ligands into supramolecular chains. Similarly, the metal centres are connected to the organic chains through C–H···Cl interactions.

All the Au(III) compounds prepared in this study have interionic Au···Cl interactions similar to those reported by Asaji *et al.*[3]

An analogues pyridinium ligand, (2,6-Diphenylpyridinium), adopted NH...Cl–Au synthon that is different to those reported in this study.[8]

A series of related organic-inorganic hybrid salts based on tetrachloroplatinate $[PtCl_4]^2$ and tetrachloropalladate $[PdCl_4]^{2-}$ with organic cations containing pyridinium and piperidinium groups have been reported.[9, 10] Unlike in **Au2** and **Au3**, the BPE and DPE ligands form bifurcated hydrogen-bonded 1D ribbons in which two Cl^- act as acceptors. These salts contain the ligand in a planar conformation, similar to the compounds reported in this thesis. A similar kind of N–H...$[Cl_2MCl_2]^{2-}$ synthon ribbon motif was also observed in perchlorocuprates.[11,12] Two fluoromanganates(III) of BPE and DPE: $(BPEH_2)$ $[MnF_4(H_2O)_2]_2$ and $(DPEH_2)$ $[MnF_4(H_2O)_2]_2$ were prepared.[13] The $[MnF_4(H_2O)_2]_2^-$ anion displays an octahedral geometry. The organic cations are linked to the anionic octahedral by strong N–H...F hydrogen bond synthon. The anions are linked to a puckered 2D network through hydrogen bonding between coordinated water and fluorine atoms.

The reaction mixture which contained $[Co(H_2O)[ClO_4]_2$, neutral 2.2'-dipyridylamine (Hdpa) and an acidic solution of HCl in a methanol/acetonitrile mixture produced crystal of a cation containing H_2dpa^- species and corresponding anion $[CoCl_4]^{2-}$.[14] The tetrachlorocolbaltate anion adopts the tetrahedral coordination geometry. The ions are linked through hydrogen bonds between N–H bond and a chloride ion of the $[CoCl_4]^{2-}$.

Furthermore, a compound bis(3,3'-dimethylene-2,2-biquinolium) tetrabromo-aurate(III) dibromoaurate (I) $\{(C_{20}H_{15}N_2)[AuBr_3]\}$. which consists of two anions $\{[AuBr_4]^-$ and $\{[AuBr_2]^-$ have been reported.[15] The $[AuBr_4]^-$ anion has a traditional square planar geometry while $[AuBr_2]^-$ is linear. Hydrogen bonding between C –H... Br contribute to the cohesion of the structure.

References

1. F.H. Allen, O. Kennard, D.G. Watson, L. Brammer, A.G. Orpen, R. Taylor, *J. Chem. Soc. Perkin Trans.*, 1989, S1-S83.
2. T. Asaji, F. Tajima, M. Hashimoto, *Polyhedron*, 2002, **21**, 2207.
3. T. Asaji, E. Akiyama, F. Tajima, K. Eda, M. Hashimoto, Y. Furukawa, *Polyhedron*, 2004, **23**, 1605.
4. M.S. Hussain, E. O. Schlemper, *J. Chem. Soc., Dalton Trans.*, 1982, 751.
5. M.S. Hussain, S. A. A. Al-Hamoud, *Inorg. Chim. Acta*, 1984, **82**, 111.
6. M.S. Hussain, *Permagon*, 1996, **15**, 645.
7. D.B. Brown, A.J. Floyd, M. Sainsbury, Organic Spectroscopy, Chapter 3, John Wiley and Sons Ltd, New Delhi, 1988.
8. G.P.A. Yap, A.L. Rheingold, P. Das, R.H. Crabtree, *Inorg. Chem.*, 34, 3474.
9. A. Angeloni, A.G. Orpen, *Chem. Commun.*, 2001, 343.
10. C.J. Adams, A. Angeloni, A.G. Orpen, T.J. Podestra, B. Shore, *Cryst. Growth and Des.*, 2005, **6**, 411.
11. D. K. Kumar, A. Ballabh, D.A. Jose, P. Dastidar, A. Das, *Cryst. Growth and Des.*, 2005, **5**, 651.
12. D. K. Kumar, A. Mas, P. Dastidar, *Cryst. Growth and Des.*, 2005, **6**, 216.
13. P. Núñez, J.C. Ruiz-Morales, A.D. Lozano-Gorrin, P. Gili, V.D. Rodriguez, J. Gonzalea-Pltas, T. Barriuso, F. Rodriquez, *Dalton. Trans.*, 2004, 273.
14. F.A. Cotton, L.M. Daniels, G. T. Jordan IV, C.A. Murillo, *Polyhedron*, 1998, **17**, 589.
15. R.F. Baggio, *Acta Crystallogr.*, 1994, **C50**, 1701.

Chapter 7

(a) Coordination polymers of Lanthanides using bpdo: Crystal structures and kinetics study.

(b) A coordination polymer of uranyl(VI) nitrate with bpdo.

(a) Coordination polymers of Lanthanides using bpdo.

Different coordination polymers of Gd(III), Tb(III), and Tl(III) were prepared using bpdo and characterised by thermal analysis (TG, DSC and HSM determine the stability and stoichiometry of a compound) and microanalysis (to confirm elemental composition of compounds). Thallium is not a lanthanide; it has been included in this chapter as it has characteristics similar to those of lanthanides. Crystal structures have been refined and elucidated by single x-ray diffractometry.

Crystal structures obtained had either a 1D zigzag shape (which extends to 3D through interchain hydrogen bonding) or 2D ladder shapes. The latter formed structures with channels that permit the inclusion of small entities such as CH_2Cl_2 and $CHCl_3$.

These polymers have guest-free frameworks which are thermally stable up to >200°C. Kinetics of desolvation of CH_2Cl_2 and $CHCl_3$ guest molecules and decomposition of the structure framework using isothermal TG have also been studied. Elemental analysis corresponded well with the stoichiometries of the elucidated crystal structures.

Crystallographic data, experimental and refinement parameters are given in Table 7.3. 7.7 and 7.12. Final atomic coordinates, bond lengths and angles, torsion angles, thermal parameters and tables of observed and calculated structure factors for each of the crystal structure are given in the appendices.

Preparation of polymers

Suitable crystals for data collection of coordination polymers were obtained by solvent layering at ambient temperature (295 K – 298 K) using the method described in Chapter 2. These polymers were crystallised by layering of alcoholic solutions on top of chlorinated solvents.

The compounds obtained as well as their abbreviations are as follows:

Part (A)

$[Gd(NO_3)_3(bpdo)CH_3OH]_n$: **Gd1**

$[Tb(NO_3)_3(bpdo)CH_3OH]_n$: **Tb1**

$[Tl(NO_3)_3(bpdo)CH_3OH]_n$: **Tl1**

Part (B)

$[Gd_2(NO_3)_6(bpdo)_3]_n \cdot 2CH_2Cl_2$: **Gd2**

$[Gd_2(NO_3)_6(bpdo)_3]_n \cdot 2CHCl_3$: **Gd3**

$[Tl_2(NO_3)_6(bpdo)_3]_n \cdot 2CH_2Cl_2$: **Tl2**

Microanalysis

Elemental analysis results are given in Table 7.1 and 7.2. The experimental elemental mass percentages corresponded well with the calculated. The small discrepancies observed could be attributed to the preparative techniques used during microanalysis. Elemental analysis for **Tl1** and **Tl2** was not done due to the limited sample prepared and experiments using thallium metal salt were discontinued due to its harmful characteristics. Only crystal structure elucidation and thermal analysis will later be discussed in this chapter.

Table 7.1: Elemental analysis results for **Gd1** and **Tb1**

Element	Gd1		Tb1	
	Found %	Calc. %	Found %	Calc. %
C	22.67	23.45	22.88	23.38
H	1.59	2.15	1.65	2.14
N	11.55	12.43	11.47	12.39

Table 7.2: Elemental analysis results for **Gd2** and **Gd3**.

Element	Gd2		Gd3	
	Found %	Calc. %	Found %	Calc. %
C	27.13	27.04	25.70	25.79
H	1.61	1.99	1.47	1.76
N	11.67	11.83	10.84	11.28

PXRD

The calculated (red) and experimental (blue) PXRD patterns for **Gd1**, **Tb1**, **Gd2** and **Gd3** are shown in Figures 7.1 – 7.4. The calculated and experimental PXRD patterns for **Gd1** are a good match (Figure 7.1).

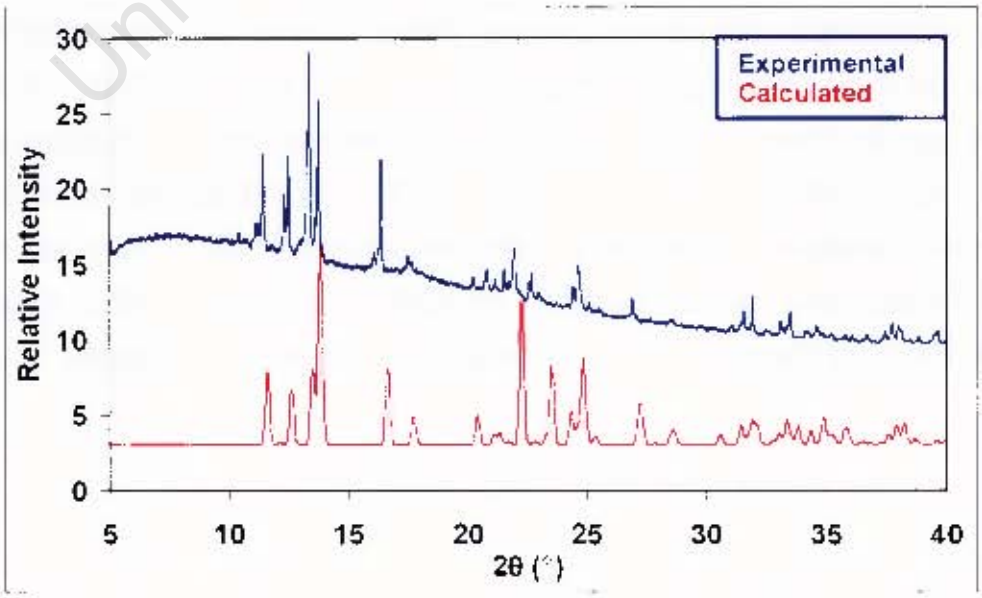

Figure 7.1: An overlay PXRD patterns for **Gd1** compound.

The calculated and experimental PXRD patterns for **Tb1** matched (Figure 7.2).

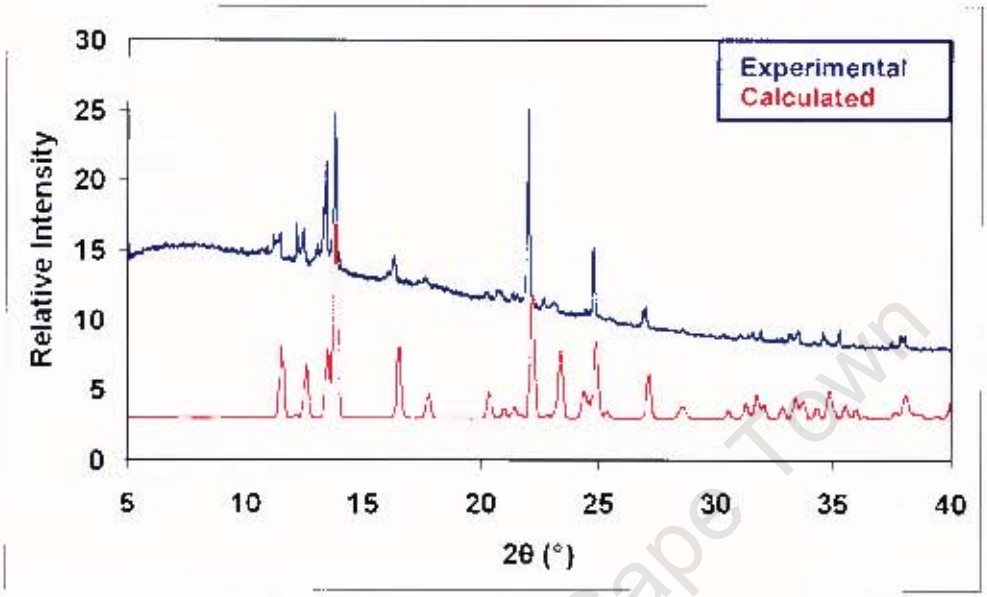

Figure 7.2: An overlay PXRD patterns for **Tb1** compound.

The calculated and experimental PXRD patterns for **Gd2** are also a good match (Figure 7.3).

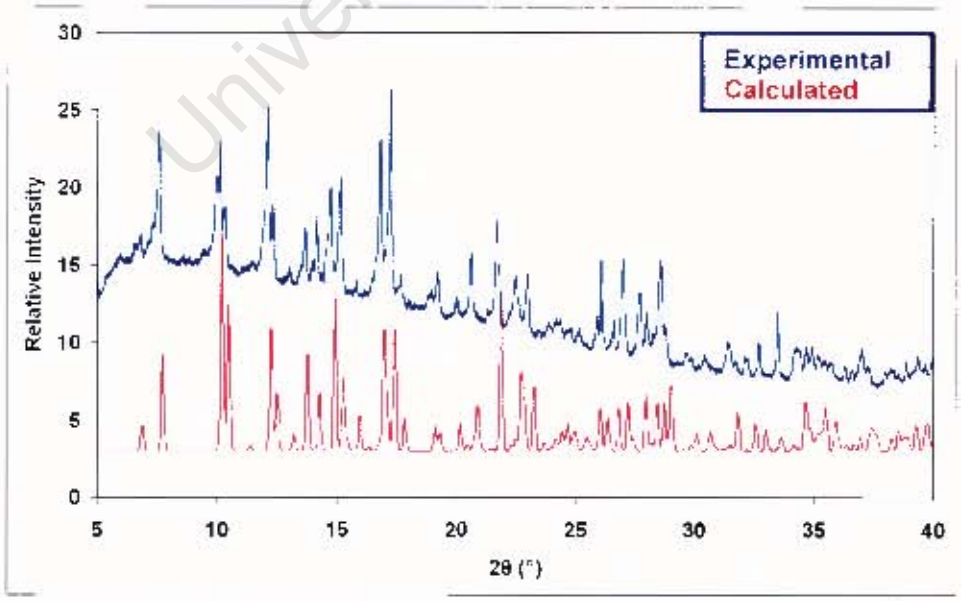

Figure 7.3: An overlay PXRD patterns for **Gd2** compound.

The calculated and experimental PXRD patterns for **Gd3** are generally a match (Figure 7.4). There are some extra peaks at low 2θ (5 – 10) in the experimental pattern which could be due to the loss of some solvent caused by sample preparation prior analysis.

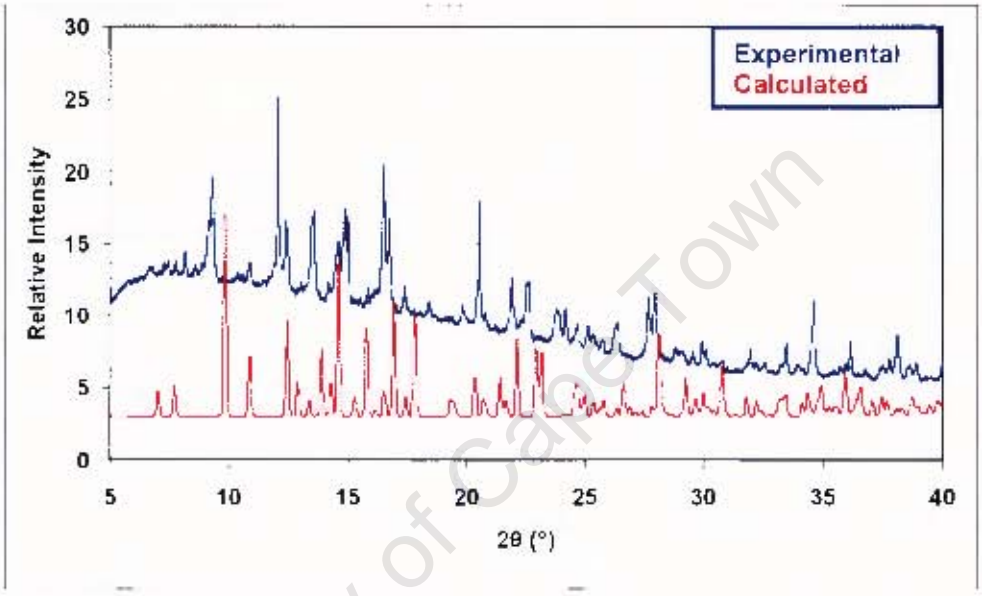

Figure 7.4: PXRD patterns for **Gd3** compound.

Crystal solution and refinement

Gd1, Tb1 and Tl1

Table 7.3: Crystal Data and Refinement Parameters of **Gd1**, **Tb1** and **Tl1**.

Molecular Formula	$Gd(NO_3)_3$ $(C_{10}H_8N_2O_2)CH_3OH$	$Tb(NO_3)_3$ $(C_{10}H_8N_2O_2)CH_3OH$	$Tl(NO_3)_3$ $(C_{10}H_8N_2O_2)CH_3OH$
Formula weight (g mol^{-1})	563.48	565.18	610.63
Temperature (K)	203	203	203
Wavelength (Å)	0.71073	0.71073	0.71073
Crystal System	Monoclinic	Monoclinic	Monoclinic
Space Group	*C2/c*	*C2/c*	*C2/c*
a (Å)	15.3284(4)	15.4010 (4)	15.337 (3)
b (Å)	8.3355(5)	8.2992 (2)	8.337 (2)
c (Å)	14.0833(4)	14.1139 (4)	14.091 (3)
α (°)	90	90	90
β (°)	93.318 (1)	93.7006 (15)	93.40 (3)
γ (°)	90	90	90
Volume (Å^3)	1796.4 (1)	1800.22 (8)	1798.6 (6)
Z	4	4	4
Calc. Density (g.cm^{-3})	2.084	2.085	2.255
μ (mm^{-1})	3.768	4.004	9.057
F (000)	1092	1096	1160
Crystal Size (mm)	0.03 x 0.06 x 0.10	0.04 x 0.06 0.10	0.09 x 0.10 x 0.10
θ Range Scanned (°)	1.02 – 27.48	1.00 – 25.03	1.02 – 27.48
Index Range	-19 < h < 19, -10 < k < 10, -18 < l < 18	-18 < h < 18, -9 < k < 9, -16 < l < 16	-19 < h < 19, -10 < k < 10, -17 < l < 18
No. Reflections Collected	12793	9905	12558
No. Unique Reflections	2050	1589	1975
Data completeness (%)	99.3	99.8	95.7
Refinement Method	Full-matrix L.S. on F^2	Full-matrix L.S. on F^2	Full-matrix L.S. on F^2
Data / Restraints / Parameters	2050 / 0 / 156	1589 / 0 / 161	1975 / 0 / 156
Goodness-of-fit on F^2	1.085	1.115	1.206
Final R Indices [$I>2\sigma(I)$]	0.0235, 0.0477	0.0235, 0.0494	0.0378, 0.1101
R Indices (all data)	0.0346, 0.0501	0.0297, 0.0517	0.0435, 0.1129
Largest Diff. Peak and Hole (e.Å^{-3})	0.80, -1.61	0.39, -0.56	0.98, -2.17

Gd1, **Tb1** and **Tl1** are isostructural, so their description will mainly be outlined with reference to **Gd1**, but crystallographic interactions will be tabulated for all prepared crystal structures.

The initial data processing of this compound suggested the space group $P2_1/n$ with unit cell parameters a = 14.0910 b = 16.6740 c = 15.3375 β = 93.40, but the structure could not be solved in this space group. Careful inspection of data revealed systematic absences consistent with C-centering and a peculiar absence condition of k=4n on 0k0 reflections. Transformation of the unit cell via the matrix

$$\begin{bmatrix} 0 & 0 & 1 \\ 0 & -0.5 & 0 \\ 1 & 0 & 0 \end{bmatrix}$$

produced a new unit cell with parameters a = 15.337 Å, b = 8.337 Å, c = 14.091 Å, β = 93.40° which could be solved in space group *C2/c*. The asymmetric unit is composed of half a molecule. The ligand lie on a centre of inversion, *-1*, at Wyckoff position c, while the metal have a twofold axis at Wyckoff position e. Figure 7.5(A) shows the thermal ellipsoids and labeling of **Gd1**. This compound adopts irregular octahedral symmetry.

Gd1 is a one-dimensional zigzag coordination polymer (Figure 7.6) in which the Gd^{III} is coordinated by one bpdo, one methanol and three nitrate ligands. The Gd–O bond lengths are in the range 2.285 – 2.573 Å and thus close to expected values.[1] The C_2 symmetry of the molecule causes one of the nitrate ligands and the methanol to be disordered over two positions with symmetry-defined site-occupancy factors of 0.5. All non-H atoms were refined anisotropically, except for O(9) of the disordered methanol. The deepest residual electron-density hole is 0.88 Å from the Gd atom. Figure 7.5 (A) shows the disordered molecule while (B) and (C) shows disconnected branch of the disorder to clarify atomic orientation. All the nitrate ligands are bidentate, giving nine-coordinated Gd. The metal centers are connected by the bpdo ligand. The zigzag polymeric chains run in parallel to [101] (Figure 7.6).

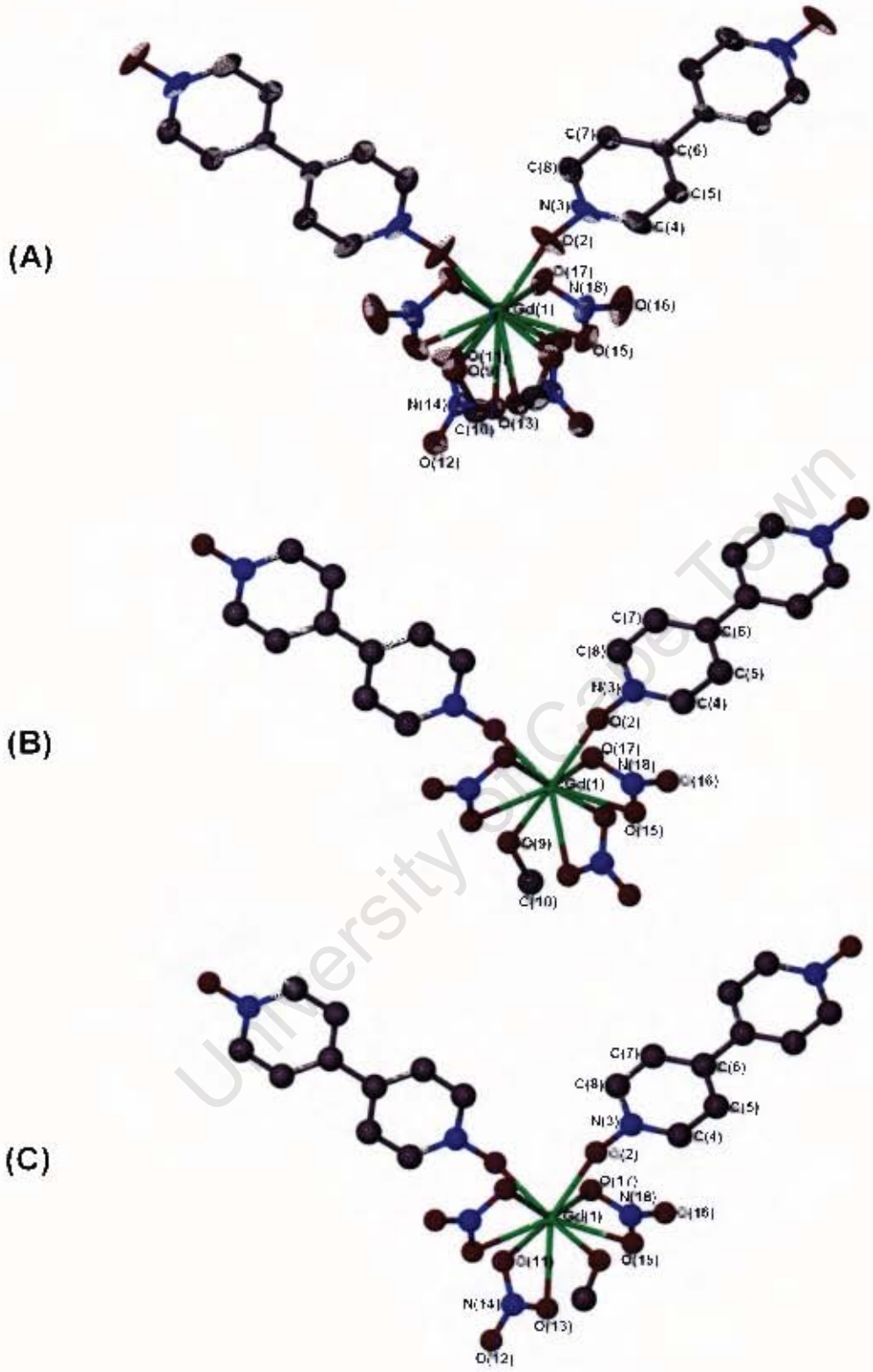

Figure 7.5: **(A)** Part of the polymeric chain structure of **Gd1** showing the atom labeling. Displacement ellipsoids are drawn at 50% probability and H–atoms are omitted for clarity. Atoms of the asymmetric unit are labeled.

These chains are linked by weak hydrogen bonding through (methanol)C–H···O(nitrate) and C_{ar}–H···O(nitrate) (Figure 7.7). The hydrogen bonding details are given in Table 7.4.

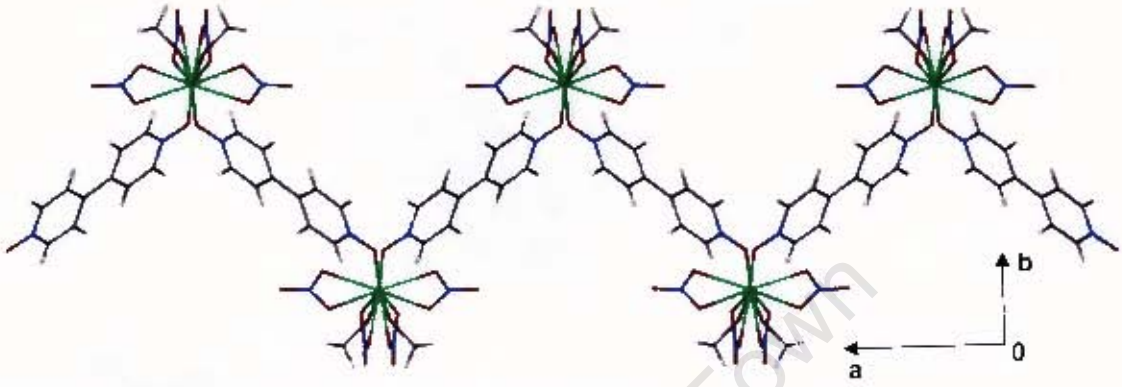

Figure 7.6: The zigzag polymeric chain in **Gd1**.

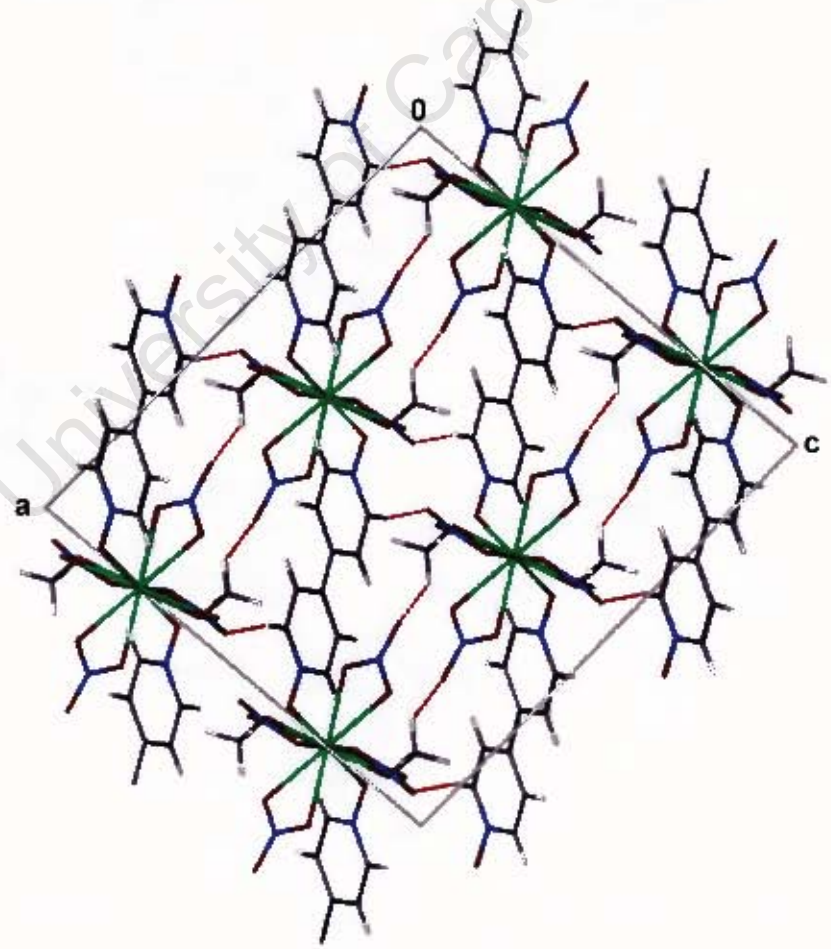

Figure 7.7: Packing of **Gd1** compound, viewed along [010], showing hydrogen bonds and polymeric chains running parallel to [101].

Table 7.4: Hydrogen bonding details.

	D–H (Å)	D···A (Å)	D–H···A (°)	Symmetry operator
Gd1				
C(4)–H(4)···O(12)	0.94	3.281 (5)	169	½-x, -½+y, 3/2-z
C(10)–(10A)···O(16)	0.97	2.861 (9)	111	x, -y, ½+z
Tb1				
C(4)–H(4)···O12	0.94	3.293 (6)	169	1-x, -y, -z
C(10)–(10C)···O(16)	0.97	2.894 (11)	112	½+x, -½+y, z
Tl1				
C(4)–H(4)···O12	0.94	3.286 (10)	169	x, -y, z-½
C(10)–(10A)···O(16)	0.97	2.90 (2)	112	x+½, y-½, -z+½

Isostructurality

Tb1 and **Tl1** polymers are isostructural to **Gd1**, with respect to similar molecular shapes, similar unit cell parameters and similar atomic coordinates as detailed in Table 7.3. The thermal displacement diagrams of **Tb1** and **Tl1** compounds are shown in Figure 7.8, and the packing diagrams thereof are illustrated in Figure 7.9. Hydrogen bonding details can be seen in Table 7.4. The Tb–O and Tl–O bond lengths are in the range 2.275 – 2.552 Å and 2.284 – 2.569 Å respectively and thus close to expected values. The Tb compound had been reported by Long *et al.*[2]

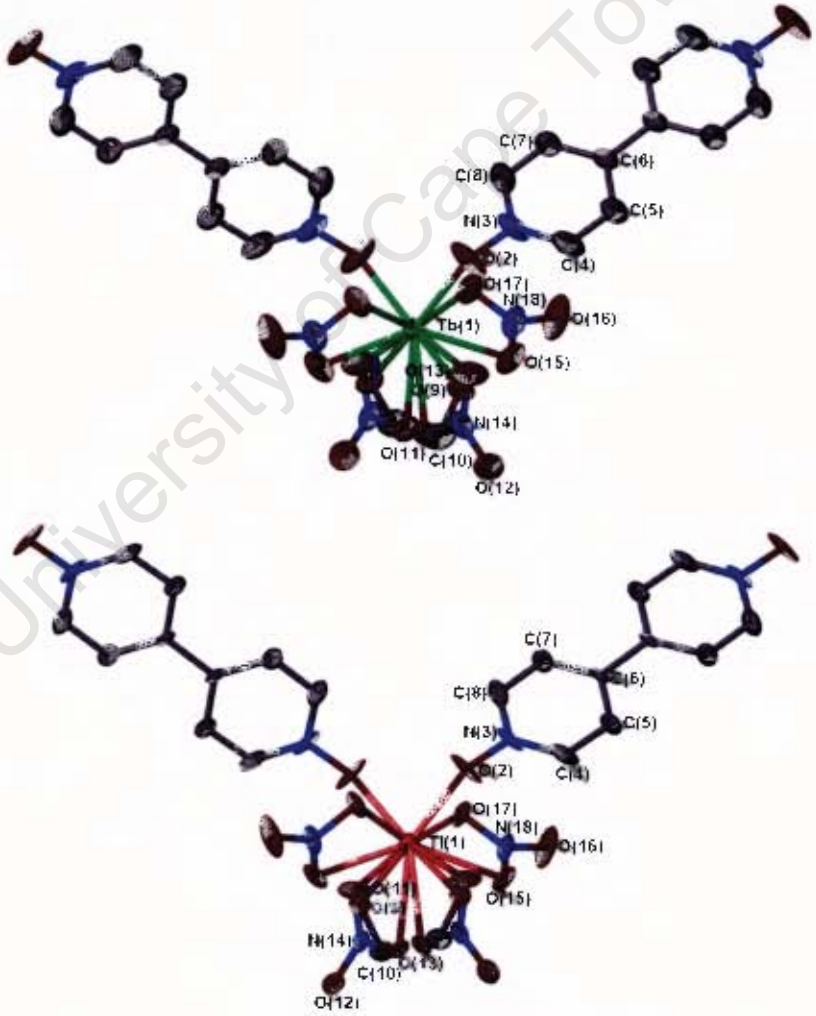

Figure 7.8: Part of the polymeric chain structure of **Tb1** and **Tl1** showing the atom labeling. Displacement ellipsoids are drawn at 50% probability and H-atoms are omitted for clarity. Atoms of the asymmetric unit are labeled.

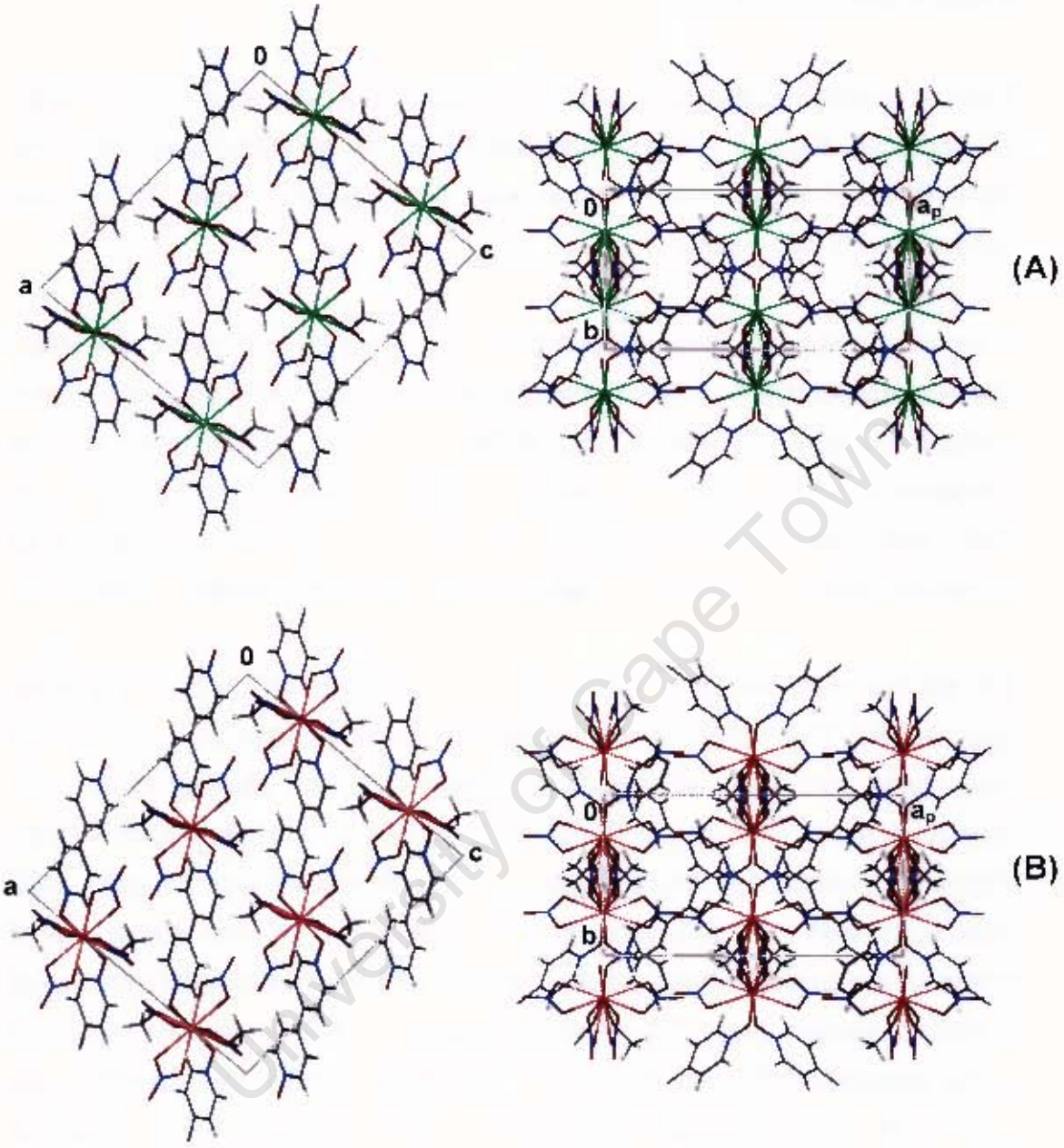

Figure 7.9: Packing diagrams of **(A) Tb1** and **(B) Tl1**, respectively viewed along [010] and [001], showing isostructurality in these compounds.

Thermal analysis

Thermal analysis of the lanthanide coordination polymers was carried out by TG and DSC. Figures 7.10(a)–(c) shows the combined TG/DSC traces of the **Gd1**, **Tb1** and **TI1** polymers, respectively. The TG/DSC traces for **Tb1** are comparable to **Gd1** traces.

In Figure 7.10(a), TG trace shows a three step mass loss. The first step mass loss is associated with desorption of methanol coordinated to the metal centre (details are given in Table 7.5). Methanol release occurs over a wide temperature range (region A) as shown in Figure 7.10(a). The compound is so labile that experimental methanol loss (2.99 %) did not correspond to calculated mass loss (5.69). Similarly for **Tb1** compound (details in Table 7.5).

The second mass loss of 11.88 % does not correspond to the loss of a whole bpdo moiety. Therefore we surmise that this decomposition step results in a new stable compound of unknown composition (after heating to 250 °C, microanalysis corresponds to $Gd(NO_3)_3(C_{10}H_6NO)$ as possible stoichiometry). Figure 7.11 shows the PXRD patterns of this compound and the calculated pattern for **Gd1**. The experimental pattern shows a different compound of unknown composition. Nevertheless we have analysed the kinetics (discussed in kinetics section, page 257) which corresponds to this partial decomposition of the compound. We note that for the **Tb1** compound this second mass loss is 7.31 %, significantly different from the **Gd1** compound. This implies a different decomposition reaction, which is confirmed by the differing values of the activation energies.

Mass loss C is the complete decomposition of a compound. The TG mass losses corresponds to endotherm A, exotherms B and C in the DSC trace (Figure 7.10(a)). DSC onset temperatures are summarised in Table 7.5.

In Figure 7.10(c), TG trace shows a three step mass loss. The first step mass loss is attributed to loss of methanol (Table 7.5). The experimental methanol loss corresponds to calculated mass loss. The second step corresponds to this partial decomposition of the compound, while mass loss C is the complete decomposition of a compound. The DSC could not resolve the first thermal event observed in the TG trace (Figure 7.10(b) mass loss A). Exotherm B and C corresponds with the TG mass loss B and C.

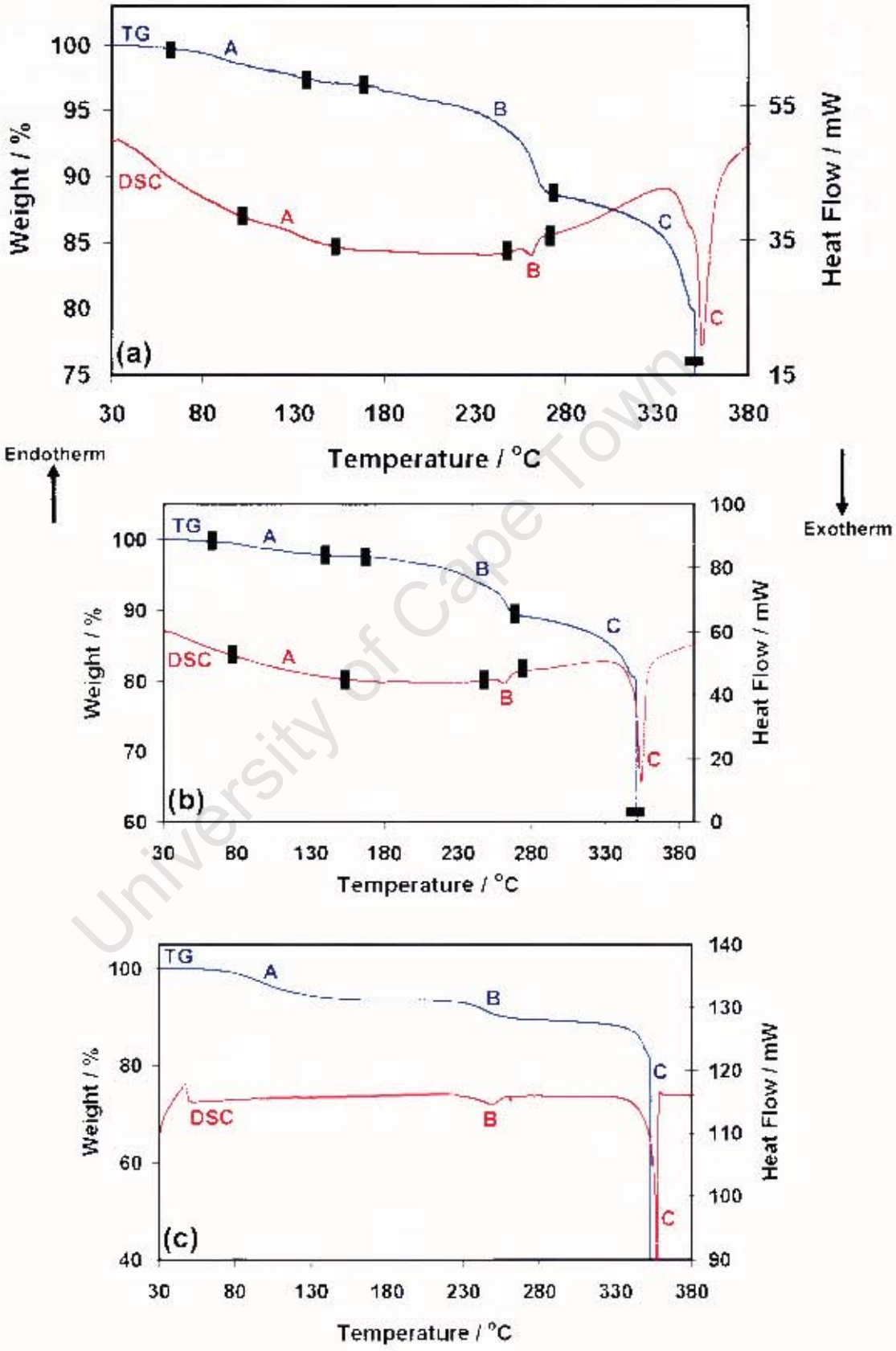

Figure 7.10: TG and DSC traces of **(a) Gd1**, **(b) Tb1** and **(c) Tl1**

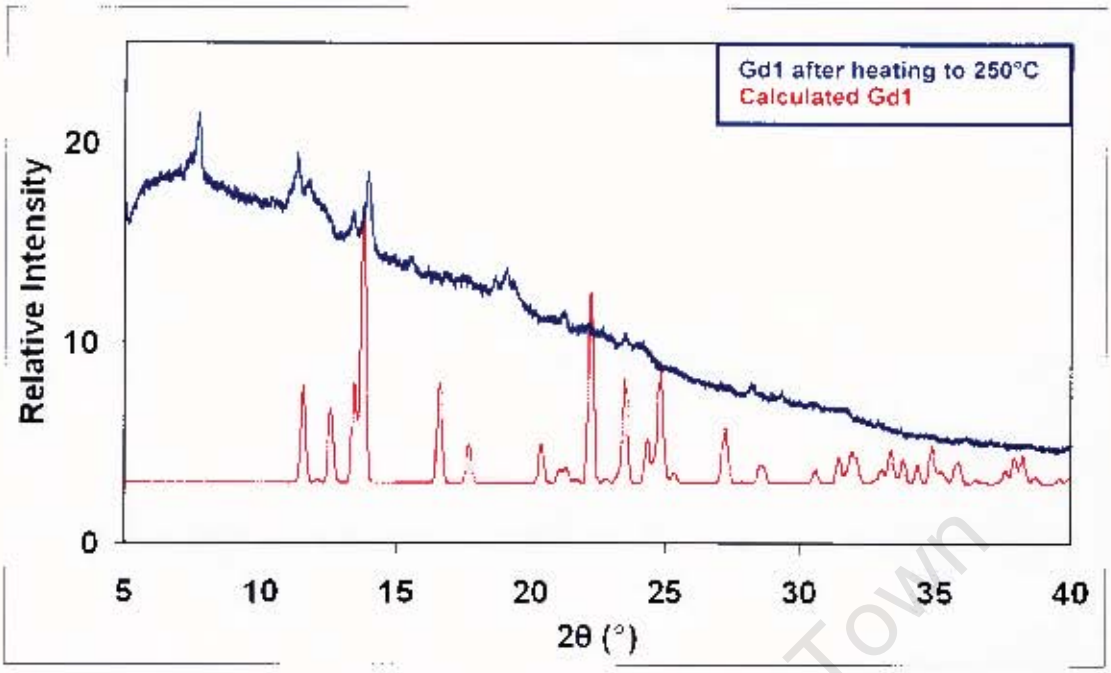

Figure 7.11: Calculated PXRD pattern of **Gd1** (red) is matched with experimental pattern after heating to 250 °C (blue).

Table 7.5: Thermal analysis results.

Polymer	TG Results				DSC Results		
	Calc. % mass loss A	Exp. % mass loss A	Calc. % mass loss B	Exp. % mass loss B	T_{on} (°C) Peak A	T_{on} (°C) Peak B	T_{on} (°C) Peak C
Gd1	5.69	2.99	33.39	11.88	112.4	262.1	266.1
Tb1	5.67	2.65	33.36	7.31	81.3	255.7	354.4
Tl1	5.25	4.75	30.82	8.18	–	240.0	355.8

Hot stage microscopy

Crystals of **Gd1**, **Td1** and **Tl1** complexes were observed during thermal decomposition using the hot stage microscopy. The photographs for thermal events are shown in Figure 7.12, 7.13 and 7.14. respectively.

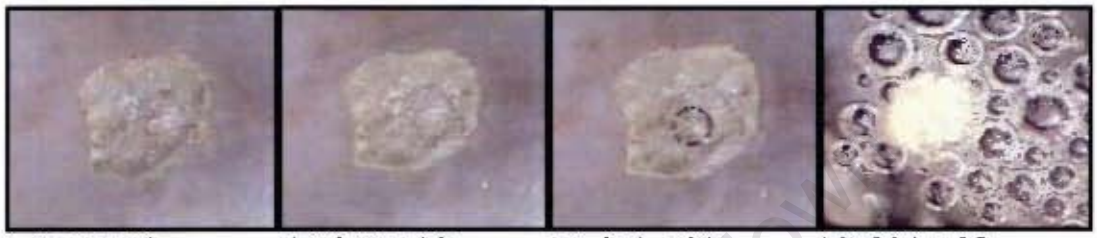

(a) 31.5 °C (b) 120.2 °C (c) 148.5 °C (d) 264.2 °C

(e) 384.5 °C

Figure 7.12: Crystal of **Gd1** compound during thermal decomposition.

Photographs; **(a)** crystal at room temperature, **(b)** crystal retains its integrity at temperatures greater than boiling point of methanol, owing to the strength of the coordination bond. **(c)** coordinated methanol ligand is released at 148.5 °C depicted by a bubble. **(d)** loss of bpdo which leads to complete decomposition observed in **(e)**.

(a) 28.5 °C (b) 120.8 °C (c) 149.9 °C (d) 266.9 °C

(e) 370.2 °C

Figure 7.13: Crystals of **Tb1** during thermal decomposition.

The thermal decay for **Tb1** is comparable to **Gd1**. Photographs; **(a)** room temperature, **(b)** crystal retains its rigidity **(c)** methanol released at 149.9 °C depicted by bubbling, **(d)** loss of bpdo which leads to complete decomposition observed in **(e)**.

(a) 64.2 °C (b) 78.1 °C (c) 255.1 °C (d) 360.1 °C

Figure 7.14: Crystals of **Tl1** during thermal decay.

Photographs; **(a)** crystal stable at 64.2 °C, **(b)** release of coordinated methanol shown by bubbles, **(d)** loss of bpdo which leads to complete decomposition observed in **(e)**.

Kinetics of decomposition

Kinetics of bpdo loss for **Gd1** and **Tb1** were analysed by carrying out a series of isothermal TG experiments. For both compounds the experiments were done for the second step mass loss. **Tl1** analysis could not be done due to limited sample and experiments with thallium were discontinued due to its toxicity.

In the case of **Gd1**, isothermal TG experiments were carried out over the temperature range 230 to 240°C at intervals of 2-3°C, while for **Tb1** the temperature range was 235 to 250°C. The mass loss versus time curves obtained were converted to extent of reaction (α) versus time curves and typical curve is shown in Figure 7.15.

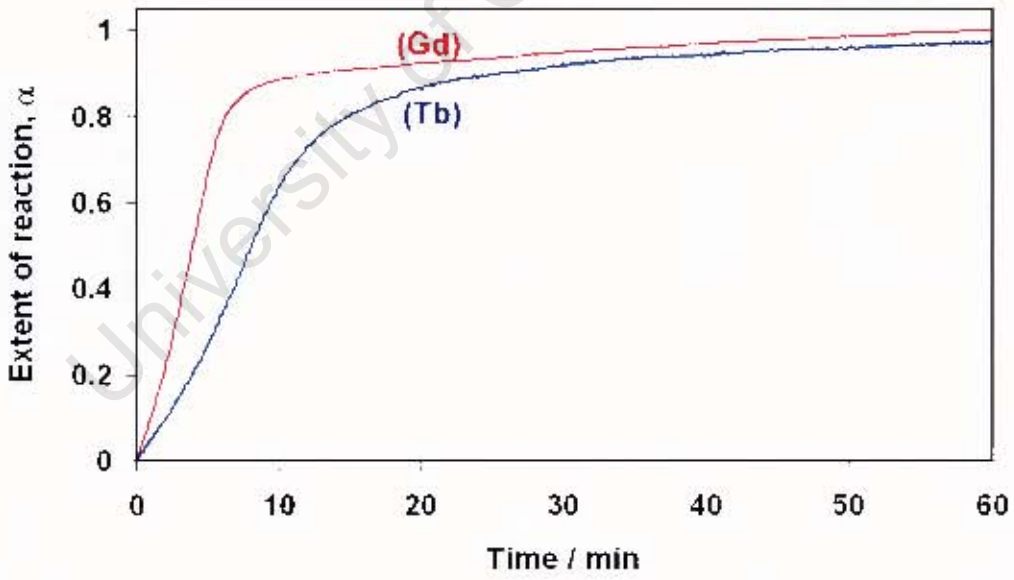

Figure 7.15: Typical α versus time curves for the decomposition of **Gd1** (at 235 °C) and **Tb1** (at 237.5 °C).

The α versus time curves for **Gd1** compounds were best described by the one dimensional diffusion equation ($f(\alpha) = \alpha^2$) over an α-range of 0.05-0.95 and the rate constants, k_{obs}, were derived.[3] The semilogarithmic plots of ln k_{obs} versus 1000 K/T are shown in Figure 7.16(a) and yielded activation energy of 106.3 kJ.mol^{-1}.

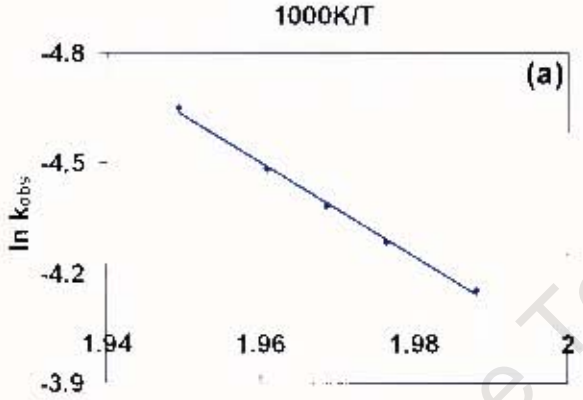

Figure 7.16(a): The semilogarithmic plots of ln K_{obs} versus 1000 K/T for **Gd1** of the decomposition step.

The α versus time curves for **Tb1** compounds were best described by the contracting volume equation, $[1-(1-\alpha)^{1/3}]^2$ over an α-range of 0.05-0.95 and the rate constants, k_{obs}, were derived.[3] The semilogarithmic plots of ln k_{obs} versus 1000 K/T are shown in Figure 7.16 (b) and yielded activation energies of 50.8 kJ.mol^{-1}.

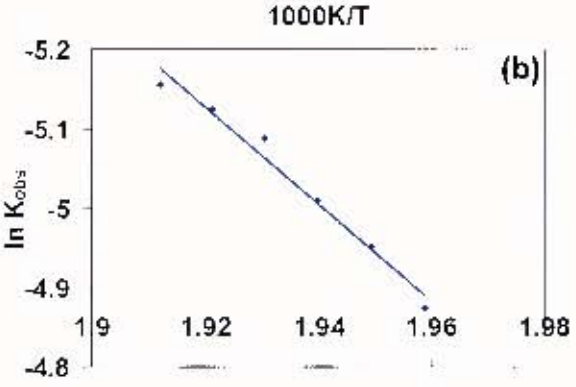

Figure 7.16(b): The semilogarithmic plots of ln K_{obs} versus 1000 K/T for **Tb1** of the decomposition step.

Gd2 and Tl2

Table 7.7: Crystal Data and Refinement Parameters of **Gd2** and **Tl2**.

Molecular Formula	$Gd_2(NO_3)_6(C_{10}H_8N_2O_2)_3 \cdot 2CH_2Cl_2$	$Tl_2(NO_3)_6(C_{10}H_8N_2O_2)_3 \cdot 2CH_2Cl_2$
Formula weight ($g.mol^{-1}$)	1420.96	1515.22
Temperature (K)	203	203
Wavelength (Å)	0.71073	0.71073
Crystal System	Triclinic	Triclinic
Space Group	$P\,\bar{1}$	$P\,\bar{1}$
a (Å)	8.0460 (1)	8.043 (2)
b (Å)	11.6902 (1)	11.687 (2)
c (Å)	13.0803 (2)	13.079 (3)
α (°)	86.5445 (5)	86.51 (3)
β (°)	79.7811 (5)	79.83 (3)
γ (°)	78.7490 (6)	78.75 (3)
Volume ($Å^3$)	1187.12 (3)	1186.3 (4)
Z	1	1
Calculated Density ($g.cm^{-3}$)	1.9873	2.121
μ (mm^{-1})	3.093	7.107
F (000)	692	726
Crystal Size (mm)	0.04 x 0.10 x 0.10	0.08 x 0.10 x 0.15
θ Range Scanned (°)	1.02 – 27.88	1.6 – 27.48
Index Range	-10 < h < 10, -15 < k < 15, -17 < l < 17	-10 < h < 10, -15 < k < 15, -16 < l < 16
No. Reflections Collected	42216	35318
No. Unique Reflections	5650	5387
Data completeness (%)	100.0	100.0
Refinement Method	Full-matrix L.S. on F^2	Full-matrix L.S. on F^2
Data / Restraints / Parameters	5650 / 0 / 335	5387 / 0 / 319
Goodness-of-fit on F^2	1.076	1.119
Final R Indices $[I>2\sigma(I)]$	0.0251, 0.0485	0.0358, 0.1026
R Indices (all data)	0.0346, 0.0507	0.0422, 0.1068
Largest Diff. Peak and Hole ($e.Å^{-3}$)	0.66, -0.61	1.38, -0.71

Gd2 and **Tl2** are isostructural, so their description will mainly be outlined with reference to **Gd2**, but crystallographic interactions will be tabulated for both.

Solving the structure in $P\bar{1}$, with two molecules in the unit cell, revealed a Gd ion coordinated to three nitrate counterions and three half bpdo ligands. resulting in irregular octahedral coordination geometry. The bpdo lies on a centre of inversion, *-1*, at Wyckoff position *a* while metal is located on a general position. Figure 7.17(a) and (b) shows the labeled asymmetric unit for **Gd2** and **Tl2**, respectively. Figure 7.17(b) shows the pyridyl O atoms O9 and O16 disordered over two positions, with the site-occupancy factors of 0.60:0.40; these disordered atoms were refined isotropically. Neither **Gd2** or **Gd3** showed the same disorder.

The bond lengths of Gd–O(NO_3^-) range from 2.466 Å – 2.505 Å (2.467 A – 2.505 Å for **Tl2**) and Gd–O(bpdo) is 2.322 Å – 2.355 A (2.320 Å – 2.350 Å for **Tl2**). Full bond length data is given in the Appendix.

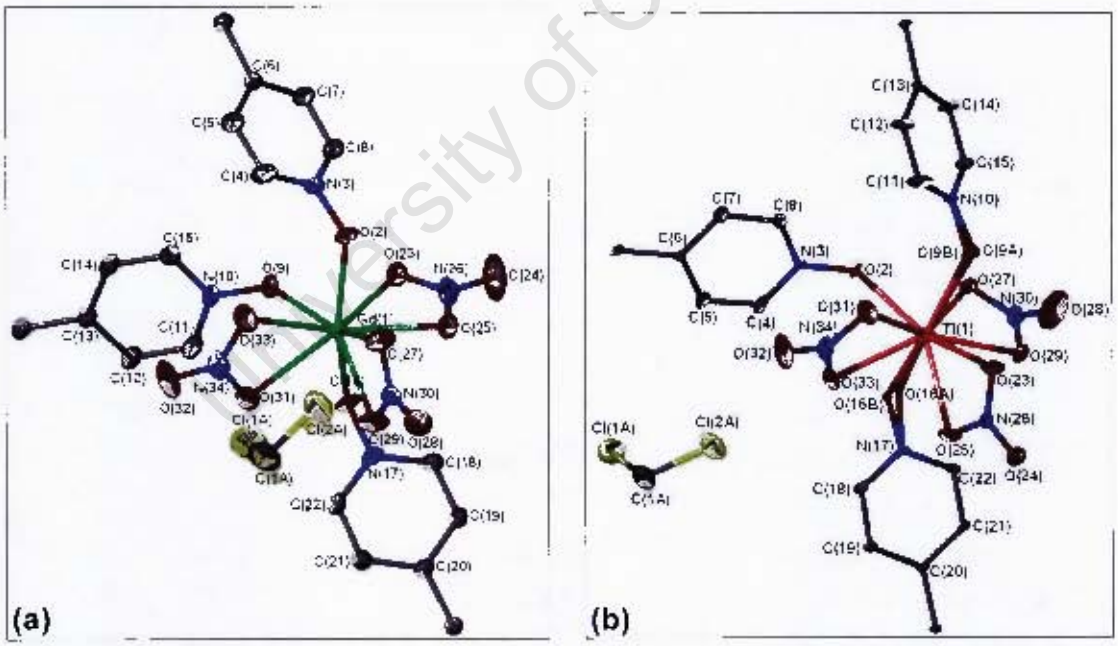

Figure 7.17: The asymmetric unit of **Gd2** and **Tl2** structure. Displacement ellipsoids are drawn at 50% probability level. H atoms have been omitted for clarity. Both components are shown for the disordered atoms in **Tl2**.

This compound comprises a ladder-shaped coordination polymer (Figure 7.18); forming channels which accommodate CH_2Cl_2 guest molecules as shown in Figure 7.19. Bridging bpdo ligands form both the upright and the rungs of the ladder, while all the nitrate ligands are bidentate, giving nine-coordinated Gd atom. The upright bpdo ligand rings are twisted by 37.75°, but those in the rungs are co-planar.

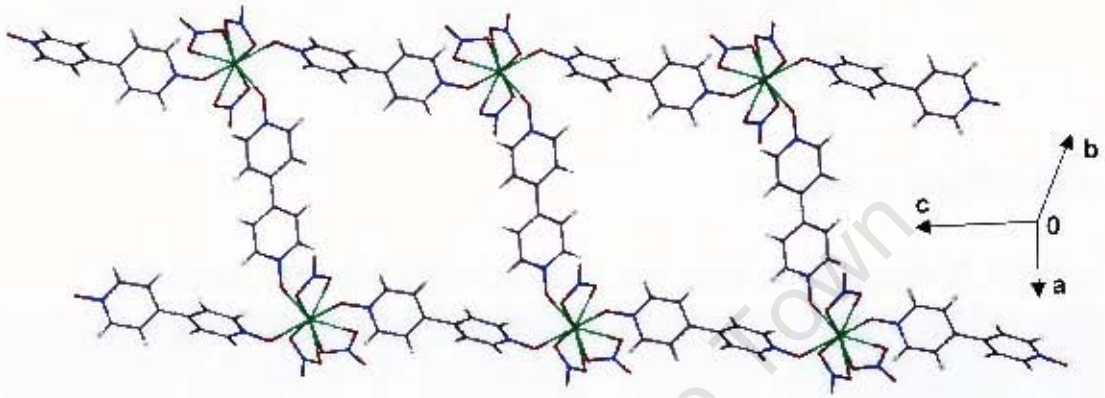

Figure 7.18: The ladder polymeric structure. Solvent molecules are not shown.

The guest position is stabilised by weak hydrogen bonds to polymer nitrate O atoms (detailed in Table 7.9), while the ladder-shaped polymer chains stack above one another, also stabilised by C–H···O hydrogen bonds (Table 7.9).

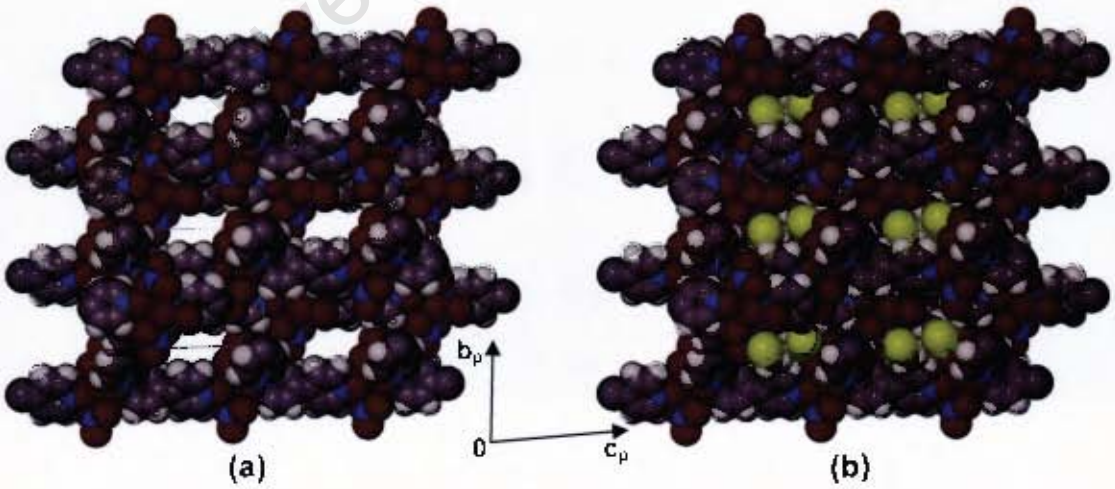

Figure 7.19: Packing diagrams for **Gd2** viewed along [100], represented by van der Waals radii. **(a)** CH_2Cl_2 molecules are not shown; **(b)** shows guest molecules resided in the channels.

Figure 7.20 illustrates the π interactions and details are given in Table 7.10.

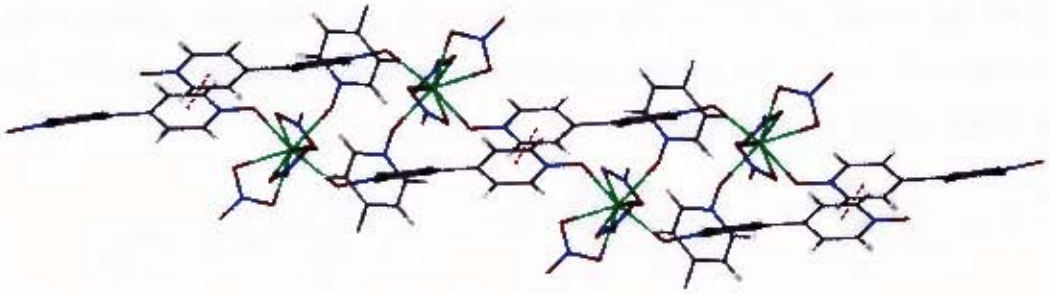

Figure 7.20: π interactions in **Gd2**.

Table 7.9: Hydrogen bonding interactions in **Gd2** and **TI2** compounds.

	D–H (Å)	D···A (Å)	D–H···A (°)	Symmetry operator
Gd2				
C(1A)–H(1A)···O(28)	0.98	3.153 (4)	122	-2-x, -y, 1-z
C(1A)–H(1A)···O(29)	0.98	3.368 (4)	137	-2-x, -y, 1-z
C(1A)–H(2A)···O(24)	0.98	3.297 (5)	143	x, -1+y, z
C(5)–H(5)···O(32)	0.94	3.128 (3)	120	-1-x, -y, -z
C(7)–H(7)···O(16)	0.94	3.332 (3)	148	-1-x, 1-y, -z
C(11)–H(11)···O(27)	0.94	3.107 (3)	128	1+x, y, z
TI2				
C(1A)–H(1A)···O(28)	0.98	3.292(11)	143	x+1, y-1, z
C(1A)–H(2A)···O(24)	0.98	3.148 (9)	122	-x+1, -y, -z+1
C(1A)–H(2A)···O(25)	0.98	3.362 (9)	137	-x+1, -y, -z+1
C(4)–H(4)···O(23)	0.94	3.100 (7)	129	x+1, y, z
C(12)–H(12)···O(32)	0.94	3.119 (8)	120	x+1, -y, -z
C(14)–H(14)···O(16A)	0.94	3.260(17)	144	-x+1, -y+1, -z

Table 7.10: π interactions in **Gd2** and **TI2** compounds.

	Distance	Symmetry operator
Gd2		
*Cg(N17–C22)···Cg(N17–C22)	3.925 (1)	-1-x, 1-y, 1-z
C(15)–H(15)···Cg(N3–C8)	3.183	x, y, z
C(18)–H(18)···Cg(N17–C22)	3.233	-1-x, 1-y, 1-z
N(26)–O(24)···Cg(N3–C8)	3.868 (4)	-2-x, 1-y, -z
N(34)–O(32)···Cg(N10–C15)	3.730 (3)	x, y, z
TI2		
Cg(N17–C22)···Cg(N17–C22)	3.925 (3)	1-x, 1-y, 1-z
C(22)–H(7)···Cg(N17–C22)	3.247	1-x, 1-y, 1-z
C(8)–H(9)···Cg(N10–C15)	3.169	x, y, z
N(30)–O(28)···Cg(N10–C15)	3.870 (9)	-x, 1-y, -z
N(34)–O(32)···Cg(N3–C8)	3.730 (6)	x, y, z

*Cg = ring centroid

Thermal analysis

The TG traces for **Gd2** and **TI2** are shown in Figure 7.21(a) and (b) respectively. Region A in Figure 7.21(a) occurs over a wide temperature range and it is due to loss of CH_2Cl_2 guest molecule. Experimental and calculated mass losses for **Gd2** and **TI2** are given in Table 7.11. Endotherm A in the DSC trace corresponds to region A of the TG trace. Exotherm B may be due to rearrangement of a compound. This exotherm could not be confirmed by the TG trace. DSC onset temperatures are summarised in Table 7.11. TG and DSC runs were performed up until 300°C. At higher temperatures, complete decomposition of the compound causes the DSC sample pan to distort and result in an instrumental error. In Figure 7.21(b), the TG shows a two step mass loss. The first step is due to CH_2Cl_2 loss while the second loss is attributed to compound decomposition. DSC was not done due to inadequate sample being available.

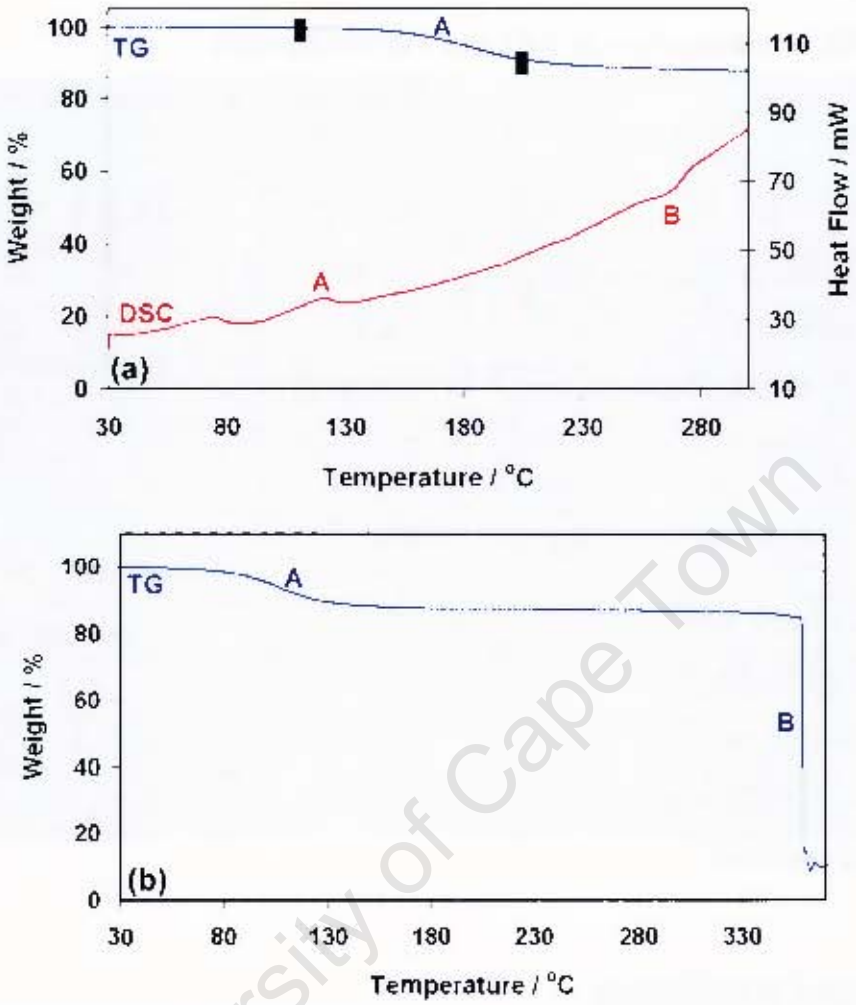

Figure 7.21: TG and DSC traces for **(a) Gd2** and **(b) TI2**

Table 7.11: Thermal analysis results.

Compounds	TG Results		DSC Results	
	Calc. % mass loss	Exp. % mass loss	T_{on} (°C) Peak A	T_{on} (°C) Peak B
Gd2	11.96	12.31	112.2	254.7
TI2	11.24	10.78	–	–

Hot stage microscopy

The crystal of **Gd2** and **Tl2** complexes were observed during thermal decay using the hot stage microscopy. The photographs for thermal events are shown in Figure 7.22(a) and (b).

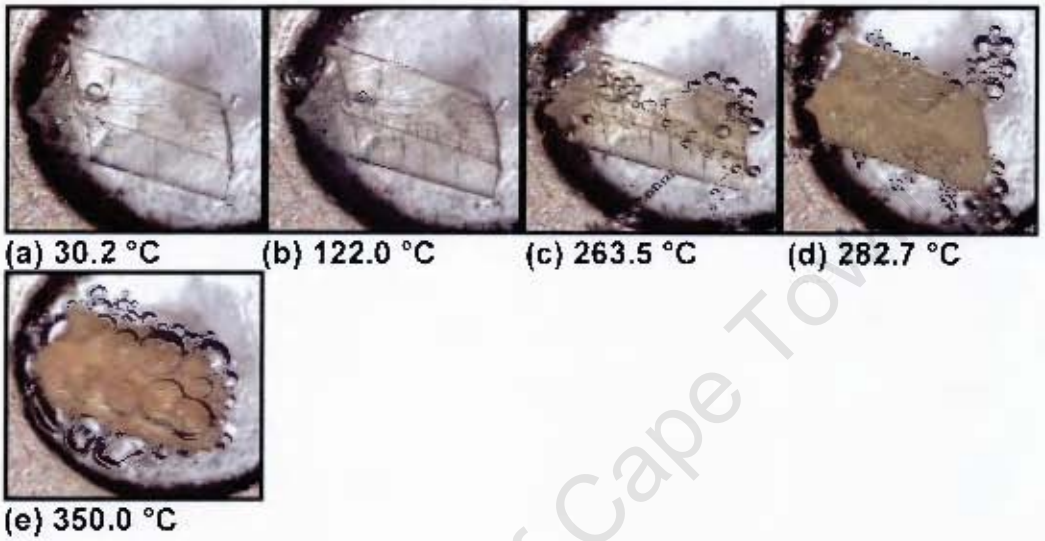

Figure 7.22(a): Thermal decomposition for **Gd2** compound.

Photographs; **(a)** crystal at room temperature, **(b)** bubble is observed which depicts loss of CH_2Cl_2 solvent, **(c)** crystal starts to lose bpdo, **(d)** bubbling continues until the color changes to brown, **(e)** complete decomposition of the compound.

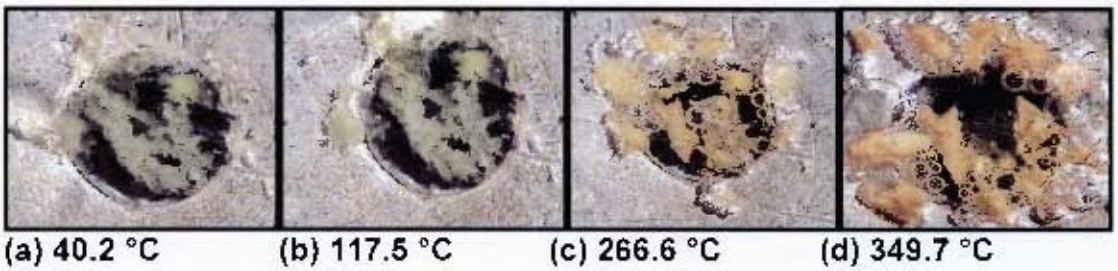

Figure 7.22(b): Thermal decay for **Tl2** compound.

The thermal decomposition for **Tl2** is comparable to **Gd2**. Photographs; **(a)** crystal stable at 40.2 °C, **(b)** loss of CH_2Cl_2 solvent depicted by bubbles, **(c)** loss of bpdo, **(e)** complete decomposition of the compound.

Gd3

Table 7.12: Crystal Data and Refinement Parameters of **Gd3**.

Molecular Formula	$Gd_2(NO_3)_6(C_{10}H_8N_2O_2)_3 \cdot 2CHCl_3$
Formula weight ($g.mol^{-1}$)	1489.84
Temperature (K)	113
Wavelength (Å)	0.71073
Crystal System	Triclinic
Space Group	$P\bar{1}$
a (Å)	7.9982 (1)
b (Å)	11.8988 (2)
c (Å)	13.1536 (2)
α (°)	82.7069 (6)
β (°)	80.0802 (6)
γ (°)	81.0247 (9)
Volume ($Å^3$)	1211.54 (3)
Z	1
Calculated Density ($g.cm^{-3}$)	2.0417
μ (mm^{-1})	3.142
F (000)	724
Crystal Size (mm)	0.04 x 0.02 x 0.20
θ Range Scanned (°)	1.02 – 27.48
Index Range	-10 < h < 10, -15 < k < 15, -17 < l < 16
No. Reflections Collected	10192
No. Unique Reflections	5490
Data completeness (%)	99.6
Refinement Method	Full-matrix L.S. on F^2
Data / Restraints / Parameters	5490 / 0 / 344
Goodness-of-fit on F^2	1.040
Final R Indices $[I>2\sigma(I)]$	0.0204, 0.0448
R Indices (all data)	0.0243, 0.0458
Largest Diff. Peak and Hole ($e.Å^{-3}$)	0.50, -0.81

Gd3 is isostructural to **Gd2** and **Tl2**. Hydrogen bonding and π interactions in all these compounds are comparable. The only difference is that the included guest for **Gd3** is $CHCl_3$. The bpdo lies on a centre of inversion, *-1*, at Wyckoff position *d*. The asymmetric unit of **Gd3** is shown in Figure 7.23. Similarly, **Gd3** comprises the ladder shape which forms channels where solvent reside (Figure 7.24).

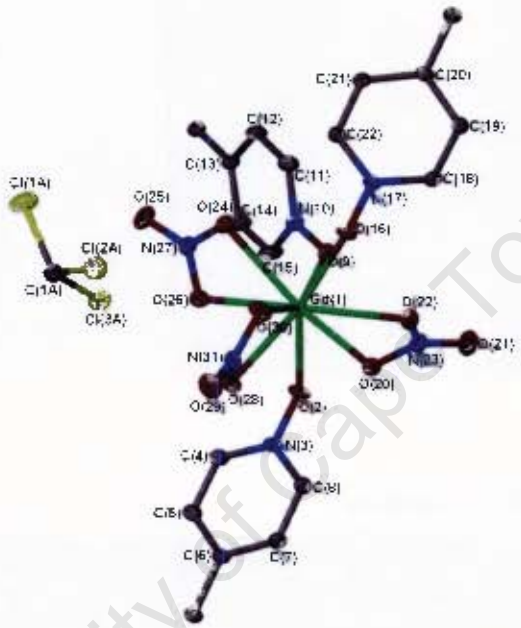

Figure 7.23: The asymmetric unit of **Gd3** structure. Displacement ellipsoids are drawn at 50% probability level. H atoms have been omitted for clarity.

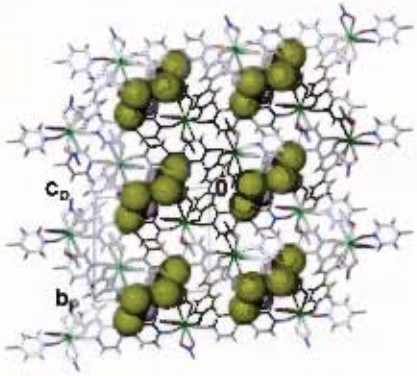

Figure 7.24: Packing diagrams for **Gd3** viewed along [100] showing $CHCl_3$ molecules residing in channels. Guests are represented by van der Waals radii.

The H bond geometry and π interactions are detailed in Table 7.13 and 7.14, respectively.

Table 7.13: Hydrogen bonding details in **Gd3** compound.

	D–H (Å)	D···A (Å)	D–H···A (°)	Symmetry operator
C(1A)–H(1A)···O(28)	1.00	3.387 (3)	162	-1-x, -y, 1-z
C(1A)–H(1A)···O(29)	1.00	3.170 (3)	133	-1-x, -y, 1-z
C(4)–H(4)···O(29)	0.95	3.030 (3)	110	1+x, y, z
C(12)–H(12)···O(24)	0.95	3.331 (3)	142	-x, -y, -z
C(14)–H(14)···O(24)	0.95	3.342 (3)	141	-x, -y, -z
C(15)–H(15)···O(30)	0.95	3.050 (3)	136	1+x, y, z
C(19)–H(19)···O(2)	0.95	3.253 (3)	134	-x, 1-y, -z
C(21)–H(21)···O(25)	0.95	3.132 (3)	136	-x, -y, -z

Table 7.14: π interaction details.

	Distance	Symmetry operator
*Cg(N3–C8)···Cg(N3-C8)	3.854 (1)	-x, 1-y, 1-z
N(23)–O(21)···Cg(N10-C15)	3.269 (2)	-x, 1-y, -z
N(23)–O(21)···Cg(N17-C22)	3.109 (2)	-1-x, 1-y, -z
N(27)–O(25)···Cg(N10-C15)	3.641 (2)	x, y, z

Thermal analysis

TG trace showed a two step mass losses (Figure 7.25). The first step mass loss is attributed to loss of $CHCl_3$. Experimental and calculated mass losses of this step are given in Table 7.13. The second step mass loss is due to decomposition of the compound. The DSC trace showed endotherm A and B (Figure 7.25). Endotherm A corresponds to first step mass loss in TG trace. Exotherm B may be due to rearrangement of a compound. This exotherm could not be confirmed by the TG trace. DSC onset temperatures are

summarised in Table 7.15. DSC was run up until 300°C to avoid instrument problems on compound decomposition.

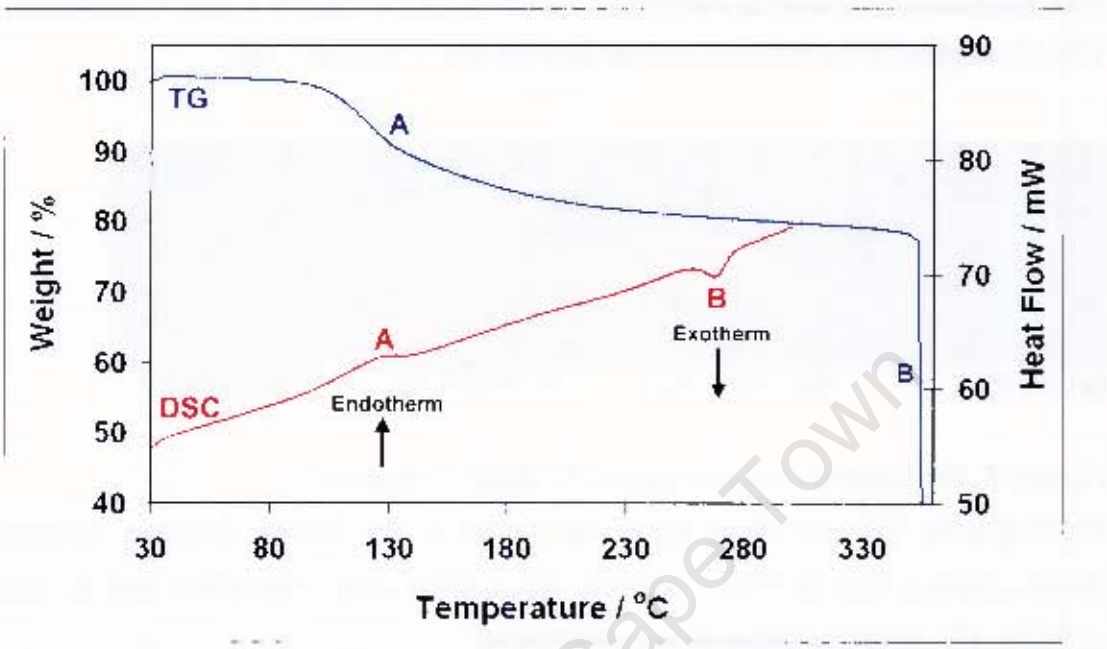

Figure 7.25: TG and DSC traces for **Gd3** compound.

Table 7.13: Thermal analysis results.

Compound	TG Results		DSC Results	
	Calc. % mass loss	Exp. % mass loss	T_{on} (°C) Peak A	T_{on} (°C) Peak B
Gd3	16.00	15.95	109.7	271.9

Hot stage microscopy

Gd3 was observed during thermal decomposition using hot stage microscopy. The photographs for thermal events are shown in Figure 7.26.

(a) 30.2 °C **(b) 115.5 °C** **(c) 283.9 °C** **(d) 391.0 °**

Figure 7.26: Thermal decomposition for **Gd3** compound.
Photographs; **(a)** crystal at room temperature, **(b)** crystal became opaque demonstrating loss of $CHCl_3$ solvent, **(c)** opaque color intensified due to loss of bpdo, **(d)** decomposition of the compound.

Isostructurality

Gd2, **Gd3** and **Tl2** coordination polymers are isostructural with respect to their similar molecular shape, unit cell parameters and atomic coordinates as shown in Table 7.7 and 7.12.

Figure 7.27 shows packed diagrams of **Gd2**, **Gd3** and **Tl2** viewed along [001], showing packing similarities in these compounds.

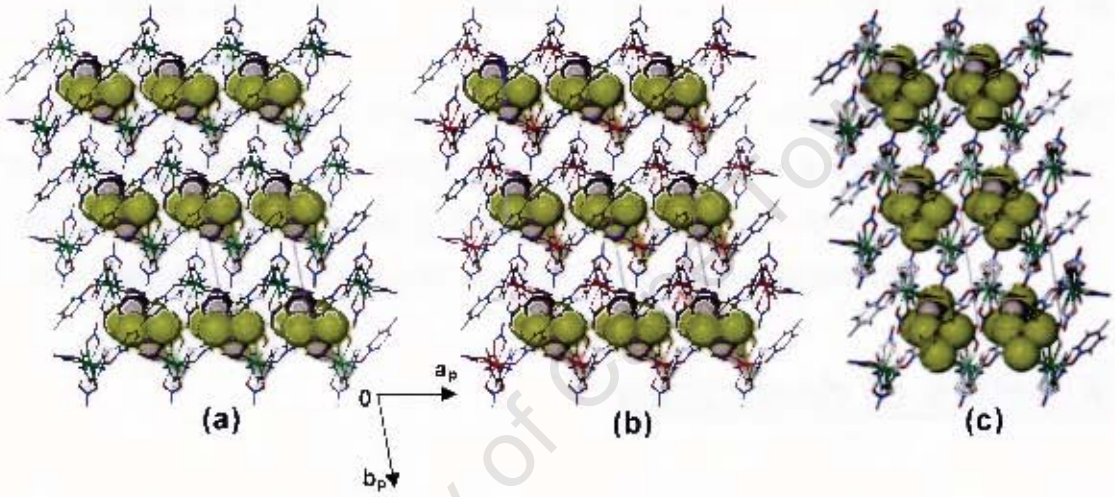

Figure 7.27: Packing diagrams for **(a) Gd2, (b) Tl2** and **(c) Gd3** are viewed along [001]. Guest molecules are represented by van der Waals radii.

The channels for **Gd2** were examined using the program SECTION,[4] which was used to view sections through the unit cell along [100]. Sections are illustrated in Figure 7.28 with guest molecules omitted for clarity. Guests in **Gd2** (similar for **Gd3** and **Tl2)** are found in hour glass channels running parallel to [100]. The top and bottom diameter of the glass is about 3.3 Å while the middle is 2.9 Å. The coordinated nitrate ligands penetrate into the channels and are accountable for narrowing the channels. The length of the cavity is 8.18 Å.

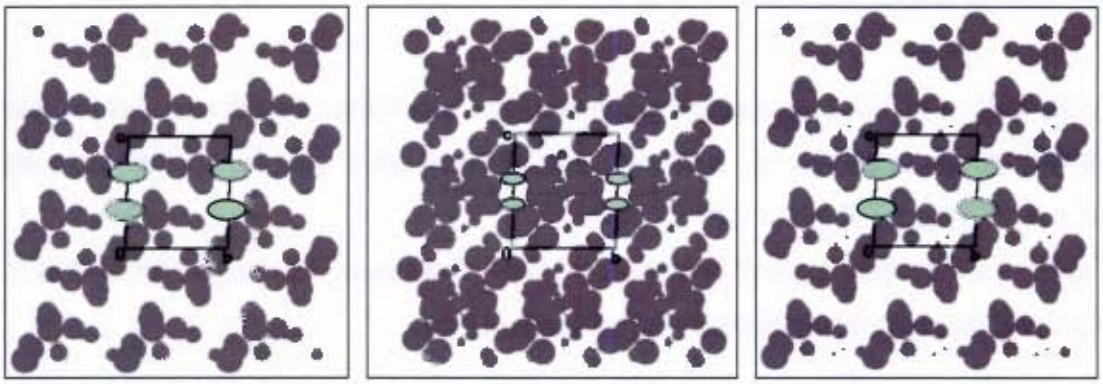

(a) 0 Å along [100] **(b)** 4 Å along [100] **(c)** 8 Å along [100]

Figure 7.28: SECTION of **Gd2** with guest molecules omitted and host molecules represented by grey areas; viewed along [100] with the unit cell sectioned at **(a)** 0 Å **(b)** 4 Å showing channels narrowing and **(c)** 8 Å. The channel position is showed in green.

Kinetics of desorption

Kinetics of desorption of **Gd2** and **Gd3** were analysed by carrying out a series of isothermal TG experiments for the first step mass loss.

Isothermal TG experiments were carried out over the temperature range 165-205°C at intervals of 5°C for both compounds. The mass loss versus time curves obtained were converted to extent of reaction (α) versus time curves and a typical curve is shown in Figure 7.29. The α versus time curves for **Gd2** and **Gd3** were both best described by the three dimensional equation, ($f(\alpha) = [1-(1-\alpha)^{1/3}]^2$) over a α-range of 0.05-0.95 and the rate constants, k_{obs}, were derived. [3] The semilogarithmic plots of ln k_{obs} versus 1000 K/T are shown in Figure 7.30 [(a) and (b)] and yielded activation energies of 9.8 and 11.7 kJ.mol^{-1}, respectively. Kinetics parameters are summarised in Table 7.13.

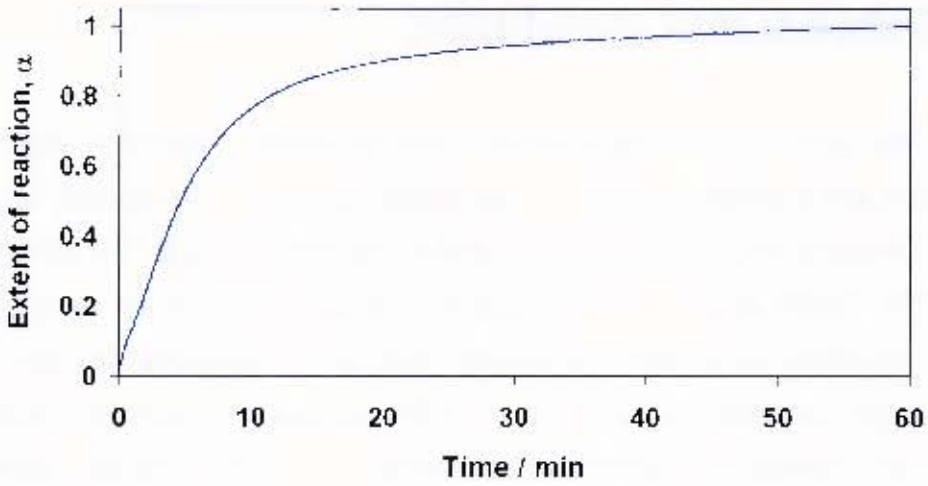

Figure 7.29: Typical α versus time curve for the desolvation of **Gd3** at 180 °C.

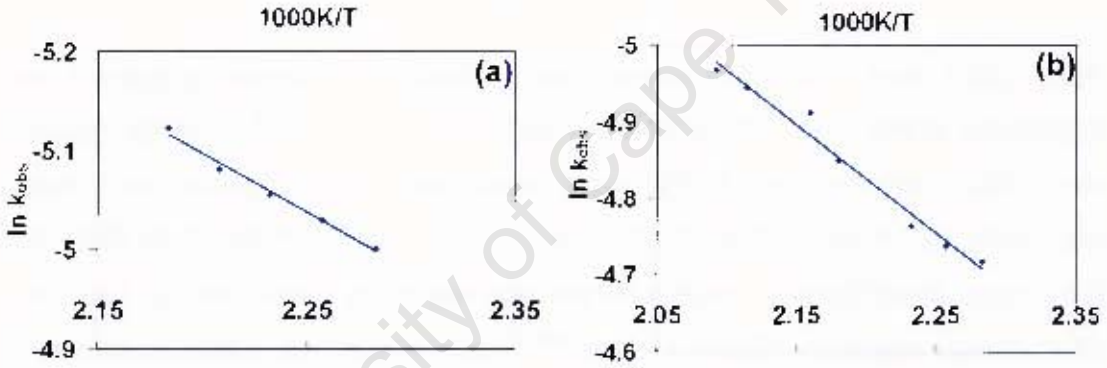

Figure 7.30: The semilogarithmic plots of ln K_{obs} versus 1000 K/T for **(a) Gd2** and **(b) Gd3** of the desolvation mass loss step.

Table 7.13: Kinetic parameters for desolvation of **Gd2** and **Gd3**

Coordination Polymer	Temperature range (°C)	Alpha range	Kinetic equation	E_a (kJ.mol^{-1})
Gd2	165–190	0.05–0.95	$f(\alpha)=[1-(1-\alpha)^{1/3}]^2$	9.8
Gd3	165–205	0.05–0.95	$f(\alpha)=[1-(1-\alpha)^{1/3}]^2$	11.7

Discussion and conclusion

Gd1, **Tb1** and **Tl1** are isostructural. They all show a common disorder of methanol and a nitrate ligand over two positions with site occupancy factors of 0.50. The methanol ligand is coordinated to the metal centre. The construction of Gd(III), Tb(III) and Tl(III) coordination polymers using bpdo as a bridging ligand resulted in crystal structures that are analogues to the Tb(III) compounds reported by Long *et al.*[4] Tl(III) carries structure characteristics which are similar to those of lanthanides. Thermal stability, elemental analyses and PXRD were performed and the structures have been elucidated by single crystal diffractometry. Kinetics of decomposition for **Gd1** and **Tb1** were investigated. Activation energy for **Tb1** is lower than that of **Gd1**.

Gd2, **Gd3** and **Tl2** are isostructural. Crystal structures prepared are analogues to the Tb(III) compounds reported by Long *et al.*[4] Thermal stability, elemental analyses and PXRD were done and the structures have been elucidated by single crystal diffractometry. Kinetics of desolvation for **Gd2** and **Gd3** were investigated. Both compounds are best described by the three dimensional equation, ($f(\alpha) = [1-(1-\alpha)^{1/3}]^2$) and yielded comparable activation energies.

Kinetics of thermal dehydration and decomposition of some mixed metal oxalates,[5,6] oxides and hydroxides,[7] malonates,[8,9] perchlorates[10] have been previously studied. Activation energies of these compounds ranged from 56 – 1012 kJmol^{-1}. Galwey[11] surveyed over 400 kinetic studies on solid state and concluded that there is no characteristic magnitude for pre-exponential factor (*A*) for solid state reactions. It is clear that the host-guest desolvation reactions in **Gd2** and **Gd3** show relatively low activation energies, compared with decomposition of **Gd1** and **Tb1** and other metal-organic complexes[12]. This could be due the fact that guest desolvation does not require the breaking of covalent bonds, but at most the breaking of hydrogen bonds. In addition, **Gd2** and **Gd3** compounds do not have traditional (strong) hydrogen bonding interactions.

Notable advances have been made to construct lanthanide coordination polymers using bpdo.[4,13-29] These compounds are coordination polymers and mostly open frameworks which accommodate guest molecules in their channels. Interestingly, Hill *et al* recently reported four unique 2D bilayer networks; $\{[La(bpdo)_2(NO_3)_3]\}_\infty$ (1), $\{[Yb(bpdo)_3(CF_3SO_3)_3]\}_\infty$ (2), $\{[Er(bpdo)_5](I_3)_3(bpdo)_{0.5}(MeOH)\}_\infty$ (3), $[La(bpdo)_4](ClO_4)_3{\cdot}C_6H_5{\cdot}CH_3OH\}_\infty$ (4), $\{[La(bpdo)_{2.5}(MeOH)_2\,(C_7H_{11}CH_2CO_2)\}_\infty$ (5).[13] Compound 1 forms square grids (Figure 7.31) with neighboring grids interpenetrating into the voids. Compound 2 – 5 accommodated guest molecules such CF_3SO_3, I_3, MeOH, H_2O, ClO_4, C_6H_5Cl and BPH_4 into their networks. **Gd2**, **Gd3** and **Tl2** have similar voids (ladder shapes) which are extended to 3 dimensions, with CH_2Cl_2 and $CHCl_3$ guest molecules located in channels.

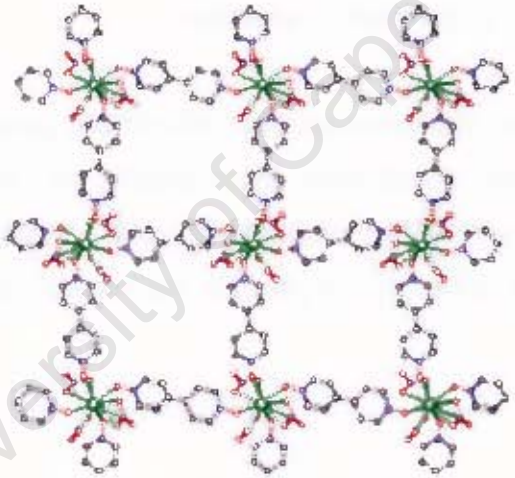

Figure 7.31: View of a square grid of compound 1.[13]

In this thesis, two kinds of coordination polymers, zigzag and ladder shapes, were obtained. Preparation of these compounds is dependent on selection of either methanol for zigzag shapes or ethanol for ladder shapes, both in conjunction with CH_2Cl_2/$CHCl_3$.

(b) A coordination polymer of uranyl(VI) nitrate with bpdo.

A compound of uranyl(VI) nitrate using bpdo was prepared by solvent evaporation. The crystal structure has been refined and elucidated by single x-ray diffractometry. Thermal stability of this compound was examined by TG, DSC and HSM. Microanalysis was done to determine elemental composition of the compound.

This is a 1D coordination polymer with adjacent chains connected through hydrogen bonding of guest water molecules and oxygens of the bpdo ligand. The polymer chains run in parallel to (101). The compound forms channels which accommodates guest water molecules.

Crystallographic data, experimental and refinement parameters are given in Table 7.14. Final atomic coordinates, bond lengths and angles, torsion angles, thermal parameters and tables of observed and calculated structure factors for each of the crystal structure are given in the appendices.

Polymer preparation

Crystals of suitable quality for data collection were prepared by slow evaporation at room temperature as described in Chapter 2. The uranyl(VI) nitrate was dissolved in methanol and mixed with an equal volume solution of bpdo in methanol. The mixture was heated to 65 °C, filtered and allowed to crystallise at 5 °C.

The compound obtained is abbreviated as follows:

$[UO_2(NO_3)_2(bpdo)]_n \cdot 3H_2O$: **U**

Microanalysis

Experimental and calculated percentages corresponded well.

Found: C, 19.33; H, 2.05; N, 8.68

Calculated: C, 18.87; H, 2.22; N, 8.80

PXRD

Unfortunately, PXRD could not be performed as a very low yield of compound was obtained.

U crystallises in the space group *C2/c* with four molecules in the unit cell. The compound is an irregular octahedron (Figure 7.32) with two coordinated oxygens, two nitrate ligands and one bpdo ligand. The nitrate ligands are bidentately coordinated forming eight-coordinate uranium. The U O(2) bond distance is 1.770 A. This bond distance corresponds well with literature value (1.763 Å).[1] U O(bpdo) and U--O(nitrate) bond length are 2.359 A and 2.537 Å and they corresponded with well with literature values of 2.329 Å and 2.528 Å, respectively.

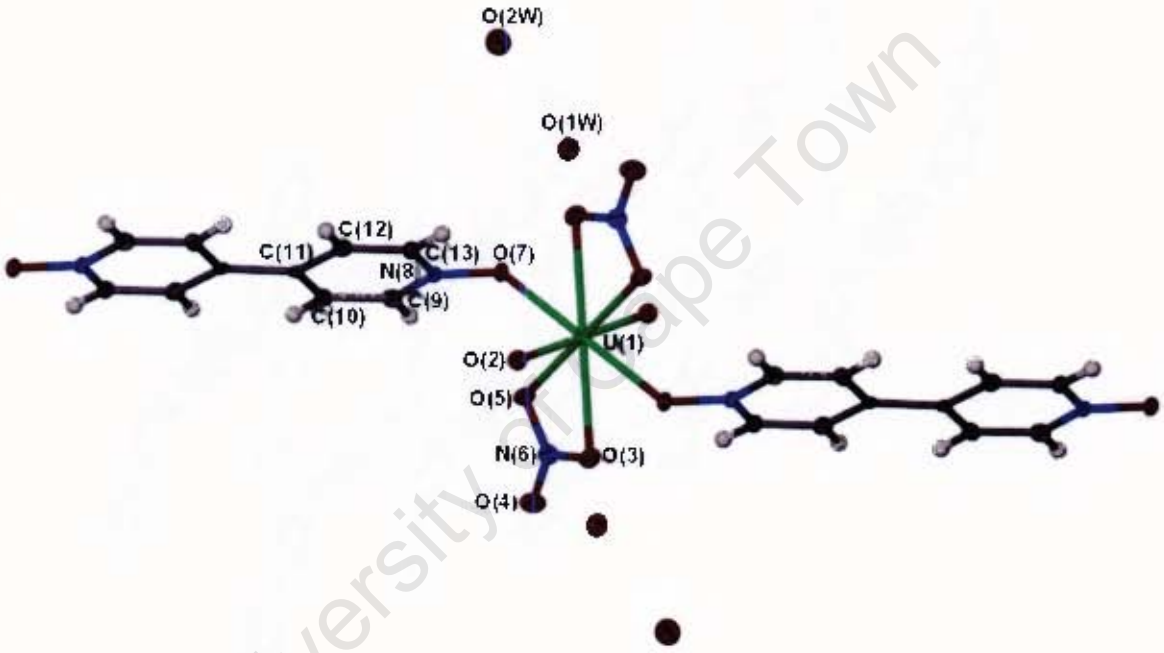

Figure 7.32: Part of the polymeric chain structure of **U** showing the atom labeling. Displacement ellipsoids are drawn at 50% probability. Atoms of the asymmetric unit are labeled.

This compound is a 1D zigzag polymer (Figure 7.33) with polymer chains running parallel to (101) as shown in Figure 7.34.

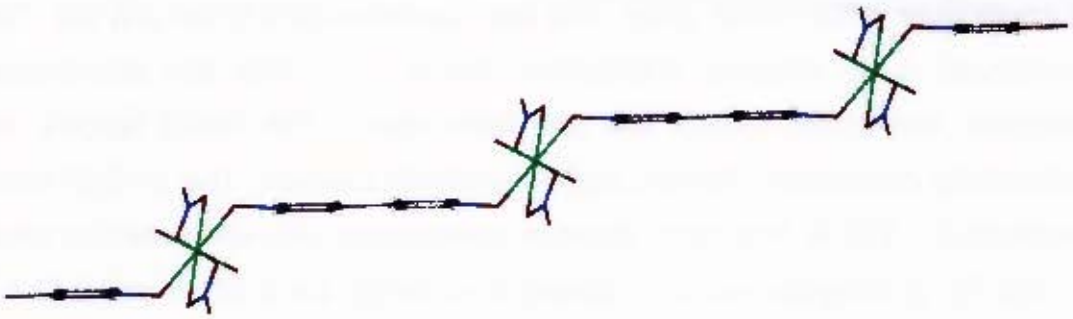

Figure 7.33: The zigzag polymeric chain.

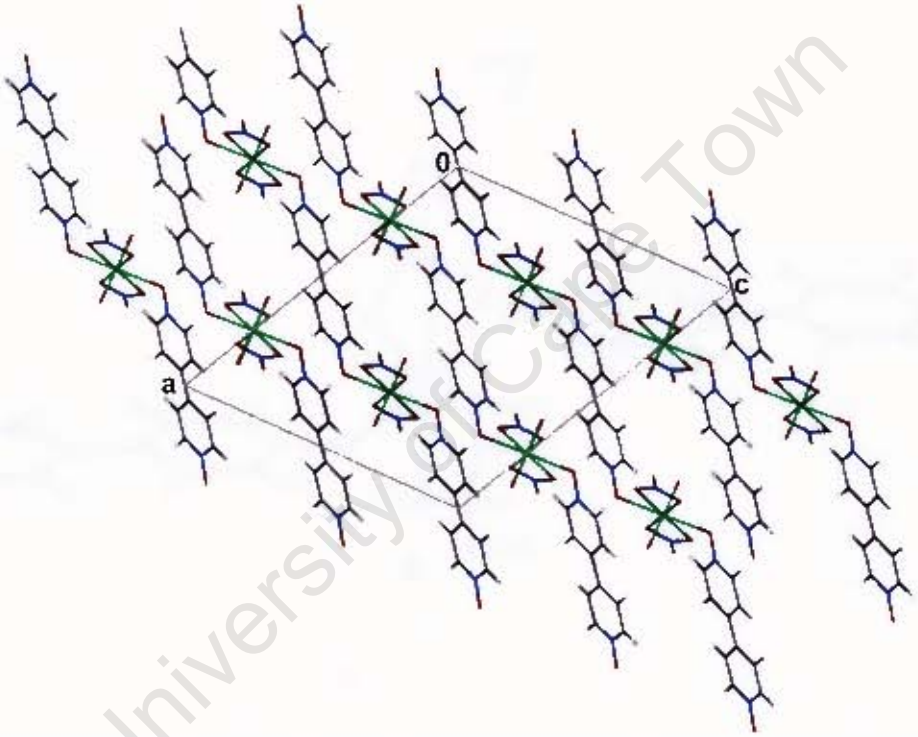

Figure 7.34: Packed molecules viewed along [010], showing polymer chains running in parallel to (101). Guest water molecules omitted for clarity.

The adjacent chains are connected through hydrogen bonding of guest water molecules and coordinated oxygens of the bpdo ligand (Figure 7.35), with O1W···O7(bpdo), O1W···O2W and O1W···O1W bond distances of 3.014 Å, 2.742 Å and 2.782 Å, respectively. Hydrogen bond details are given Table 7.15. Guest water molecule (O2W) has a site occupancy factor of 0.5 (owing to its position on two-fold rotation axis, Wyckoff position *e*) while O1W has site occupancy factor of 1. Hence there are three guest water molecules per

uranyl moeity. The metal is positioned on a centre of inversion, *-1*, at Wyckoff letter *c*.

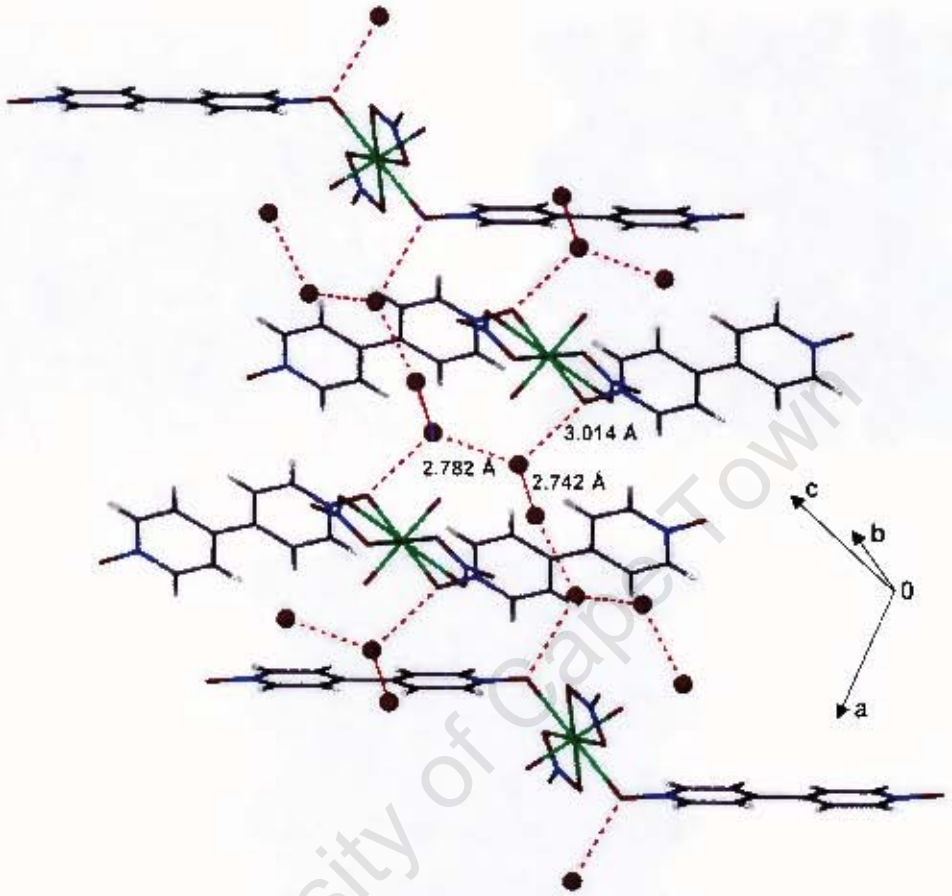

Figure 7.35: Hydrogen bonding interactions.

Table 7.15: Hydrogen bonding details.

	D–H (Å)	D···A (Å)	D–H···A (°)	Symmetry operator
O(1W)···O(7)		3.014		x, y, z
O(2W)···O(1W)		2.742		½-x, -½+y, ½-z
C(10)–H(10)···O(1W)	0.95	3.265 (5)	142	-½+x, ½-y, -½+z
C(12)–H(12)···O(1W)	0.95	3.366 (4)	140	½-x, ½+y, ½-z
C(13)–H(13)···O(4)	0.95	3.133 (4)	139	x, 1+y, z
O1W···O1W		2.782		-x, 2-y, -z

The compound forms channels in which guest water molecules are located as shown in Figure 7.36.

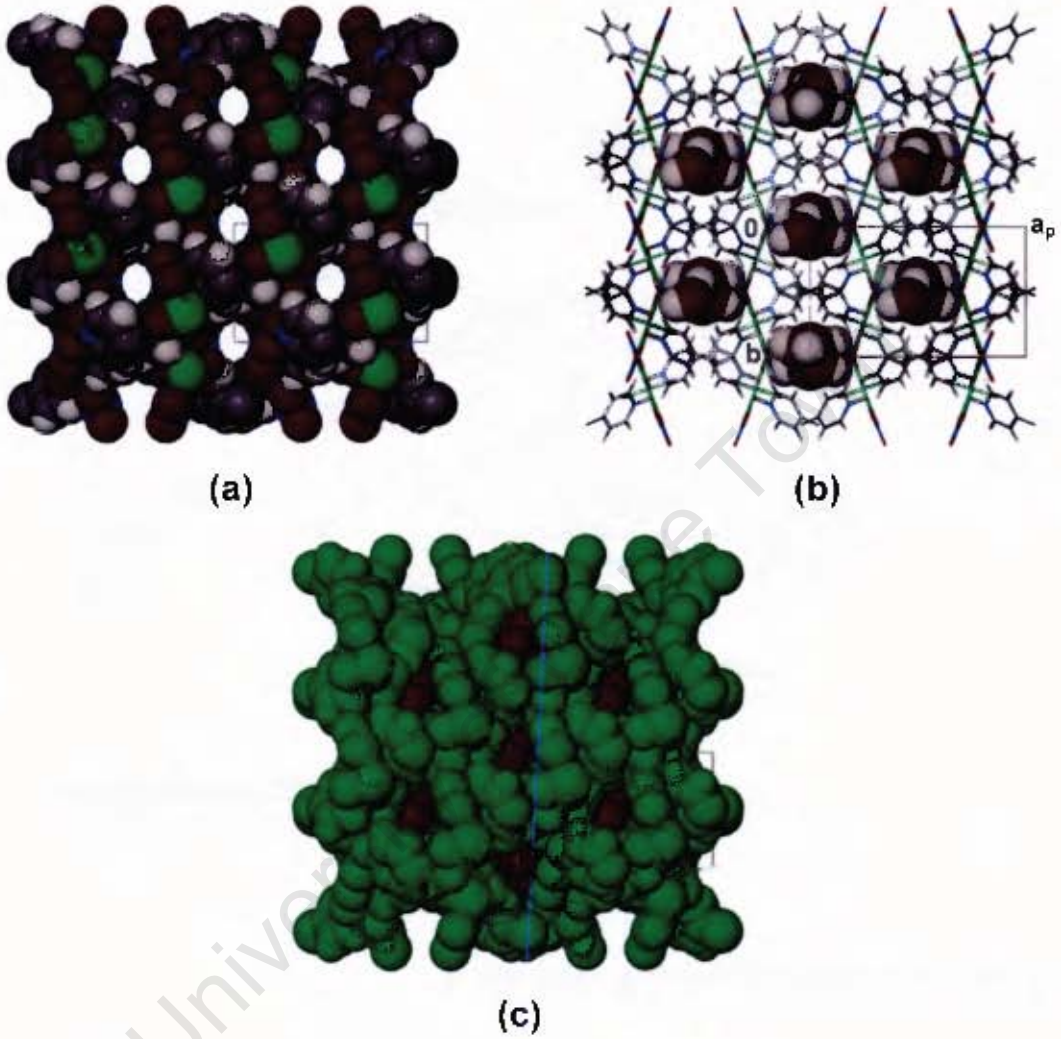

Figure 7.36: Packing diagram of **U** viewed along [001]. **(a)** guest water molecules are not shown, **(b)** guest water molecules are shown by van der Waals radii, **(c)** guest molecules (maroon) are residing in channels.

The polymer chains do not interweave, but run in parallel to one another forming transverse planes as shown in Figure 7.37.

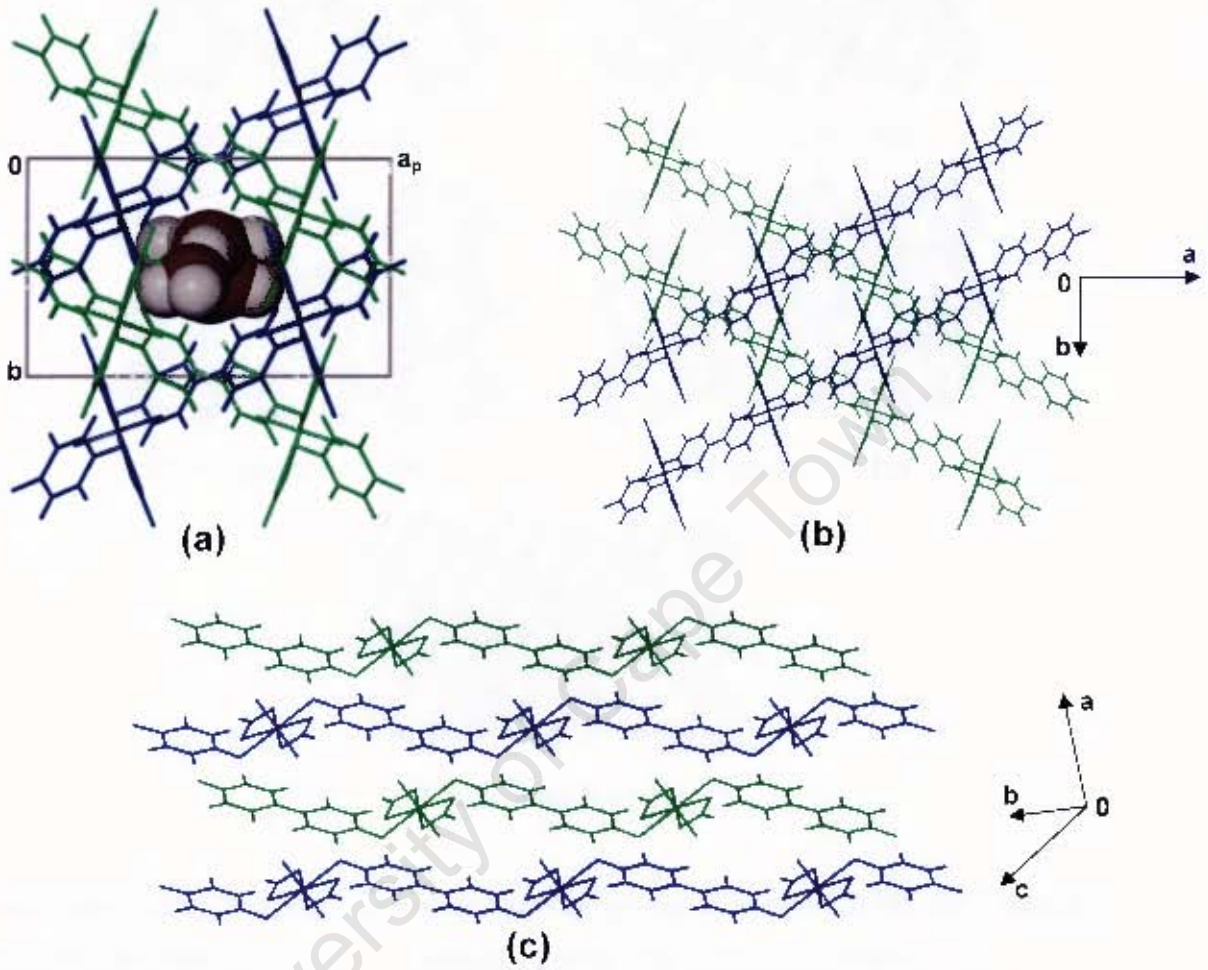

Figure 7.37: The polymer chains for **U**. **(a)** enclosed water molecules, **(b)** chains running in parallel to on another forming transverse planes, **(c)** demonstrates that polymer chains are not interweaving.

The channels were examined using the program SECTION,[4] which was used to view sections through the unit cell along [001]. The sections are illustrated in Figure 7.38 (a-e) with the guest molecules omitted for clarity. The channels have a shape which narrows and widens systematically forming sinusoidal shapes, with a maximum diameter of 6.46 Å and a minimum diameter of 3.45 Å.

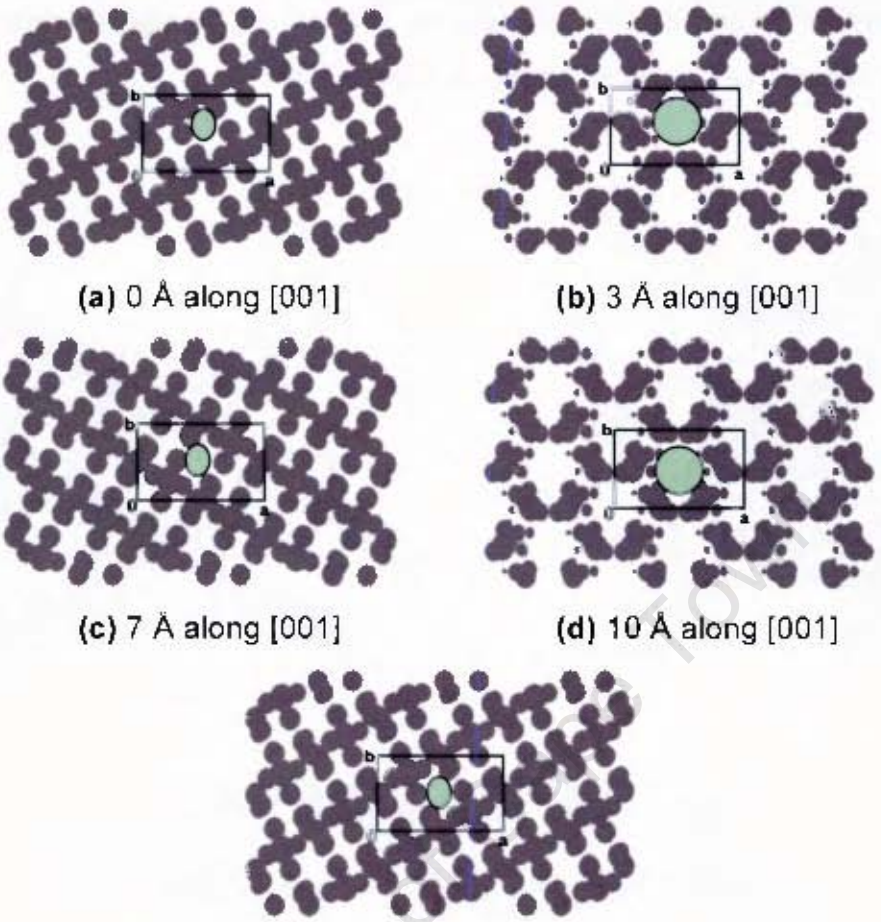

(a) 0 Å along [001] **(b)** 3 Å along [001]

(c) 7 Å along [001] **(d)** 10 Å along [001]

(e) 14 Å along [001]

Figure 7.38: SECTION of **U** with guest molecules omitted and host molecules represented by grey areas; viewed along [001] with the unit cell sectioned at 0 Å, 3 Å, (c) 7 Å, 10 Å and 14 Å, respectively. Channels gave continuous sinusoidal shapes which encapsulates guest water molecules. The channel position is showed in green.

Thermal analysis

The thermal analysis results of **U** are given in Table 7.16 and the TG/DSC traces are illustrated in Figure 7.39.

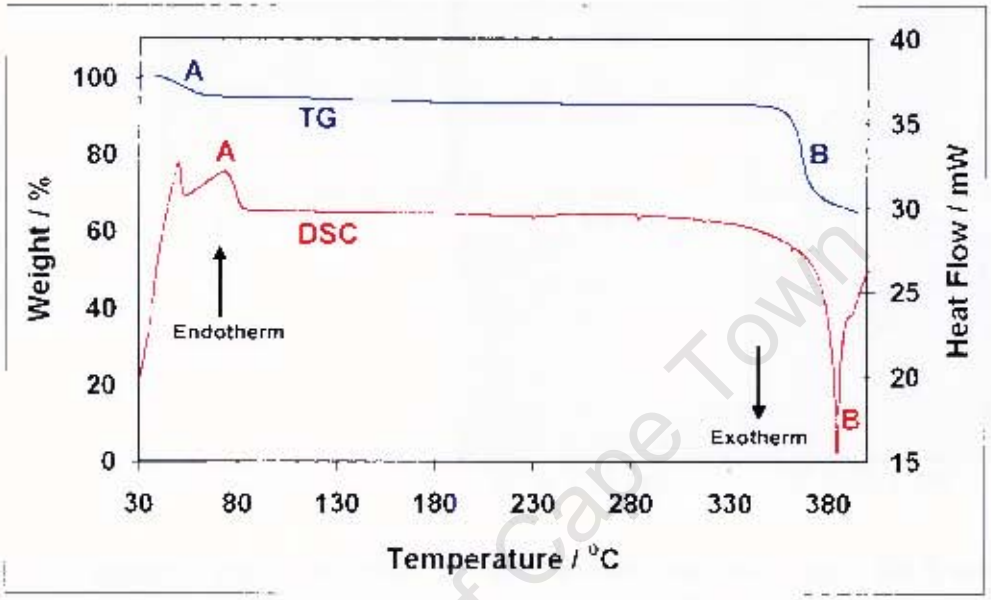

Figure 7.39: TG and DSC traces of **U**.

TG trace shows a two-step mass loss. The first step mass loss is attributed to loss of guest water molecules. This mass loss did not correspond with the calculated mass loss due to the immediate loss when compound is removed from its mother liquor. The second mass loss is due to compound decomposition. The first step mass loss values are given in Table 7.16. DSC trace shows endotherm A (corresponds to water loss) and exotherm B (compound decomposition). DSC onset temperatures for both thermal events are given Table 7.16.

Table 7.16: Thermal analysis results.

Coordination polymer	TG Results		DSC Results	
	Calc. % mass loss	Exp. % mass loss	T_{on} (°C) Peak A	T_{on} (°C) Peak B
U	8.49	5.48	51.2	366.9

Hot Stage Microscopy

The thermal decay of the **U** crystal was observed by using the hot stage microscopy and the images are shown in Figure 7.40.

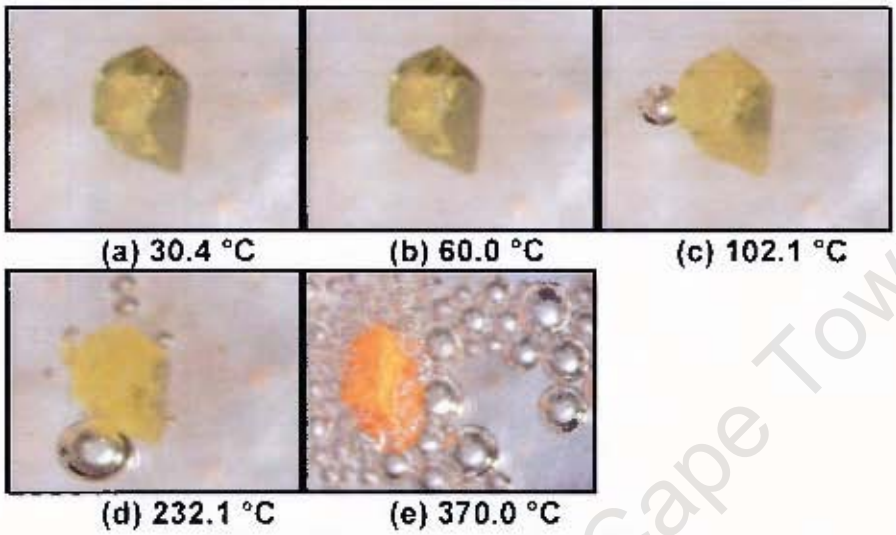

Figure 7.40: The thermal decay for **U** complex. **(a)** crystal at room temperature, **(b)** crystal is still stable, **(c)** bubbling due to loss of guest water molecules, **(d)** an intense yellow colour appeared due to loss of bpdo, **(e)** compound decomposition.

Discussion and conclusion

It appears that actinides are very resistant to form complexes with bpdo. A literature and CSD[14] (Version 5.27, November 2005) search revealed that no actinide complexes of bpdo have been reported. Moreover, only nine actinides complexes were reported using bpdo analogue, 4,4'-bipyridine (bpy).[15-21] This finding shows that more actinides research using bidentate ligands still need to be explored. Of the nine bpy actinide compounds, three are coordination polymers and six showed discrete compounds with 1-, 2- or 3D networks joined through supramolecular interactions. One interesting network contains two metals, nickel and uranium {$[Ni_2(H_2O)_2\ (QA)_2(bpy)_2U_5O_{14}(H_2O)_2(QAc) \cdot 2H_2O$ (HOAc = acetic acid, H_2QA = quinolinic acid).

In this study, **U** was synthesised and characterised by thermal analysis and the crystal structure has been elucidated using single crystal diffractometry. This compound is a 1D zigzag shaped polymer with polymer chains running parallel to (101). Polymer chains do not interweave. **U** forms sinusoidal channels which accommodates guest water molecules.

16. D-L. Long, A.J. Blake, N.R. Champness, C. Wilson and M. Schröder, *Chem. Int. Ed.*, 2001, **40**, No. 13.

17. D-L. Long, A.J. Blake, N.R. Champness and M. Schröder, *Chem. Commun.*, 2000, 1369.

18. S. Tanase, M Andruh, A. Müller, M. Schmidtmann, C. Mathonière and G. Rombaut, *Chem. Commun.*, 2001, 1084.

19. S-L. Ma, C-M. Qi, Q-L. Guo, M-X. Zhao. *J. of Mol. Struc.*, 2005, **646**, 99.

20. S-L. Ma, W-X. Zhu, G-H Huang, D-Q. Yuan, X. Yan, *J. of Mol. Struc.*, 2003, **646**, 89.

21. S.J. Dalgarno, M.J. Hardie, J.L. Atwood, and C.L. Raston, *Inorg.Chem.*, 2004, **43**, 6351.

22. F.H. Allen, *Acta Crystallogr.*, 2002, **B58**, 380.

23. Z-T. Zu, Z-L. Liao, Y-S. Jiang, G-H. Li, G-D. Li, J-S. Chen, *Chem Commun.*, 2004, 1814.

24. S. Lu, L. Ke, J. Li, S. Zhou, X. Wu, W. Du, *Cryst.Res. and Technol.*, 2003, **38**, 1004.

25. N.W. Alcock, D.J. Flanders, *Acta Crystallogr., Sect. C: Cryst. Struct. Commun.*, 1987, **43**, 1267.

26. A.J. Norquist, M.B. Doran, P.M. Thomas, D. O'Hare, *Dalton Trans.*, 2003, 1168.

27. N.N. Rammo, K.R. Hamid, B.A. Khaleel, *J. Less-Common Met.*, 1990, **162**, 1.

28. N.N. Rammo, K.R. Hamid, T.K. Ibrahim, *J. Alloys and Compounds*, 1994, **210**, 319.

29. C-M. Wang, C-H. Liao, H-M. Kao and K-H. Lii, *Inorg. Chem.*, 2005, **44**, 6294.

Chapter 8

Final remarks

Final remarks

The field of crystal engineering has developed rapidly in recent years and the design of complexes with novel topologies and functionality is of current interest. In this study, a number of metal-organic complexes have been prepared from commercially available materials. Their structures have been refined and elucidated using single x-ray diffractometry. Other various analytical techniques such as PXRD, thermal (DSC, HSM and TG) and elemental analyses were used to characterise the newly prepared crystalline complexes.

The overall study demonstrated that coordination polymers of transition metals are not likely to form with bpdo. The complexes prepared were either non-porous frameworks or have channels or voids which accommodate various guest molecules. All these complexes are governed by hydrogen bonding networks and $\pi\cdots\pi$ interactions.

Co(II) shows a range of interesting complexes of different topologies, prepared while changing the couter anion. This includes isostructural CoX_2 (X=Br, Cl) complexes with hydrogen bonding giving rise to organic-inorganic layers. In contrast, CoI_2 forms a high symmetry 3D supramolecular network. It was revealed that replacing I with NO_3 and SO_4 resulted in a network of hydrogen bonding interactions separating metal ions and organic regions. Six different $Co(NO_3)_2$ complexes were obtained by crystallisations at various temperatures (278 K, 295 K – 298 K, 295 K, 298 K and 313 K) and using different solvent ratios. CoX_2 (X=Br, Cl) complexes transformed into 1D polymers which displayed voids occupied by guest water molecules.
Co-grinding of $Co(NO_3)_2$ and bpdo constantly produced crystal structure $[Co(H_2O)_4(NO_3)_2] \cdot 2(bpdo)$, **CoN(E)**.

Crystal structures of Cu(II) and Pb(II) were different, despite the fact that they were prepared similarly. Cu(II) gave z-shaped discrete molecules which extends through supramolecular interaction to form channels accommodating DMSO solvents, while PbX_2 (X=Cl, Br and I) formed 2D coordination polymers with adjacent chains bridged by halides ligands in a sinusoidal shape.

The study has also shown that using the same metal salt but employing different solvents and crystallisation methods can produce different crystal structures. This behaviour was demonstrated by ZnX_2 (X=Br and SCN) compounds. Layering of ethanolic bpdo solution on top of $CHCl_3/CH_2Cl_2$ where the metal had been placed, but not dissolved, gave 2D coordination polymer (**ZnB1**) with metal centres linked by bpdo ligands. A replacement of bromide with thiocynate afforded a zigzag chain coordination polymer (**ZnN**) with adjacent chains connected by hydrogen bonding. The compound forms cavities which encapsulated guest water molecules.
Solvent evaporation produced two different crystal structures (**ZnB2** and **ZnB3**). In each crystal structure, two Zn ions have different coordination geometries: octahedral and tetrahedral. Both compounds form channels where bpdo guest molecules reside.

Crystal structures of gold complexes reported in this thesis revealed that the dipyridyl molecules are protonated. Bpdo was protonated on one end, while BPE and DPE are on both terminals. Protonation induced hydrogen bonding between dipyridyl molecules forming supramolecular chains. The structure is stabilised by interionic interactions, Au···Cl.

Generally, lanthanides and actinides have shown resistance in forming novel hybrid organic-inorganic materials. Synthesis of lanthanides polymers using methanol afforded disordered zigzag polymer, while ethanol produced ladder shaped polymer with channels accommodating $CHCl_3/CH_2Cl_2$ solvents. Kinetics of decomposition for **Gd1** and **Tb1** gave activation energies of 106.3 $kJ.mol^{-1}$ and 50.8 $kJ.mol^{-1}$, respectively. Both compounds are isostructural and based on diffusion mechanisms, D1 and D3. Kinetics of desolvation for

Gd2 and **Gd3** gave activation energies of 9.8 kJ.mol^{-1} and 11.7 kJ.mol^{-1}, respectively and are both based on D3 diffusion mechanism.
A 1D zigzag chain of uranyl nitrate has been synthesised by solvent evaporation. The compound formed channels which accommodate guest water molecules. To our knowledge, this compound is the first of its kind.

This thesis therefore makes a contribution to coordination chemistry, kinetics, structural studies and interactions, and thermodynamics of organic-inorganic hybrid materials. Such studies are of significant importance to understand dynamics and stability of crystal structures and what they can be utilised for. Crystal structure refinement and elucidation have allowed us to analyse the strengths and directions of the intermolecular interactions of various organic-inorganic compounds. It remains impossible to predict all but the simplest crystal structures[1] and this study have confirmed that fact. Nonetheless, this study can contribute to the understanding of which crystal structures form and what can be done to improve crystallisation and design of novel compounds. It has contributed to crystal engineering and structural chemistry of inorganic coordination complexes.

It is hoped that contribution of the work done in this thesis will contribute to new research avenues which will add to the principles of crystal engineering.

References

1. J.D. Dunitz, *Chem. Commun.*, 2003, 545.